Ship detection and measurement of ship motion by multi-aperture Synthetic Aperture Radar

Chuck Livingstone
DRDC Ottawa

Marina Dragosevic;
MD TerraBytes Inc, 1260 Kingston Ave., Ottawa

Shen Chu
Ishuwa Sikaneta
DRDC Ottawa

Defence Research and Development Canada

Abstract

SAR (Synthetic Aperture Radar) GMTI (Ground Moving Target Indication) studies of ship signatures over a ten year period have developed an adaptive approach to the creation of ensembles of adaptive range-history models that characterize ship motion, ship length and ship heading from multi-aperture airborne and space-based radar measurements. The ships being detected and measured are assumed to be rigid bodies that move in response to propulsion and sea motion forces. Non-parametric moving target detection and motion estimation metrics are applied to radar returns from ship targets to represent each observed ship as an ensemble of spatially clustered moving targets whose motions, clustered into domains over the ship target area, estimated metrics are fed back to range-history models to improve the SAR focusing of the ship and to improve the motion estimation accuracy. DPCA (Displaced Phase Center Antenna) moving-target detection algorithms were used to generate lists of moving-target candidate points from two and four aperture SAR-GMTI scenes and the signal data corresponding to these points were analyzed to cancel sampling ambiguities from ships and littoral zone land targets prior to target motion estimation for each sample point. At the end of the estimation process target samples were clustered to extract the ensemble (bulk) properties of the ship target. When highly over-sampled GMTI data are acquired from airborne radars, coherent processing intervals that correspond to ocean wave periods that influence ship motion are obtained and ocean motion estimates can be extracted from the ship data using time-frequency analysis. The incorporation of the ocean motion estimates into the range history set that represents the ship allows fine SAR focussing of the ship image. An example is shown for a 167 m ship transiting off the coast of Newfoundland. The coherent processing interval for space-based SAR-GMTI data is too short for use in sea motion estimation, but the large platform velocity of space radars reduces the SAR sensitivity to sea motion and the sea motion effects on SAR focusing are not too severe for moderate sea states. SAR-GMTI results from 49 ships transiting the Strait of Gibraltar and from 23 ships in the Strait of Georgia used AIS (Automated Information System) reports to validate SAR-GMTI measurements made from RADARSAT-2 data. Results showed that the SAR-GMTI measurements can estimate ship speed to within ± 0.25 m/s, can estimate ship heading to within ± 12.4°, can estimate ship length to within 34.5 m (± 35% of reported ship length) and can estimate ship position to within 37 m at one standard deviation.

Significance to defence and security

Space-based SAR-GMTI R&D (Synthetic Aperture Radar-Ground Moving Target Indication Research and Development) has established the feasibility of detecting moving marine targets and measuring target properties including speed, size, heading and radar cross section. From the data set used in this study for ships that are longer than 100 m and that have been imaged with 3 m to 5 m SAR resolution, GMTI measurement improves ship focus sufficiently to allow a vessel type estimates to be made. This is particularly true for airborne sensor systems that allow coherent observation times up to nine seconds. ISAR (inverse SAR) processing has not been applied to the targets used in this study. Since ISAR implicitly estimates motion as part of its imaging process, comparable results may be obtainable for long-enough coherent observation periods. The minimum coherent observation time for ISAR is unknown. Studies conducted span the full range of ship sizes identified in the Canadian coastal surveillance requirements and include a number of known vessels with length less than 25 m.

A knowledge base, data processing tools and information extraction tools have been developed and tested to show that a space-based SAR-GMTI ship surveillance capability has been developed and is ready for exploitation. Exploitation of this capability as part of Canadian surveillance operations will require that the experimental satellite systems, used for capability development, be replaced with spacecraft that have operational SAR-GMTI modes designed to support a marine surveillance role.

Résumé

Des études en matière de SAR-GMTI (radar à synthèse d'ouverture et indicateur de cible terrestre mobile) menées pendant dix ans sur les signatures de navires ont permis l'élaboration d'une méthode adaptative de création d'ensembles de modèles adaptatifs en fonction de l'historique de la distance, ensembles qui caractérisent le mouvement, la longueur et le cap d'un navire à partir de mesures relevées par radars spatiaux et aéroportés à ouverture multiple. Les navires détectés et mesurés sont considérés comme des corps rigides se déplaçant en fonction des forces de propulsion et du mouvement de la mer. Nous avons appliqué des mesures d'estimation du mouvement et de détection de cibles mobiles non paramétriques aux échos radar de navires afin de représenter chaque navire observé comme un ensemble de cibles mobiles spatialement regroupées dont les mesures estimées du mouvement, regroupées par domaines dans la zone des cibles, sont retransmises aux modèles en fonction de l'historique de la distance pour améliorer la focalisation du SAR sur le navire et l'exactitude de l'estimation du mouvement. Nous avons utilisé des algorithmes de détection de cibles mobiles par antenne à centre de phase déplacé (Displaced Phase Center Antenna – DPCA) pour générer des listes de points s candidats de cibles mobiles à partir de scènes SAR-GMTI à deux et à quatre ouvertures, puis nous avons analysé les données de signaux correspondant à ces points afin d'éliminer toute ambiguïté d'échantillonnage de navires et de cibles terrestres le long du littoral, avant d'estimer le mouvement de la cible pour chaque point échantillon. Une fois l'estimation terminée, nous avons regroupé des échantillons de cibles pour extraire l'ensemble des propriétés du navire. Lorsque des données GMTI considérablement suréchantillonnées sont acquises par des radars aériens, on obtient les intervalles de traitement cohérent correspondant aux périodes des vagues océaniques qui influent sur le mouvement du navire, ce qui permet d'extraire des données de celui-ci les estimations du mouvement de l'océan au moyen d'une analyse temps-fréquence. L'intégration d'estimations du mouvement de l'océan à l'ensemble en fonction de l'historique de la distance représentant le navire permet une focalisation SAR fine de son image. Le rapport comporte l'exemple s'un navire de 167 m se déplaçant au large des côtes de Terre-Neuve. Bien que l'intervalle de traitement cohérent des données SAR-GMTI spatiales soit trop court pour être appliqué à une estimation du mouvement de la mer, la vitesse de plateforme élevée des radars spatiaux réduit la sensibilité SAR au mouvement de la mer, et celui-ci a peu d'incidence sur la focalisation SAR dans le cas d'états de mer modérés. Les résultats SAR-GMTI obtenus de 49 navires traversant le détroit de Gibraltar et de 23 autres dans le détroit de Georgia reposaient sur des rapports SIA (système d'information automatisé) destinés à valider les mesures SAR-GMTI calculées à partir de données RADARSAT-2. Les résultats ont montré que les mesures SAR-GMTI permettent d'estimer la vitesse d'un navire à ±0,25 m/s, le cap à ±12,4 °C, la longueur à 34,5 m près ou mieux (±35 % de la longueur signalée du navire) et la position à 37 m près ou mieux (à un écart-type).

Importance pour la défense et la sécurité

La R et D en matière de SAR-GMTI (radar à synthèse d'ouverture et indicateur de cible terrestre mobile) dans l'espace a démontré la faisabilité de la détection de cibles marines mobiles et de la mesure des propriétés de cibles, dont la vitesse, les dimensions, le cap et la section efficace en radar. D'après l'ensemble des données utilisées durant l'étude, les mesures GMTI améliorent la focalisation suffisamment pour permettre de déterminer le type de bâtiment dans le cas d'un navire de plus de 100 m de longueur imagé à une résolution SAR de 3 à 5 m. Cela s'applique tout particulièrement aux systèmes de capteurs aériens permettant des temps d'observation cohérente de neuf secondes ou moins. Le traitement SAR inverse (ISAR) n'a pas été appliqué aux cibles utilisées dans le cadre de l'étude. L'ISAR permettant d'estimer le mouvement de façon implicite durant le processus d'imagerie, nous pouvons obtenir des résultats comparables pour des périodes d'observation cohérente d'une durée suffisante. La période d'observation cohérente minimale de l'ISAR est inconnue. Les recherches menées visaient toute la gamme de tailles de navires figurant dans les exigences de la surveillance côtière du Canada, dont un certain nombre de bâtiments connus d'une longueur inférieure à 25 m.

Nous avons développé et expérimenté une base de données, des outils de traitement de données et des outils d'extraction de données pour démontrer que la capacité de surveillance spatiale SAR-GMTI des navires est au point et qu'elle a atteint la phase de l'exploitation. Toutefois, l'exploitation de cette capacité dans le cadre des opérations de surveillance canadiennes nécessitera le remplacement des systèmes de satellites expérimentaux (utilisés pour le développement de ladite capacité) par des astronefs munis de modes SAR-GMTI opérationnels et conçus pour jouer un rôle de surveillance maritime.

Table of contents

List of figures

List of tables

Acknowledgements

1 Introduction

Canada has a long and sparsely populated coast line and has both national interest and international obligations to monitor maritime vessel traffic both within and beyond its economic zone boundaries. Figure 1 illustrates the spatial extent of Canadian maritime surveillance concerns [1]. Space-based surveillance sensors provide the only means to address major parts of the vessel traffic monitoring problem.
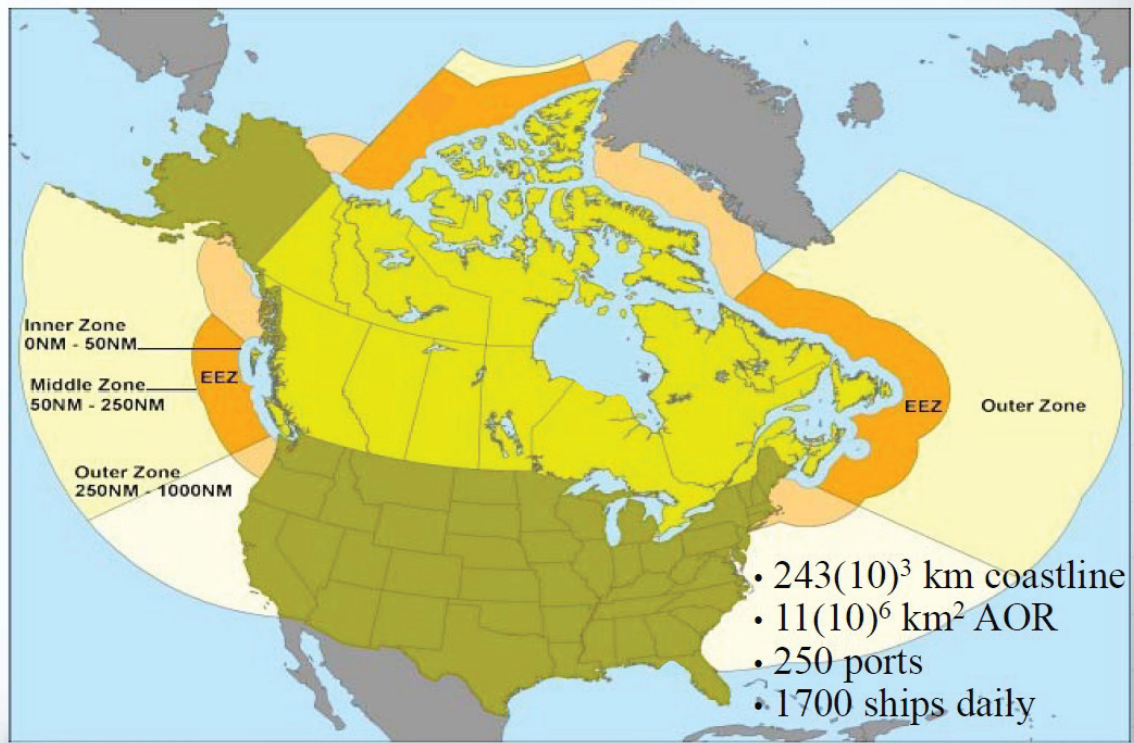
Figure 1: *Canada's areas of responsibilities and maritime surveillance zones.*

The Canadian maritime surveillance problem has many layers [2]. Those parts that are related to marine traffic can be summarized as:

1. Detect targets,

2. Classify targets,

3. Identify targets,

4. Track targets, and

5. Determine the target's intent.

For a defined information confidence level:

- the level of difficulty for implementation,

- the number of different information sources required, and

- the level of effort needed for information integration.

increase as you progress down the list and as you approach sparsely inhabited parts of the Canadian coast.

1.1 The open ocean ship surveillance problem

The ocean surface area covered by the exclusive economic zone (EEZ) and the outer zone in Figure 1 is very large. Currently available surveillance tools that can provide useful information for these areas are space-based, wide swath synthetic aperture radars (SARs) and automatic identification system (AIS) transmissions that are legally required for ships with mass greater than 300 tons. AIS transmissions can be received by space systems and can provide information for each of the five surveillance layers above. Although AIS use is legally required, the ship-based transmitters are under the control of the ship's officers and reports need to be screened by correlation with independent measurements. SAR detection of ship targets provides one approach to AIS validation and the detection of non-compliant vessels. For radar modes that offer large coverage areas (ScanSAR mode variants), ship detections provide geographic position information but provide limited additional information about the ship target.

Large swath ScanSAR modes come in several flavors. The most commonly used modes use a small number of radar beams activated in bursts within the synthetic aperture time of the radar beam. These modes have been designed to map the sea surface to provide information for oceanographic and meteorological applications. Ships that are present in the covered radar swath are embedded in the sea surface returns and only the larger vessels can be reliably detected [1]. ScanSAR modes that are designed for ship detection divide the radar synthetic aperture time into as much as eight beams and tailor the radar operating parameters to optimize ship detection at the cost of reduced or lost sea surface information.

Using current technologies, a space-based SAR system can be optimized for ship detection by employing a specialized, multi-beam ScanSAR mode. The Maritime Satellite Surveillance Radar (MSSR) mode [2] has been designed to detect ships longer than 25 m in open-ocean over a 450 km swath in sea surface conditions up to sea state 5 using RADARSAT-2 and successor radar- surveillance satellites. Two variants of this mode have been developed and are being tested using RADARSAT-2. MSSR mode outputs for ship detections are the geographic coordinates of the radar detections and image chips that contain a few samples of the ship target. The ship target is effectively a dot in the image. The geographic position of the ship dot is computed from the radar orbit and imaging geometry. The MSSR mode beam designs try to optimize the detection of vessels that are embedded in the radar returns from the sea surface.

Although a single satellite such as RADARSAT-2 has insufficient area coverage to seriously address maritime surveillance for the Canadian EEZ and outer zones it is adequate to develop the surveillance technologies that will be used by surveillance radar constellations. The augmentation and eventual replacement of RADARSAT-2 by a radar satellite constellation, RCM [1] will

resolve much of the coverage issue but will be limited by its orbit to providing one or two coverage bands per day in its initial three satellite form. The RCM satellites will carry AIS receivers so that the radar data and the AIS messages will be temporally correlated to within the AIS reporting frequency. MSSR mode ship detection, combined with AIS message interception are expected to work well together in open ocean areas where the number of reporting vessels within the AIS receiving mask is sufficiently small that data are not lost by AIS message collisions. Modelling studies [3] show that AIS message capture degrades rapidly as the number of vessels in a space-based AIS reception mask increases from 1000 to 2000 vessels. The all ships density map for winter 2009 [4] shown in Figure 2 identifies major ports and some coastal areas as potential high density problem areas. Satellite AIS systems whose coverage intersects significant parts of the European North Sea, Mediterranean and Baltic Sea regions will experience signal collision saturation problems. Similar effects are expected along the US eastern coast.

It is expected that combined MSSR SAR and AIS measurements will perform very well for the east and west coast EEZ and outer zones shown in Figure 1. Space-based AIS should work well in sparse traffic areas such as the Canadian North West Passage but the performance of the MSSR modes in coastal areas and areas with narrow waterways is unproven.
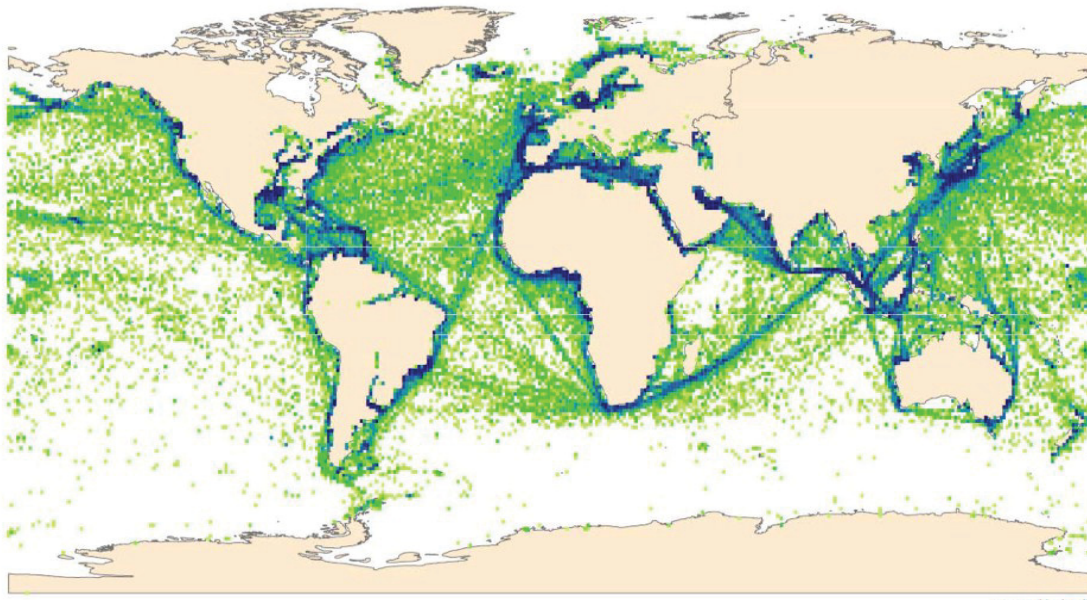
Figure 2: *Global mean ship density from AIS reports from November 2009 to January 2010.*

1.2　The coastal and Arctic archipelago ship surveillance problem

As we move through the inner zone of Figure 1 to the coastal areas and as we move through the Canadian Arctic Archipelago, very large area SAR coverage becomes less significant and the ability to use space-based SAR systems to extract ship target parameters becomes more significant. The significance change is based on several factors: small vessels are more common in the inner zone and many of these are not required to carry AIS transmitters, vessel transits along and near the coast are common, vessels need to be separated from rocks, small islands and

other coastal features and vessel signatures can be embedded in radar sampling ambiguities of nearby land. Radar systems that are capable of providing information to directly determine ship class and motion characteristics use finer resolution than large-area search systems and have smaller coverage swaths.

Space-based SAR surveillance and in land-enclosed shipping channels when small vessels are present requires a different radar observation and auxiliary information strategy than that successfully used in the open ocean. To offset the decreased surveillance reliability, the space-based SAR system properties can be modified to increase the amount of surveillance information that can be extracted from the radar data.

1. Radar information that indicates the size, shape, orientation and scattering center distribution within a ship target becomes important.

2. Dynamic motion of the ship target becomes important.

3. Discrimination between the characteristics of the radar signature of a ship and the radar signature of a shore target become important.

4. Discrimination between ship targets and radar ambiguities of shore targets becomes important.

5. Discrimination between ship targets and rocks, small islands and floating ice forms becomes important.

6. Observation time of day becomes important.

Points 1 and 2 suggest that the use of fine resolution radar modes is important. Point 2 suggests that the use of a multiple-aperture radar that can measure target motion is important. Points 3, 4 and 5 suggest that the use of multiple channel radars that measure different ship target signal properties is important. Point 6 identifies a space based radar satellite constellation issue where multiple satellite orbit planes are in use. Points 1 through 5 indicate that multiple radar channels must operate simultaneously and Point 1 indicates that many radar samples are required over the observed vessel. Most of these requirements create a situation in which the radar coverage swath allowed for ship surveillance is much smaller than that which can be used for open ocean surveillance. If large, nearly coincident, observation swath coverage is required for these regions, a constellation of multiple, closely spaced satellites is required. This surveillance satellite constellation design driver is not compatible with the multiple time of day constellation design driver.

Items 3, 4 and 5 in the preceding list identify a requirement of multiple radar channels that can be used in combination to increase the available information about the observed targets. We note here that polarimetric signature data can provide information to address item 3 and 5 issues. We also note here that target motion measurements by space based SAR-GMTI systems can address item 3, 4 and 5 issues.

Current and planned space-based radars that can provide finer resolution and motion measurement capabilities do not provide sufficiently dense spatial coverage to contiguously map

the width of the inner zone and do not have sufficiently frequent temporal coverage to provide tracking information. Developments in radar technology (high-resolution, wide swath modes with GMTI capability) promise to relax some of the coverage constraint issues over the next decade. Expanded temporal frequency is a satellite constellation design choice that couples to other surveillance requirements and may be addressed over the same period. From the viewpoint of a single, space-based SAR, a ship is a transient target in that it is only seen while the radar illuminates it and may not be seen again near its observed location.

Although space-based AIS coverage provides valuable information to address many or most of the surveillance requirements, vessels that do not carry AIS transmitters are invisible to this information source. Vessels that are operating in high-traffic areas commonly found in the vicinity of major ports may be missed due to AIS signal collisions. Vessels operating in lower density areas that do carry AIS transmitters may not provide useful information because of equipment failures, human error or because the equipment has been intentionally turned off for some reason. AIS alone is not a sufficient surveillance tool, especially in coastal areas.

Space based radars can be used to provide surveillance capability in coastal regions provided that the correct radar modes are available and enabled. These modes typically have fine enough resolution that each vessel is represented by a cluster of detected radar samples so that size and shape information becomes available for classification. When the radar has only a single radar aperture, separation for the vessel return from shore ambiguities and from rocks or floating ice can be problematic. When multi-aperture radar modes are used sea surface and stationary target information can be suppressed to reveal moving vessels, shore ambiguities can be suppressed and vessel direction and speed can be estimated through signal processing. Various trades are available between area coverage and measurement capability.

1.3 The SAR ship-detection problem

SAR detection of ships in transit and the measurement of their motion properties use radar observations of the ship target embedded in its ocean environment. The ship is moving under power along its planned course and is responding to sea surface motion by dynamic, rigid body rotations and translations. The SAR returns from the ship can be focused to form an image of the vessel when its motion model in the radar range direction fits the target dynamics over the radar synthetic aperture time.

The detection of a ship in a SAR image requires that the ship signal components of the received radar data are separable from radar signal components that have different physical origins:

- the sea surface,
- stationary off-shore structures,
- adjacent land features,
- floating ice, and
- shore ambiguities.

For a single-channel SAR, ship detection is based on the brightness contrast between the SAR image of the vessel and the SAR image of the surrounding ocean for the radar polarizations

needed to provide strong radar returns from the ship. Contrast depends on the polarization and the incidence angle. In general, best results for large coverage areas require that the transmitted and received radar polarizations be the same. Co-polarized radar modes, VV (V polarization transmit and V polarization receive) or HH (H polarized transmit and H polarized receive) are most commonly used and the HH combination provides somewhat better ship to sea contrast. Cross-polarized SAR images have been considered for ship detection and ship property estimation by some authors [5] and [6] and may be useful at certain incidence angles. Single channel ISAR (inverse SAR) processing has been very useful for generating focussed images of land [84] and marine [85] targets. INSAR processing treats the target as an ensemble of spatially distributed resolution cells and estimates the motion terms of cell subsets to control the processing function so that local target areas are focused. It works best for airborne sensors that have coherent dwell times that are comparable to the periods of ocean waves whose wavelengths correspond to ship dimensions (> 6 seconds) [85]. Fully polarimetric SAR imaging enhances ship detectability as radar scattering mechanisms for ships differ from those of the ocean surface [7] as illustrated by the color differences in Figure 3 (where the RGB code is: blue for HH+VV, red for HH-VV and green for HV+VH). Ship detection enhancement by the use of polarimetric SAR comes at the same cost as four-aperture GMTI as it requires two physical radar channels and a doubled PRF.
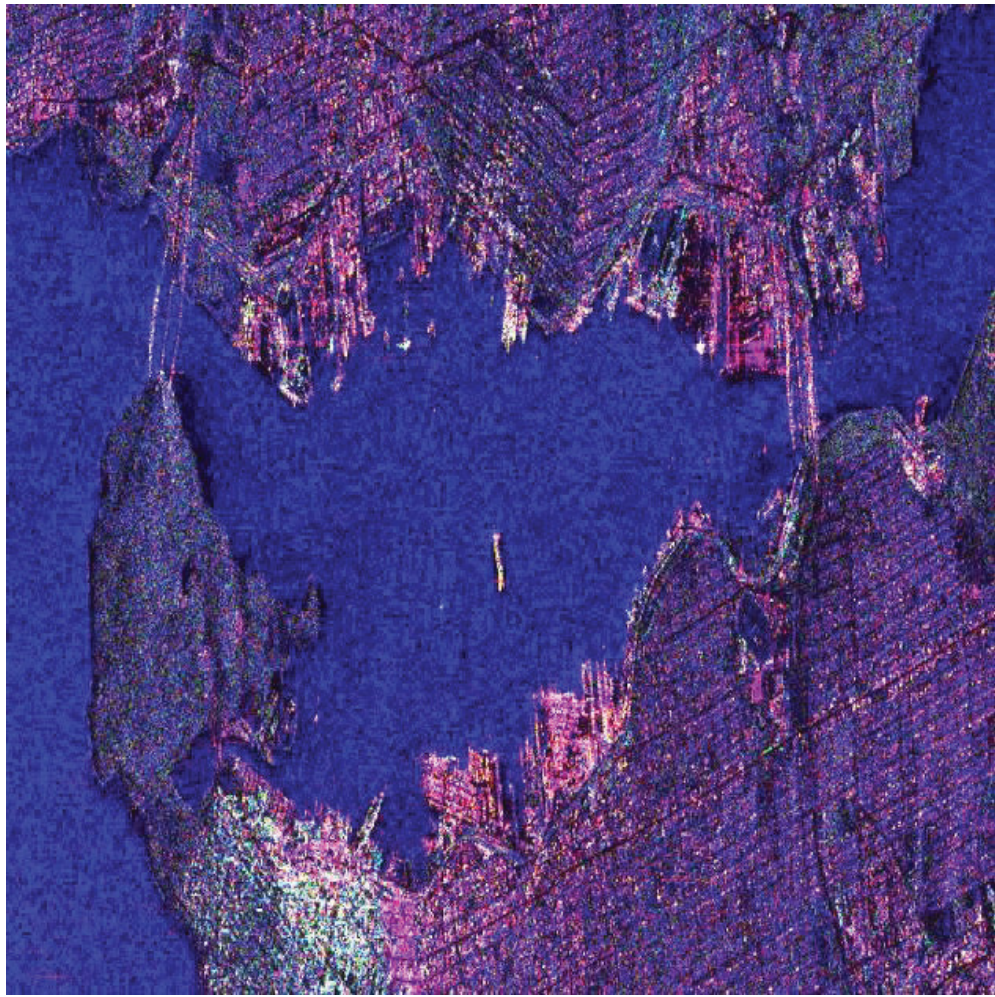
Figure 3: *Polarimetric SAR image of a large ship in Vancouver Harbour.*

Although the polarimetric signatures of ships differ from the signatures of the sea surface, they share many of the features of terrestrial surfaces and polarimetric SAR ship detection may become problematic in coastal areas.

The effects of ship motion are observable in some single-aperture SAR images and some polarimetric SAR images. Observed effects may yield some ship motion information under favorable conditions such as:

- the presence of wakes,

- sufficient signal to clutter and noise ratio (SCNR) to measure Doppler frequency offset due to ship motion, and

- sufficiently long dwell time to allow micro-Doppler tracking.

Detectable single-channel motion effects do not, in general, enhance ship detection for polarimetric radars.

The direct, more reliable and more efficient measurement of ship motion requires two or more active radar antenna apertures that are distributed along the direction of motion of the radar and separate radar receiver channels associated with each aperture. When the sufficient number of physical receiver channels is not available, it is still possible to create similar information channels by time division multiplexing of data streams from different radar antenna apertures. When data from the multiple radar apertures are registered, short-time change detection analysis (GMTI processing) can be used to enhance ship detection by suppressing the local sea returns and by extracting radar return features of the ship that are caused by its motion. Signal processing to extract ship motion information can be used to modify the radar range history models of ship features that are required for SAR processing. The SAR returns from the ship can be focused to form an improved image of the vessel when its motion model in the radar range direction fits the target dynamics over the radar synthetic aperture time. Repeated, iterative signal processing can be used as a tool to enhance the detection of rapidly moving, weak ship targets.

1.4   Report outline

The use of multi-aperture space based radars for marine target measurements has been a research topic for many years and enough has been learned to explore possible surveillance roles for instruments of this class. This report collects and summarizes DRDC research on the application of SAR-GMTI (Ground Moving Target Indication) modes to the detection and measurement of moving ships.

Section 2 presents the scientific background to SAR-GMTI measurements of ship targets.

Section 3 discusses airborne SAR-GMTI observations of ship dynamics.

Section 4 discusses ship motion observations using RADARSAT-2 MODEX measurements.

Section 5 summarizes the key findings of the DRDC work and presents conclusions.

2 The scientific background to SAR-GMTI observations of ship targets

Exploitation of SAR-GMTI technology for the detection of moving ships and for the measurement of their motions requires:

- an understanding of the radar properties needed to make SAR-GMTI measurements,
- an understanding of the radar properties of the targets,
- an understanding of the radar properties of the background scene,
- an understanding of how the target and background signals combine in the radar observation process,
- an understanding of radar sampling effects in information capture, and
- an understanding of features and properties of processed SAR-GMTI signals.

Each of these topics spans a broad area of knowledge that has been accumulated from many scientific disciplines. This section summarizes key features of this knowledge base as they apply to the detection and measurement of ship targets using SAR-GMTI technology.

2.1 Radar properties required for SAR-GMTI measurements

SAR-GMTI is a short-time change detection process that uses a coherent radar designed for synthetic-aperture radar operation to measure the difference between radar range history of a target moving on the surface of the earth and the radar range history that would have been observed if the target was stationary. At a very basic level, the minimum requirements for SAR-GMTI radar can be expressed as follows:

1. The radar receiving antenna must have at least two real apertures aligned in the direction of radar motion. In common parlance, the antennas are aligned in the azimuth direction.

2. The corresponding two-way antenna phase center separation must be stable and known or amenable to calibration.

3. The radar pulse repetition frequency (PRF) must be chosen so that the transmitted radar pulse occurs at least once every time that one of the two-way antenna apertures passes through the spatial point that was previously occupied by a preceding aperture. An integer number of pulses over the aperture transition time is highly desirable. The antenna aperture spacing and the aperture beam width must be selected so that the PRF adequately sample the received signal.

4. The radar receiving antenna beams must be spatially aligned, must observe the terrain that has been illuminated by the transmitting antenna and must have very similar antenna patterns. Ideally the receiving antenna patterns are identical.

5. The radar receiving system requires at least two real or virtual, nearly identical signal channels that capture the signals from each of the receiving antenna apertures. Real receiving channels offer the best signal-to-noise performance.

6. At the output of the receiving channels the relative timing of the signals must be known to within a fraction (usually 10% or less) of the radar range impulse response function and the channels must be phase-coherent.

7. The transfer functions of the receiver channels must have temporally-stable relative group-delays that are known (or can be calibrated) to within a fraction (usually 10%) of the range and cross-range impulse response times for a focused target (after signal processing).

8. The transfer functions of the receiver channels must have known and temporally-stable signal amplitude and signal phase characteristics.

9. The time histories of the radar position, the attitude of the radar antenna and the radar beam pointing must be known by the SAR processor to within the precision required for SAR imaging and image geo-location at the selected radar resolution.

10. The SAR-GMTI signal processor must balance the amplitude and phase characteristics of all active GMTI channels.

11. The GMTI processor output must be in complex signal form.

SAR-GMTI radars require two or more antenna apertures that are distributed in the radar's motion direction. In the simplest design, the radar transmits a signal from the entire antenna and time-multiplexes the radar returns from two along-track-separated receive apertures through a single receiving channel to form two SAR-GMTI data channels from each pair of transmitted pulses (TerraSAR-X configuration). A somewhat more complex configuration uses one physical receiving channel for each antenna aperture. In the case of full antenna transmission, this configuration provides two channels for each transmitted pulse and it can also be used for more advanced modes. When designed to allow the formation of two transmitting apertures with programmable length, a two channel radar can be operated in a time–multiplex (toggled transmit) mode to generate four GMTI channels [8] and [9] (RADARSAT-2 configuration). Each GMTI channel provides one space-time degree of freedom for signal processing.

To extract valid target motion measurements from SAR GMTI data, the following information must be derivable from: external sources, the radar signal metadata, and the radar signal data:

1. the radar frequency,

2. the transmitted signal waveform and power,

3. the number of antenna apertures,

4. the two-way antenna aperture spacing,

5. the two-way antenna beam associated with each aperture,

6. the radar channel transfer function associated with each aperture,

7. the radar noise floor spectrum,

8. the radar position history,

9. the radar beam attitude history,

10. the radar sampling rates and sampling strategy, and

11. the radar range history of each point in the observed scene.

2.2   A ship as a large radar target

For coastal areas the vessel size and aspect ratios vary considerably. Typical vessel length-to-width ratios range from approximately 3:1 for ocean going tug boats to 9:1 for large container vessels. Typical height to width ratios are between 1:1 and 2:1 when mast and derrick structures are included and height is measured from the waterline. Vessel lengths range from 10 m for inshore fishing vessels to 20 m for Arctic supply tugs to 130 m for coastal and Arctic supply vessels to 400 m for very large container vessels. Many fishing vessels operating along the east coast of North America have lengths in the 20 m to 25 m range. With the exception of large tankers loading cargo at off-shore oil production facilities, the large ships pass near or through coastal areas in transit to major sea ports. Most large vessels use dynamic roll suppression to stabilize the ship while under way.

For open ocean navigation commercial ship size is driven by lock and port restrictions, by route length and by economic return. The vast majority of these vessels exceed 50 m in length [10]. Ships that operate on the continental shelves for fishing and oil platform support range in length from approximately 20 m to 100 m. Pleasure vessels as small as 10 m in length are occasionally found in the open ocean environment but are much more common in coastal areas.

2.2.1   Ships as rigid bodies

All ships flex in response to interactions with the sea surface otherwise they would break. Both transverse and torsional modes are present and are driven by the ship structure, the shape of the sea surface, bow slamming into the ocean wave field and propulsion system forces. A ship's response to the motion drivers is determined by the hull design, the construction used, the ship's loading and the ship's operation [11], [16]. Very large vessels are the most flexible. The schematic shown in Figure 4 [12] provides and exaggerated illustration of the longitudinal flexure of a large (> 300m) container vessel.
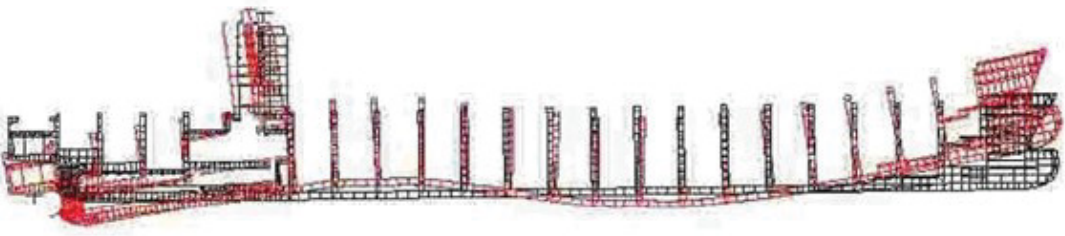
Figure 4: *Schematic illustration of the longitudinal flexure of a > 300 m container ship in a swell wave field.*

The amount of flexure allowed for a specific design is determined by survival in extreme sea conditions and by fatigue life. A typical design life is 25 years. Typically sag deflection (the center is lower than both ends) is greater than the hog deflection (the center is higher than both ends). Drummen [13] notes that an extreme sag deflection of 4.3 m is expected for a 300 m vessel in a large-amplitude, 300 m swell wave. This is a rare case. Measurements on 170 m military vessels [14] showed a one standard deviation hull deflection of .056 m over a 64 m span. In all cases one large-amplitude hull flexure cycle requires several seconds.

Since vessel flexural motion represents radar radial velocities at or below GMTI velocity measurement limits for RADARSAT-2 GMTI modes, the discussions in the rest of this report will treat ships as large, rigid bodies that move on the sea surface with six degrees of freedom in the coordinate system [11] illustrated in Figure 5. Ship flexure and vibration modes can become significant for SAR-GMTI radar systems that have finer resolution.
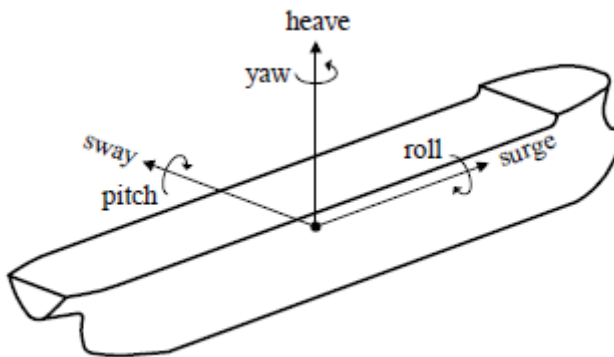
Figure 5: *Rigid body coordinate system for a ship.*

The interaction between a ship and the sea surface depends on the sea surface shape over distances comparable to twice the length of the vessel over the time that is required for the vessel to pass through a spatial point and the vessel speed. It is noted in [12] and [15] that although some ship-ocean interactions can be expressed in terms of linear relationships, others are non-linear and depend on vessel speed. For the rigid-body models used here, non-linear effects become evident in limiting the effectiveness of dynamic roll control for some sea surface conditions and pose some constraints on the vessel orientation with respect to the wave field [12].

Using the rigid body model shown in Figure 5, and noting that most large vessels use dynamic roll control to minimize motion in this direction, we see that vessel heave and pitch are the primary, uncompensated sea-driven vessel motions observable over SAR-GMTI coherent observation time. For the normal range of sea conditions, yaw effects will primarily occur during course changes. For very rough sea conditions, yaw and roll may be dynamically coupled by the sea surface shape. Motion along the sway axis will be mainly surface current effects and motion along the surge axis will be primarily determined by the ship's propulsion system but can be modulated by large amplitude, long-period ocean waves in very disturbed seas.

2.2.2   Ships as radar targets

From the point of view of SAR-GMTI observations, a ship target is a three dimensional structure that extends from the waterline (a variable height surface over the length and breadth of a vessel) to the top of the ship superstructure radar and communications masts (or loading derricks if these are carried). The structural distribution over this height depends on the vessel type and loading. Examples of different vessel configurations are shown in Figure 6. The ship types and configurations illustrated in Figure 6 show a tiny fraction of the vessel types and configurations in the world's oceans and ports but there are enough different features to illustrate ship target properties that are important for SAR-GMTI measurements.

Figure 6: Example ship configurations: (a) Large container vessels and a pilot boat; (b) General purpose cargo ship; (c) Large oil tanker; (d) Naval destroyer.

A very common deck cargo item that forms part of the radar signature of a ship is the marine shipping container, Figure 7. A close examination of Figure 7 as a radar target shows that most of the radar scattering situations listed in Points 1 to 7 below are present at some radar observation angles. The transverse corrugation of the outer shell has a 0.28 m period and 0.04 m depth and can generate either a very large radar cross section or a very low radar cross section depending on the radar frequency and observation angles. There are several standard container sizes with the most common being the 6.1 m x 2.44 m x 2.9 m and the 12.19 m x 2.44 m x 2.9 m models. These units are designed to be stacked up to seven modules deep. The containers are mounted longitudinally on the ship deck as shown in Figure 6(a) and 6(b). Figure 9 shows a radar image of a loaded container cargo vessel.

Figure 7: Standard 12.19 m dry cargo shipping container.

A SAR-GMTI radar illuminates a ship at some, initially unknown azimuth and incidence angle with respect to the ship coordinates system shown in Figure 5. The incident radar signal is scattered from the ship and its deck cargo as each transmitted pulse sweeps over the ship. The scattered signals, that return to the radar, are received at range-times that correspond to the two-way (transmit path plus receive path) distance of each scattering center from the radar (measured in radar wavelengths). The magnitude of the signal received from each radar scattering point on the ship is determined by the radar cross section of that point at the local radar observation angle. For a typical ship, at a typical radar observation angle, the dynamic range of the scattering cross sections can exceed 50 dB.

Although very accurate, detailed radar scattering models can be constructed for any structure whose shape, dimensions and materials are known, these models are expensive to set up and run and the results for each model are specific to the exact configuration of the target object and to the observation geometry and radar frequency used. They are not generally used to interpret radar observations. A small set of basic ideas are useful to know.

1. Metal surfaces whose local deformations are less than 0.25 radar wavelengths over areas comparable to or larger than a radar resolution cell act as mirrors and only provide radar returns when they are observed normal to the surface (specular reflection).

a. Specular reflections from surfaces that are larger than the radar antenna length are only observed for times related to the reflector beam width which will be shorter than the synthetic aperture time. These surfaces provide radar glint returns.

2. Metal surface deformations whose dimensions are comparable to a radar wavelength act as resonant scatterers (e.g., bolt heads and rivets). Their contribution to the radar return from a surface depends on their concentration and distribution over the surface.

   a. Cavities whose dimensions are comparable to a radar wavelength can act as resonant scatterers.

3. Metal structures where three different planes join to form a corner act as radar corner reflectors.

4. Metal plates that are joined at right angles form radar dihedrals whose radar cross section is dependent on the plate sizes and the angle between the radar range vector and the seam joining the plates.

   a. Cylindrical structures fastened at right angles to metal plates form a dihedral known as a top-hat reflector whose radar cross section is independent of the radar aspect angle (for a circular cylinder) and whose radar cross section depends on the cylinder diameter and length and on the radar wavelength.

5. Edges, seams between plates at different orientations and thin (with respect to a radar wavelength) rods and cables act as linear diffraction centers. The orientation of the diffraction centers with respect to the radar wave front and the radar polarization vector will determine the strength of the radar return.

6. Cylindrical structures of various cross sections (cables, posts, rails, masts, spars, etc.) have radar cross sections that depend on the shape and size of the cylinder cross section, the length of the object, its orientation with respect to the radar observation angle and the radar wavelength.

7. The presence of vertical relief allows radar signals to be reflected from one object in a forward-scattering direction, reflect from another object in a forward scattering direction and return to the radar. This is a double-bounce radar return. More complex scattering geometries allow multiple-bounce radar returns to be included in the signals that are received by the radar.

The transmitted radar signal has a defined band width which determines the range resolution of the radar. During range focussing, the complex (amplitude and phase) received signals that lie within one range resolution cell, independent of their physical location of the vessel as illustrated in Figure 8 , are summed to define a radar range sample. Depending on the exact two-way range of a scattering center, its radar returns may be distributed across adjacent range cells.

Radar range vector

Resolution cell tube
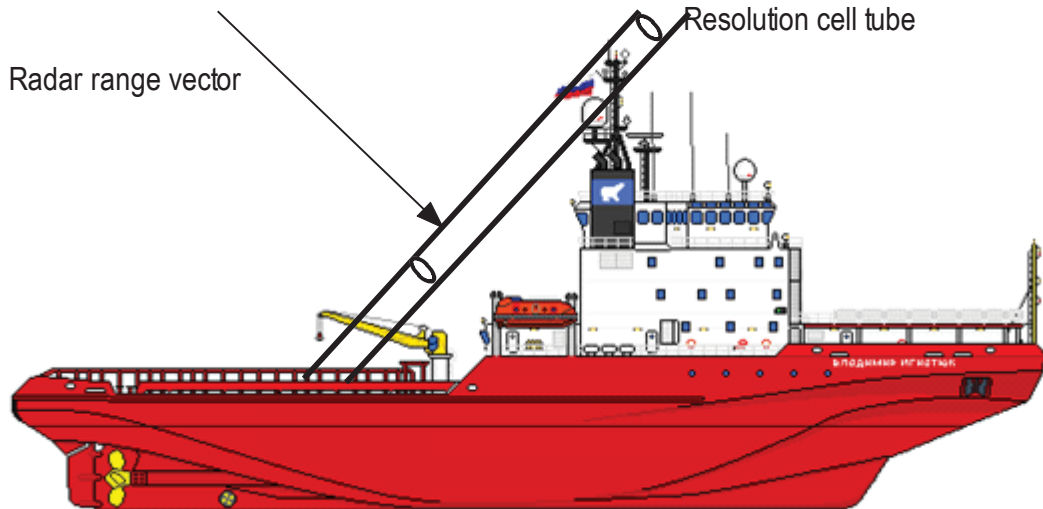
Figure 8: *Illustration of a 100 m long ice breaker showing radar reflection contributors to a single SAR resolution cell.*

Detailed discussions of the properties of multiple reflection radar observations can be found elsewhere [16] and [17] and are not discussed here. There are several simple points that are worth retaining for further consideration:

- In Figures 6(a), 6(b) and 6(d), if the vessels are observed by a radar when the radar range vector is normal to the direction of motion of the vessels and the local radar incidence angle is in the 30° to 45° range, direct reflection from ship components or ship cargo components will be observed in the same radar resolution cell as some sea surface returns. The highest point of the vessel or its cargo will appear at the smallest radar slant range. This is the radar lay-over effect. The summed signals will contain motion effects from each of the signal components.

  - For the near container vessel in Figure 6(a), there will be some radar resolution cells that contain summed signal components from the pilot vessel and from cargo containers. Other resolution cells will contain contributions from cargo containers and the sea surface.

  - For the general purpose cargo vessel in Figure 6(b) the ship resolution cells at the smallest slant range will contain a superposition of the tall cargo towers and the sea surface.

  - For the military destroyer in Figure 6(d), the top of the ship's mast, summed with sea surface returns will occur at the nearest slant range.

- In Figure 6(a), the ship's hull surface forms a radar mirror and the stacked cargo forms a distorted radar mirror. Double bounce signals radar-sea-ship-radar and radar-ship-sea-radar will modulate the sea return by the relative motion of the ship and the sea surface (projected along the radar propagation path) and will sum these signals with those whose direct slant

range are equal to the bistatic slant range for the forward scatter. Double-bounce ship-sea interation is discussed in more detail in Section 4.5.1.

- In Figure 6(d) forward scatter, double-bounce sea returns from the hull sides are likely but the angle of the ship's superstructure will minimize these effects as long as the ship's roll does not create a right-angle between the ship and the sea surface at the appropriate radar range.

- In Figure 6(c), the smooth tanker deck plates act as radar mirrors and return little scattered signal to the radar. Radar returns from the tanker deck will come from pipes, fittings and cargo-handling equipment that are mounted to the deck surface.

For SAR and SAR-GMTI radars, the received signals from each scattering center are accumulated over the radar pulses within one synthetic aperture time. This is the time interval during which the scattering center lies within the cross-range, two-way real aperture of the radar as it passes over the ship. In principle, SAR processing uses a model of the range history of each dominant scattering center on the ship to spatially reposition signal contributions over a synthetic aperture time (focus the signal) to define a cross-range impulse response for that target component. The set of all two-dimensional, range / cross-range impulse-responses, sums to form the complex image of the ship. Constructive and destructive interference will be present in the summing process. From a SAR image point of view, the peak of each two dimensional impulse response function can be considered to be a constant-range tube which is centered at the radar as illustrated in Figure 8. For vessels undergoing complex motions, the range-history modelling based on ship and cargo structure can be a challenge.

2.2.3   Ship motion implications for SAR-GMTI measurements

Noting that a strip-mapping SAR GMTI resolution cell is a constant-range cylinder whose cross sectional area is a slice through the peak of the radar impulse response function, the complex sum of radar reflections of all items in the cell forms a point in the complex image. For the steep incidence angles (30° to 45°) used by RADARSAT-2 and most other space-based SAR-GMTI systems, the vertical distribution of ship and cargo features will determine how various elements combine within radar resolution cells and, for dynamic changes in the ship attitude, how the radial (radar range direction) motions of the ship and cargo components are distributed over the ship image. Radar lay-over and shadowing effects are common.

For SAR-GMTI measurements of ship motion, the ship can be considered to be an asymmetrical mechanical low-pass filter that has little response to ocean waves whose wavelengths are less than the ship dimension in the direction that is normal to the ocean wave crests and whose response to longer wavelengths is determined by the wavelength, the ship speed and motion direction with respect to the ocean wave field and by the ship's mass to buoyancy relationship. For large to medium sized ships operating in relatively calm seas, the sea motion effects are small. Small ships can be quite responsive to local sea motion components whose wavelengths are greater than the ship dimensions.

A moving ship can be modelled as a three dimensional set of radar scattering surfaces that is transiting the sea surface, driven by its propulsion system, and responding to sea motion components that have sufficient magnitude and scale length. When the three dimensional structure of the ship is taken into account, dynamic attitude variations at the ship's center of

buoyancy can be resolved about the axes shown in Figure 5. The attitude variations act through the position vectors to each radar-observable point on the ship and its exposed cargo to define a local relative velocity vector for each point with respect to the ship's center of buoyancy. The time history of each of these relative position or velocity vectors, projected onto its radar range vector over the synthetic aperture time of the radar, defines the range history signal model for each scattering point. The range history for each point contains the bulk motion of the vessel (the motion of its center of buoyancy) and the range-projected relative motions of each vessel component with respect to the center of buoyancy. The motions that are generated by the ship's response to the sea surface will not be constant over the radar observation period but will contain acceleration effects due to the rotational motions. In the worst case each radar resolution cell that contains ship information could require a different range history to focus it.

A SAR groups radar returns from a target by radar range. Where the target contains multiple radar scattering centers at the same range, these are summed and are only separable in terms of their cross-range signal spectra. In Figure 8, the ship is travelling away from the radar and the constant range tube that represents a single radar resolution cell sums radar returns from the antenna mast, the ship's crane and part of the ship's deck. If this ship is pitching in the sea, the antenna mast component and the crane and deck components will be moving in opposite relative range directions. An examination of Figure 6 reveals a large number of possible combinations for different radar incidence and aspect angles with respect to the ship's direction of travel. Ship, cargo and sea surface components that are mapped at the same radar range may or may not be separable through SAR processing in terms of their range histories.

We can use Figure 5 to generate a conceptual model of the ship dynamics by examining the dynamics of the radar-observable components of the three dimensional ship with its deck cargo. Choose the center of buoyancy as the coordinate reference and choose time t_0 as the time at which the ship is centered in the synthetic aperture time, T, of the radar. Choose an earth-referenced ship coordinate system x_S, y_S, z_S where:

- x_S = the surge axis in Figure 5,

- y_S = the sway axis in Figure 5,

- z_S = the heave axis in Figure 5

and fix the heave axis to the local earth normal in geodetic coordinates. The x_S axis lies along the geodetic heading of the ship. Chose a ship-fixed coordinate system x, y, z so that $x=x_S, y=y_S,$ and $z=z_S$ when the ship is level in the water. From the radar-scattering point of view, the ship and its deck cargo can be described as the set of vectors $\{r_i = [x_i, y_i, z_i]\}_{i=1:M}$ where each vector points to a ship scattering center (a physical point) that contributes to the set of radar returns that describe the ship. M is very large.

Looking at the wave induced ship dynamics, the ship has a time varying:

- yaw angle, $\alpha(t-t_0)$,

- roll angle, $\beta(t-t_o)$,

- pitch angle, $\gamma(t-t_0)$

- surge displacement, $h_x(t-t_0)$,

- sway displacement, $h_y(t-t_0)$, and

- heave displacement, $h_z(t-t_0)$

where $-T/2 \leq t-t_0 \leq T/2$.

The attitude dynamics relate $[x_{Si}(t), y_{Si}(t), z_{Si}(t)]$ to $[x_i, y_i, z_i]$ by

$$\boldsymbol{r_{Si}(t)} = \begin{bmatrix} x_{Si}(t) \\ y_{Si}(t) \\ z_{Si}(t) \end{bmatrix} = [\Gamma(t)][B(t)][A(t)]\begin{bmatrix} x_i \\ y_i \\ z_i \end{bmatrix} \; where$$

$$[\Gamma(t)] = \begin{bmatrix} \cos(\gamma(t)) & \sin(\gamma(t)) & 0 \\ 0 & 0 & 1 \\ -\sin(\gamma(t)) & \cos(\gamma(t)) & 0 \end{bmatrix}, [B(t)] = \begin{bmatrix} 0 & 0 & 1 \\ \cos(\beta(t)) & \sin(\beta(t)) & 0 \\ -\sin(\beta(t)) & \cos(\beta(t)) & 0 \end{bmatrix} \; and$$

$$[A(t)] = \begin{bmatrix} \cos(\alpha(t)) & \sin(\alpha(t)) & 0 \\ -\sin(\alpha(t)) & \cos(\alpha(t)) & 0 \\ 0 & 0 & 1 \end{bmatrix}\begin{bmatrix} x_i \\ y_i \\ z_i \end{bmatrix} \tag{1}$$

Over the synthetic aperture time, the ship position on the earth's surface is defined by the earth-centered, earth-fixed (ECEF) position vectors $\boldsymbol{R_{Ship}}(t-t_0) = \boldsymbol{R_E}(t-t_0) + \boldsymbol{H}(t-t_0)$ where $\boldsymbol{R_E}(t-t_0)$ defines the nominal ship trajectory on the earth ellipsoid and $\boldsymbol{H}(t-t_0)$ is the time-varying vessel heave displacement along the z_S axis at time $t-t_0$. In the earth coordinate system the ship scattering centers are at positions $\{\boldsymbol{S_i}(t-t_0) = \boldsymbol{R_{Ship}}(t-t_0) + \boldsymbol{r_{Si}}(t-t_0)\}$.

During the radar observations of the ship, the radar follows a trajectory defined by the time history of its position vector $\boldsymbol{R_{Rad}}(t-t_0)$. Defining the radar position vector in the ECEF coordinate system used to define the ship position, the radar observes the ship as an ensemble of radar targets with radar cross sections are $\sigma_i \, m^2$ and whose range vectors are in the set

$$\{\boldsymbol{R_i}(t-t_0) = \boldsymbol{R_{Rad}}(t-t_0) - \boldsymbol{S_i}(t-t_0)\} \tag{2}$$

Defining the radar range as the magnitude of $\boldsymbol{R}$, $R_i = |\boldsymbol{R_i}|$ and reordering the radar returns from the ship scattering centers from the smallest to the greatest value of R_i, the ship returns for a radar pulse that was transmitted at time t will appear at the radar receiving antenna over the time interval $dt = 2/c(R_{imax} - R_{imin}) + \tau$, where c is the speed of light and τ is the duration the radar pulse code, starting at time $2R_{imin}/c$.

The set of all samples of R_i over the time interval T is the range history of scattering center i.

Noting that the ship motion has a displacement component that applies to all scattering centers and a rotation component that imparts different motions to different scattering centers, the vector manifold, $\{\boldsymbol{R_i}\}$ can be rewritten as

$$\{\boldsymbol{R_i}\} = \boldsymbol{R_{Rad}} - \boldsymbol{R_{Ship}} - \{\boldsymbol{r_{Si}}\} \tag{3}$$

the range history of each scattering center on the ship can be expressed as the range history of the ensemble of scattering centers (the ship) and the range histories of the individual scattering centers with respect to the ship. This has important implications for SAR-GMTI measurements.

The radar return from scattering center i at time t-t_0 will contribute the complex signal

$$s_i(t - t_0) = \frac{AH(\tau)\sigma_i}{R_i^4(t-t_0)} e^{-j\frac{4\pi R_i(t-t_0)}{\lambda}},$$

(4)

where A contains the radar equation constants, $H(\tau)$ is the radar pulse code and λ is the radar wave length, to the output of the radar receiving antenna. The signal output from the receiving antenna is the phasor sum of the time-ordered set of the radar returns from all M scattering centers on the ship. The time t-t_0 in the synthetic aperture time T is not continuous but is sampled by the radar PRF so that the radar returns represented by equation (4) form a set of discrete signal samples. These signals are sampled at high frequency in the radar to quantize the range code for processing. Each sampling process captures the phasor sum of all signals present at the sample time.

During the range focussing part of SAR processing, the range histories of all received signals for each radar pulse are grouped in time intervals of ρ/c by the range compression process, where ρ is the range resolution cell length, and the phasor sum of all processed signals for reach range cell forms the range sample of the data. Similarly, a cross-range model of the target range history is used to combine all similar range histories in each range resolution cell (taking into account systematic range migration effects) into a single, cross-range impulse response for each cross-range target position. If the signal models used for processing are a good representation of the composite received signal, the processor output is a focussed SAR image [18] similar to that shown in Figure 9.
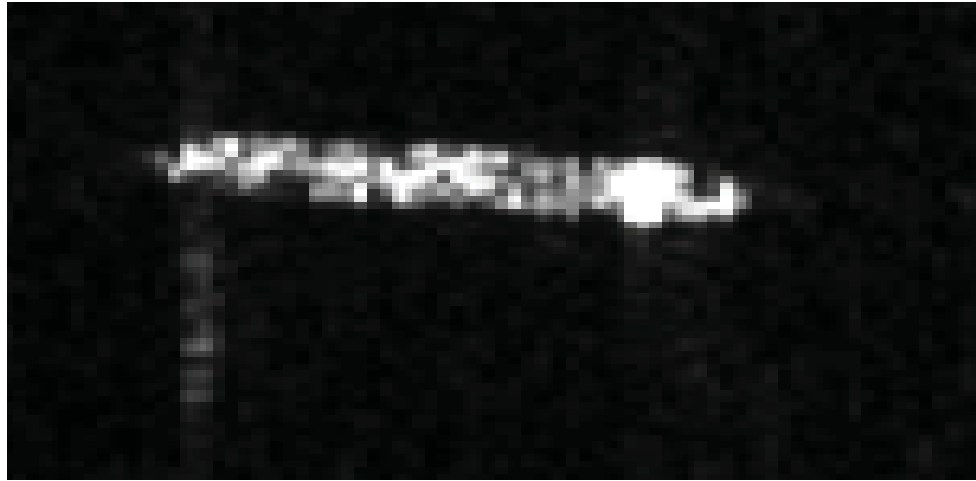
Figure 9: *A SAR image of a container ship moving in the radar range direction in a calm sea.*

In practice, this only works if the range-histories of all scattering centers on the ship are dominated by the translational motion of the ship. This means that the manifold $\{r_{Si}\}$ in equation (3) contains little differential motion. If this is not the case, a ship image similar to that shown in Figure 17 results even when the bulk motion estimates are valid. This badly distorted image can

be refined through more detailed signal analysis if the observation time is long enough. The analysis and processing requirements for the compensation of sea motion dynamics will be discussed later.

Although the number of radar scattering centers, M, that contribute to the radar signature of a moving ship is very large, the number of focussed resolution cells representing the ship is much smaller. The ship shown in Figure 9 is similar in form to the most distant container vessel shown in Figure 6. Figure 9 has 296 SAR resolution cells that can be associated with the ship. When we look at the role of phasor sums in the signal processing flow, it becomes evident that the output of a SAR-GMTI processor will be dominated by the strongest radar scatterers that are mapped to each image cell location.

Although the scattering center model, based on the geometrical structure of a ship and the ship motion is instructive, and does reveal some useful information, it does have some serious limitations in practical use in that:

- The model is based on the motion of the center of buoyancy as the prime reference for ship dynamics and the center of buoyancy lies within the vessel and is not observable by the radar.

- A moving ship, detected in a radar image is an unknown target with initially unknown speed and heading and is moving on a sea surface that has unknown dynamics.

- Bulk motion of the vessel will be estimated about the radar return centroid of the ship and this will be determined by the position of the strongest radar scatterers carried on the ship.

- The inference of sea motion from the analysis of SAR-GMTI signals will be biased by the physical locations of the strongest radar scatterers.

From the form and content of Figure 9, it is reasonable to treat a ship target as an ensemble of individual, closely spaced, radar resolution cells for SAR-GMTI analysis and information extraction.

2.3 The ocean as a radar target

The ocean surface dynamics are driven by wind fields and, in a local area, the normalized radar cross section σ^0 of the sea surface reflects the capillary wave field generated by the local wind. SAR response to wind-sea interaction is used to measure oceanic wind fields to drive meteorological models and has been thoroughly studied for many years [19] [20]. SAR observations of the sea surface have driven the development of a complete sub-discipline of radar remote sensing [21] and [22]. Ocean waves of interest for SAR-GMTI measurements of ships are generated by wind-sea interactions [23]. Short (capillary) wave fields determine the radar reflectivity of the sea surface through a resonant Bragg scattering mechanism where the significant sea surface wavelength, λ_S, is related to the radar wavelength, λ_R, and the local incidence angle, θ, by

$$\lambda_S = \frac{\lambda_R}{2\sin(\theta)}\,. \tag{5}$$

For co-polarized radar observations, the radar brightness of the sea surface is a function of both the local incidence angle and the aspect angle between the radar range vector and the wind vector that is generating the capillary wave field [20]. Figure 10 [20] illustrates the relationship between the radar cross section of the ocean at C-band and local incidence angle for wind speeds between 0 m/s and 22 m/s for 546 scenes centered on oceanographic meteorological buoys. In this figure, the radar noise floor is captured by the parameter σ^0_{NE}.
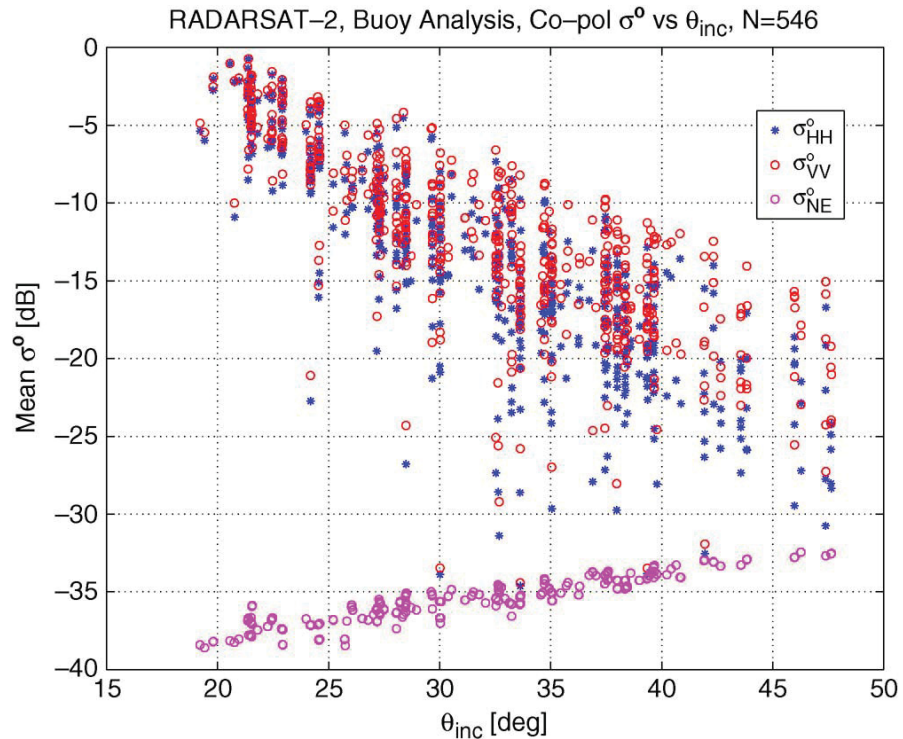
Figure 10: C-band radar cross section of the sea surface as a function of incidence angle.

At coarse radar resolution, the radar sea return image shows large scale ocean features and the scene intensity is determined by the integral of the local radar cross section over the radar resolution cell. In broad terms, radar observable features of the sea surface become visible when several radar resolution cells (nominally, at least four to ten cells are required) span the characteristic dimension of the observed feature. Ship detection in coarse resolution radar scenes depends on the contrast between SAR image cells containing a ship and cells containing only sea returns.

For co-polarized radar observations, the mean radar cross section of the sea surface is a multi-variable function that depends on [24]:

1. the radar frequency,

2. the local radar incidence angle,

3. the wind speed,

4. the wind direction relative to the radar look direction, and

5. the sea surface viscosity.

The vertical spread in Figure 10 results from: the wind speed, relative wind direction and sea surface viscosity terms of the radar cross section [20].

It is evident that the radar clutter-to-noise ratio (CNR) decreases with increasing radar incidence angle. This enhances ship detection capability at large incidence angles. It is also evident that sea clutter returns become increasingly important at small incidence angles and can hamper ship detection for coarse resolution radar modes. SAR GMTI processing can be used to suppress sea clutter and enhance the radar ship detection probability. This capability promises to be important for wide-swath, coarse resolution surveillance operations but it does impose swath width constraints. SAR GMTI clutter suppression can also be important in cases where only small incidence angle radar beams are available over time-critical sites of interest and target motion in the scene contains significant information.

At coarse radar resolutions, the relationship between the wind speed and the radar cross section of the sea surface has the form shown in Figure 11 for HH polarized C-band radar observations.

The point scatter in Figure 11 is determined by the statistical variation of the measurements and the angular terms of the radar-cross section / wind speed relationship. The parameter U10N in Figure 10 is the measured wind speed adjusted to 10 m above the sea surface. Application of the semi-empirical CMOD 5 wind-speed retrieval model [25] combined with the VV to HH polarization scaling ratio [20]

$$\frac{\sigma_{VV}^0}{\sigma_{HH}^0} = 0.283\exp(2.452\theta_{inc}) + 0.350 \tag{6}$$

yields RADARSAT-2 wind measurements UHH shown in Figure 12. These data are compared to the buoy wind measurements, U10N to validate the accuracy of the model.
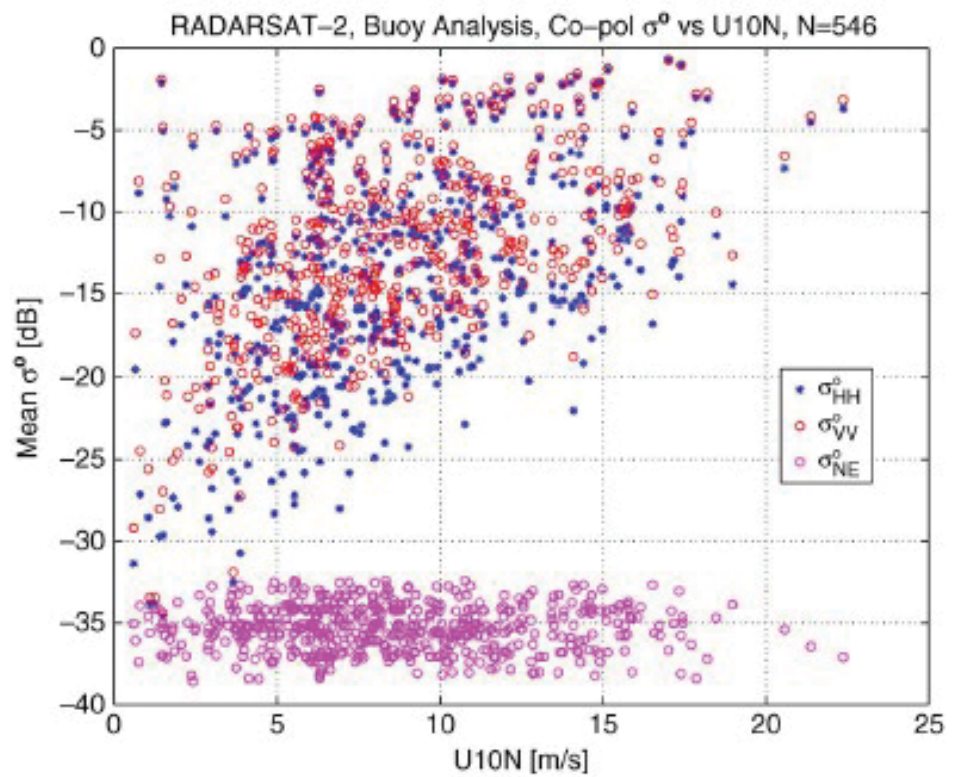
Figure 11: *Sea surface, normalized radar cross section for an HH polarized C-band radar.*
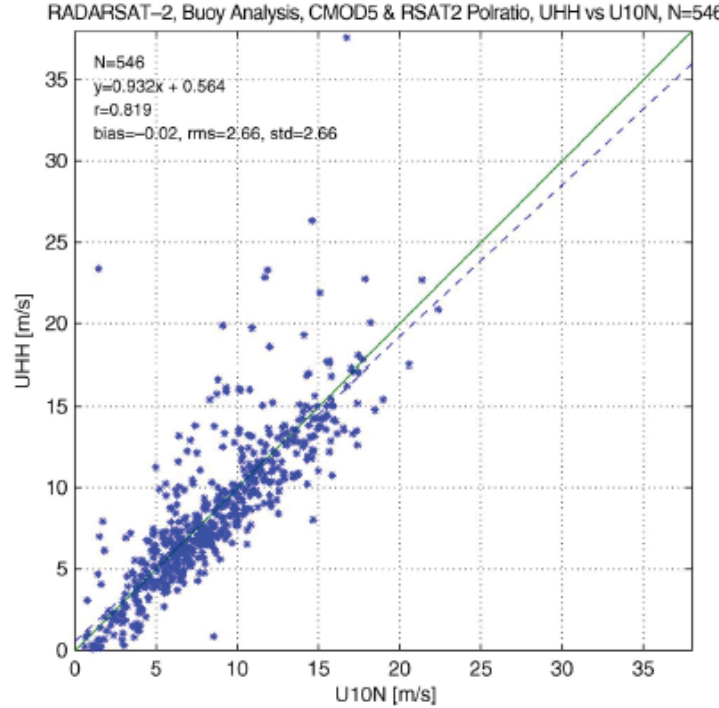
Figure 12: Radar derived wind speed compared to buoy measurements.

The point scatter in Figure 12 is determined by the statistical variability of the data and limitations of the model that links radar cross section to wind speed measurement when observation angle dependences are accounted for.

The relationship between wind speed and co-polarized ocean radar cross section generated by geophysical model functions such as CMOD5 [25] contain a wind direction dependence of the form [26]:

$$\sigma^0 = B_0[1 + B_1\cos(\varphi) + B_2\cos(2\varphi)]^z \tag{7}$$

where the coefficients B_0, B_1 and B_2 are functions of wind speed, local incidence angle, radar polarization and radar frequency, φ is the angle between the local wind direction and the ground projection of the radar range vector and z is a model tuning parameter. The wind direction angle φ has a 180° directional ambiguity.

Wind-driven wave fields grow through non-linear interactions between wind stress on the water surface, gravity, and the resulting sea motion over the time and distance needed to create a wind-wave spectrum [23] where non-linear wave-wave interactions generates longer period waves from shorter period waves. Results from the Joint North Sea Wave Project (JONSWAP) experiments [27] showed that the wind-generated wave spectrum is dependent on the fetch (the distance from the lee shore to the measurement point or the scale distance over which the wind field is constant) as shown in Figure 13.
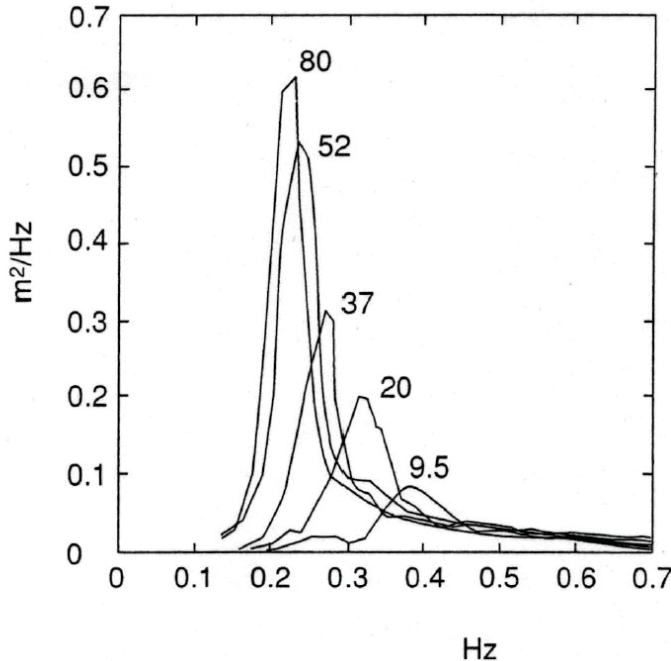
Figure 13: Spectra of fetch-limited wind waves [27] labeled by the fetch in km

When fetch limitations are not present wave spectra developed from the theoretical developments in [23] come very close to the semi-empirical Pearson Moskowitz wave spectrum (parametric in wind speed) shown in Figure 14.
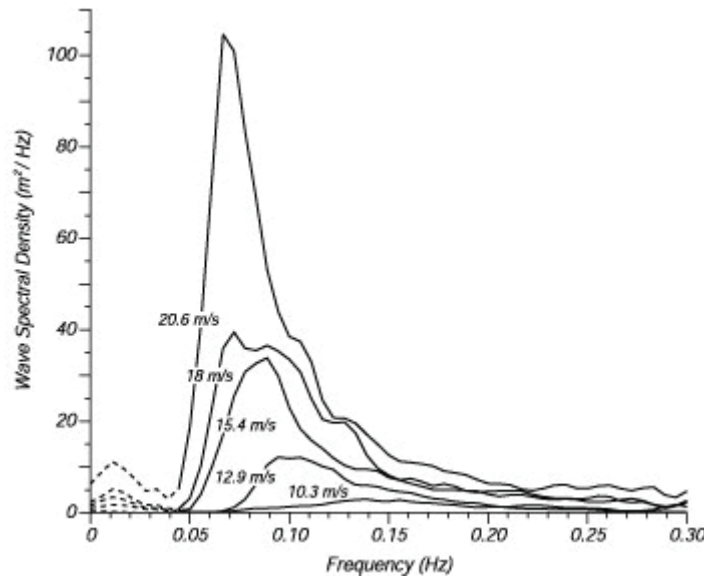
Figure 14: Pearson-Moskowitz wave spectrum.

Subsequent work [28] showed that the wind energy transfer efficiency decreases with wave age (fetch) as the wavelength increases and the phase velocity of the wave approaches and then

exceeds the wind speed. The wind-wave phase velocities are distributed over approximately $\pm 80°$ with respect to the wind velocity vector [27] with the most wave energy being found near the wind direction vector. Analytically, the Pearson-Moskowitz wave spectrum that models the empirical data shown in Figure 14 can be expressed as [23]

$$F_{PM}(f) = \frac{\alpha g^2}{(2\pi)^4 f^5} exp\left[-\frac{5}{4}\left(\frac{f_{PM}}{f}\right)^4\right] \tag{8}$$

where:

- F_{PM} is the wave spectrum,

- f is the wave frequency in Hz,

- $\alpha = 0.0081$ is a constant,

- g is the acceleration of gravity,

- $f_{PM} = 0.13\frac{g}{U_{10}}$ is the peak frequency of the wave spectrum, and

- U_{10} is the wind speed at 10 m above the sea surface.

Wave energy and wind drag considerations [23] result in a wave directional distribution

$$F(f,\theta) = F_{PM}\frac{cos^{2p}\left(\frac{\theta}{2}\right)}{N_p} \tag{9}$$

for a growing wind-sea where:

- θ is the angle between the wave phase velocity and the wind direction,

- $p = 9.77\left(\frac{f}{f_{PM}}\right)^\mu$ is a frequency scaling factor,

- $\mu = \begin{cases} 4.06, & f < f_{PM} \\ -2.34, & f > f_{PM} \end{cases}$ is the wave-frequency-dependent exponent, and

- $N_p = 2^{1-2p}\pi\frac{\Gamma(2p+1)}{\Gamma^2(p+1)}$ is the spreading factor normalization.

The phase velocity or celerity of ocean waves is a dispersive function of wavelength λ_W and depth d and is usually expressed in terms of the depth to wavelength ratio, d/λ_W in three regimes as indicated in Table 1.

Table 1: *Ocean wave regimes and phase velocity.*

Relative Depth λ_W/d	Wave regime	Wave celerity V_W	Wave length λ_W
< 0.05	Shallow water	$\sqrt{gd}$	$T\sqrt{gd}$
$0.05 < d/\lambda_W < 0.5$	Intermediate depth	$\sqrt{\dfrac{g\lambda_W}{2\pi}\tanh\left(2\pi\dfrac{d}{\lambda_W}\right)}$	$\dfrac{gT^2}{2\pi}\tanh\left(2\pi\dfrac{d}{\lambda_W}\right)$
> 0.5	Deep water	$\sqrt{\dfrac{g\lambda_W}{2\pi}}$	$\dfrac{gT^2}{2\pi}$

In Table 1, g is the acceleration of gravity and T is the ocean wave period in seconds. The Pearson Moskowitz wave spectrum peaks at wave frequency .075 Hz for a long-term 20 m/s wind. This corresponds to a deep water wavelength of 277 m. In most SAR-GMTI measurements of ships occur at lower wind speeds and swell waves with wavelengths of 100 m and greater propagate into the observation area from previous, distant storm systems. From the relationships in Table 1, swell waves whose wavelengths approach 200 m will begin to show refraction effects as they enter continental shelf regions and sea-bottom effects on wave direction and steepness can become significant near coastlines.

The relationship between the local wind field and the radar cross section of the sea surface provides a means to map and observe large-scale ocean and wind features. These are readily seen over large areas using coarse radar resolutions.

Starting from the deep water wave celerity (phase velocity) and wave length relationships in Table 1 we see that the celerity can be expressed as

$$V_W = \frac{g}{2\pi f_W} \tag{10}$$

where f_W is the wave frequency shown in Figures 13 and 14. For any wind speed, there is a continuum of ocean wavelengths each of which has a different phase velocity. The radar returns from the sea surface are primarily determined by the resonant Bragg waves, equation (5), that form the sea surface scattering patches. The Bragg waves are riding on the surface of longer wavelength ocean waves that are superimposed to form the spectra in Figures 13 and 14. The water surface carrying the Bragg wave patches oscillates vertically and the radar observation point moves circularly (wave orbital motion) with velocities that are determined by the wavelengths and wave amplitudes that are superimposed.

When the radar resolution is significantly finer than the wavelengths present in the ocean wave field, the radial component of wave orbital motion, generates cross range (azimuthal) shifts in SAR images and makes the wave field visible to the radar through a process known as velocity bunching [24], [29]. Although other SAR modulation effects are present in sea surface imaging, the velocity bunching mechanism is the primary means by which ocean wave fields become visible in SAR images of the sea surface and in loose floating ice. The SAR response to ocean wave fields determines the local signal-to-clutter ratio for ship targets, Figure 15, and the ocean surface motion components that are captured in the radar signal and are coupled into SAR-GMTI

measurements of ship motion. Aspects of the properties of scattered signals and their influence on SAR measurements of marine targets are discussed in [17].

In Figure 15, the ship image amplitude has been scaled to allow observation of the sea surface. The observed swell wavelengths are long enough in this case to have some effect on the ship motion.

Figure 15: *Large container vessel travelling in the radar range direction in a wave field that contains ~ 100 m wavelength swell components.*

2.4   Properties of SAR-GMTI measurements for ship observations

A SAR is a fully coherent radar that captures the time-history of radar returns to construct an image of the observed terrain. Most SARs are pulse-compression radars where a relatively long encoded radar pulse is transmitted and is compressed to a range-length $\rho = \frac{c}{2W_R}$, where c is the speed of light in free space and WR is the radar bandwidth, by a convolution of the received signal with a model of the radiated pulse. All signals that lie within the real aperture of the radar at each radar range contribute to the focused image point in the SAR signal spectrum. The signal processing uses a model of the temporal history of the radar range to each point on a surface to temporally reposition signal components within the real aperture in order to create a focussed image of the point. SAR principles and signals and signal processing possibilities are well understood and can be found in many books such as [30], [31], [32]. This section of the report focuses on specific points that relate to SAR-GMTI measurements of moving ships.

To place the following discussions in context it is useful to note that the ship target responds to both its propulsion system and to ship-scale sea surface motion as discussed in Section 2.2.2 and that the ship signal, displaced by its motion, is superimposed on a moving ocean surface as discussed in Section 2.3. The ship motion and the ship-sea signal interactions are discussed in detail in the rest of this report in terms of their effects on SAR-GMTI measurements.

2.4.1   Target motion effects and range-history models

The synthetic aperture imaging process for moving targets is identical to that for fixed targets in that both require models of the range history of a target point to create a focussed image. For fixed targets, the range history of every point is based on the assumption that image points do not move with respect to each other and that the imaging geometry combined with the motion of the radar system with respect to all target points at a common range provides sufficient information to create the required model. For a simple moving target case where all observable elements of the target move over the earth surface with a constant velocity, the moving target model must take into account both the motion of the radar with respect to the fixed terrain background and the motion of the radar with respect to the target. These are two different models and the model that focusses the background does not correctly focus the target and the model that focusses the target does not correctly focus the background. The terrain or the target, when processed with the appropriate model, will be correctly positioned geographically when the imaging geometry is accounted for.

For a greatly simplified range-Doppler radar processing mode, the range history difference between the two cases can be expressed in terms of a difference in FM rate for the signals scattered from the two target types. Figure 16 illustrates the effect of FM rate mismatch between the received signal and the range history model on the image magnitude on the focus of a point in a scene for a linear FM chirp with a rectangular pulse envelope [33]. The degree of focus degradation depends on the effective FM rate error. A 4% FM rate error results in a peak impulse response reduction of 6 dB and impulse response broadening by a factor of ~ 3.3.
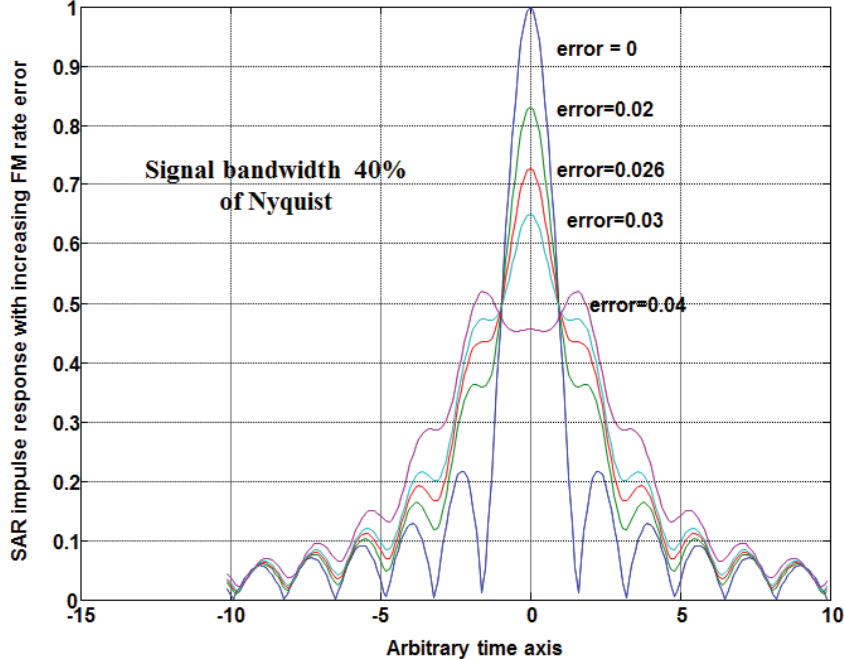
Figure 16: *The effect of range-history model FM rate mismatch on SAR focus.*

A radar range history is defined over the time required for the real-aperture of the radar to pass over an observation point in the observed terrain. The cross-range radar signal spectrum of the observed point is proportional to the time derivative of the range history of the point. When a moving target trajectory is centered at a fixed terrain point, the Doppler centroids (DCs) of the fixed point and the moving target cross-range signal spectra differ due to the difference in projected radial velocity of the two target types. These signal spectra are superimposed in the SAR signal set that is processed to form an image.

Independent of the range history model that is used for processing, the DC difference between the moving target and the stationary background spectra at the same physical location will result in a relative displacement of the moving target and stationary terrain in the cross-range direction by a scaled image distance [34]

$$d_A = \left(R \frac{v_R}{V_{Rel}} \right) mod(R\beta) \tag{11}$$

where: R is the radar range of the target, v_R is the residual radial velocity after compensation by the range history model used in the signal processing model, V_{Rel} is the relative velocity of the radar platform and the target, mod( ) is the modulo operator and β is the radar antenna beam width that has been processed to create a SAR image. The commonly used formula is $R\,V_R/V_{Rel}$. The modulo operator in equation (11) accounts for rare cases where V_R/V_{Rel} exceeds the real beamwidth β.

This relative-velocity-dependent displacement is responsible for the ocean wave velocity-bunching phenomenon. For general moving target observations, the complex, moving

target image signal is always superimposed on the complex signal from the background terrain whose cross-range location is given by equation (11).

The cross-range SAR signals are sampled at the radar PRF by the radar illumination-reception cycle and so the range histories of all points in a SAR scene are discrete, sampled functions. The range-history models used for SAR focussing are often applied as constant amplitude phase functions where the phase angle is defined in terms of the radar range normalized to the radar wavelength. Though often ignored in models, the received signal amplitude is modulated by the two-way antenna gain pattern and the target reflectivity pattern. Several phase history models have been developed under different conditions and approximations and the following are such examples.

Single cell, moving target acceleration models [35] result in a (quadratic approximation) radar range history of the form

$$R(t) \approx R_0 + \frac{y_0 v_{y0}}{R_0} t + \frac{1}{2R_0}\left[(v_{x0} - v_a)^2 + v_{y0}^2\left(1 - \frac{y_0^2}{R_0^2}\right) + y_0 a_{y0}\right]t^2 +$$

$$\frac{1}{2R_0}\left[v_{y0}a_{y0}\left(1 - \frac{y_0^2}{R_0^2}\right) + a_{x0}(v_{x0} - v_a) + \frac{y_0 \dot{a}_{y0}}{3}\right]t^3. \tag{12}$$

Equation (12) expands the radar range of a point target as seen from an airborne radar platform operating a broadside-pointed, strip-mapping radar over a plane earth where:

- R_0 is the radar range to the target seen at the point of closest approach.
- y_0 is the ground distance from the target to the ground projection of the radar at the point of closest approach.
- v_{y0} is the ground speed of the target towards or away from the point of closest approach.
- t is time measured from the time of closest approach.
- v_{x0} is the ground speed of the target parallel to the radar track at the point of closest approach
- v_a is the speed of the radar platform.
- a_{y0} is the ground acceleration of the target towards or away from the radar at the point of closest approach.
- a_{x0} is the target's ground acceleration parallel to the radar flight track.
- $\dot{a}_{y0}$ is the ground rate of change of target acceleration towards or away from the radar position at the point of closest approach.

As seen in the quadratic term of equation (12), the radial component of the target acceleration affects the FM rate and thus the SAR focussing of a target point. In detailed work [35] showed that the target along-track acceleration appears in the cubic term for the phase history and influences the cross-range SAR impulse-response side lobe distribution and symmetry. An extension to the target acceleration work [36] showed that both the impulse response broadening and the side lobe symmetry problems can be compensated when the acceleration effects are correctly modeled in the phase history function.

For ship motion, the velocities and accelerations are not constant but can be expressed in terms of a dominant periodic function. When the sea surface conditions are sufficiently disturbed that ship

response to the local wave field is significant, the rigid body motions of the ship result in the radar system observing different radial motions at different parts of the ship. Each of the observed points on the ship moves relative to other points and has a different range history over the SAR-GMTI observation period. These range histories will contain variable acceleration effects. This is captured in the following range history model:

$$R(\boldsymbol{r_i}, t) \approx R_0(\boldsymbol{r_i}) + v_r t + \frac{v_{rel}^2}{2R_0} t^2 + \varepsilon_r(\boldsymbol{r_i}, t) \tag{13}$$

where:

- $\boldsymbol{r_i}$ is the displacement of i-th scattering point from the center of buoyancy in the rigid body coordinate system shown in Figure 5.

- $v_{r=} v_y y_0 / R_0$ is the radial component of the ship's cruising velocity.

- v_{rel} is the relative speed of the SAR platform, which will be explained later.

- R_0 is the slant range at the ship's center of buoyancy when it is broadside from SAR.

- $R_0(\boldsymbol{r_i})$ is the slant range of i-th scattering point when it is at broadside from SAR.

- $\varepsilon_r(\boldsymbol{r_i}, t)$ is the radial projection of the excursions exercised by the i-th point of the rigid body, due to quasi-periodic dynamics, which includes translations (mainly heave) and position-dependent rotations according to equation (1).

In comparison to equation (12), the cubic term, associated with constant acceleration, is dropped from equation (13) and replaced by the excursion term that varies over the surface of the ship and over the observation time. As in equation (12), it is assumed that the SAR is broadside pointing so that the range vector and the radar velocity vector are orthogonal (for airborne SAR) and time origin is chosen to be at the moment when the target is broadside from radar. The linear term is the same in equations (12) and (13) and the quadratic term is the same if the relative speed is properly defined. In equation (12) the potential acceleration of the SAR platform was not considered since it is usually cancelled by motion compensation for airborne SAR.

For a space-borne SAR the satellite acceleration cannot be neglected since it is responsible for the orbital curvature. This additional term, proportional to the radial projection of the satellite acceleration, can be conveniently included into the expression for the relative speed in (13) to provide a range history model that is valid for both airborne and space-borne systems. Space-based SAR computations must compensate for earth rotation.

Equations (12) and (13) are derived for a single-aperture SAR.

For a multiple-aperture SAR-GMTI radar operating on an aircraft or a spacecraft, the slant range history for a target moving at constant acceleration can be modelled as [37]

$$R_p(t) \approx R_0 + D_p \Psi + v_r t + \frac{D_p}{R_0}(v_t - v_{gr})t + \frac{1}{2R_0}(v_{eff}^2 - 2v_s v_t + R_0 a_r)t^2 \tag{14}$$

where:

- R_p is the radar range for antenna phase center p,

- R_0 is the radar range to the target at the point of closest approach,

- D_p is the two-way antenna baseline, the aperture separation between phase center p and 0,

- Ψ is the squint angle between the radar beam center and the broadside.

- p is the phase center index, $p \in (0,1)$, for pair-wise phase centers,

- v_r is the projection of the target velocity onto the radar range vector

- v_t is the component of the target velocity that is parallel to the SAR velocity (the along-track speed of the target),

- a_r is the radial acceleration of the target.,

- v_s is the SAR platform speed in the ECEF reference system

- v_{gr} is the SAR ground speed (for space-borne geometry $v_{gr < v_s}$), and

- v_{eff} is the SAR platform effective speed, which accounts for the SAR platform curvature in case of space-borne SAR.

Equation (14) is valid as a parabolic approximation to the hyperbolic phase history function for both airborne and space-based, strip-mapping SAR systems that are observing constant acceleration targets. For an airborne system, $v_{gr} = v_{eff} = v_s$. For an orbiting system, $v_{eff}^2 = v_s^2 - \boldsymbol{R}^T \boldsymbol{a}_s \approx v_s v_{gr}$ where $\boldsymbol{R}$ is the target range and $\boldsymbol{a}_s$ is the SAR acceleration defined by its orbit. Time is again measured from t=0, which is set at the *a priori* unknown moment when the target is broadside from the reference aperture (p=0). Arbitrary time reference is considered in [37] and it requires additional offset terms to describe the range history. At the same time, equation (14) introduces multiple phase centers (not considered in equations (12) and (13) and a phase term between them $D_p \Psi$ which must be compensated by channel balancing.

From our discussion of ships as ensembles of radar targets, it was noted that sea-surface effects on ship motion impose variable acceleration terms on the scattering centers in a SAR resolution cell as opposed to the constant term assumed in equation (14). When such target acceleration effects are included in the range history model, it is necessary to add a dominantly periodic term to equation (14) similarly as equation (13) amends equation (12). This addition will be considered later in this document for ship observations that are based on long and short radar observation intervals.

When the range history model for the ship is based on the bulk motion of the ship target and the sea surface is sufficiently disturbed, images similar to Figure 17 are obtained. To correctly image the vessel, a ship motion model needs to be inferred from the radar measurements and different range histories need to be applied to different portions of the ship signal during SAR processing.
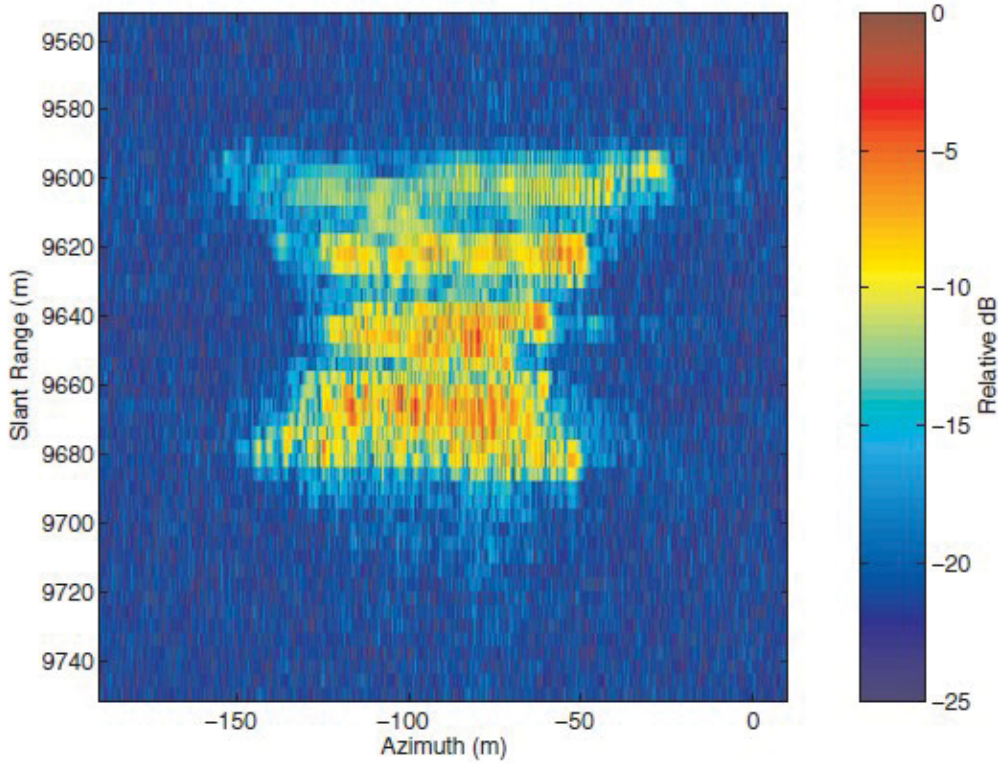
Figure 17: Airborne SAR-GMTI observations of a ship heaving and pitching in a swell wave field as imaged near its translational radial velocity.

In Figure 17, no part of the vessel is correctly imaged due to the exclusion of vessel heave and pitch dynamics from the range history model used for SAR focussing. In many, but not all, cases, models based on a single, moving cell can be applied to each observed cell that forms the ship image provided that the dominant model parameters can be deduced from the radar measurements [38]. We will use this concept for more detailed discussions of SAR-GMTI studies of ships using airborne SAR-GMTI sensors.

2.4.2 SAR-GMTI signal sampling effects

SAR data are sampled by the transmitted radar pulses as the radar proceeds along its trajectory. The sampling process has two major effects on the signal data used to generate SAR-GMTI measurements: signal bandwidth truncation, and the generation of sampling ambiguities.

The shape of the pulse-sampled signal spectrum is determined by the two-way illumination pattern of the radar antenna in the flight-direction of the radar. To generate an accurate SAR image representation of the observed terrain, the radar PRF should capture as much of the main lobe of the antenna pattern as possible. To maximize the useful SAR swath width, the lowest possible sampling rate should be used. These two conflicting requirements represent a design and operating trade-off for the radar which is normally resolved by choosing the PRF to adequately sample the peak of the antenna pattern that lies within a spectral interval whose width is close to the -6 dB width of the two way pattern. The shape of the sampled spectrum for a uniformly

illuminated array antenna is close to the error = 0 contour of Figure 16. If this represents the two-way signal amplitude, the -6 dB width is the width of the curve at 0.5. The sampled signal spectrum envelope is thus a shaped peak on a constant width pedestal.

Image formation over a signal spectrum that has this shape has processing side lobes that are somewhat, but not greatly, smaller than those shown in Figure 16. For a single point target, the combined range and cross-range focussing will result in an image signal magnitude of the form shown in Figure 18 for the ESA (European Space Agency) calibration transponder at Edam NL [39]. For ships, the side lobe pattern of strong radar reflectors are often clearly visible in the surrounding sea surface as shown in Figure 19 for a 30 MHz bandwidth SAR mode where the ship is travelling through a weakly disturbed sea surface. In this case the range side lobes are very much smaller than the azimuth side lobes. For ship targets, the side lobes from some strong reflectors may equal or exceed the peak returns from other ship components.

For the example shown in Figure 19, sea-motion effects on the ship image focusing are negligible due to the calm sea conditions and minimal swell waves during the radar observation of the ship.
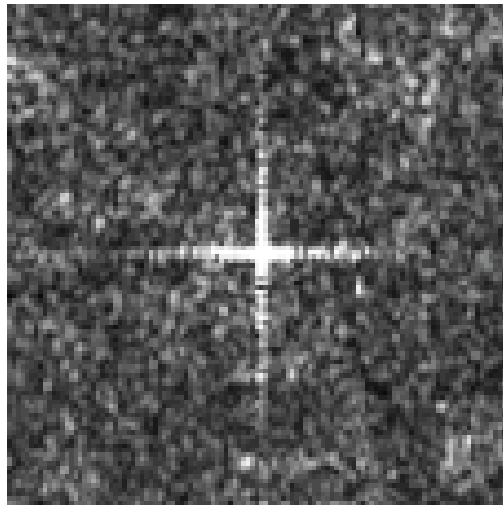
Figure 18: EVISAT ASAR image of the ESA calibration transponder at Edam NL.
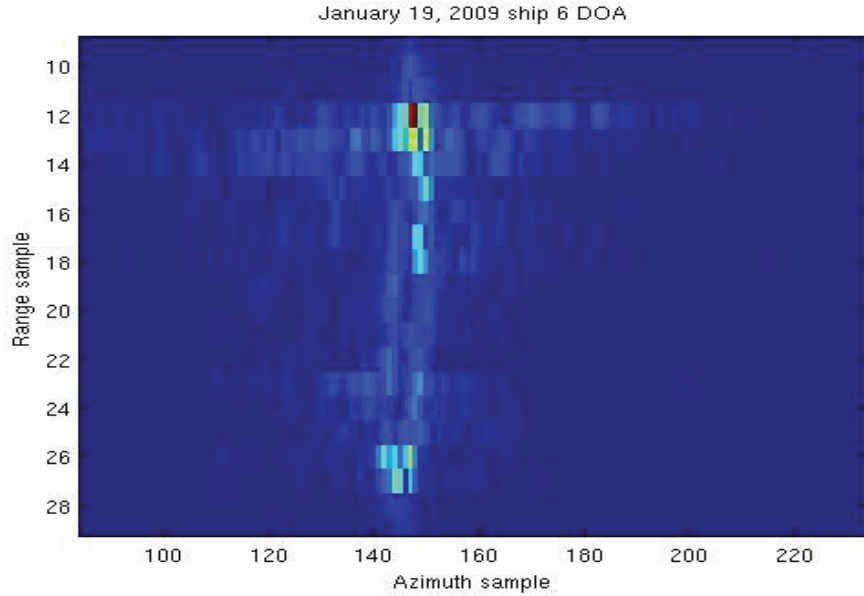
Figure 19: *RADARSAT-2 GMTI ship image with suppressed sea background. The signal strength is colour coded.*

Employing a radar PRF selection approach that captures the peak of the cross-range signal spectrum results and adequately samples a selected signal bandwidth about the spectral peak means that the signal spectrum at frequencies where $|f| > |f_s|$[1] is shifted in frequency by $-f_s/2$ for frequencies greater than $f_s/2$ and by $f_s/2$ for frequencies less than $-f_s/2$ and is summed with the adequately sampled signal to form the first-order sampling ambiguity. Higher order ambiguities are generated from the next lower order by a similar process. The properties of sampling ambiguities are discussed in detail elsewhere [40], [18].

For SAR-GMTI radars the sampling ambiguity structure becomes important for signal processing operations that couple data from multiple radar apertures. If the radar antenna aperture properties are matched to each other, and if the radar PRF is chosen so that the radar transmits an integer number of pulses (the minimum number is one) during the time that it takes for one two-way antenna aperture move to the spatial position that was previously occupied by a previous aperture (the DPCA sampling condition), apertures can be registered to a single point in space by integer shifts in the signal sample space. With this constraint, sampled signal data from each can be spatially registered to create the GMTI stationary radar condition[2] while preserving the sampling ambiguity structure. This maximizes the signal coherence between GMTI apertures. If the DPCA sampling condition is not met, signals from different radar apertures must be interpolated to spatially register them for GMTI measurements. The interpolation process will accurately match the adequately sampled portion of the signal but will alter the symmetry of the sampling ambiguities from channel to channel [18] and will degrade channel-to-channel signal coherence.

---

[1] The convention used here is that the signal spectrum is presented on a scale that has positive and negative frequencies about 0 Hz.

[2] All GMTI channels observe the terrain from a fixed point for a single transmitted pulse so that signal differences between channels represent temporal changes in the scene. This is called the DPCA (displaced phase center antenna) condition.

For SAR design and operation, PRF selection is constrained by both the spectral sampling requirement and by the aperture spacing requirement. This is relatively easy to accomplish while maintaining a uniform sample spacing on the observed terrain for a space-based radar but is much more difficult to accomplish for an airborne instrument. Airborne SAR-GMTI mitigates the sampling problem by selecting the PRF to provide large (≥ 2) over-sampling ratios to decrease the sampling ambiguity content of each sample and to minimize interpolation distances.

From the spectral folding property that defines the sampling ambiguity, the ambiguous signals, that sum with the adequately sampled spectrum, come from parts of the imaged terrain that are displaced parallel to the radar flight track by approximately

$$d_{Amb} = \pm \frac{\lambda R f_s}{4 V_{RS}},$$ (15)

where V_{RS} is the radar speed along its flight track, from the correctly sampled terrain. When the terrain at the imaged point has a weak radar return (for example an ocean surface that has relatively calm winds) and the target in the ambiguous position has a large radar return (for example, a large ship), the ambiguous signal spectrum may exceed the local, adequately sampled terrain spectrum and the ambiguous target will appear as an image at that point. Every strong target has a pair of ambiguous friends (first-order ambiguities), one of which precedes the target position and one of which trails the target position along the radar trajectory direction. Higher order ambiguities will be present but these are usually too weak to be observed. The ambiguous target image will be somewhat defocussed due to an FM rate mismatch[3] between the target signal and the phase history model used for processing and due to the skewed envelope of the target ambiguity signal. The skewed shape of the ambiguous spectrum will cause the target ambiguity separation from the target to be somewhat less than $d_{Amb.}$ [40].

2.4.3   Signal superposition effects

For ships moving on ocean surfaces, the ship and the ocean surface data are shifted with respect to each other by the target and surface motions. Modelling a moving ship as an ensemble of radar resolution cells, the signal data for each cell will contain radar signals from scattering centers on the ship, radar signals from the sea surface that is displaced from the ship position and sampling ambiguity signals from terrain surface (land or sea) that lie at ambiguous displacements along the radar flight track direction from the target. The superimposed and summed signals will influence SAR GMTI measurements of the ship target [41, 42].

At the single cell level, the signal model [18] for a focused SAR image of a ship has the form of the phasor sum

$$S_k = U_k e^{j\gamma_k} = U_{Tk} e^{j\varphi_k} + U_{Ck} e^{j\theta_k} + U_{Afk} e^{j\xi_k} + U_{Aak} e^{j\nu_k} + N_k e^{j\eta_k}.$$ (16)

In equation (16):

- S_k is the complex amplitude of the kth ship resolution cell.

---

[3] The center of the ambiguous signal spectrum is at a different radar range than the center of the adequately sampled spectrum.

- U_k is the amplitude of the kth phasor sum.

- γ_k is the phase of the phasor sum.

- $j = \sqrt{-1}$

- U_{Tk} is the sum of all ship returns that ended up in the kth resolution cell.

- φ_{Tk} is the phasor-summed phase angle corresponding to the signals that contributed to U_{Tk}.

- U_{Ck} is the amplitude of the sea return that the moving ship has been displaced over or is the amplitude of the sea return that has been displaced over the ship return by sea motion effects.

- θ_k is the phase angle of the kth sea return.

- U_{Afk} is the amplitude of the sampling ambiguity of the image surface in the direction of the radar travel (the fore ambiguity) that is superimposed on the kth ship resolution cell.

- ξ_k is the phase angle of the kth fore ambiguity.

- U_{Aak} is the amplitude of the sampling ambiguity of the image surface in the direction opposite of the radar travel (the aft ambiguity) that is superimposed on the kth ship resolution cell.

- v_k is the phase angle of the kth aft ambiguity.

- N_k is the system noise amplitude for the kth ship resolution cell.

- η_k is the corresponding noise phase angle.

- All phase angles consist of a static term that comes from the imaging geometry and is the same for all SAR GMTI channels plus a dynamic term that comes from the ship and scene motions and varies from channel to channel. Thus the phase angle $\zeta_{Nk} = \zeta_{Gk} \pm \frac{\zeta_k}{2}$ where ζ_{Nk} represents the composite angle, ζ_{Gk} represents the geometric angle and $\pm \frac{\zeta_k}{2}$ represents the motion contribution in the fore and aft channel.

In Figure 9, $1 \leq k \leq 296$ and the ship is considered to be a 296 cell ensemble for bulk measurements of its motion.

When the ship is observed by a multiple-aperture SAR-GMTI radar and when the radar timing is adjusted so that each aperture observes the ship from the same point in space, each sample represented by equation (16) occurs at a different time. For space-based radars, the time differences between spatially registered channels corresponding to one SAR-GMTI sample interval are less than 1 ms and for airborne radars the time differences are in the vicinity of 2 ms. For analysis, it is assumed the amplitude terms, U_{Tk}, U_{Ck}, U_{Afk}, and U_{Aak} do not change over the channel registration time. This is not true for the phase terms φ_k, θ_k, ξ_k, and v_k which contain target and sea motion effects and will differ somewhat between channels.. The amplitude term N_k and the phase term η_k are uncorrelated random numbers from channel to channel.

When the radar observation parameters U_k and γ_k are extracted in multi-channel analysis, the non-target terms that have been embedded through the phasor sum become measurement contaminants (phase-noise contributors) [18] when non-linear metrics such as ATI phase

extraction and covariance matrix term extraction analyses are employed. The data set for the ship shown in Figure 7, observed by a four-channel SAR_GMTI radar would contain four sets (one per channel) of 296 observations, where each observation is a realization of equation (16).

Multi-path scattering has not been explicitly included in the equation (16) target model but will be embedded in the measured parameters as will be demonstrated in the experimental analysis sections of this report.

2.4.4 Signal channel registration

As the SAR antenna moves along its trajectory, different phase centers occupy the same spatial locations at different times. Phase center p will reach the position of the reference (foremost) phase center with a time delay $\tau_p = \frac{D_p}{v_s}$ depending on the phase center separation (baseline) D_p and the radar speed along its trajectory v_s. If the radar has a uniform phase center separation D, then $D_p = pD$. The signals from each phase center form a data channel. If the antenna is squinted with respect to its velocity vector normal, these positions will not be identical, which introduces an undesired phase offset ($D_p\psi$ in equation (14)). This is only one of the terms that need to be compensated by data-adaptive calibration and it can be achieved by adaptive channel balancing discussed in the next section. Registration can also be accomplished adaptively within the same balancing algorithm or it can be performed explicitly. Either way, registration and balancing have an impact on the data model which will be used in signal processing.

Starting from equation (14) and considering that all signal samples are available only at discrete time intervals $t = k/f_s$ where f_s is the PRF and k is the pulse index, the following equations compare the range history for the reference phase center ($p=0$) with the range history for another phase center ($p>0$) shifted in time by some time increment τ_p:

$$R\left(\frac{k}{f_s}\right) \approx R_0 + D_s \frac{v_r}{v_s} k + \frac{D_s^2}{2R_0}\left(\frac{v_{gr}}{v_s} - 2\frac{v_t}{v_s} + \frac{R_0 a_r}{v_s^2}\right) k^2 \text{ for p = 0 and} \tag{17}$$

$$R\left(\frac{k}{f_s} + f_s\tau_p\right) \approx R_0 + D_p\Psi + D_s \frac{v_r}{v_s} f_s\tau_p + D_s \frac{v_r}{v_s} k + \frac{D_s D_p}{R_0}\left(\frac{v_t}{v_s} - \frac{v_{gr}}{v_s}\right) k +$$

$$\frac{D_s^2}{R_0}\left(\frac{v_{gr}}{v_s} - 2\frac{v_t}{v_s} + \frac{R_0 a_r}{v_s^2}\right) f_s\tau_p k + \frac{D_s^2}{2R_0}\left(\frac{v_{gr}}{v_s} - 2\frac{v_t}{v_s} + \frac{R_0 a_r}{v_s^2}\right) k^2 + O\left(\frac{D_p}{R_0}\right) \text{ for p > 0.} \tag{18}$$

In equations (17) and (18) the parameter R_p(t) has been replaced with $R\left(\frac{k}{f_s} + f_s\tau_p\right)$ to minimize confusion when $p = 0$, otherwise the parameter definitions are the same as those used in equation (14).

The parameter $D_s = v_s/f_s$ is the pulse spacing along the SAR trajectory and the last term in equation (18) contains high-order components that can be neglected as they are small and do not significantly effect the accuracy of our parabolic approximation.

1. The quadratic term is the same for all apertures and the Doppler rate needed for focusing depends on the SAR and target motion in the same way as discussed earlier;

2. The linear term can be made equal for both apertures on condition that the fifth and sixth term in the second equation can be cancelled out;

3. The remaining terms differ by the amount that depends linearly on the radial speed (as expected and desired) and a quantity related to the antenna squint (not desirable), which will cause bias if uncompensated.

The condition for canceling the difference in the linear terms is $D_p \approx D_s f_s \tau_p = v_s \tau_p$ as expected. The cancellation approximation neglects the influence of the target's along-track speed and radial acceleration. If D_p/D_s is an integer, then $k_p = f_s \tau_p$ is also an integer and channel registration can be achieved by picking the appropriate samples from the data contained in each channel. This is the ideal DPCA sampling condition and it guarantees perfect registration for the base-band and for the ambiguous side-lobe portion of the sampled SAR signal.

When the DPCA condition is not met, it is necessary to use interpolation between the available samples in each channel to reconstruct the values that would be collected at the registration time so that $D_p = n D_S$ for the revised sample distance D_S and some integer n. Both the DPCA sampling condition and the interpolation condition constrain the radar design to make all values of D_p be integer multiples of the smallest phase center separation. Several channel registration methods are in use, all have advantages and drawbacks.

One registration method is to interpolate each data channel to the reference channel by applying a phase ramp in the Doppler frequency domain using the time shifting property of the Fourier transform. The ramp slope is proportional to the required time shift and the ramp must be smooth around the DC of the signal spectrum. Signal ambiguities get registered with an incorrect phase resulting in an imbalance between the fore and aft sampling ambiguities and an increase in the peak ambiguity level. Since the moving targets and the clutter do not share the same DC, this registration artifact necessarily affects one or the other and generally results in a reduction in the signal coherence between channels.

An equivalent approach that is used in some polarimetric SAR processors uses Fourier transform over-sampling operation to increase the sample rate in a channel and then uses an interpolation kernel (often a sinc function that models the expected radar impulse response) to generate registered samples. A cross-channel coherence metric is often used to achieve a "best" registration. This approach is equivalent to the phase ramp approach. It also disturbs the sampling ambiguity balance and results in reduced coherence between the registered samples. Since the coherence metric is a non-linear process cross modulation effects between signal components (equation (16)) will limit the registration accuracy in some cases.

Another registration method is adaptive processing, as discussed in the next section. The knowledge of the baseline or the DC is not required as input to the adaptive process. The phase slope is automatically removed as illustrated in Figure 20, as part of the full channel balancing. This outcome is very convenient, but it is not perfect. The adaptation is driven by the bulk data and may affect adversely the signatures of moving targets as they are also a source of imbalance. It can be noticed in Figure 20 that the portion of the spectrum is attenuated for the channel that is adjusted by adaptive balancing. This automatically suppresses the aliased (ambiguous) part of the signal at the outskirts of the main lobe. Unfortunately, this will also suppress the returns from fast moving vehicles that lie in that part of the Doppler spectrum. Again, this approach uses non-linear

metrics to achieve the channel registration and both ambiguity enhancement and cross-modulation effects are sometimes evident.

2.4.5 Channel balancing

Multiple SAR-GMTI channels can only be used for target motion estimation when the channel gains, group delays, phases and timing have been normalized to each other. The normalization process is called channel balancing and registration. The first channel balancing level occurs in the radar hardware through data path normalization and control adjustments. Residual channel balance deviations are corrected by signal processing manipulations based on system metadata and measurements of signal data made during early processing stages. Due to the fact that moving target signals that focus to a single image point may contain components that have different range histories, ideal channel balancing operations should use linear data manipulations to the greatest possible degree. Data resampling may be required for fine registration of data from different channels but its use should be minimized.

Investigations into signal processing approaches for land [43] and marine [44] targets, working from range-compressed signal samples used coherence and phase estimates between two signal channels to perform range registration, group-delay and phase compensation. Since the channel balancing uses phase estimates and since these are generated by a correlation (non-linear) process, caution must be used when employing phase estimation to compensate radar channel imbalance for sea surface scenes that contain multiple targets and shore ambiguities. On an individual scene basis, bulk sea motion (ocean currents and wind-drift effects) and wave motion (scene phase noise) will influence channel balance estimates. If the sensor system is sufficiently stable, correction tables that have been derived from less complex scenes should be used. In this case, the system stability should be verified regularly. Alternatively, for very stable radar systems, the relative properties of the radar channels can be measured using calibration procedures and the tabulated values of relative gain, relative group-delay, relative phase and relative timing can be used to adjust signal outputs relative to a reference channel to correct for radar system artifacts.

An adaptive approach to channel balancing using along-track interferometric (ATI) processing (channel correlation) and a two dimensional, iterative estimation of the relative channel transfer functions [43] has been shown to be robust for land data that have a low concentration of moving targets. Figure 20 illustrates the adaptive channel-balancing process for an airborne SAR GMTI system. This approach has been used for marine targets but has the limitation that it combines bulk motion in the imaged scene with the channel transfer function estimates.
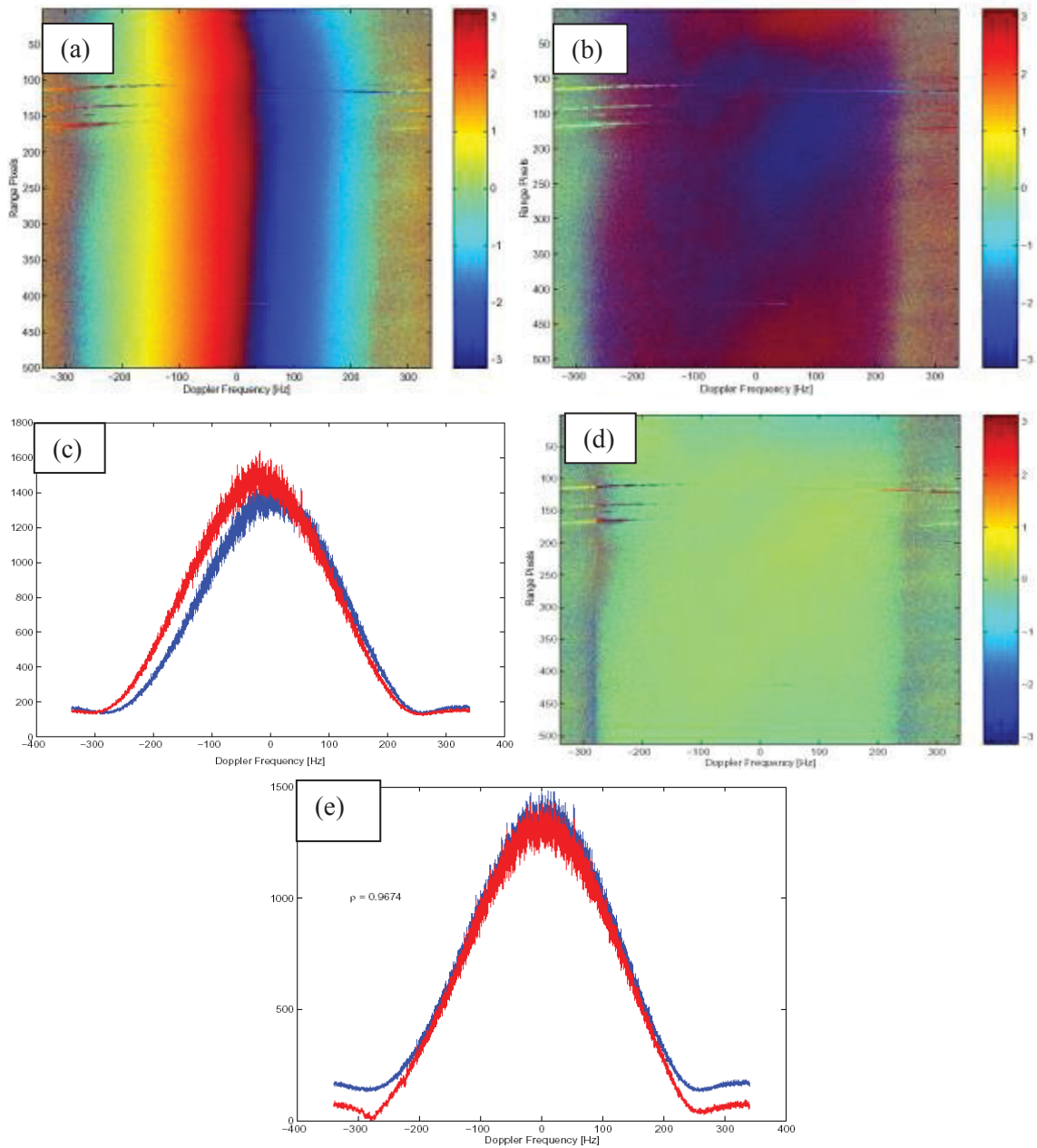
Figure 20: *(a)Raw 2-channel ATI signal phase, (b) ATI signal phase with aperture separation compensation, (c)spectra with mismatched transfer functions, (d) ATI phase after channel balancing, (e) signal spectra after channel balancing.*

Figure 21 presents the cumulative effect of the iterative channel balancing procedure between two SAR GMTI channels of RADARSAT-2. The magnitude and phase characteristics (presented on the left and right side respectively) are shown in the spectral domain compensation of channel 3 (as slave) with respect to channel1 (as master) in a four channel signal set. The phase characteristic has the form of a smooth ramp that is linearly sloped in azimuth (Doppler) frequency and has no variation over the range frequency.
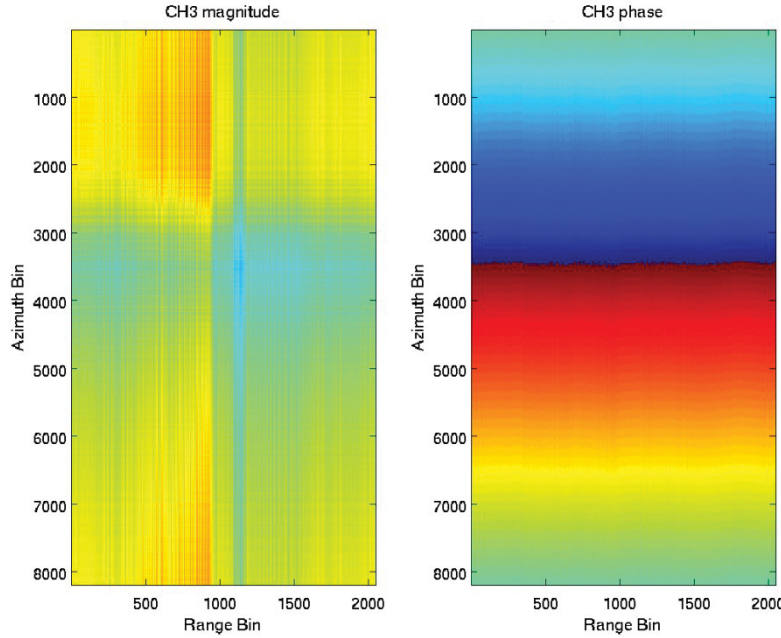
Figure 21: *Magnitude and phase characteristics as a result of adaptive balancing between a pair of RADARSAT-2 channels in SAR GMTI four channel mode.*

When more than two ATI apertures are available, covariance matrix manipulation can be used for channel balancing.

2.5   SAR-GMTI signal processing considerations

From a radar surveillance point of view, moving targets are *a priori* unknown rare events whose unknown radar signal properties differ from the signal properties of the scene that they are embedded in. SAR-GMTI processing of moving targets needs to address three broad problems:

1. Find the moving target signal starting from the raw SAR data.

2. Estimate the target motion properties.

3. Infer the appropriate range history model for each moving target.

Moving target detection provides the key to locating the raw data that must be processed differently than the background scene. Moving target detection uses a space-time observation set to identify signal blocks that have significantly different properties than the background terrain signals [45], [46], [47], [48], [49], [50]. Detection of signal properties that correspond to potential moving targets creates a moving target candidate list.

Analysis of moving target candidate signals by time-frequency decomposition [51], [52], matched filter maps [53], [40] or fractional Fourier transform analysis [54], [55] provide moving target range-history estimation approaches that are based on radar signal properties. If the range history

of a moving target can be correctly estimated, the focused SAR image of the target is correctly positioned in a geographic sense from the radar position data.

Target motion properties that are estimated to determine a "best" range history model are GMTI outputs.

2.5.1 Moving target detection

The SAR-GMTI Moving target detection process can be reduced to the problem of detecting spatially sparse signal changes between SAR GMTI channels that observe a common piece of terrain from the same point in space at different times. The time interval between channels is the time required for one two-way GMTI aperture to move to the position occupied by the previous aperture. As mentioned previously, the detection process identifies moving target candidates that need to be confirmed by subsequent analysis.

Since the time intervals are short (of the order of 0.2 to 0.8 ms for space-based radars), moving-target detection approaches need to find signal changes that correspond to localized range history differences of fractional radar wavelengths between two GMTI channels.

The problem of ship detection can be cast into the classical form of a statistical target detection test, namely

$$H_0 : \boldsymbol{S} = \boldsymbol{c} + \boldsymbol{n}, \ H_a : \boldsymbol{S} = \boldsymbol{c} + \boldsymbol{n} + \boldsymbol{t_s} \tag{19}$$

where H_0 is the hypothesis that no ship target signal is present and H_a is the hypothesis that a ship target signal is present. In equation (19) s is the radar signal vector containing samples from all GMTI channels, c is the radar return vector from ocean clutter, n is radar system noise vector and t_s is the radar signal vector from a ship target.

To choose between these two hypotheses, a test statistic is first computed. One class of such test statistics is formed by feeding the multiple-channel measurements into a linear combiner. In particular, the test statistic T may be defined as

$$T = |\boldsymbol{b}^H \boldsymbol{S}|^2, \tag{20}$$

where the superscript H denotes the Hermitian transpose and where the vector $\boldsymbol{b}$ is chosen to produce desirable signal to clutter plus noise characteristics. If the noise and clutter measurements follow a complex zero-mean Gaussian distribution N with $\boldsymbol{c} \sim N(\boldsymbol{0}, a\boldsymbol{\mathcal{R}_c})$ and $\boldsymbol{n} \sim N(\boldsymbol{0}, \boldsymbol{\mathcal{R}_n})$, where a is some random variable with mean value 1 that describes the non-homogeneity of the clutter RCS, $\boldsymbol{\mathcal{R}_c}$ and $\boldsymbol{\mathcal{R}_n}$ are the clutter and noise covariance matrices respectively and the first component of the argument of N is the distribution mean, then the distribution of the test statistic may be expressed as [49]

$$f_{T|a}(t|a) = \left(\frac{t}{a\boldsymbol{b}^H \boldsymbol{\mathcal{R}_c} \boldsymbol{b} + \boldsymbol{b}^H \boldsymbol{\mathcal{R}_n} \boldsymbol{b}} \right)^{n-1} \frac{e^{-\frac{t}{a\boldsymbol{b}^H \boldsymbol{\mathcal{R}_c} \boldsymbol{b} + \boldsymbol{b}^H \boldsymbol{\mathcal{R}_n} \boldsymbol{b}}}}{\Gamma(n)(a\boldsymbol{b}^H \boldsymbol{\mathcal{R}_c} \boldsymbol{b} + \boldsymbol{b}^H \boldsymbol{\mathcal{R}_n} \boldsymbol{b})}. \tag{21}$$

In equation (21) $f_{T|a}$ is the probability density function of the test statistic T given the homogeneity assumption a, n is the number of complex looks (independent samples) that are summed to make the estimate and $\Gamma(n)$ is the normal form of the gamma function. More detailed discussions of test statistic distributions can be found in [45] and [47].

It can be shown that by choosing the distribution for a to be a gamma distribution, and by ignoring the $b^H \mathcal{R}_n b$ term, one arrives at a K-distributed test statistic [56], [57] and [58]. The impact of ignoring the noise contribution (to arrive at the K-distribution) in this type of product model becomes significant when the radar measurements become noise limited, as they are when the CNR is low or when clutter is suppressed or removed through the vector b.

Under the assumption that the distribution for the test statistic is known, one computes a threshold under the null hypothesis such that the integration of the distribution for all values to the right of the threshold yields the desired false alarm rate.

The statistics of land clutter and maritime clutter are significantly different. To ensure that the test uses only the statistics of maritime clutter in the littoral ship-detection problem, one must eliminate any land clutter in the radar acquisition. This can be done by obtaining an *a priori* known shoreline map and applying a binary mask to the processed imagery. Alternatively, the land clutter can be removed if the processing vector b provides adequate clutter suppression.

If a ship is not moving very fast, then clutter suppression can also suppress the response of the ship. In fact, if a ship is at anchor in calm seas, then the ship will experience the same level of clutter suppression as land surfaces.

The moving target detection process has no *a priori* target motion information and a stationary-world assumption is often used for SAR processing to support an initial target search. Two-aperture GMTI data does allow the use of a DPCA cancellation technique where $b = \begin{bmatrix} 1 \\ -1 \end{bmatrix}$ to suppress the sea return component. The sea is a moving surface and its radar returns cannot be completely cancelled by DPCA analysis, but the sea surface decorrelation time is long enough {20 ms to 150 ms} that sea returns can be significantly suppressed. Sea return suppression by DPCA enhances the moving-ship component of the composite signal to increase the vessel detection probability and to identify the SAR signal samples that contain moving-ship data. Although the detection of moving vessels does not require SAR image formation, complex images are often used to improve target to background contrast and to increase target detection probability.

2.5.1.1 DPCA detectors

DPCA moving target detection subtracts signals from two registered, balanced channels (it is defined in terms of channel pairs). Signal contributions that are unchanged between the two observation times are cancelled and moving target signal amplitudes are dependent on the radial velocity of the target [59]

$$A_{DPCA} = 2 \left| sin\left(2\pi \frac{V_R \delta t}{\lambda}\right) \right| \left| S_{Targ}(x,y) \right|. \tag{22}$$

In equation (22):

- A_{DPCA} is the focused target amplitude after background cancellation,

- V_R is the radial velocity of the target,

- δt is the time required for one aperture to move to the position of the previous aperture,

- λ is the radar wavelength,

- $||$ is the absolute value operator, and

- S_{Targ} is the complex amplitude of the focused target image at image coordinate x,y.

Moving target detection succeeds if A_{DPCA} exceeds a threshold η that is based on the statistics of the residual clutter in the scene and radar noise [18]. Since the DPCA signal amplitude distribution cannot be reliably modelled for all cases, one of the weaknesses of this approach is the selection of the threshold T that provides the best trade-off between target detection probability and false alarm rate.

Provided that the background scene contains little internal motion, DPCA clutter cancellation works well for land. The sea is a moving target whose radar coherence time is a hyperbolic function of radar frequency [60] and decreases monotonically with increasing wind speed [61]. The sea coherence time at 5.3 GHz ranges from approximately 170 ms for 1 m/s wind speed to ~ 20 ms for 10 m/s wind speed. DPCA clutter suppression is in essence a pulse-by-pulse operation and will degrade with increasing wind speed. Sea clutter suppression degradation should not be very significant for RADARSAT-2 (0.25 ms to 0.8 ms between apertures) or CV 580 aircraft measurements (~2 ms between apertures).

DPCA is a sub-optimal moving target detection strategy [18] whose efficacy depends on the ratio of the filtered target power $A_{DPCA}{}^2$ to the residual, suppressed clutter. The minimum detectable target velocity (MDV) has the form [18]

$$|MDV| = \frac{\lambda V_{Radar}}{2\pi d_{Ap}} sin^{-1}\left(\frac{\sqrt{\eta^2 - \Delta U^2}}{2U}\right) \tag{23}$$

where:

- V_{Radar}, is the radar velocity,

- d_{Ap} is the distance between the radar antenna apertures,

- η is the detection threshold estimated from the statistics of the suppressed clutter,

- ΔU is the difference between the target signal magnitudes from the two radar channels, and

- $U = \sqrt{U_1 U_2^*}$ is the geometric mean amplitude of the target signals in channels 1 and 2.

In our discussions, a ship is considered to be an ensemble of moving-target resolution cells, whose signals contain both ship motion and sea motion effects as described by equation (16). The absolute value function in equation (23) will result in the rejection of ship signal DPCA components whose relative phases

$$\gamma_{k(1,2)} = \gamma_{k(1)} - \gamma_{k(2)} = 2\pi \frac{V_{Rk}\delta t}{\lambda} \tag{24}$$

are sufficiently small that $A_{DPCAk} < \eta$ and the acceptance of ship signal DPCA components whose relative phases yield $A_{DPCAk} \geq \eta$ for the same value of $|S_{Targk}(x,y)|$. In equation (24):

- $\gamma_{k(1,2)}$ is the phase of the complex DPCA signal representing ship sample k,

- $\gamma_{k(1)}$ is the phase of the complex channel 1 signal representing ship sample k,

- $\gamma_{k(2)}$ is the phase of the complex channel 2 signal representing ship channel k, and

- V_{Rk} is the radial velocity of ship sample k.

The effect of the DPCA detection approach is to create a composite-phase dependent amplitude bias into the target candidate cluster that captures the ship returns. When a ship is moving through a calm ocean, a DPCA detector will identify the ship sampling ambiguities as moving target candidates. When the detection threshold is selected to extract weak targets, the group of target candidates can contain a large number of false alarms due to signal to interference plus noise (SINR) peaks in the DPCA cancelled signal data.

Analysis of the properties of two-channel clutter covariance matrix [62] has shown that DPCA detection rules will generate false alarms when strong, stationary targets occur in the presence of target phase noise.

DPCA detectors are not necessarily limited to two-channel SAR. They can be extended to multiple channels simply by using different channel pairs or by using a suitable linear combination of all channels.

When multiple, uniformly-spaced GMTI channels are available with phase center separation d between adjacent channels, the number of channel pairs is the number of combinations on N things taking two at a time. For four channels there are six channel pairs, there are three pairs with phase center separation d, two pairs with phase center separation $2d$ and one pair with phase center separation $3d$. From equation (19), the DPCA amplitude is suitable for the detection of fast targets and unsuitable for the detection of slow targets at the shortest phase center separation (smallest δt in equation (22)), and is suitable for the detection of slow targets and unsuitable for the detection of fast targets at the largest phase center separation (largest δt in equation (22)). The three sets of channel pairs represent three overlapping moving-target speed detection regimes. Each regime defines one statistical degree of freedom for moving target detection. For a RADARSAT-2 four channel mode $d = 1.875$ m. Ordering the channels in the direction of flight with channel 1 being the aft channel, we have the situation shown in Table 2 for each point (x,y) in the data.

Table 2: *GMTI channel pairs for the four aperture GMTI modes of RADARSAT-2.*

Channel pair	Phase-center separation	Time separation
s_1, s_2		
s_2, s_3	1.875 m	0.25 ms
s_3, s_4		
s_1, s_4	3.75 m	0.5 ms
s_2, s_4		
s_1, s_4	5.625 m	0.75 ms

Following the previous example and defining a channel vector $S(x,y) = \begin{bmatrix} s_1(x,y) \\ s_2(x,y) \\ s_3(x,y) \\ s_4(x,y) \end{bmatrix}$ we can

define three permutation operators

$$G_1 = \begin{bmatrix} 0 & 0 & 0 & 0 \\ 1 & 0 & 0 & 0 \\ 0 & 1 & 0 & 0 \\ 0 & 0 & 1 & 1 \end{bmatrix}, G_2 = \begin{bmatrix} 0 & 0 & 0 & 0 \\ 0 & 0 & 0 & 0 \\ 1 & 0 & 1 & 0 \\ 0 & 1 & 0 & 1 \end{bmatrix}, G_3 = \begin{bmatrix} 0 & 0 & 0 & 0 \\ 0 & 1 & 0 & 0 \\ 0 & 0 & 1 & 0 \\ 1 & 0 & 0 & 1 \end{bmatrix} \tag{25}$$

so that the non-zero elements of

$$S_p = S - S^t G_p \,, \tag{26}$$

where t is the vector transpose operator and p =1:3, contain the differences between the channels signals for the channel pairs shown in Table 2. The non-zero elements of S_p are generally highly correlated. Noting that the largest time interval in Table 2 is much less that the sea surface decorrelation time [18], a DPCA detection threshold, η^2 can be defined from the statistics of any channel-difference pair imag region that does not contain targets or shore ambiguities. In principle there is a different value of η for each degree of freedom p. In practice, the estimated η_p are nearly identical. There are three detection rules of the form

$$S_p^2 - \eta_p^2 > \epsilon \; for \; p = 1, 2 \; or \; 3 \tag{27}$$

where the values of p correspond to the rows of Table 2 and $\epsilon \sim 0$. At each point *(x,y)* in the data set, a group of six detection findings will be made and these findings will have a coarse velocity dependence as a function of p. The declaration of a target detection at any point will be determined on the weighting of the detection findings from each of the three groups. The selection of a declaration rule will depend on the detection problem being addressed.

In general, after any multi-channel clutter cancellation, A_{DPCA} will still depend on the radial speed V_R of the target, but this dependency is determined by the combination of the channel weights for that multi-channel strategy. The extra degrees of freedom can be used to cancel out ambiguities or to favour certain target velocities and, eventually, to estimate these target velocities [63].

As was discussed in [18], DPCA clutter cancellation also suppresses some of the moving target signal by an amount that depends on the target's radial speed.

2.5.1.2 Rare event detectors

Along-track interferometry uses the correlation between the signals from two GMTI channels to generate a complex signal power product whose phase angle is the phase difference of the signals from two registered and balanced GMTI antenna apertures. For ship measurements, the resulting ATI signal resolution cells

$$S_{k,ATI} = S_{k(1)}S_{k(2)}^* = \left|S_{k(1)}S_{k(2)}^*\right|e^{j\gamma_{k(1,2)}} \tag{28}$$

combine two phasor sums of the form shown in equation (16) in a non-linear (product) manner. From [18] the resulting product has the form

$$S_{k,ATI} = S_{k(1)}S_{k(2)}^* = \Bigg(U_T^2 e^{j\varphi(1,2)} + U_C^2 e^{j\theta(1,2)} + U_{Af}^2 e^{j\xi(1,2)} + U_{Aa}^{jv(1,2)} + N_1 N_2 e^{j\eta(1,2)} +$$
$$2U_T U_C \cos(\varphi - \theta)e^{j\left(\frac{\varphi+\theta}{2}\right)} + 2U_T U_{Af}\cos(\varphi - \xi)\, e^{j\left(\frac{\varphi+\xi}{2}\right)} + 2U_T U_{Aa}\cos(\varphi - v)\, e^{j\left(\frac{\varphi+v}{2}\right)} +$$
$$2U_C U_{Af}\cos(\theta - \xi)\, e^{j\left(\frac{\theta+\xi}{2}\right)} + 2U_C U_{Aa}\cos(\theta - v)\, e^{j\left(\frac{\theta+v}{2}\right)} + 2U_{Af} U_{Aa}\cos(\xi - v)\, e^{j\left(\frac{\xi+v}{2}\right)} +$$
$$F\big(All, (\Re(N_1) + j\Im(N_1), (\Re(N_2) + j\Im(N_2))\big)\Bigg)_k \tag{29}$$

where:

- $(\ )_k$ represents the kth ATI sample,
- The subscript (1,2) denotes the phase difference between channels 1 and 2,
- $F()$ executes all cross products involving system noise,
- $\Re$ denotes the real part of its argument,
- $\Im$ denotes the imaginary part of its argument, and
- All other symbols are defined for equation (16).

The terms in equation (29) contain the signal power for each of the signal components and all of the cross-modulation terms that are generated by the ATI product. To compactly express the ATI phase γ_k for each point given by equation (14) in terms of the channel correlation expansion shown in equation (29) let us define some indexed variables.

- Define the amplitude variables W_k (k=1:6) as:
  - $W_1 = U_T$, $W_2 = U_C$, $W_3 = U_{Af}$, $W_4 = U_{Aa}$, $W_5 = N_1$, $W_6 = N_2$
- Define the static, random phase variables, Ψ_k as:
  - $\Psi_1 = \varphi$, $\Psi_2 = \theta$, $\Psi_3 = \xi$, $\Psi_4 = v$, $\Psi_5 = 0$, $\Psi_6 = 0$
- Define the dynamic phase terms, Ω_k as:
  - $\Omega_1 = \varphi_T$, $\Omega_2 = \theta_M$, $\Omega_3 = \xi_M$, $\Omega_4 = v_M$, $\Omega_5 = \eta_1$, $\Omega_6 = \eta_2$

We can now express the ATI phase for a target point as:

$$\gamma_k = tan^{-1}\left(\frac{\Im(S_1 S_2^*)}{\Re(S_1 S_2^*)}\right)_k = tan^{-1}\left(\frac{A+B}{C+D}\right)\ where: \tag{30}$$

$$A = \sum_{m=1}^{4} W_m^2 \sin(\Omega_m) + W_5 W_6 \sin\left(\frac{\Omega_5 + \Omega_6}{2}\right),$$

$$B = 2\sum_{m=1}^{5}\sum_{n=1, n\neq m}^{6} W_m W_n \cos(\Psi_m - \Psi_n)\sin\left(\frac{\Omega_m + \Omega_n}{2}\right),$$

$$C = \sum_{m=1}^{4} W_m^2 \cos(\Omega_m) + W_5 W_6 \cos\left(\frac{\Omega_5 + \Omega_6}{2}\right), and$$

$$D = 2\sum_{m=1}^{6}\sum_{n=1, n\neq m}^{6} W_m W_n \cos(\Psi_m - \Psi_n)\cos\left(\frac{\Omega_m = \Omega_n}{2}\right).$$

The joint probability density function of the ATI amplitude, $|S_{ATI}|$, and phase for a scene describes the ATI statistics of the scene based on equations (29) and (30) when no moving targets are present ($W_T = 0$). Unfortunately, this function cannot generally be expressed in closed form. An empirical approach to estimating the joint ATI amplitude-phase distribution [48] uses a point proximity condition to the ATI amplitude-phase histogram to estimate the boundary of the joint distribution for the target-free scene. Moving targets appear as outliers to the distribution boundary and are detected as rare events using an amplitude-phase threshold that is defined by a moving-target proximity distance. Figure 22 illustrates the detection process.
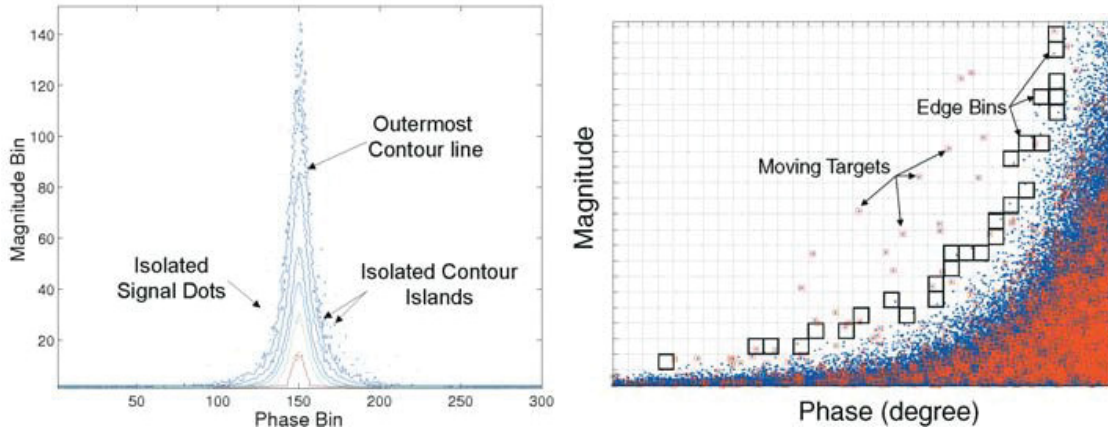
Figure 22: *Empirical estimation of the ATI amplitude-phase joint distribution showing moving targets as rare event outliers.*

Multiple tests have shown this rare-event detector to be robust, but the theoretical estimation of the detector false alarm rate and the probability of detection for moving targets remains an unsolved problem. When the target recognition threshold is set too close to the ATI amplitude-phase distribution, the number of false alarms contained in the detected target candidate set will increase.

The rare-event detector uses all available amplitude and phase information from a pair of GMTI channels and may be close to an optimum two-channel GMTI detector. Like the DPCA detector, it is initially constrained to operate on GMTI data channel pairs. Its extension to a multi-channel case is still an interesting open problem.

2.5.1.3 Covariance matrix detectors for moving targets

The imaging geometry of SAR-GMTI radars imposes a wide range of illumination angles (local incidence angles) on radar observations of a scene. When the scene includes groups of terrain elements whose scattering properties differ significantly with illumination angle from the properties of surrounding terrain, the scene statistics will be locally inhomogeneous and the effectiveness of GMTI clutter suppression will vary discontinuously over the data set. For marine target observations, clutter suppression issues are most significant in littoral zones that contain terrain whose radar scattering properties show strong local variations. Space-based SAR-GMTI sensors capture a smaller range of illumination angles in a scene and do not exhibit the same terrain clutter homogeneity issues as airborne sensors.

When Eigen decompositions of the SAR-GMTI space-time covariance matrix are used to define metrics for moving target detection, a number of two-channel moving-target detectors that can accommodate significant scene inhomogeneity have been examined for airborne SAR-GMTI radars [47], [49]. Some of these have been found to be reasonably robust for airborne SAR-GMTI data.

In particular, Eigen decomposition studies of the two-channel GMTI covariance matrix [49], [62] have shown that the extraction of the component of the sample covariance matrix that is orthogonal to the clutter covariance matrix can be used to define a metric that selectively detects moving targets and allows them to be separated from most stationary target false-alarms. The resulting Eigen-projection detector

$$m_\perp = \lambda_1 \sum_{k=1}^{n} |s_{1k} - s_{2k}|^2 - \lambda_2 \sum_{k=1}^{n} |s_{1k} + s_{2k}|^2 = \sum_{k=1}^{n} \vec{s}_k^H V^H \begin{bmatrix} -\lambda_2 & 0 \\ 0 & \lambda_1 \end{bmatrix} V \vec{s}_k \qquad (31)$$

has the property that stationary target false-alarms will have negative values of $m_\perp$ and moving targets will have positive values of $m_\perp$.

In equation (31)

- $\lambda_1 > \lambda_2 > 0$ are the Eigen values of the sample covariance matrix for signals from GMTI channels 1 and 2,

- $\vec{s}_k = \begin{bmatrix} s_{1k} \\ s_{2k} \end{bmatrix}$ is the kth sample vector composed of signals from channels 1 and 2,

- $\sum_{k=1}^{n}$ represents a local sum (multi-look) in the signal data stream,

- H is the Hermitian transpose operator, and

- V is the matrix that diagonalizes the sample covariance matrix.

A target detection threshold in the vicinity of $m_\perp = 0$ needs to be defined to control the detector false alarm rate.

When more than two GMTI channels are available, the n-channel complex covariance matrix can be used to estimate the maximum number of degrees of freedom in the total data set and, thus the measurement space dimension available for moving-target detection and motion estimation.

Extensive investigation of the properties of the joint covariance matrix [64], [65], [66] have shown that near optimum moving target detectors for small land targets can be developed using four-channel SAR-GMTI measurements. A two channel version of this detection/estimation class of algorithms has been applied to ships in the Strait of Georgia (Section 4.7).

Covariance matrices are generated by a cross-correlation process and are subject to the target-clutter intermodulation effects shown in equations (29) and (30). This is especially important for locally estimated covariance matrices based on a small sample set, as assumed in equation (31). This effect disappears (becomes a noise contributor) when a covariance matrix is estimated over a large region since targets are rare events that are statistically independent of the clutter and the system noise.

2.5.2 Estimating target motion parameters

Moving target detection and target motion estimation can be considered to be two sequential steps in the identification of moving targets and in the estimation of their motion properties. The target detection process filters the full set of SAR GMTI data to identify those signal blocks whose properties pass the detection test to create a set of target candidates. The estimation process works on signals belonging to the target candidate set to accept or reject detection candidates and to estimate target motion parameters.

Beyond this concept, there are combined detection/estimation algorithms that search through the target parameter space to maximize the detection test statistic which is compared against an appropriate detection threshold. The target parameters that provide the highest value of the metric used in detection are accepted as estimates of the motion parameters [66], [63]. This type of combined detection/estimation scheme is more advanced, but also more time consuming (computationally intensive) if applied on all data samples. The efficiency is improved by examining only detection candidates after preliminary first-level detection. There is always a trade-off between efficiency and performance, which plays an important role in the over-all design.

Depending on the detection filter that is used, the data set that is selected for motion analysis may contain detector artifacts and biases.

2.5.2.1 Doppler frequency and azimuth offset analysis

Doppler frequency analysis is the oldest motion measurement technique for radar data and uses frequency measurements of the radar return history over a time window. Its most common use in SAR and SAR-GMTI measurements is to estimate the Doppler centroid of range-focussed data over a radar scene and to thus estimate the relative motion or, for a processed SAR scene, the residual relative motion between the radar and the observed terrain. When Doppler centroid (DC) analysis is applied to processed SAR data, it can be used to identify mismatches between the radar phase history (equation 12) used to process the data and the relative motion of the scene caused by errors in the imaging geometry models used [67] or by motion present in the scene. The measured Doppler centroid can be used to adapt the SAR processing filter. Due to the wide Doppler bandwidth of the SAR data, it is difficult to measure DC offsets of individual targets. The DC offset of moving targets can be practically used only if the SCNR is sufficiently large, as

is the case for large ships observed by regular strip-map SAR [68] or if the clutter is well suppressed by multi-aperture processing [38], [69].

In time-frequency analysis, the Doppler frequency history of a range-focused target in a clutter-suppressed scene provides the primary data needed to construct a target dynamics model. The inferred target motion model, combined with the radar imaging geometry, generates the phase-history function (equation 13) needed for SAR processing.

When a SAR image contains features that identify the probable location of a target (roads on land or wakes in the ocean), the displacement of the imaged target from its probable location provides a measurement of the radial velocity of the target using equation (11). Azimuth displacement of a moving target, as quantified by equation (11), is proportional to the target's radial speed (and hence the DC offset), but it can only be used if there are stationary image features to serve as a reference, such as rail tracks for a moving train or visible wakes for a moving ship [70]. Wakes are not always present in SAR imagery and typically they are difficult to detect [71].

When a pair of target candidates is displaced in the along-track direction by d_{Amb} in equation (13) and is displaced in range by the expected radar range curvature for the observed azimuth distance, the smaller amplitude target at the larger image range is identified as the ambiguity of the other target. This applies to both land and ship sampling-ambiguities on the sea surface. For land ambiguities, the stationary ambiguity source can be suppressed by DPCA processing but the land target ambiguity on the sea surface is usually not suppressed below the residual clutter plus noise level.

2.5.2.2   ATI estimates of target velocity

When target candidate signals from a pair of balanced and spatially registered GMTI aperture channels are correlated to produce an ATI image of the target candidate scene (equation 24), estimates of the phases of the resolution cells in the ATI scene are given by the model described by equation (26) for radial motion components. For the situation where a target sample totally dominates the radar return, the relationship between the ATI phase angle and the target sample velocity components [73] can be expressed as

$$\gamma_k \approx 4\pi \frac{V_{Rk}D}{V_S\lambda} + 4\pi \frac{V_{Ak}D}{\lambda R_k f_S}. \tag{32}$$

where:

- V_{Rk} is the radial velocity of the kth target sample,

- D is the two-way spacing between the GMTI antenna apertures,

- λ is the radar wavelength,

- V_S is the radar platform speed,

- V_{Ak} is the cross-range (azimuth) velocity component of the kth target sample,

- R_k is the radar range of the kth target sample, and

- f_S is the radar pulse frequency (PRF).

Considering a ship as an ensemble of clustered resolution cells, the ATI radial velocity estimate for each cell is approximately given by

$$V_{Rk} \approx \frac{\gamma_k \lambda V_S}{4\pi D} - \frac{V_S V_{Ak}}{R_k f_S}. \tag{33}$$

Equation (33) demonstrates the GMTI measurement coupling between azimuthal and radial target velocities [72], [73]. Since the target azimuth velocity contribution to the radial velocity estimate in equation (31) is considerably smaller than the ATI phase term most of the time, it can be ignored for this discussion but becomes increasingly important as the target direction of motion approaches the tangential radar observation geometry.

The moving target detection process works point by point through the GMTI aperture data to select signal spectra or complex image points that meet the target selection criteria of the detector. The set of target candidate points are assumed to contain target data and candidates can be selected or rejected based on the properties of target motion estimates that are generated from the detected data. From the form of equation (30), signals that originate from non-target sources (superimposed clutter, ambiguities and radar noise plus all cross-products of these). Cross products between target signals and the superimposed sources combine to create a phase noise that corrupts the target motion phase estimate. For a cluster of detections from a common target such as a ship, the ATI phase estimates will be purest for target returns that are large with respect to all other signals and will be most contaminated (spread) for target components whose magnitudes are closest to the magnitudes of the other terms. When a DPCA detector is used to find target candidates, the shape of the threshold function in the ATI amplitude-phase plane will affect the contributions of low amplitude signals to the ATI Phase estimation process as shown in Figure 23 for a large ship that is moving towards the radar, at a constant speed, in a calm sea. In this case the ship (image shown in Figure 9) is a correctly focused moving target.
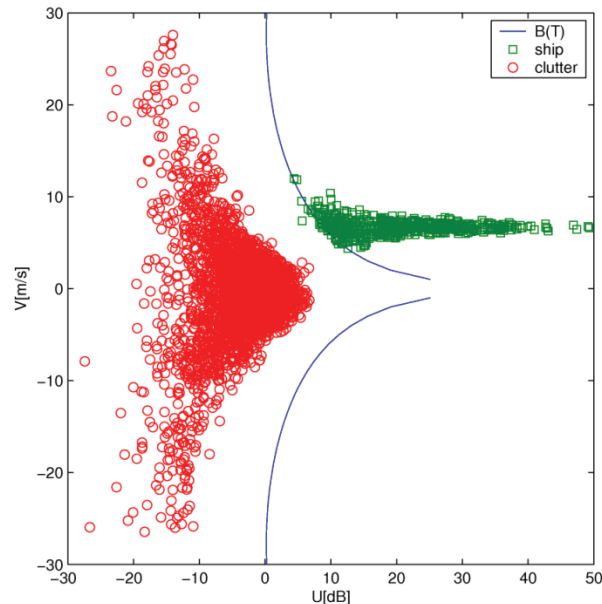
Figure 23: *Sea surface returns, red, and ship samples, green, in the ATI velocity-magnitude plane.*

In Figure 23, the horizontal axis is the sample point ATI magnitude, defined by equation (22) and expressed in dB and the vertical scale is the ATI velocity estimate defined by equation (31). The blue curves are the DPCA detection threshold, mapped into the ATI magnitude-velocity plane using equation (23) with $\Delta U = 0$. The effect of the DPCA detection filter on the ATI velocity estimates for small-amplitude target signals is to introduce a velocity-dependent cut-off boundary in the phase-noise spread that is an inverse sine function of the threshold to velocity ratio.

If the target candidate cluster belongs to a ship ambiguity, the ATI magnitude-velocity representation of the target signal will be similar to the representation shown in Figure 22 but will have fewer points, a somewhat larger phase noise spread and a smaller peak amplitude.

When the rare-event moving-target detector is used instead of the DPCA detector, the ATI magnitude-velocity plane target-detection boundary is offset from the sea return histogram, shown as red circles in Figure 23, by the selected sample proximity ratio. The same form of weak target cut-off boundary will be seen for the high phase noise target estimates as is seen for the DPCA case.

The ATI magnitude-velocity representation for ship targets that were detected by a covariance matrix detector are not shown here since other ship motion measurement algorithms are usually used when more than two GMTI channels are used in a covariance analysis.

2.5.2.3   Time-frequency decomposition analysis

The range history model determines the phase history of the moving target return via equation (2). As any SAR signal, the moving target return has a large time-bandwidth product with a variable instantaneous frequency over the real aperture duration. The time derivative of the range history (from equation 14) provides the instantaneous Doppler frequency in any one of the channels, registered to the leading channel:

$$f_{\mathrm{D}}(t) = -\frac{2}{\lambda} \frac{dR_p\left(t + \frac{D_p}{v_{\mathrm{s}}}\right)}{dt} = -\frac{2}{\lambda}\left(v_{\mathrm{r}} + \frac{D_p}{R_0}\left(\frac{R_0 a_{\mathrm{r}}}{v_{\mathrm{s}}} - v_{\mathrm{t}}\right) + \frac{v_{\mathrm{rel}}^2}{R_0}t\right) \tag{34}$$

This equation models the Doppler history of a moving target as a linear ramp with a frequency offset depending on the radial speed of the target at $t = 0$ and a slope that combines in v_{rel}: the speed of the radar, the along-track speed of the target and the constant radial accelerations of both.

When the DPCA technique is used on a pair of balanced and registered channels, the phase structure and the instantaneous Doppler frequency structure of the signal is preserved at least in the unambiguous portion of the signal, which is not distorted by channel balancing and registration. The amplitude of the difference signal from the two channels has the form given by equation (22) where the resulting amplitude depends on the target's radial speed through the sine law. In this way, stationary targets are suppressed to the noise level and time-frequency analysis of the residual signal becomes feasible.

A DPCA frequency-time plot of a target that is moving with constant velocity appears as a linear ramp in a noise background as illustrated by Figure 24 from [74] which contains time-frequency ramps for a group of vehicles that are moving on a highway. The constant velocity offset terms

can result in target-track wrapping about the phase angle discontinuity at $\pm\pi$ as can be seen in Figure 24. Variations in slope in Figure 24 correspond to combined linear acceleration differences between the observed targets.
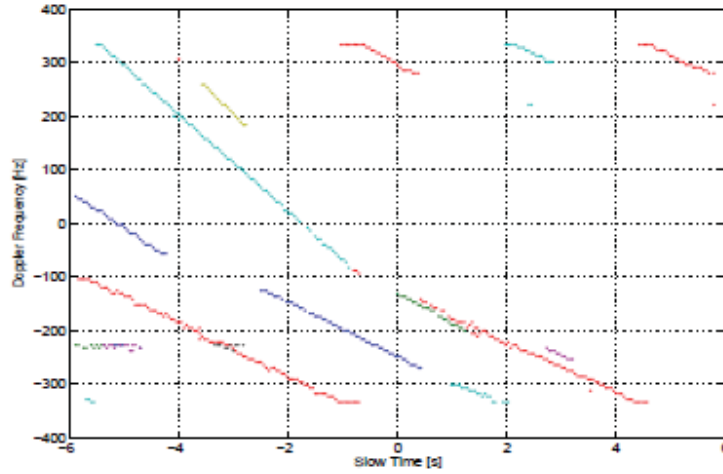
Figure 24: Doppler frequency-time data from airborne GMTI measurements of highway vehicles, frequency is given in Hz and time is given is seconds.

Target accelerations that are common for ship targets act to change the slope of the frequency time relationships for the target points and can add non-linear effects (time-frequency history curvature) due to the functional form of the accelerations over the observation interval.

Time-frequency decompositions are primarily useful for tuning phase history-models that are used for target focussing. Target motion information is a secondary output of the tuning process.

Although the model in equation (34) provides a tool to visualize the roles of various parameters in time-frequency results, many of these are unknown for an arbitrary detected target. The time-frequency trace for detected targets in a DPCA data plane needs to be extracted from the measured data.

The short-time Fourier transform approach partitions the target observations time window into a number of blocks and uses a Fourier transform calculation for data segments that overlap adjacent blocks to estimate the spectral peak and thus the target Doppler frequency at the center of each block. This estimation approach has the disadvantage that there is an inherent trade-off between time and frequency resolution and has the advantage that the process is linear and does not create intermodulation products.

2.5.2.3.1 Cohen class time-frequency decompositions

There are many time-frequency estimation algorithms that use signal energy using quadratic and bilinear calculations. Among these Cohen class distribution functions [75] is the frequently used Wigner-Ville distribution

$$WVD_{s1,s2}(t,f) = \int_{-\infty}^{\infty} s_1\left(t+\frac{\tau}{2}\right) s_2^*\left(t-\frac{\tau}{2}\right) e^{-j2\pi f\tau}\, d\tau \tag{35}$$

for two GMTI signal channels, s_1 and s_2. The computed distributions can be represented by the matrix

$$M(t,f) = \begin{pmatrix} WVD_{s1,s1}(t,f) & WVD_{s1,s2}(t,f) \\ WVD_{s2,s1}(t,f) & WVD_{s2.s2}(t,f) \end{pmatrix}. \tag{36}$$

The calculation can be generalized to any number of GMTI channels. For a two-channel radar using a DPCA channel combination there is only one channel in equations (35) and (36). Since the signals of interest are only available for a limited time, a weighting function $h(\tau)$ can be inserted into the integral in equation (32) to select the desired time interval. The time-frequency output of equation (36) can be analyzed to determine the functional form of the time-frequency relationship [38], [36].

All of the Cohen class time-frequency estimators are non-linear and are subject to intermodulation effects when several signals are present in the estimation window. Care must be used in interpreting the results in some cases.

2.5.2.3.2 Frequency tracking algorithms

Yet another way of extracting the instantaneous frequency modulation of the SAR signal is by frequency tracking.

Considering the discrete nature of the SAR measurements, the discrete-time angular frequency (phase increment from sample k to sample $k+1$) can be defined as the discrete-time counterpart of the continuous Doppler frequency given in equation (34).

$$\omega_{\mathrm{D}}(\boldsymbol{r}_i, k) = \frac{2\pi}{f_{\mathrm{s}}} f_{\mathrm{D}}\left(\frac{k}{f_{\mathrm{s}}}\right) = -\frac{4\pi D_{\mathrm{s}}}{\lambda}\left(\frac{v_{\mathrm{r}}}{v_{\mathrm{s}}} - \frac{\dot{\varepsilon}_{\mathrm{r}}(\boldsymbol{r}_i, k)}{v_{\mathrm{s}}} + \frac{D_{\mathrm{s}}}{R_0}\frac{v_{\mathrm{rel}}^2}{v_{\mathrm{s}}^2}k\right) \tag{37}$$

Range history perturbations (from equation (13)) have been introduced to better suit the nature of the radar signal returned from a ship, which is seen as an ensemble of target points. In equation (37), $\dot{\varepsilon}_{\mathrm{r}}(\boldsymbol{r}_i, k)$ is the time derivative of the radial projection of the wave-induced motions for the i-th scattering point on the ship. As the dynamic motions of these points are predominantly periodic, so is the time derivative, which is proportional to the amplitude and inversely proportional to the period of this periodic motion. A recursive model for the moving target signal $s(\boldsymbol{r}_i, k)$ embedded in noise $n(\boldsymbol{r}_i, k)$ [52], [38] provides an estimation metric:

$$n(\boldsymbol{r}_i, k) = s(\boldsymbol{r}_i, k) - \exp(j\omega_{\mathrm{D}}(\boldsymbol{r}_i, k)(s(\boldsymbol{r}_i, k-1) - \rho(\boldsymbol{r}_i, k)n(\boldsymbol{r}_i, k-1)) \tag{38}$$

where model parameters $\omega_{\mathrm{D}}(\boldsymbol{r}_i, k)$ and $\rho(\boldsymbol{r}_i, k)$ can be estimated adaptively by recursively minimizing the cost function $\sum_k |n(\boldsymbol{r}_i, k)|^2$. Such a recursive adaptive-estimator acts as a Doppler frequency tracker and it provides an estimate $\hat{\omega}_{\mathrm{D}}(\boldsymbol{r}_i, k)$ using all previous samples of the noisy returns $s(\boldsymbol{r}_i, n)$ up to sample k in the increasing order (forward tracking) or decreasing order (backward tracking). Algorithm details are presented in [76]. An illustration from [76] of the estimated Doppler frequency history is shown in Figure 25 for a large ship (238m) in calm sea and in Figure 26 for a small ship (25m) affected by the wave regime. Both cases were acquired in the polarimetric SAR mode and the examples show that frequency tracking can be successful even without the DPCA step if the ship SCNR is sufficiently large.

Forward and backward tracking can be combined to compensate for the tracker latency. This can be observed in the Figure 25 and 26 examples.
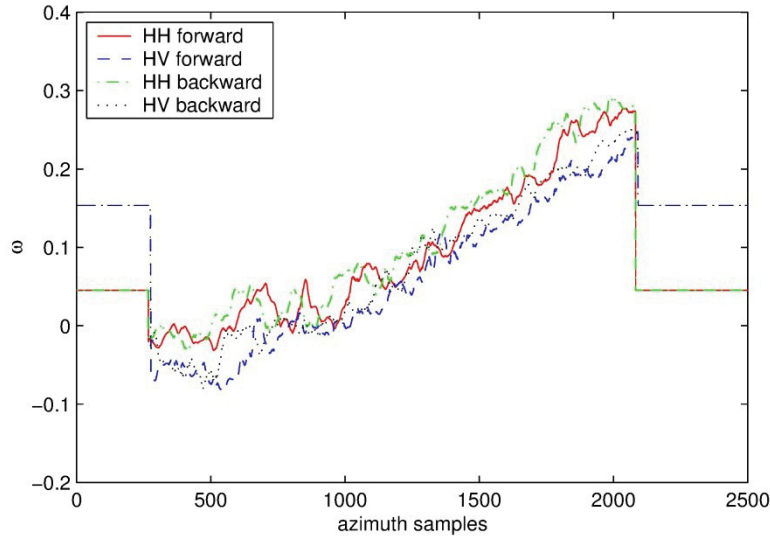
Figure 25: *Time-frequency plot generated by Doppler frequency tracking for a large ship.*
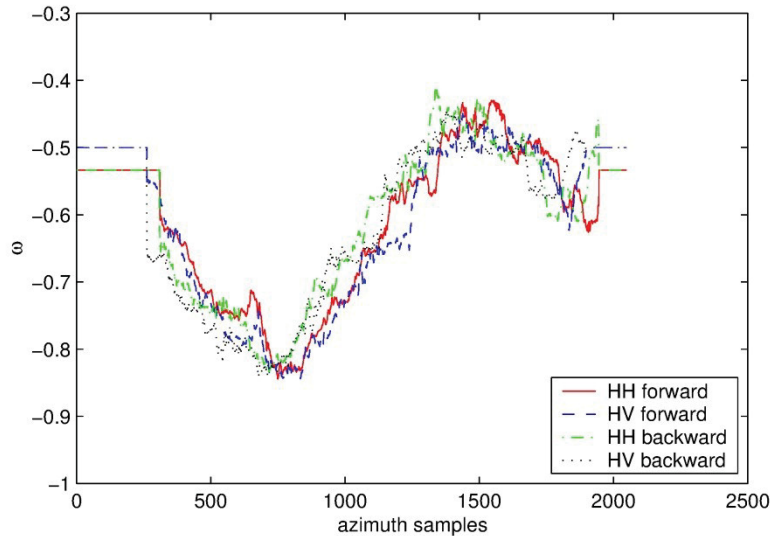
Figure 26: *Time-frequency plot generated by Doppler frequency tracking for a small ship.*

The ordinate parameter ω in Figures 25 and 26 is frequency in radians per unit sample spacing. In the case of the small (~25 m) vessel in Figure 26, the ship acts as a mechanical low-pass filter for sea surface motions spectra and shows a significant motion response to a single wave component whose period is approximately 5.4 s and wavelength is approximately (Table 1) 45.5 m. Although swell waves with wavelengths greater than 190 m and wind waves with wavelengths less than

11 m may be present, their properties cannot be deduced from the ship response to the sea surface in this case.

For the case shown in Figure 25, the vessel length was noted to be 238 m and the sea surface was described as calm. The displayed data could support the hypothesis that a weak, very long wavelength (950 m) swell wave was present but the evidence for its existence is, at best, fragile.

2.5.2.4   Covariance matrix analysis.

Expansion of the GMTI channel covariance studies referred to in Section 2.5.1.3 to accommodate GMTI data channels from three or more antenna apertures has resulted in two nearly optimum processing algorithms, EDPCA and ISTAP [64], [65], [66] for extracting target motion measurements. Both algorithms try to optimize the target motion parameters in a statistical target parameter vector

$$\boldsymbol{\vartheta} = \begin{bmatrix} \sigma_S \\ \theta_S \\ t_{S0} \\ v_{x\perp} \\ v_x \end{bmatrix} \tag{39}$$

to maximize the SINR of the target.

In equation (39):

- σ_S is the radar cross section of the target,

- θ_S is the phase angle of the target signal,

- t_{S0} is the time that the target is broadside to the GMTI flight track in ECEF coordinates,

- $v_{x\perp}$ is the component of the target velocity that is perpendicular to the radar velocity vector in ECEF coordinates, and

- v_x is the component of the target velocity that is parallel to the radar velocity vector.

The EDPCA algorithm tests successive estimates of $\boldsymbol{\vartheta}$ by generating trial phase histories, processing the GMTI channel data and cancelling the n-channel clutter in a sequence of iterated calculations. Processing terminates when the target SINR is maximized. The best $\boldsymbol{\vartheta}$ contains the desired target motion parameters.

The ISTAP algorithm uses the post-Doppler STAP (space-time adaptive processing) approach to clutter cancellation by applying the inverse of the clutter covariance matrix to the signal data in the frequency domain and then iterates processing runs based on successive trial estimates of $\boldsymbol{\vartheta}$ until a test statistic that indicates the SINR maximum for the tested target is satisfied. The final form of $\boldsymbol{\vartheta}$ contains the desired target motion estimates.

When DPCA sampling conditions are met for data acquisition, both algorithms yield equivalent results. When the DPCA sampling condition is not met, the ISTAP algorithm has somewhat better performance. The EDPCA algorithm requires more computational resources than the ISTAP algorithm as the clutter cancellation process needs to be repeated for each trial value of the target parameter vector.

The EDPCA and ISTAP algorithms have been tested for land targets [66]. EDPCA is applied to ship targets in Section 4.7.

3 Airborne SAR-GMTI observations of ship dynamics

3.1 Environment Canada CV580 SAR-GMTI radar parameters

The discussions of airborne SAR GMTI measurements of ship targets are based on data obtained by the Environment Canada (EC) CV580 SAR system (now decommissioned) [77] that was operated in its temporal SAR interferometer (ATI) mode shown in the block diagram B in Figure 27.
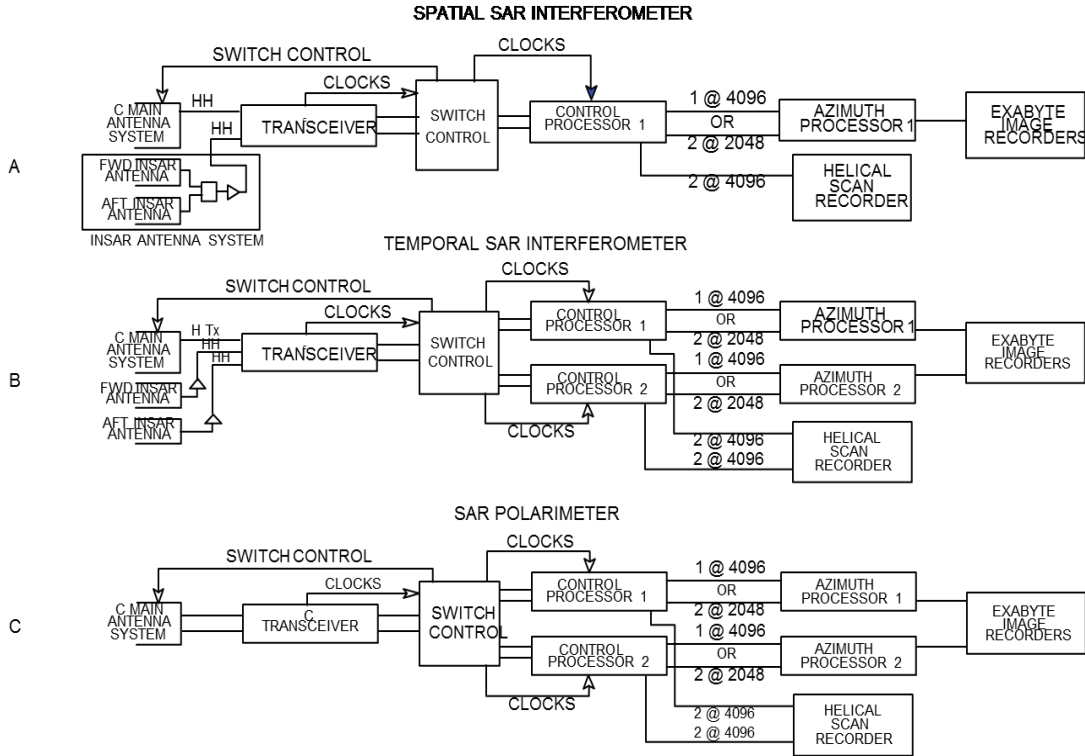
Figure 27: CV 580 SAR system mode configurations.

For GMTI operation, this radar transmitted signals from a belly-mounted, azimuth and elevation steered antenna C Main Antenna system, Figure 27. The main antenna pitch steering was locked for GMTI modes. Received signals were acquired from a side-mounted, azimuth steered, two-aperture antenna (InSAR antenna system, Figure 27B). The antennas were separated by 2.8 m along a line inclined at 41° to the aircraft vertical axis and relative antenna motions due to aircraft attitude changes were compensated by lever arm calculations in the radar's motion compensation system.

The radar pulse timing for GMTI operation was slaved to the inertial navigation system (INS) aircraft velocity V_A estimate by a scaling factor $f_S = 5.14 V_A$ (PRF/V = 5.14) so that the radar pulses were uniformly spaced at 0.195 m along the flight track. The CV 580 radar parameters that are significant for GMTI analysis are listed in Table 3.

The main antenna was steered in elevation to compensate the aircraft roll angle and was steered in azimuth to compensate the aircraft yaw angle. The yaw angle was referenced to the flight track angle (estimated great circle from the present aircraft position estimates to the flight-line end-point coordinates). Inertial measurements were compensated for beam squint measured from the Doppler centroid of the radar returns over a 12 second interval. The InSAR antenna was fixed in elevation and was steered to compensate the aircraft yaw angle and the measured beam squint.

Typical flight altitudes were 6700 m and nominal flight speeds were 123 m/s. For data analysis, INS data was combined with GPS (global positioning system) measurements and nadir return data to estimate the true aircraft speed and its height above the sea surface. A plane-earth approximation was used for imaging geometry estimation.

Aircraft flight tracks were controlled to place the measured targets between 50° and 75° incidence angles.

Time–tagged navigation and GPS position data were recorded in parallel with the signal data.

Table 3: CV 580 SAR-GMTI parameters.

Parameter	Value
Radar frequency	5.30 GHz
Radar bandwidth	26.32 MHz
Range pulse chirp length	7 μs
Compressed range pulse duration	38 ns
Compressed range pulse length	5.7 m
Peak transmitter power	16 kW
Receiver noise figure	5.2 dB
Noise bandwidth	34 MHz
Noise-equivalent σ^0	-36 dBm^2
Range compression	Surface acoustic wave device
Range-compressed signal quantization	6I, 6Q bits
Instantaneous dynamic range (raw data)	33 dB
Main antenna azimuth beam width (-3 dB)	3.03°
InSAR antenna ATI aperture azimuth beam width (-3 dB)	6°
Two-way ATI aperture beam width (-3 dB)	3.52°
Two-way antenna gain per aperture (-3 dB)	34 dB
PRF/V	5.14 m^{-1}
ATI aperture separation oversampling ratio	2.364
Relative two-way antenna gain at Nyquist sampling	-13.26 dB

The radar sample-spacing was slaved to the INS platform speed estimates and the DPCA sampling condition could not be achieved at any aircraft speed. Data interpolation is required for ATI channel registration. Noting that the along-track radar over-sampling ratio was 2.32, the sampling rate corresponded to a relative two-way antenna gain < -27 dB for Nyquist sampling at 8.17° beam width. Based on the measured one-way pattern of the main (transmitting) antenna shown in Figure 28 and the sinc pattern of the ATI receiving antenna apertures, the first side-lobe of the two-way antenna pattern was approximately -32 dB at 4.5° from bore-sight and the second side-lobe of the two way pattern was approximately -37 dB at 7° from bore-sight. The sampling

ambiguity was dominated by the first main antenna side-lobe from each side of the antenna pattern and the side-lobe pair are symmetrically located in the first sampling ambiguity interval of the reference channel. Ambiguity content shifting caused by sample interpolation to DPCA sampling altered the symmetry of the first ambiguity content but did not change the ambiguity magnitude. It is expected that the 1.4 sample shift needed to register fore and aft ATI aperture limited DPCA sampling ambiguity suppression to approximately 10 dB, and resulted in residual ambiguity levels comparable to the residual strength of the suppressed clutter.
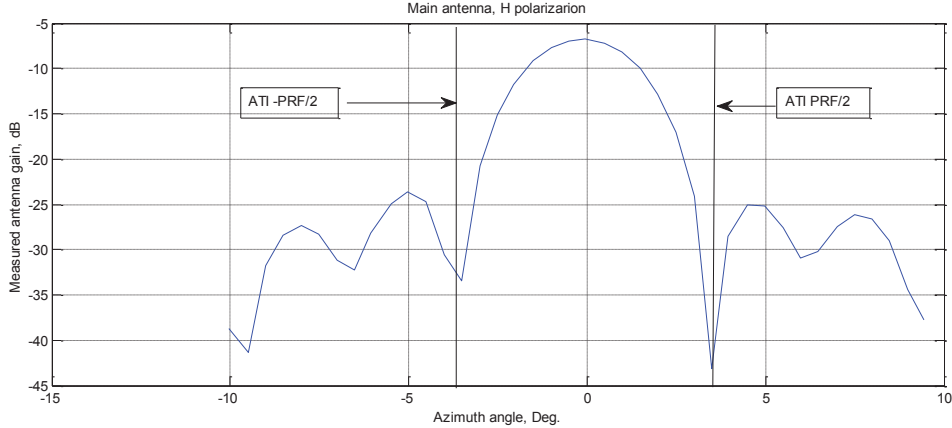
Figure 28: One-way azimuth gain of the ATI transmitting antenna.

The radar oversampling ratio will allow access to useable data over an increased dwell time interval (synthetic aperture time) that is 2.36 times larger than the nominal synthetic aperture time defined by the -3 dB beam width of the two-way antenna gain. For an aircraft speed of 120 m/s, the nominal aperture time is 5.1 seconds at 10 km range and the maximum usable time is 11.8 seconds for targets with large enough radar cross sections to provide useable signals at -27 dB antenna gain. For medium sized ships, time windows up to 10 seconds in length have been found to be useful [52].

3.2   SAR-GMTI model for long observation intervals

A general range history model has been presented in the previous discussions and it will be used in this section after performing some variable transformations [37] to accommodate both airborne and space-based observation geometries with arbitrary time reference and to account for the excursions of different scattering points on the ship in response to the wave regime [38].

Starting from the quadratic approximation to the range history model described in equation (14), the range history $R_p(t)$ for radar aperture p can be expressed in sampled time k as the phase history $\varphi(p,k) = 4\pi \frac{R_p(k)}{\lambda}$ where the range is now expressed in radar wavelengths ., p is an integer $p=0,1,…,P$-1 and the radar aperture position $D_p = pD$ for uniform aperture spacing D to yield

$$\varphi(p,k) \approx -4\pi\frac{R}{\lambda} + 4\pi\frac{D}{\lambda}(\Phi - \Psi)p - 4\pi\frac{D_S}{\lambda}(\Phi - \mu)pk +.$$

$$4\pi\frac{DD_S}{\lambda R}(\beta^2 - \nu)pk - 2\pi\frac{D_S^2}{\lambda R}(\beta^2 - 2\nu + \eta)k^2 + \zeta(p,k) \tag{40}$$

where:

- R is the radar range,

- D is the two way antenna aperture baseline distance (the separation between phase center p and phase center $p\pm1$),

- D_S is the spatial displacement of an aperture over one pulse repetition interval $D_S = \frac{V_S}{f_S}$ for radar speed V_S and sample frequency f_S,

- Φ is the direction of arrival of the SAR signal at the radar antenna,

- Ψ is the squint angle between the radar beam center and the broadside direction from the radar trajectory,

- μ is the projection of the target velocity onto the radar range vector normalized by V_S,

- β is the ratio (≤ 1) of the ground projection of the sample spacing to the sample spacing at the radar platform ($\beta = 1$ for airborne SAR),

- ν is the component of the target velocity that is parallel to the SAR velocity vector (the along-track speed of the target) normalized to V_S,

- η is the radial acceleration of the target normalized to the product V_S^2/λ, and

- ζ is the radar phase noise plus higher order terms that are not accounted for in the second order expansion.

For the airborne radar system discussed in the previous section:

- Ψ is variable and is driven by the symmetry of the scene clutter spectrum through a clutter-lock servo-control system with a 12 second time constant,

- $\beta = 1$,

- $D = 0.27$ m,

- $f_S = 5.14V_S$, (using the INS V_S estimate)

- $D_S = 0.195$ m, (using the radar f_S estimate)

- $\lambda = 0.0566$ m, and

- $p = 0$ or 1 (there are two phase centers).

To derive valid signals and imaging geometry estimates to apply equation (40) for phase history estimation, combinations of INS, GPS measurements, range delay measurements and signal Doppler spectrum measurements were used to:

1. compensate the acquired signal data for aircraft motion and trajectory estimates,

2. refine the V_S and D_S estimates,

3. compute Ψ from Doppler centroid data, and

4. estimate the true platform height above the sea surface from the nadir return time.

The two GMTI channels were registered by interpolation of the slave channel and the amplitude and phase balancing operations were performed. A time-frequency decomposition of the ship target signal was used to estimate the range cell migration compensation function over the full analysis time window to be used for target motion estimation and range cell migration compensation was applied to the signal data block containing the ship target.

With reference to equation (40) the remaining unknown's to be estimated for each point of the ship target are:

- Φ the direction of arrival of the SAR signal at the radar antenna,

- μ the projection of the target velocity onto the radar range vector normalized by V_S,

- v the component of the target velocity that is parallel to the SAR velocity vector, the along-track speed of the target, normalized to V_S, and

- η the radial acceleration of the target, normalized to the product V_S^2/λ.

These parameters are derived from the target motion estimation process.

3.3 Target motion estimation algorithms

This section describes in more detail the general SAR-GMTI algorithms tailored to the analysis of ship signatures collected by EC CV580 SAR when it was operated in its temporal interferometer (two-aperture GMTI) mode shown in Figure 25 B.

From the previous discussions it is clear that multidimensional observations are made available by the multi-aperture SAR signal acquisition of ship returns. These dimensions are provided by:

1. the response duration in the slow time (or pulse index count k use in equation (37)),

2. the physical dimensions of the ship expressed as a group of scatterers in the range direction, and

3. the channel diversity (or phase center index p).

The applied analysis algorithms are discussed in terms of the information extraction problem that needs to be addressed:

1. Doppler history estimation in the slow time domain,

2. rigid body motion analysis using range diversity (scattering from different range bins),

3. array processing techniques (channel processing), and

4. algorithm combinations.

3.3.1   Doppler history estimation for ships

Doppler history estimation in the slow time domain was discussed in subsection 2.5.2.3. Different approaches that were presented can be used in the analysis of ship signatures to extract the instantaneous Doppler frequency as a function of slow time. By definition, the instantaneous Doppler frequency is the time derivative (or difference for PRF sampled data) of the phase history, which is modeled by equation (40).

Following the approach outlined in [38], the discrete slow time signal is first array-multiplied (modulated) by the conjugate of a unit-amplitude, synthetic deterministic signal that has the phase history shown in equation (40) for stationary world parameters. This synthetic signal plays the role of a reference chirp with linear and quadratic coefficients computed for the given imaging geometry assuming no target motion. Modulation of the signal with this reference chirp removes the bulk of the quadratic term in the phase history and significantly reduces the slope (Doppler rate) of the instantaneous frequency. The frequency modulation operation is similar to aircraft motion compensation, which cancels the phase perturbations due to SAR deviation from the straight trajectory. The removal of the geometric contributions to the Doppler rate of the ship response (signal de-ramping) provides two, significant signal analysis advantages:

1. Instantaneous frequency tracking is improved since slower changes are typically tracked with increased fidelity. The time-frequency plot shown in Figure 24 is generated after modulating the ship returns with the reference azimuth chirp. The residual slope observable in this figure is due to the ship motion and directly proportional to the normalized along-track speed of the ship in equation (37).

2. The visibility of fine-scale (micro-Doppler) modulations of the instantaneous Doppler frequency is increased as illustrated in Figure 26. The micro-Doppler frequency modulations are not caused by the cruising speed nor by a constant acceleration (such as maneuvering) of the ship, which are accounted for in equation (40) but are results of sea surface modulation of the hull motion. The quasi-periodic frequency modulation shown in Figure 24 comes from the oscillating motion of a small ship which is experiencing periodic acceleration caused by the ocean waves. In the range history shown in equation (13), these oscillations are represented by the term ε_r in the phase history, they are normalized by the wavelength, and in the time-frequency representation, they are the phase derivatives, as indicated in equation (37). Since the ship acts as a mechanical low-pass filter for the sea surface motion, these terms are periodic or quasi-periodic.

As the example in Figure 26 shows, long synthetic aperture intervals allow the observation of the ship dynamics in the wave field because the SAR aperture is of the same order of magnitude as, or longer than, the wave period. This feature of the airborne SAR (not shared with the standard space borne SAR) is valuable because it permits the separation of the constant velocity measurements and the measurements of the wave dynamics.

From the radar observation perspective, a ship can be considered to be a mechanical low pass filter that is applied to sea motion. To a first approximation, only sea motion components whose wavelength is greater than one half of the ship dimension in the wave propagation direction will

have significant effects on ship motion. In Figures 25 and 26, the instantaneous Doppler frequency history of a ship target has two different waveforms, one is linear and the other is periodic. In an arbitrary case, any combination of the two can occur. Therefore the instantaneous Doppler frequency is assumed to take the form:

$$\omega_D(k) = p_0 + q_0 k + \sum_{n=1}^{N}(p_n \cos(\Omega_n k) + q_n \sin(\Omega_n k)) \tag{41}$$

where p_0 and q_0 are the linear component parameters and p_n, q_n and Ω_n describe the periodic components of the waveform. In practice, the useful number of periodic components is very limited, $0 < N \leq 2$. Assuming one periodic component, $\frac{2\pi}{\Omega_1}$ is the swell encounter period and $\sqrt{(p_1^2 + q_1^2)}$ is the magnitude of the Doppler frequency modulation. The phase of the swell is given by the ratio of p_1 and q_1 and is random as the ship may be at any stage of its periodic motion when it enters the SAR footprint. Higher-order terms are included in equation (41) to model the superposition of ocean waves that may have different periods and directions. The problem of decomposing the ship motion into the constant cruising component and the periodic components is actually the problem of estimating all of the unknown parameters in (41). This problem is solved by an iterative procedure that includes three steps:

1. harmonic analysis based on the Root-MUSIC algorithm [78] is used to estimate the encounter frequencies Ω_n,

2. linear fits to the composite results estimate all p and q amplitudes, and

3. the linear term is removed before the next harmonic analysis in the iteration.

The details of this procedure are presented in [52], [38]. Having in mind that wave frequencies Ω are very low, the correlation matrix for the Root-MUSIC (MUltiple SIgnal Classification) algorithm is composed using large correlation lags (L,2L, … instead of 1,2,…). This Root-MUSIC modification is done simply by extracting L interleaved down-sampled sequences from the input sequence $\{\omega_D(k)\}$ and then applying the standard form of the algorithm [78]. Once frequencies Ω are estimated, linear fitting of all p and q amplitudes is a straight forward minimum least-squares task.

3.3.2   Rigid body motion estimation using range diversity

The range extent of the ship as a rigid body was taken into account in equation (13). It is noted that the oscillatory component ε_r depends on the distance of the observed scattering point from the center of buoyancy. The normalized and differentiated value corresponding to this oscillatory component is also oscillatory and may also depend on the position of the scattering point on the ship. Going back through our ship modeling study, we see that the cause of this spatial diversity is the set of rotations of the rigid body expressed in (1). For a rigid body, we assume that the periods of yaw, pitch and roll motion are the same for all scattering points, but the resulting target point motion magnitudes in the range history modulation are deterministic functions of the scattering point coordinates in the ship's frame of reference.

Most large ships have several distinct strong scattering centers along their longer axis. As discussed in Section 2.2 the spatial distribution of such scattering centers depends on the structural and surface properties of the ship and its cargo. Examples shown in Fig. 6 are very

different, but from the radar point of view they all have multiple dominant scattering centers. This fact can be used to extract the instantaneous frequency for several prominent scattering centers along the ship to provide multiple time-frequency plots for the same ship. This is only possible if:

- different scattering centers are separable in range, which is not the case for ships travelling parallel to the SAR;

- range resolution is fine enough to resolve dominant scattering centers in the range compressed and azimuth uncompressed signal.

The decomposition of a ship target into range-dependent Doppler histories uses a model of the stationary world geometric signal to remove the predictable Doppler frequency slope due to SAR platform velocity (frequency de-ramping) as was discussed in the previous section. Figures 29, 30 and 31 show the combined time-frequency plots produced for the same ship acquired from three airplane passes with different headings. The ship was 131 m long travelling at about 18 kts. It was captured by the EC CV-580 SAR at relative heading angles of 86°, 50° and 134°, respectively. Solid lines represent the results of the frequency tracking method discussed in Section 2.5.2.3.2, applied after frequency de-ramping. Dashed lines are the results of extrapolation and interpolation according to the motion model given by equation (41) and their details will be explained at the end of this subsection.

A number of important observations can be made on these figures, which prompt further questions and suggestions.

In the case shown in Figure 29, the along track component of the ship's cruising velocity is zero and mean acceleration is zero. Because of this and because of de-ramping, there is no bulk slope in the time-frequency plot. In the other two cases, there is an opposite trend (mean slope) in the time-frequency plots because the along-track component of the ship's cruising velocity is parallel to the aircraft velocity in one case and antiparallel in the other. This observation suggests that the visible trend in the time-frequency plots provides a good indication of the vessel's along track speed if:

1. the platform speed is known with high accuracy and accounted for, and

2. the linear slope can be separated from the oscillatory modulation due to the wave impact.
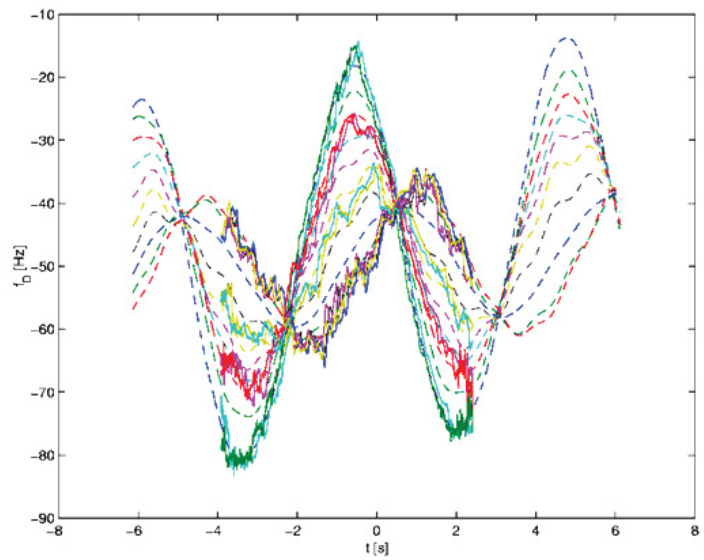
Figure 29: Time-frequency decompositions at four radar ranges for a ship moving almost perpendicularly to the SAR ground track.
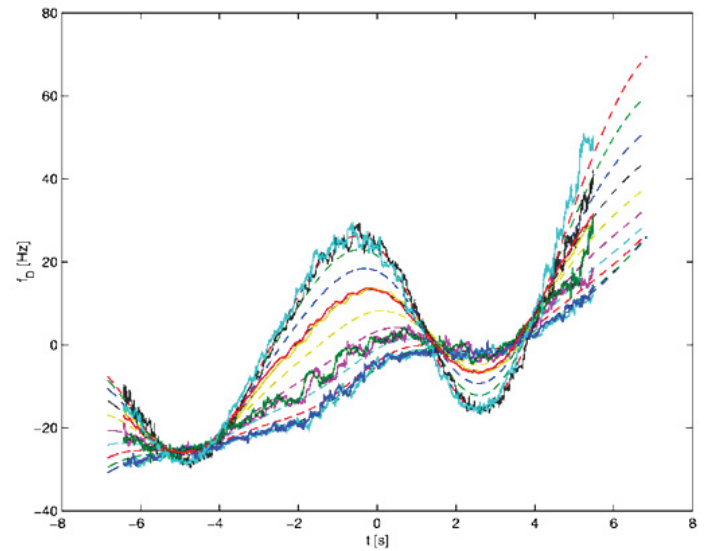
Figure 30: Time-frequency decompositions at four radar ranges for a ship moving at 50° relative to to the SAR ground track.
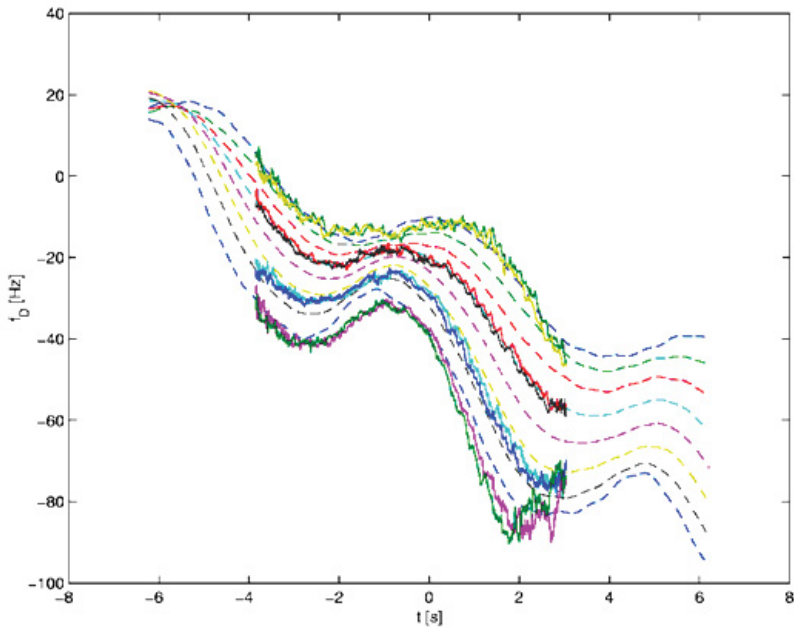
Figure 31: *Time-frequency decompositions at four radar ranges for a ship moving at 134°*
relative to to the SAR ground track.

Oscillatory modulation is visible in all three cases, but it is easiest to analyse in Figure 29 in the absence of a constant slope. Different ranges are depicted by different colors. It is evident that the swell period is the same everywhere on the ship, but the magnitude of the wave component varies, as expected for a rigid body. One of the four wave plots is out of phase compared to the other three, which suggests that it comes from the radar returns sent from the opposite side of the buoyancy center relative to the rest. At certain time instants, all instantaneous frequencies become equal regardless of the position from which the SAR signal was back scattered. At such times there is no differential Doppler shift, which means no difference in radial speed between different locations on the ship. This can happen at the moments when ship rotational motion is about to reverse its direction (e.g., maximum pitch is reached). The extremes of the Doppler oscillations indicate the maximum radial speed attributed to the wave-induced motion. Maximum radial speeds, as a function of range, can be used to characterize ship's dynamics in response to the seas.

The preceding observations:

1. support our earlier discussions about ships as rigid bodies with translational and rotational motion and provide evidence that SAR is very sensitive to all types of ship motion;

2. suggest that more information about the ship and its load may be available from long observation intervals with range diversity; and

3. motivate further investigation that aims at separating linear trends from the periodic terms in the time-frequency plots using multiple ranges.

To accommodate multiple ranges, a slight modification is implemented in the procedure for decomposing ship motion into the linear and periodic components. All available instantaneous Doppler frequencies are fed to the Root-MUSIC algorithm to estimate the ocean wave encounter frequencies Ω_n, which are common to all Doppler histories of the ship as a whole. Fitting of p and q amplitudes is done for individual ranges. For a rigid body it is expected that the amplitudes p and q vary smoothly and almost linearly with range. After these amplitudes are estimated independently at discrete range coordinates, they are splined to cover the full extent of the ship in range. In this way, the complete phase history can be reconstructed for each range bin containing ship returns. A number of fitted phase histories are shown as dashed lines in Figures 29. 30 and 31. SAR image focusing uses the estimated range history to generate an improved ship image.

This analysis relies on target motion at a subset of radar ranges to model the target dynamics. The estimated motion cannot be readily decomposed into roll, pitch and yaw components in the ship coordinate system without external data including the ship length, the ship height profile, the wave period, the wave field orientation with respect to the ship and the significant wave height. Some of these parameters can be estimated from SAR imagery of the ocean surface in the vicinity of the ship.

3.3.3   Array processing techniques

The phase history equation (40) includes a term that is linear in both k(pulse count in slow time) and p (channel index). A straight forward way to visualize the channel-to-channel difference between the phase histories is to perform the ATI operation on a pair of channels in slow time before registration. This is feasible for most ships since they are strong radar targets even before azimuth compression. An example of a slow-time interferogram between a pair of unregistered channels is shown in Figure 32 for a 76 m ship. Both the magnitude and the phase are shown in this color-coded image. The effects of the range cell migration (RCM) are visible as the signature curvature and the slope of the interferogram phase is visible as a color modulation.
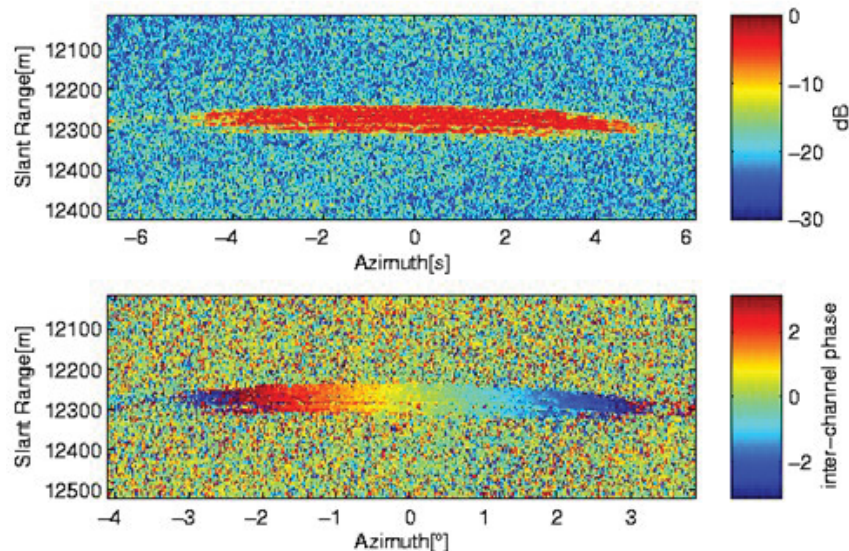
Figure 32: *Interferogram magnitude (upper image) and phase (lower image) over a ship for two unregistered SAR-GMTI channels.*

This ship target is further used to demonstrate two types of array processing techniques that are available with multi-aperture SAR [69]. They both involve manipulation of one channel using a selected channel as a reference.

Figure 33 illustrates compensation of the interferometric phase slope applying a linear phase term to one of the channels. After this operation, the interferometric phase becomes constant over slow time even without co-registration and it is proportional to the direction of arrival (DOA) of the ship returns at the reference time.

Figure 34 illustrates the effects of registration on the interferometric phase, which becomes constant over slow time and is proportional to the radial speed of the ship. This is the standard along-track interferometry (ATI) technique, but applied before azimuth focusing.
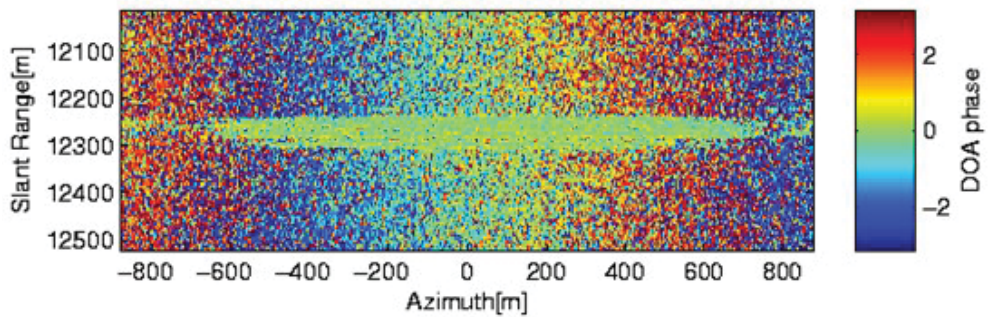
Figure 33: DOA Interferogram phase over a ship for unregistered channels after phase slope compensation and RCMC.
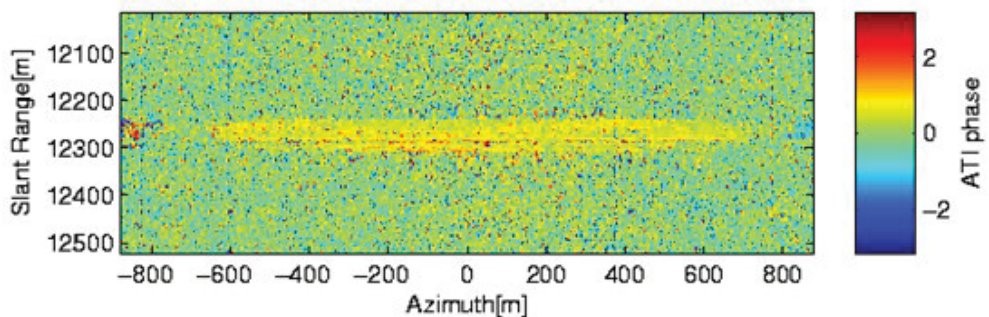
Figure 34: ATI Interferogram phase over a ship for registered (and balanced) channels with RCMC.

3.3.4   The combined methodology

SAR-GMTI ship signatures are extracted from combinations of analyses based on pulse index, range index and channel index. The analysis objective is the estimation of the unknown parameters in equation (34) and the translation of these into a ship motion signature.

The motion measurement process can be separated into two conceptual blocks:

1. the measurement of bulk motions of the entire ensemble of target points that represent the vessel, and

2. the measurement of differential motions about the vessel's center of buoyancy.

An iterative analysis process is usually required.

Bulk motions represent displacements of the entire vessel over the observation time and consist of horizontal translation motion and heave. Once imaging geometry effects are compensated, ATI processing can be used to make an estimate of the mean ship displacement rate over the observation time. This mean will include the mean horizontal velocity and the mean heave velocity. Similar but coarser results come from Doppler centroid estimates. De-ramped Doppler history data can be used to estimate the vessel heave and an iteration of the calculations can provide separated bulk vessel velocity and heave estimates.

The decomposition of the radar returns from the vessel onto several range blocks, each of which contains a significant radar returns, combined with the sea-motion model in equation (41) and a rigid-body assumption for the ship, allows the estimation of differential motions of scattering centers that are caused by ship rotations. The separation of pitch and roll effects from the estimated rotational motion is not usually possible from a single observation set without auxiliary information.

When the sea surface motion is statistically uniform over a large-enough area and when multiple SAR-GMTI observations can be made at different relative course angles between the ship and the radar platform (for example Figures 29, 30 and 31) ship motion estimates can be refined and it may be occasionally possible to separate ship pitch and roll effects.

Once a refined range history model has been developed for the ship target from analysis results, a refined SAR image of the ship can be generated and refined bulk motion estimates can be made.

3.4 Airborne SAR-GMTI Results for ship targets

Prior to the launch of RADARSAT-2 in 2008, the EC CV580 airborne SAR-GMTI system was used to collect ship GMTI observations for use in developing marine target GMTI processing methodology and to explore the ship imaging capabilities of two-aperture SAR-GMTI systems. Data from three medium size ships in this observation set are used to illustrate the results obtained. The full processing chain used to generate the outputs shown includes:

- general pre-processing steps such as aircraft motion compensation, system parameter refinement, antenna attitude tracking and channel calibration, which are based on the GPS and INS data;

- general SAR-GMTI steps such as range compression, azimuth compression, channel registration; and

- specific SAR-GMTI steps that are applicable only to ships as moving targets and implemented as a combination of techniques discussed in Subsection 3.3.

3.4.1 Sea motion effects using single observations

The results presented here illustrate the extraction of sea motion effects from the ship data using the analysis approaches discussed in Subsection 3.3 and the effects of sea-motion compensation applied to the target phase histories on vessel imaging.

The SAR signals of the three ships were collected on different dates in different sea state conditions. The ships had different lengths and speeds, as shown in Table 4, but all three were travelling perpendicular to the aircraft ground track.

Time-frequency plots for the vessels are shown in Figures 35, 36 and 37.

Table 4: Ship and observation parameters for the example vessels.

Trial	2003-10-04 [69]	2004-03-26 [69]	2006-06-12 [52], [38]
Ship length	76 m	86 m	130 m
Ship speed	4.2 kts	10.1 kts	18 kts
Integration time	9 s	6 s	10 s
Aircraft speed	130 m/s	123 m/s	115 m/s
PRF	600 Hz	634 Hz	599 Hz
Spacing D_s	0.215 m	0.194 m	0.192 m
Baseline D	0.27 m	0.27 m	0.27 m
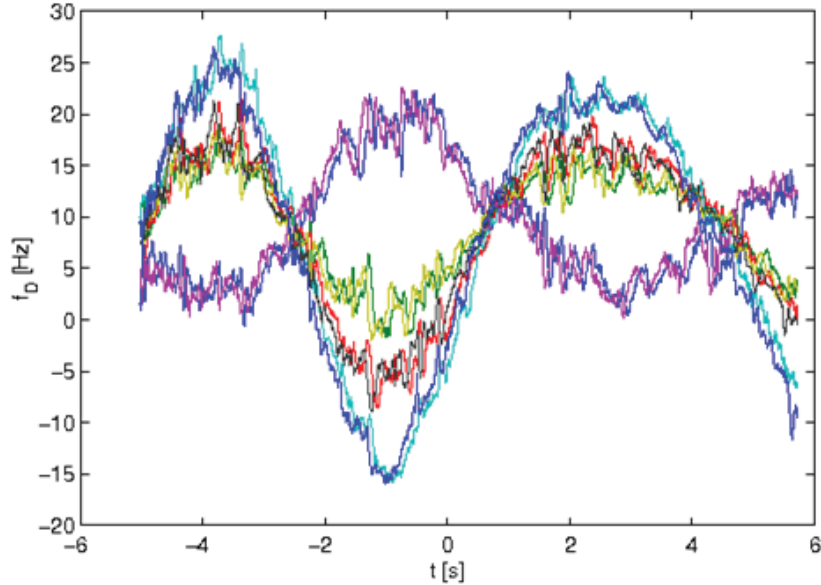
Figure 35: Time-frequency plot for the ship observed on 2003-10-04.
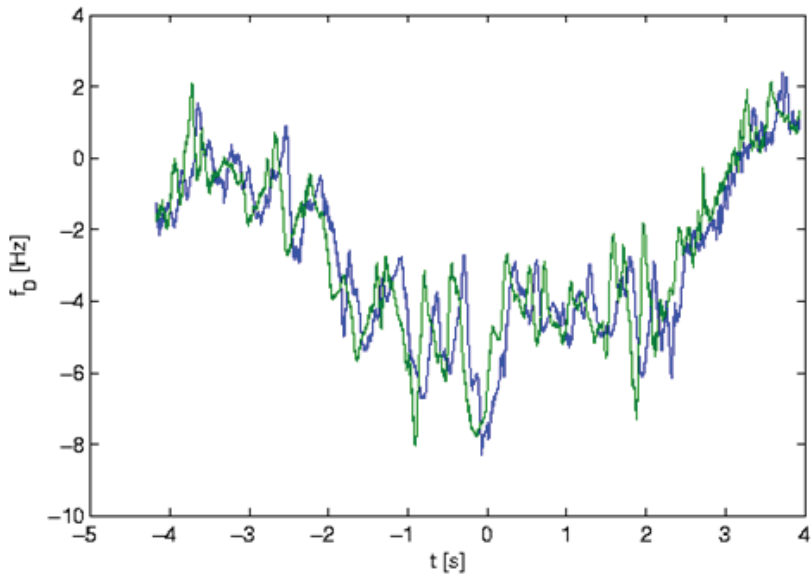
Figure 36: *Time-frequency plot for the ship observed on 2004-03-26.*
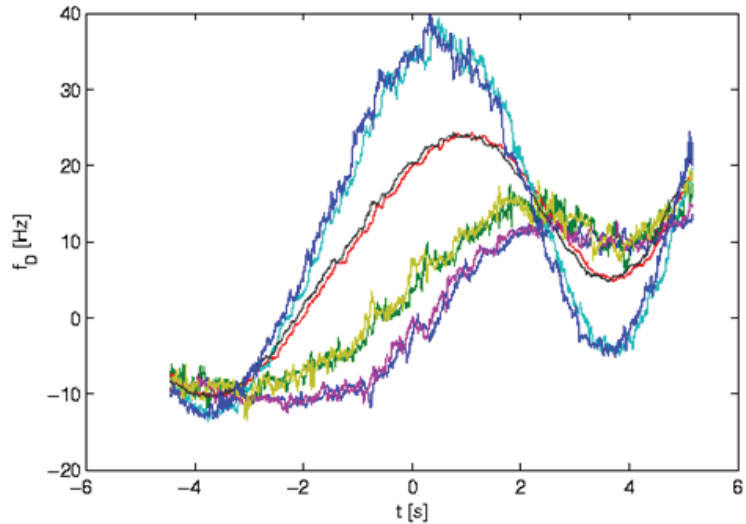
Figure 37: *Time-frequency plot of the ship observed on 2006-06-12.*

Wave motion effects are clearly seen in the range-partitioned time-frequency plot shown in Figures 35 and 37, but are much more subtle in in Figure 36 due to the calm ocean conditions that were present in this case.

Periodic ship motion effects were compensated in all three cases using the methodology explained in Subsection 3.3. The same compensation was applied to both channels and the ship data were focused to form SAR images using the same processing parameters for both channels. Interferograms were generated between the channel pairs and an ATI diagram was computed for each ship.

ATI diagrams show the relationship between the interferogram magnitudes and the interferogram phases represented in the polar coordinate system. Figures 38, 39 and 40 show the ATI diagrams obtained without wave motion compensation (left) and with wave motion compensation (right) for all three ships. For the second ship (Figure 39) there is no visible difference in the ATI diagram before and after motion compensation. However, for two other ships there is a significant improvement (less phase spread) in the ATI diagrams after motion compensation. The second case (Figure 39) is an exceptional case where standard ATI techniques, which are routinely used for ground vehicles, can be applied to ships. The other two cases are typical cases where it is necessary to compensate the effects of wave-induces motion. For example, the image focus improvement of the first ship is illustrated by Figure 41.
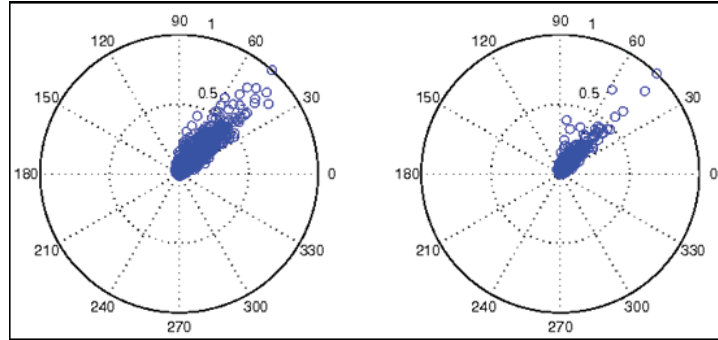
Figure 38: *ATI diagram for the ship observed on 2003-10-04 (left: no motion compensation, right: adaptive motion compensation).*
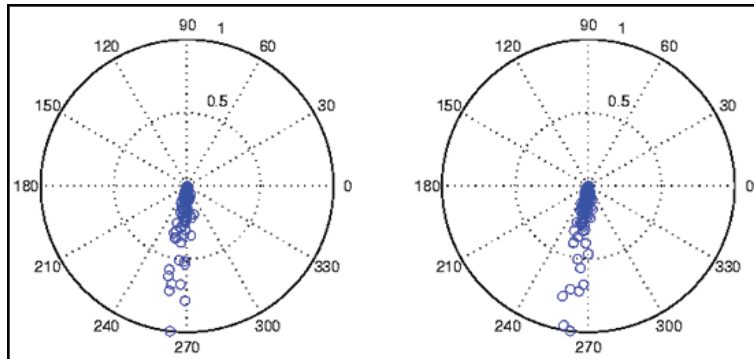
Figure 39: *ATI diagram for the ship observed on 2004-03-26 (left: no motion compensation, right: adaptive motion compensation).*
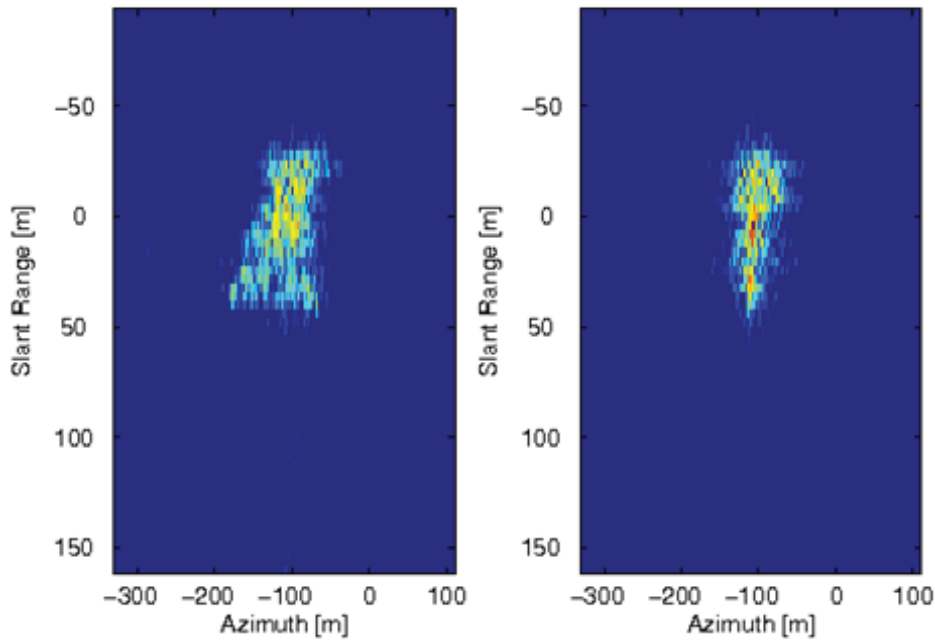
Figure 40: An example of focus improvement after adaptive motion compensation based on time-frequency tracking and harmonic analysis – standard focusing (left) compared to adaptive focusing (right).

3.4.2 Sea motion effects using multiple observations

The ship observations on 2006-06-12 consisted of three data sets that were acquired over a one hour time window using aircraft flight tracks that were oriented approximately 90° and ± 45° with respect to the AIS-reported ship course. The ship of opportunity was 130 m long and it was exhibiting complex motion, as expected in the wave field. Time-frequency diagrams for these three observation angles are shown in Figures 29, 30 and 31. The three observations were used to validate the decomposition algorithm which separates the complex motion given by equation (41) into the linear and periodic terms.

The wave-induced motion was modeled as a superposition of two dominant, periodic components. The encounter frequencies were estimated by the Root-MUSIC algorithm applied to the suitably regrouped samples of the instantaneous frequency waveforms shown in Figures 29, 30 and 31. Then the in-phase and quadrature amplitudes (p and q amplitudes) are found by linear fitting at four different ranges where the ship target had strong reflectivity. After fitting, amplitude estimates become available only at four distinct ranges. These amplitude values are then splined to cover all ranges occupied by the ship. The results of the parametric modeling are graphically presented for each of the waveforms.

Figures 41(a) and 41(b) are derived from the time-frequency waveform of Figure 29. Figure 41(a) shows the reconstructed periodic components of the Doppler history according to equation (41) for $n \in \{1,2\}$ at the four selected ranges. Figure 41(b) shows the splined amplitudes as functions

of range, where p_1 and q_1 are nearly linear with range, while p_2 and q_2 are negligible, which shows that only one swell-wave frequency is dominant.
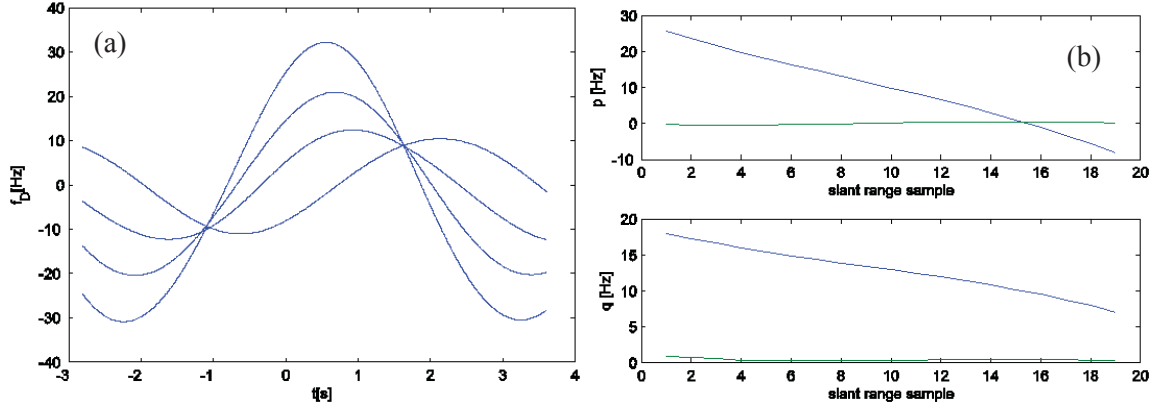
Figure 41: *(a) Reconstructed periodic components of the Doppler histories shown in Fig. 27, (b) splined harmonic component amplitudes as a function of range.*

Similarly, Figures 42(a) and 42(b) are derived from the time-frequency waveform of Figure 30. When the linear trend is removed, Figure 43(a) includes only the periodic components. They are now fairly similar to those in Figure 41(a) and they all cross at the tilt point when the ship reverses its rotational motion.
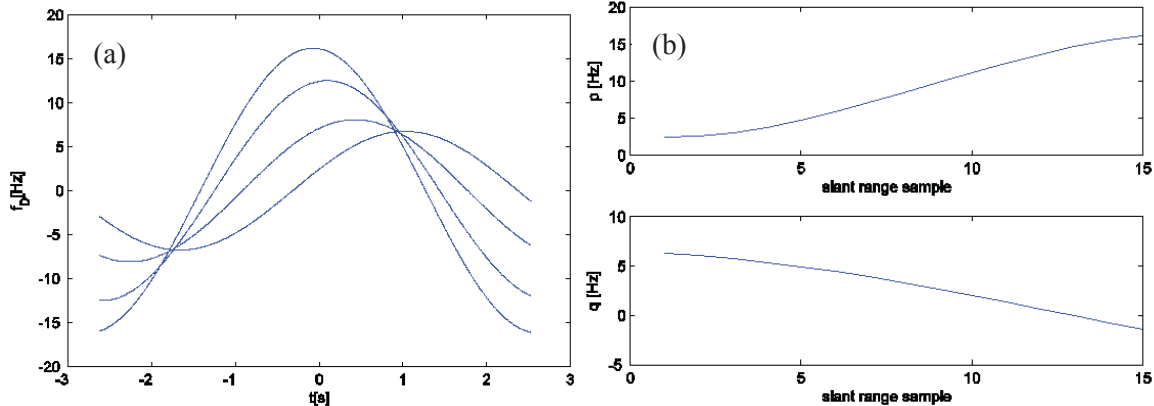
Figure 42: *(a) Reconstructed periodic components of the Doppler histories shown in Figure 30, (b) Splined amplitudes of the harmonic components.*

Using an identical procedure, Figures 43 (a) and 43(b) are derived from the time-frequency waveform of Figure 31. When the linear trend is removed, Figure 43 shows the same features as Figures 41 and 42.
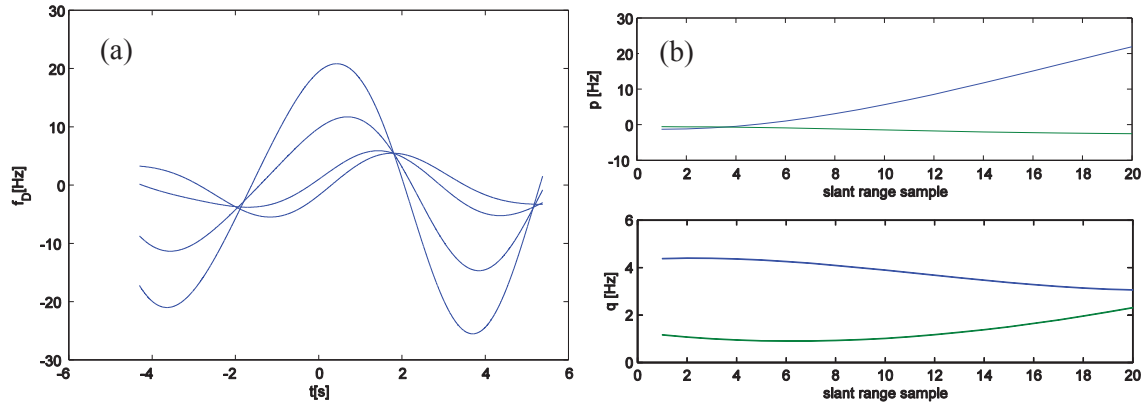
Figure 43: *(a) Reconstructed periodic components of the Doppler histories shown in Figure 29 (b) Splined amplitudes of the harmonic components.*

The effects of rotational motion were compensated via phase corrections which were incorporated into the focusing algorithm. Using the model extracted from the data, ship imaging was significantly improved as demonstrated in Figures 44, 45 and 46.
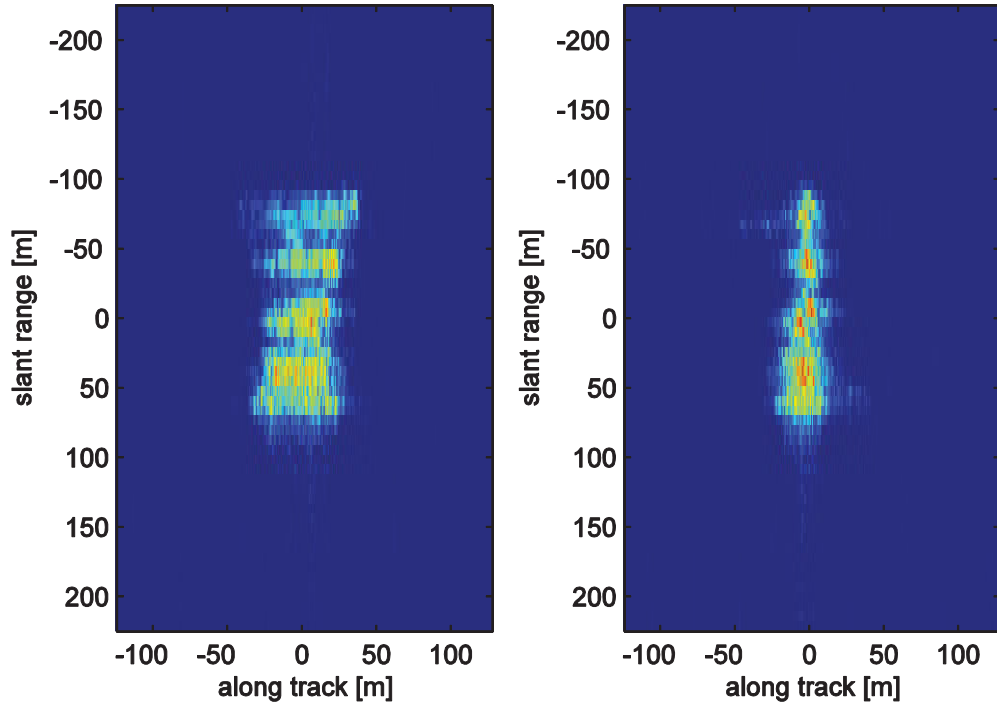
Figure 44: *Ship focusing by standard processing (left) and with phase correction modeled in Figures 41 (a) and 41 (b) (right).*
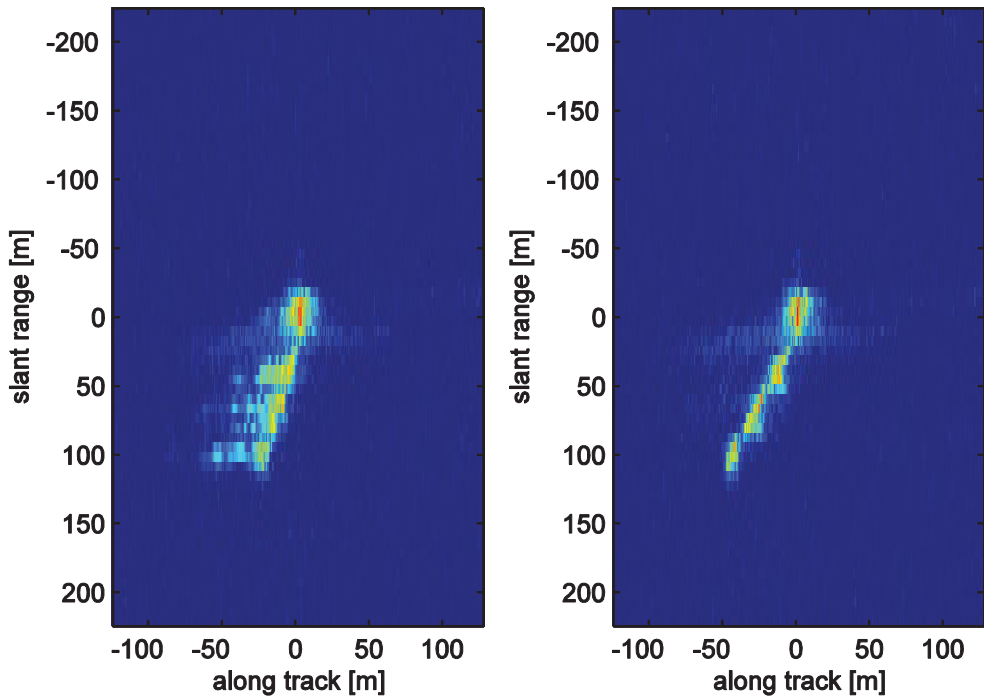
Figure 45: *Ship focusing by standard processing (left) and with phase correction modeled in Figures 42 (a) and 42 (b) (right).*
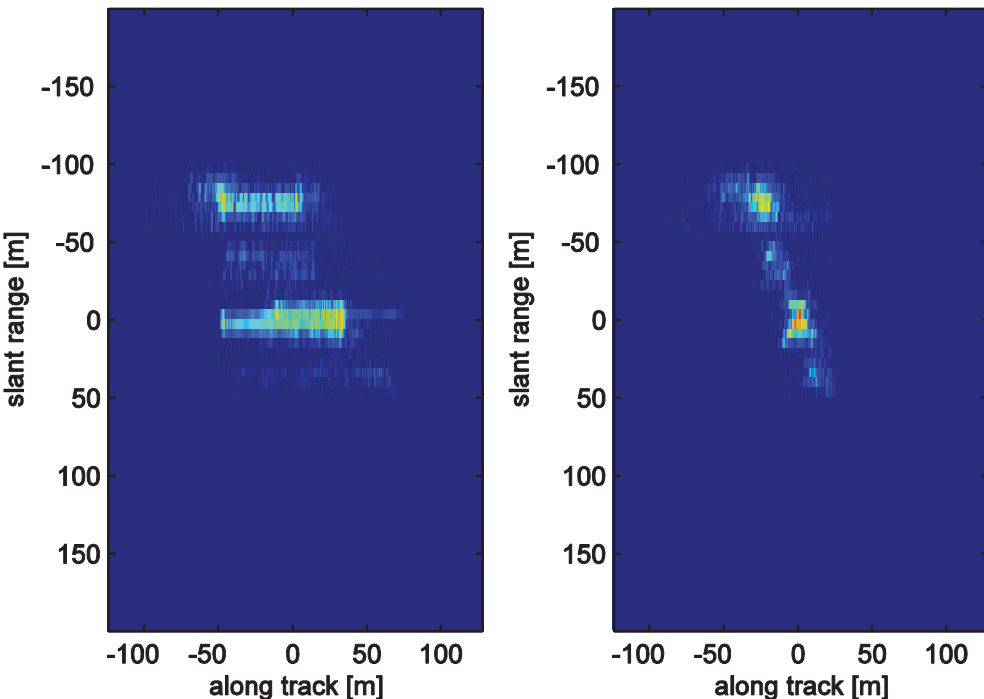
Figure 46: *Ship focusing by standard processing (left) and with phase correction modeled in Figures 43 (a) and 43 (b) (right).*

The vessel shown in Figures 44 to 46 is a refrigerated cargo ship of the class shown in Figure 47 from the Green Reefers fleet.

Figure 47: 131 m refrigerated cargo vessel shown at sea.

The large radar cross section regions of Figures 44 to 46 correspond to the aft superstructure, the large (34 ton) crane, the small (8 ton) crane and the forward navigation-light and beacon tower.

Improved imaging may be of interest for the purpose of ship classification or recognition, which is impaired by smearing. Besides improved imaging, modeling of the rotational speed improves the accuracy of the along-track speed estimates. In the examples shown, the ship speed error, as estimated from AIS data, was within 1 kt and it can be attributed to a variety of sources including calibration issues, uncertainty of various system parameters and sensitivity of the model to all unknown parameters.

4 Ship motion observations using RADARSAT-2 MODEX measurements

Although airborne SAR-GMTI measurements were used to develop marine target GMTI capability, the long-term operational role for this capability will rely on space-based observations for routine use. Although the science that underlies GMTI observations is independent of the radar platform, platform dynamics and observation geometry differences between airborne and space based sensors have effects on the measurement process. The following sub-sections discuss space-based GMTI for marine target measurements.

RADARSAT-2 GMTI measurements at two sites provide the experimental data used in the following discussions. Ship traffic through the Strait of Gibraltar was monitored to provide data for large to medium sized vessels used for international shipping and ship traffic in the Strait of Georgia was monitored to provide data for medium to small sized vessels used for coastal shipping.

4.1 RADARSAT-2 mode parameters for the Strait of Gibraltar data

The Strait of Gibraltar was selected as a primary test site for RADARSAT-2 GMTI research due to the large volume of range-travelling ship traffic, the diversity of vessel sizes, the availability of extensive shore based AIS coverage and the presence of strong shore ambiguities from coastal urban centers. A set of five GMTI data sets were acquired in 2009. Three of the data sets were acquired in MODEX-1 mode that uses a full-aperture transmit and simultaneous half-aperture receive configuration to provide two GMTI data channels. Two of these were repeat pass scenes that had identical radar observation parameters except for a difference in polarization. The other two data sets were acquired in the MODEX-2 mode that uses a toggled three-quarter aperture transmit and simultaneous half-aperture receive configuration to generate time-multiplexed four channel GMTI data. The key radar configuration parameters for all five data acquisitions are summarized in Table 5.

In all cases, RADARSAT-2 speed was around 7500 m/s, with reference to the ECEF coordinate system. The corresponding ground speed was around 6600 m/s.

The radar wavelength is 0.05546577 m. The nominal radiated power at the satellite was 3486 W per pulse for MODEX-1 and 2614 W per pulse for MODEX-2. Radar ranges of interest span the interval 900 km to 1200 km.

Table 5: RADARSAT-2 configurations for the Strait of Gibraltar data sets.

Date	2009-01-19	2009-01-21	2009-03-10	2009-10-05	2009-12-20
Phase centers	2	2	2	4	4
Nominal adjacent channel baseline separation (m)	3.75	3.75	3.75	1.875	1.875
Transmit azimuth beam width (-3 dB)	0.21°	0.21°	0.21°	0.283°	0.283°
Receive azimuth beam width (-3 dB)	0.42°	0.42°	0.42°	0.42°	0.42°
Polarization	HH	HH	VV	HH	HH
Incidence angle (°)	52	41	41	30	41
Pulse bandwidth (MHz)	30	30	30	50	50
Pulse duration (μs)	41.6	41.6	41.6	20.8	20.8
PRF (Hz)	1802.09	1825.15	1825.15	3546.36	3744.49

4.2 Short observation interval model for two physical channels

Comparing the antenna beam width entries in Tables 3 and 5, the two-way GMTI azimuth beam width for the airborne radar used in this report is 4.28° and the maximum GMTI azimuth beam width for RADARSAT-2 is 0.345°. Combining the azimuth beam widths for the two cases with the radar ranges platform speeds and azimuth over-sampling ratios, the airborne platform allows maximum useful observation times of up to 11.8 seconds at 10 km range for strong ship targets while the space-based radar allows observation times of up to 1.1 seconds at 1200 km range for strong ship targets. Airborne systems can observe ship targets over a significant fraction of long ocean wave periods and space-based systems cannot. Analysis of space-based GMTI measurements of ship targets is constrained to short observation intervals (with respect to the period of significant ocean waves).

The phase history model, given by equation (40), is equally applicable to the airborne SAR and to the space based SAR if the proper value of the model parameter β is selected. However, for short observation intervals, the quadratic approximation adequately describes the phase history and higher order terms are not directly observable. Any harmonic ship motion can be linearized within the short observation interval, as depicted in Figure 49. In this case, the last term of equation (40) stands for the phase noise, while other terms of the model absorb the contribution due to the wave-induced motion as an additional instantaneous displacement, speed and acceleration. This is demonstrated in Figure 48 (b) which is produced by SAR-GMTI processing for a simulated point target using data generated for the highlighted blocks in Figure 48 (a).
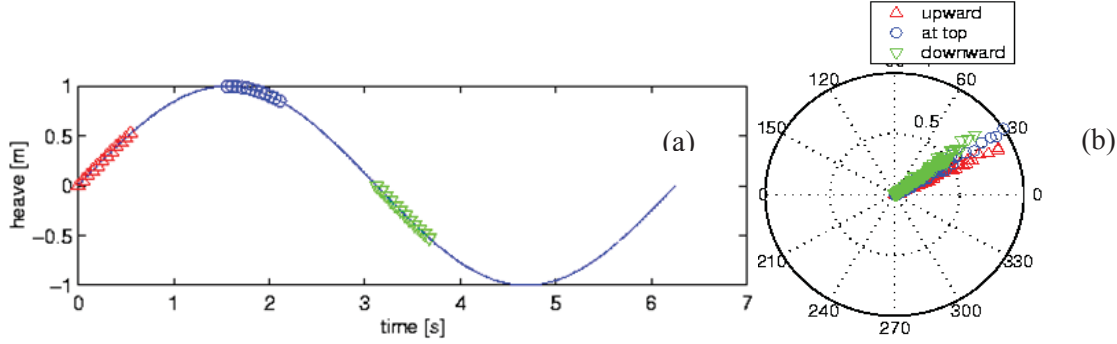
Figure 48: *Short time interval illustration; (a) short sections of a periodic motion cycle for linear approximation, (b) motion impacts on the measured ATI phase.*

Even if a time frequency decomposition was valid for the short, satellite observation window, applying the principle shown in Figure 48 to Figures 35, 36 and 37 would be ineffective for the creation of a sea-motion model (similar to that shown in Figure 41) because of the local variability of the extracted signal. For short observation times, sea motion effects on range-partitioned ship observations are primarily present in the acceleration terms of equation (40).

It is readily seen that short-time observation windows complicate the extraction of sea-motion effects from SAR-GMTI signatures since the observable variables are the sea-motion acceleration terms.

4.3   Short observation interval for four virtual channels

With a small modification, equation (40) can be used in the case of short observation intervals with four virtual channels if:

1. Parameter $\beta < 1$ is correctly set to account for the curvature of the SAR orbit.

2. Channel index $p \in \{0,1,2,3\}$ is used to enumerate the channels.

3. Pulse index k is used to count all transmitted pulses.

4. For two simultaneously-received channels, only even-indexed pulses are considered valid and defined by equation (40), while odd-indexed pulses are considered missing. and

5. For the other simultaneously-received channel pair, odd-indexed pulses are considered present and given by equation (40), but even-indexed pulses are considered missing.

The PRF per channel is half of the physical PRF. Since the radar PRF has been increased so that each channel is adequately sampled, channel balancing and registration in the preprocessing step removes the odd-even constraints on p in the list above.

The four-channel case for space based radars has the same short-time window issues for sea-motion estimation as the two channel case.

4.4 Analysis approaches

The core SAR-GMTI concepts, discussed in Section 2.5, are applicable to both airborne and space based measurements, but implemented methods must be tailored to the specific design of the SAR-GMTI system and its observation geometry.

Some of the analyses approaches that were developed for the airborne SAR-GMTI observations cannot be directly applied to the RADARSAT-2 MODEX measurements of ship dynamics. This is because the following conditions are significantly different in the MODEX case:

1. The much shorter MODEX observation interval (less than 1.1 s as opposed to up to 11 s) is insufficient for measuring swell wave dynamics by time-frequency analysis.

2. The much higher RADARSAT-2 platform speed (about 7500 m/s compared to 140 m/s) significantly reduces SAR-GMTI sensitivity to the target along-track speed.

3. The much higher platform trajectory (800 km compared to 6 km), in combination with the difference in system parameters, dictates different radiometric and CNR properties of the acquired samples.

4. PRF restrictions are much tighter in the space based SAR-GMTI case due to the inherent trade-off between the PRF, the sampling ambiguity level and the useable radar swath for fixed PRF operation with a single transmitted waveform.

5. The DPCA sampling condition is nearly achievable for RADARSAT-2 but not for the airborne system.

The airborne SAR-GMTI measurements discussed in this report were used as an experimental tool for understanding the SAR-GMTI observation processes and developing theoretical models. Airborne SAR-GMTI systems have continuing value for special-purpose, site-specific applications. Space-based SAR-GMTI measurements are meant to support the development of operational observation and monitoring systems that are not constrained by geographic location and require automated processing and information extraction capabilities. Mitigation of littoral sampling ambiguities and the ability to be adapted to new sensor properties and modes are particularly important for the space-based applications.

A comprehensive approach to ship detection and motion measurement using satellite SAR-GMTI systems includes a number of functions which need to be automatically (or semi-automatically) implemented for operational use:

- pixel level detection of target points,
- estimation of target radial speed,
- estimation of target direction of travel,
- large target clustering function,
- separation of ship targets that are in close proximity,
- relocation of motion-displaced targets,

- output the geographic location of all targets,

- target orientation estimation,

- ambiguity reduction processes,

- land masking processes,

- littoral ambiguity resolution, and

- automated integration of AIS information with radar observations.

4.4.1 Pixel-level non-parametric detection

The function of a GMTI detector is to identify radar signal features that make a point in a scene a moving target candidate and to capture these candidates as moving target detections. When a detector is applied to a focused SAR scene, the range-history that is used to create the scene becomes important since the focussing process is a function of the relative motion of the radar and each scene point that is being investigated. It may be necessary to use several matched filters to capture targets that have been miss-focused by their motion. In many cases an iterative approach is used where estimated motion for detected target candidates can be used to refine the processing filter. Depending on the local wind conditions, the strong sea returns at incidence angles smaller than 35° (Figure 10) can mask radar returns from some ships.

4.4.1.1 Image power detector

Most ship detection algorithms start by pixel-level detection against a given threshold, followed by some clustering of the individual pixel detections [79]. Traditionally, single channel ship detection is based on tests the signal power $|s(x,y)|^2$ at image coordinates (x,y) against a suitable threshold η that is derived from the statistics of the local background. A straight forward generalization of this detection rule to the multi-channel case would be to generate a signal vector $S(x,y)$ whose elements are the signals s_p at the registered point (x,y) in all channels and to create a composite power image G_{img} from the signal vectors:

$$G_{img} = \mathbf{S}(x,y)^H \mathbf{S}(x,y) = \sum |s_p(x,y)|^2 \tag{42}$$

where H is the conjugate transpose operator, $s_p(x,y)$ is the pixel value of channel p and all channels are registered. The image power G_{img} is tested against the detection threshold for every point in the image. In this case, there is no clutter suppression and detection is possible considering that ship returns are usually much stronger than the ocean surface returns. The detection threshold must be estimated from the statistics of scene elements that contain no targets. The detector can use a maximum likelihood process against the hypothesis that the tested point is or is not a moving target.

4.4.1.2 Clutter cancellation detectors

Where two or more radar apertures are available in the radar direction of travel (GMTI radars), DPCA processing, discussed in section 2.5.1.1 can be applied equally to space-based and airborne signals for the detection of moving targets using the detection rules shown in equation (27). For ocean scenes, the clutter background has significant internal motion due to waves and surface currents. For a four aperture radar, the maximum aperture registration time for RADARSAT-2

(0.75 ms in Table 2) is a factor of 27 shorter than the C-band sea surface decorrelation time (20 ms at 10 m/s wind speed) and significant sea-clutter cancellation can be achieved. It becomes advisable to independently estimate the DPCA detection thresholds in equation (27) for each of the three radar aperture separations when the wind speed significantly exceeds 10 m/s.

For GMTI radars that have more than two channels, the full, DPCA processed, data set allows several independent detection possibilities for ship targets. A three-channel radar yields three detection results that represent two degrees of freedom and a four-channel radar yields six detection results that represent three degrees of freedom. With multiple detection possibilities comes a requirement to define a detection declaration rule. The choice of the target declaration rule will influence the number of false detections and the probability of detecting a moving target that lies close to a DPCA detection boundary.

From the discussions in section 2.5.1.1, a four channel DPCA radar requires three, overlapping, detection regimes that have three different phase-center separation baselines, d, $2d$ and $3d$. From equation (23), the MDV decreases as the reciprocal of the baseline separation distance. The channel pair that has the largest baseline separation will have the highest probability of detection for the slowest targets. Where the target return to threshold ratio in equation (23) is 10, the target MDV will range from 3.6 m/s to 0.64 m/s as the baseline distance varies from 1.85 m to 5.6 m. From equations (22) and (23) the fastest detectable target will be moving at the first radar blind speed minus the MDV. The lowest blind speed occurs at the largest channel separation and for RADARSAT-2 is approximately 36.1 m/s. Since the fastest ship targets will have radial speeds less than this value, all baseline combinations can be used. From equation (22), DPCA detection applied to four-channel RADARSAT-2 data will be most sensitive to weak targets whose radial speed is one half of the blind speed for each of the three aperture separations. The greatest DPCA detection sensitivity occurs at the ATI directional ambiguity speed.

There are many possible moving target declaration rules that can be applied to the six DPCA outcomes from a four-channel GMTI radar:

- Declare a moving target detection if any of the six outcomes is a detection. This rule yields the lowest probability of missing a target and the highest probability that the detection is a false alarm.

- Declare a moving target detection if at least the longest baseline channel pair yields a detection. This rule is biased to search for the slowest targets.

- Declare a moving target detection if some number (for example three) detections are observed and at least two detections represent different degrees of freedom. This rule trades off missed targets against false alarms.

- Declare a moving target detection if six detections are observed. This rule maximizes missed targets but yields the smallest numbers of false detections.

Where the vessel being observed is large, false alarms and missed detections will not matter much since each vessel consists of an ensemble of target points. For small vessels, the declaration rule can be important. DPCA detection rules operate between the radar blind speeds and do not take the ATI directional ambiguities into account.

A variant of the multi-channel DPCA detector can be developed by defining a matrix projection operator

$$\mathbf{P}^\perp = \mathbf{I} - \frac{1}{N}\mathbf{u}\mathbf{u}^H \tag{43}$$

where $\mathbf{I}$ is the identity matrix and the unit-vector product $\mathbf{u}\mathbf{u}^H$ defines a square matrix whose elements are unity. The projection matrix has the property $(\mathbf{P}^\perp)^H = \mathbf{P}^\perp$ where H is the Hermitian transpose operator. Defining a channel signal difference parameter

$$D_{\text{DPCA}} = \mathbf{S}(x,y)^H\mathbf{P}^\perp\mathbf{S}(x,y) = \sum|s_p(x,y) - \bar{s}(x,y)|^2 \tag{44}$$

and estimating a threshold parameter η^2 from $D_{DPCA}(x,y)$ in a nearby ocean region that contains no ships, a moving target detection is declared whenever

$$D_{DPCA} - \eta^2 > 0. \tag{45}$$

The parameter $\bar{s}(x,y)$ in equation (41) is the complex average of the N GMTI channel outputs at the point *(x,y)*. In this case, the three detection tests of the previous DPCA approach are replaced by a single test and the declaration rules discussed previously are reduced to a single rule by the definition of the operator $\mathbf{P}^\perp$.

The properties of $\mathbf{P}^\perp$ are discussed in Annex B. The DPCA detection operation described by equations (43), (44) and (45) will be less sensitive to slow and weak ship targets than those described by equations (25), (26) and (27) when a slow target declaration option is exercised. The DPCA variant described by the operator $\mathbf{P}^\perp$ is computationally more efficient than that described by equation (26).

4.4.1.3   Clutter suppression detectors

Instead of clutter cancellation, clutter can be suppressed using the channel-to-channel covariance matrix $\mathcal{R}$ in a kernel that decorrelates the background (clutter plus noise) return. The covariance matrix is generated from a complex-image area that contains no targets and is sufficiently large that the ocean amplitude statistics can be considered to be stationary. The covariance-matrix target-clutter cross terms are not an issue in this case. For the ocean surface, the covariance matrix also contains the bulk motion (wind-drift and currents) of the area used to estimate its elements and may differ slightly from the covariance matrix of the sea surface that contains the targets. This issue is explored in more detail in Annex A.

For any channel pair, a possible detection test can be based on the quadratic form:

$$D_C = \mathbf{S}(x,y)^H\mathcal{R}^{-1}\mathbf{S}(x,y) = \frac{2}{\sigma^2(1-\rho^2)}(\sigma^2 - \rho(\Re(s_1^*s_2)\cos(\varphi) + \Im(s_1^*s_2)\sin(\varphi)) > \eta \tag{46}$$

for some real threshold η, under the assumption that the sea surface statistics and radial component of the bulk sea motions in the target area are the same as those used to estimate the covariance matrix. The expansion in equation (46) assumes a two channel case where:

- σ^2 is the mean power in channels 1 and 2,
- ρ is the relative coherence of channels 1 and 2,

- $\mathfrak{R}$ is the real part of a complex number,

- $\mathfrak{I}$ is the imaginary part of a complex number, and

- φ is the bulk ATI phase in the radial direction of the radar for the ocean surface area used to estimate the ocean covariance matrix **C** in an area near the ship target.

The covariance matrix inversion is only possible when the sea clutter to noise ratio is sufficiently large and finite. This algorithm retains the mean sea returns in the detection threshold definition.

Detailed investigations of multi-channel covariance matrix based detection and estimation algorithms for moving targets can be found in [64], [65] and [66] for land targets. Equation (46) may offer a good compromise for improving the detectability of ships in clutter regardless of their speed as illustrated in Figure 50 by an example taken from a RADARSAT-2 Gibraltar scene in VV polarization acquired on 2009-03-10. Two ships, one fast, other slow, were used to compare detectors based on equations (42), (44) and (46).
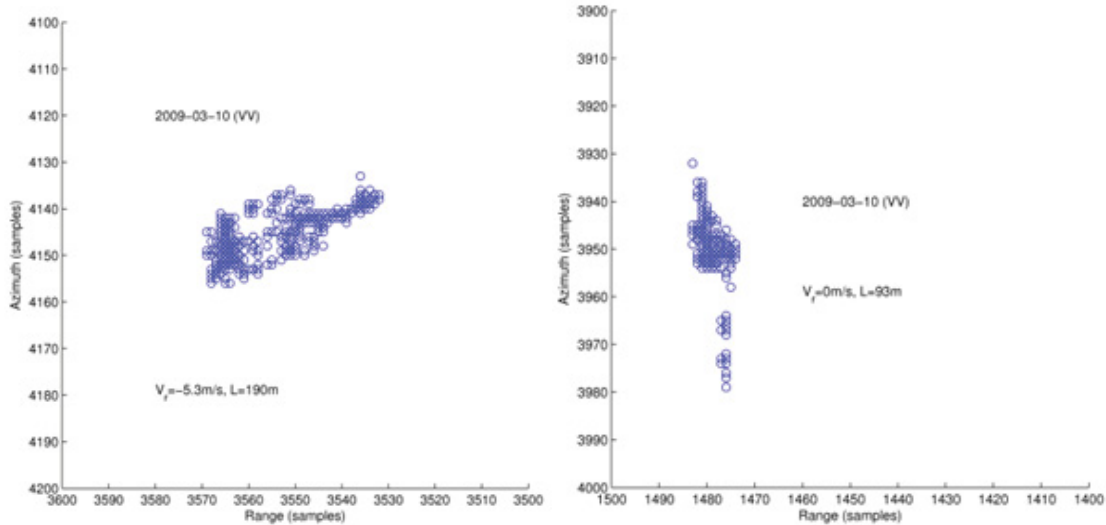
Figure 49(a): *Pixels detected by placing a threshold on the image magnitude test statistic G_"img" in equation (42) for a fast ship (left) and a slow ship (right) in the same RADARSAT-2 scene.*
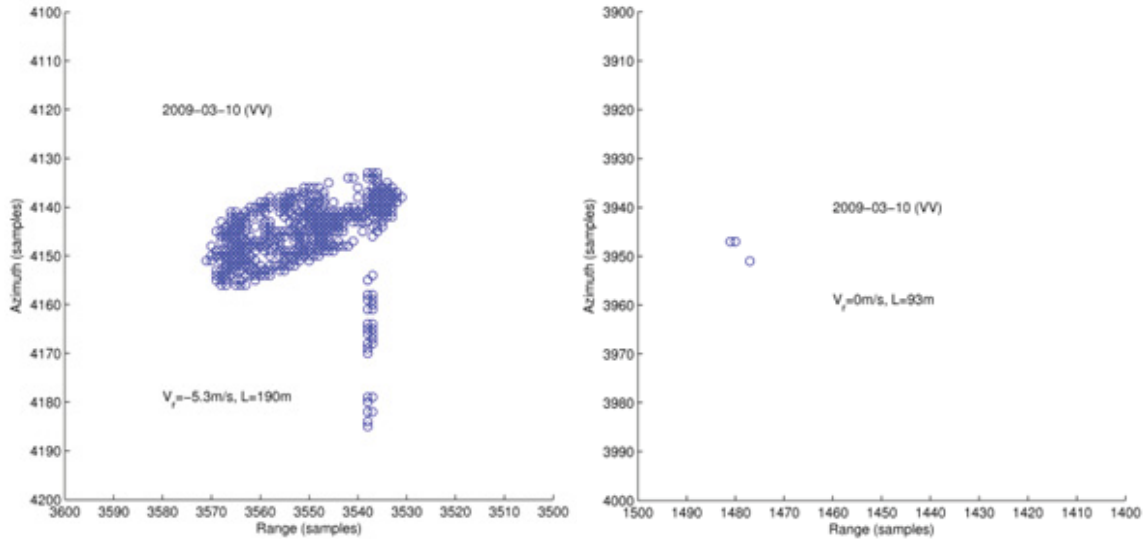
Figure 49(b): *Pixels detected by placing a threshold on the DPCA test statistic D_"DPCA" in equation (45) for a fast ship (left) and a slow ship (right) in the same RADARSAT-2 scene.*
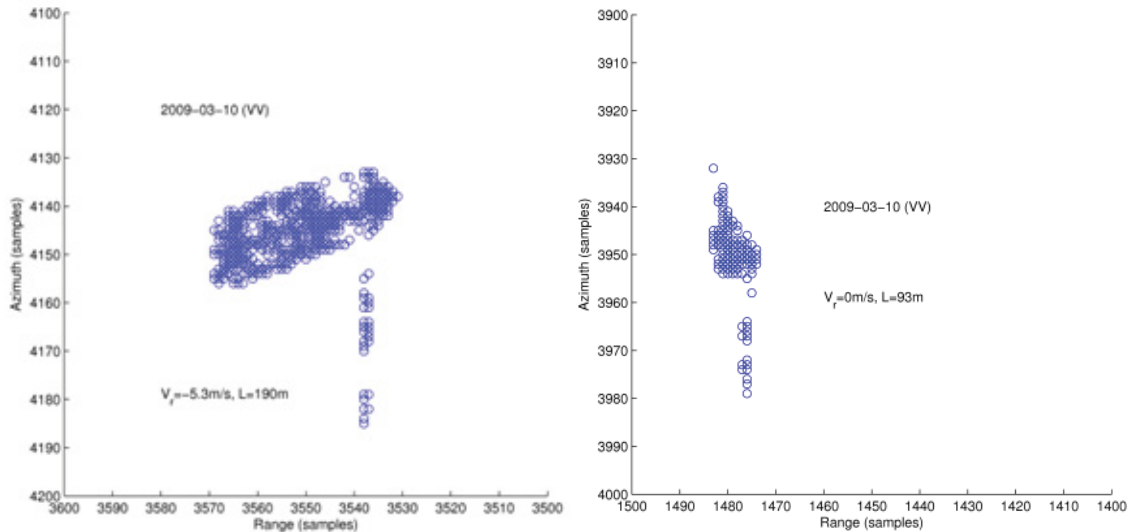
Figure 49(c): *Pixels detected by placing a threshold on the covariance matrix clutter suppression in equation (46) for a fast ship (left) and a slow ship (right) in the same RADARSAT-2 scene.*

By visual comparison of Figure 49(a) and Figure 49(b), DPCA detection improves the detectability of the fast ship as it suppresses the strong VV clutter, but it hinders detectability of the slow ship as its returns get suppressed in the DPCA process through the target motion dependence in the sine term in equation (22) since this target is essentially not moving. For both ship targets, background suppression by means of decorrelation performs well, as demonstrated by Figure 49(c).

Since target declarations are made for each point in the image set, a large ship will consist of a set of proximate detections as has been shown previously and data clustering algorithms offer some processing advantages.

The quadratic detectors shown in equations (27), (42), (45) and (46), as well as the rare event detector in Section 2.5.1.2, do not presume any target parameters. They are non-parametric.

4.4.2　Pixel-level parametric detection

Parametric detection operations operate by maximizing a target test-statistic with respect to a target parameter that influences the target detection probability. The maximization process can either use a steering vector based on a range of probable parameter values or can use an iterative search routine.

For DPCA-based detection, equation (45) can be modified by replacing $\mathbf{S}(x,y)^H$ by a model of the expected target signal $\mathbf{b}(v)^H$, which is varied by varying the target radial speed parameter v to yield the test statistic

$$D_{\text{DPCA-par}} = \max_v \left(\frac{|\mathbf{b}(v)^H \mathbf{P}^\perp \mathbf{S}(x,y)|^2}{\mathbf{b}(v)^H \mathbf{P}^\perp \mathbf{b}(v)} \right). \tag{47}$$

For covariance matrix based detection a similar parameter replacement in equation (46) results in the test statistic

$$D_{\text{C-par}} = \max_v \left(\frac{|\mathbf{b}(v)^H \mathcal{R}^{-1} \mathbf{S}(x,y)|^2}{\mathbf{b}(v)^H \mathcal{R}^{-1} \mathbf{b}(v)} \right). \tag{48}$$

The search over the v parameter space is usually performed in small steps. For a test value of the radial speed v, the data should be refocused to properly adjust the phase history at each detection attempt. Practical investigations have shown that refocusing may be done in coarser steps than the parameter increments used in equations (47) and (48) to save computation time. By choosing the granularity of the test parameter, a good compromise can be found between the computational efficiency and the performance of the algorithm. This version of the detector is efficiently implemented in the DRDC SAR-GMTI processor and was used for all Gibraltar scenes.

The parametric detector outputs yield the presence or absence of a detection and, since the maximum of the test statistic is quite broad, a rough estimate of the target speed. The EDPCA algorithm uses the test statistic defined by equation (48).

Averaging estimates made by equations (47) and (48) within a small spatial window can also be applied for ships as large targets.

4.4.3　Estimation of radial target speed

ATI estimates of radial speed were discussed in Section 2.3.2.2. Figure 51 shows the ATI results for two ships of the similar size, but under different conditions [79]. There is a conspicuous difference in the spread of the ATI speed estimates between the detected pixels of the two ships. One of the ships is moving at radial speed of 6.5 m/s in relatively calm sea. For this ship, the

spread in the speed estimates is mainly due to the unavoidable signal superposition effects as the ATI phase takes the form shown in equation (27). The other ship moves with the radial speed of -2 m/s, but it is under swell wave acceleration. For this ship, sea-surface-induced motion contributes to an increased spread of the speed estimates and the low ship speed combined with sea motion causes the DPCA algorithm to split the detected point clustert into two apparent targets that move in opposite directions. Both ships were detected using a two-channel DPCA algorithm and display the normal speed-dependent cut-off at the detection boundary [18].
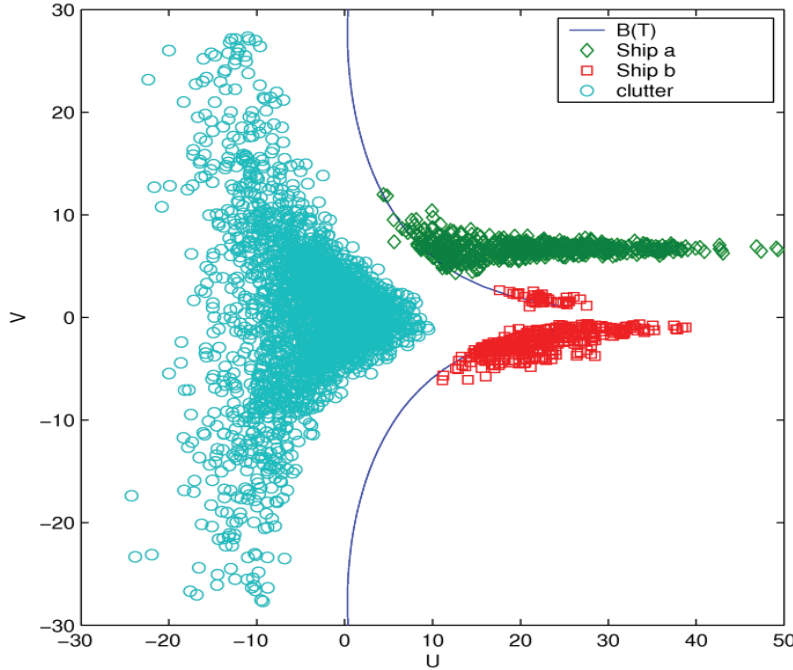
Figure 50: *Sea surface returns, cyan, and samples of two ships, green and red, in the ATI velocity-magnitude plane after DPCA detection. The blue curve is the DPCA detector boundary and defines the radar MDV as a function of target sample amplitude.*

In Figure 50, the parameter U is pixel signal amplitude and parameter V is the radial speed of the detected pixel. Since ATI is a power (correlation based) metric, the use of a clutter suppression algorithm, such as that shown in equation (46) and a detection threshold that is based on the statistics of the suppressed clutter would result in a frequency-independent detection boundary (straight vertical line) in the ATI frequency-magnitude plane. This approach yields a sub-optimal detector and the detection boundary would lie within or slightly to the right of the boundary region shown in Figure 50.

For multi-channel SAR, there are different possibilities to suppress the clutter before the ATI operation. For example, in the case of four channels, it is possible to generate six different DPCA images corresponding to the channel combinations shown in Table 2 and equation (27). From these six images it is possible to compute three different interferograms with suppressed cross-terms. Two of these DPCA-ATI images will have phase-center baseline *d* and one will have phase-center baseline 2*d* representing two different target motion sensitivity conditions (degrees of freedom). With proper averaging of the two common-baseline interferograms it is possible to further reduce the variance of the interferometric phase. Combining the analysis of interferograms

with two different baselines can enhance the speed estimation of slow targets [80]. The detector threshold boundary (MDV) effects will remain for individual points near the detection boundary.

An alternative method for radial speed estimation is closely related to parametric detection. The radial speed estimate is found as the trial parameter that provides the highest value of the detection test statistic. Since the peak of the function maximum is quite broad, the speed estimate resulting from the detection operation may need to be refined by an additional ATI step.

4.4.4   Large target clustering techniques

GMTI measurements of large ships yield many moving target detections which include radar returns from the ship itself as well as side lobes of large cross section scatterers and double bounce echoes from the ship and proximate sea surface. In a realistic scene with many vessels, it is necessary to identify the detections belonging to each ship. The detection-ship association problem can usually be solved by simple clustering algorithm that is based on a region-growing technique. A cluster is initiated by collecting adjacent detections. A detection is assimilated into an existing cluster if it is not further than a given minimum separation from any point that already belongs to the cluster. The cluster growth terminates when all points within the specified maximum separation have been identified.

Averaging the ATI phase (speed estimates) from all points within a cluster provides a single speed estimate that characterizes the bulk motion of the ship in terms of the bulk motion of the cluster. However, all information about the rotational motion is lost in the averaging process and appears in the variance of the mean speed estimate.

Detection clusters representing large ships usually contain many points and it is possible to sub-divide them into domains. Since the spatial density of detections is not uniform over the cluster and often correlates with blocks of strong radar returns from the ship structure, an initial domain estimate can be made by selecting sub-clusters that have the highest detection density (or largest radar returns). Ideally these are distributed in the range direction. Alternatively, the domain partition can start from the cluster centroid. Initial domain estimates are augmented by an iterative splitting process whereby a cluster of detected points that lies at the largest distance from the existing domain centers becomes a new domain center and the maximum domain size is limited to a fixed number of points. Then the cluster points get redistributed according to their proximity to the new domain centers. The result of this operation is shown on one example in Figure 51.
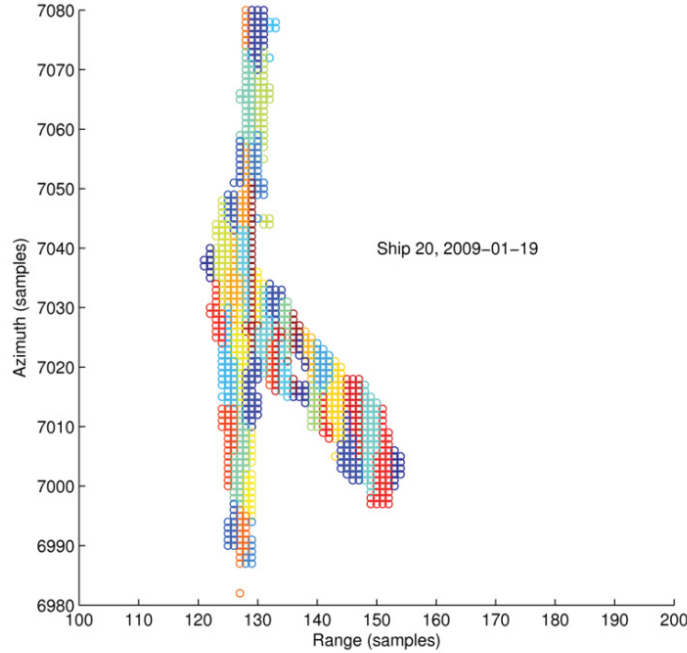
Figure 51: A cluster of detections sub-divided into smaller domains represented by different colours.

In Figure 51 the detection domains identify the ship and the azimuth side-lobes from structure at one end of the vessel. The range distribution of ship speed estimates for each domain can be used to infer some properties of the rotational motion of the ship noting that the side lobes are always oriented in the azimuth direction.

When two ships are passing in close proximity, the detection-based cluster growth process may result in a single cluster that includes both vessels. The domain-based ship motion estimates may allow these clusters to be separated into clusters for each vessel.

4.4.5   Relocation of displaced targets

Moving targets are displaced in the SAR image proportional to their radial speed according to equation (11). In practice, target relocation in the image depends on the radial speed estimate. For small, point-like, targets, this operation is straight-forward, for ships as large targets this is not necessarily the case. The spread in the ATI phase (radial speed) estimates translates into an azimuth smear if each detected pixel is relocated individually using its own ATI phase. In all cases the accuracy of target point relocation depends on the accuracy of the target velocity estimate and on the intermodulation terms in equation (30).

A speed-based relocation example [80] is shown in Figure 52. The cluster of detected pixels for this ship, Figure 53 (a), includes the returns from the ship and an interesting artefact next to it. After pixel-by-pixel relocation, Figure 52 (b), the shape of the ship is lost as the uncertainty in azimuth increases. Then the same ship cluster is sub-divided into small domains (20 samples each), Figure 52 (c), and the domains are repositioned using their resultant radial speed estimates,

Figure 52 (c). The relocated domains are much more concentrated in azimuth than the individually relocated sample. Moreover, after domain relocation, the cluster becomes well aligned with the ship's trajectory given by the AIS data for the example ship and shown as the black straight line in Figure 52.
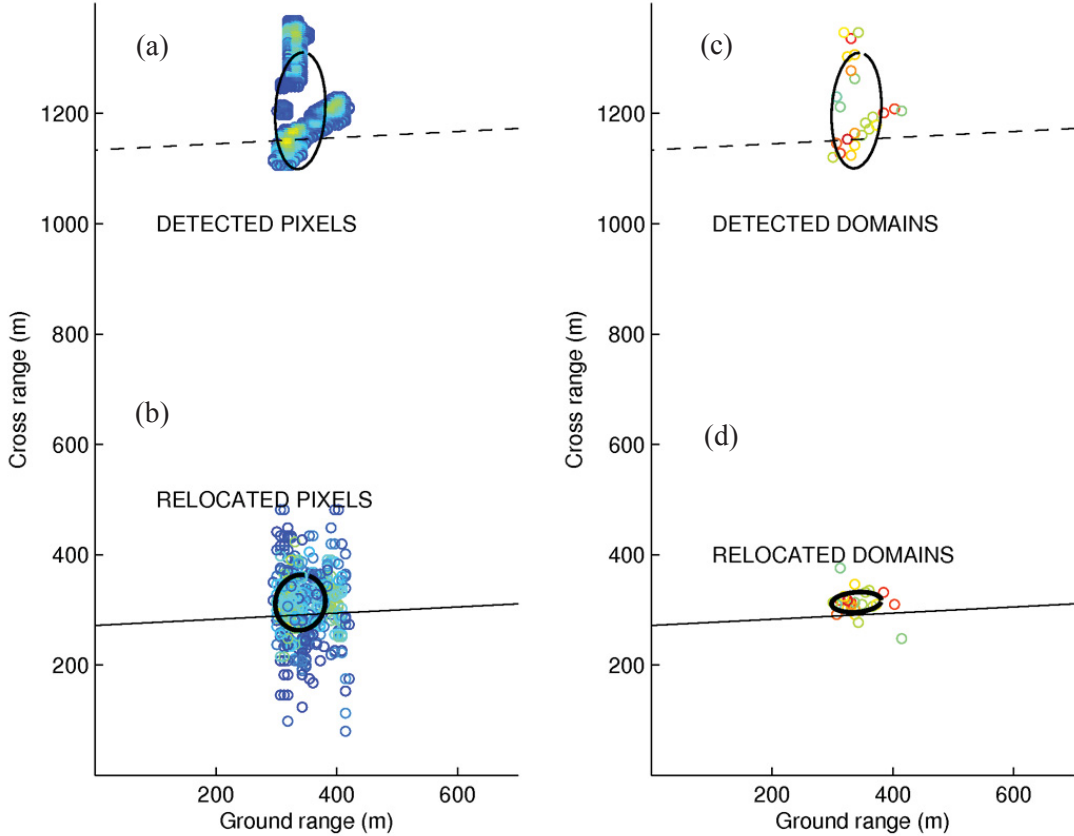
Figure 52: Detected sample cluster (a) and pixel-by-pixel relocated cluster (b) compared to sub-cluster domain centers (c) and domain-by-domain relocation (d).

4.4.6   Target orientation estimation

Elliptical contours in Figure 52 indicate the position, size and orientation of the sample cluster belonging to a ship. The elliptical contours are drawn after analysing the cluster and they represent it in a compact form according to the parametric equation

$$\begin{bmatrix} x - \bar{x} \\ y - \bar{y} \end{bmatrix} = \begin{bmatrix} \cos(\theta) & -\sin(\theta) \\ \sin(\theta) & \cos(\theta) \end{bmatrix} \begin{bmatrix} \sqrt{2\lambda_M}\cos(\phi) \\ \sqrt{2\lambda_m}\sin(\phi) \end{bmatrix} \tag{49}$$

where:

- $\bar{x}$ is the range center of the cluster and the ellipse, and defines the estimated range position of the ship;

- $\bar{y}$ is the azimuth center of the cluster and the ellipse, and defines the estimated azimuth position of the ship;

- λ_M is the maximum moment of inertia of the cluster, defines the major axis of the ellipse and is used as a measure of ship's length;

- λ_m is the minimum moment of inertia of the cluster, defines the minor axis of the ellipse and is used as a measure of ship's width;

- θ is the range-azimuth direction about which the maximum moment of inertia is found, defines the orientation of the major axis of the ellipse, and is used as ship's heading estimate;

- ϕ is the calculation parameter that takes values from $(-\pi, \pi)$ to trace points (x, y) that belong to the ellipse; and

- (x, y) are a pair of coordinates defining a point on the ellipse.

In many cases, ship's orientation can be estimated from the SAR imagery by fitting an ellipse to its detection cluster. However, in many cases this method produces erroneous results for either or both of the following reasons:

1. Ship images are often accompanied by artifacts that appear as azimuth side-lobe strings or as double bounce reflections from the ship and the sea that are visible in the image and often detected as azimuth oriented image features, as shown in Figures 49, 51 and 52.

2. Detected ship images may appear rotated with respect to their true heading because of sea surface influences on their rigid-body rotational motion that combine with bulk propulsion system motion to modulate the azimuth shift of the detected points along the ship's length.

A correction of the ship's heading is often possible based on the combination of the above techniques for clustering, domain-based relocation and fitting an elliptical contour to the relocated cluster. This option is available for medium to large ships and it must be followed by monitoring some figures of merit (such as the relationship of the ellipse axis ratio λ_m/λ_M to the ship width to length ratio and others).

4.4.7   Land masking approaches

Land masking is crucial for single channel image domain detection of ships in maritime zones. It is less necessary for SAR-GMTI systems since clutter from land can be mostly suppressed except for some coastline artifacts such as those observed in [81]. Nonetheless, land masking is useful in SAR-GMTI processing for the following reasons:

1. Due to imperfect clutter suppression with any real SAR-GMTI system, the statistics of the residual signals are not the same over land and over water. Being able to extract the appropriate statistics (land or ocean) leads to better detection performance.

2. Due to imperfect clutter suppression with any real SAR-GMTI system, some man-made targets remain detectable and contribute to a high false alarm rate. This is often the case with industrial zones close to the shore. Littoral ambiguities often appear as false targets,

especially near large coastal cities. They are easier to mitigate if the shoreline is known to the SAR-GMTI processor.

3. With a known shoreline in maritime scenes large water surfaces can be masked out so that it is possible to perform Doppler centroid (DC) estimation and channel balancing over land, which is generally less affected by surface motion and low clutter-to-noise ratio (CNR), then the results can be applied to the entire scene.

Arguably the best known and most used high-resolution shoreline data set that is available in the public domain is the Global Self-consistent, Hierarchical, High-resolution Shoreline Database (GSHHS) that was developed at the University of Hawaii and is maintained and distributed by NOAA. The GSHHS shorelines are constructed entirely from hierarchically arranged closed polygons. Polygons are given as an ordered set of vertices and are available in five resolutions (fine, high, intermediate, low and coarse). The hierarchy between the polygons has four levels as follows: seashore, lakes, islands within lakes, ponds within islands within lakes. The level 1 polygons represent continents: Eurasia, Africa, North and South America, Australia and Antarctica as well as islands in the ocean. Higher resolution implies more polygon points and a longer processing time.

The GSHHS polygons are expressed in the geodetic coordinates of latitude and longitude while land masking of a SAR image is concerned with generating a pixel mask in the image coordinates of slant range and azimuth. To make use of the GSSH database, a two stage procedure is needed. The first stage includes conversion to the same coordinate space. Either all image pixels are assigned the appropriate geodetic coordinates (geo-referencing) or all polygon vertices are converted to the slant range and azimuth coordinates (SAR-referencing). In the second stage, each image pixel is checked against each polygon to determine whether it is inside or outside. If an image pixel lies inside any one of the polygons, it is marked as a land pixel. Those pixels that remain unmasked as land are considered to be ocean pixels.

Although this concept is simple, the implementation must be carefully optimized for efficiency as there are a large number of level 1 polygons, the continents are represented by a huge number of polygon vertices and the SAR image itself includes very many pixels. The main strategy for improving the efficiency is to quickly identify the majority of level 1 polygons that have no intercept with the SAR scene and to modify other level 1 polygons by simplifying their shape outside of the scene borders.

To determine whether an image pixel (x0,y0) is inside a polygon P, the following algorithm may be used:

1. Find sides of polygon P which intersect the line y=y0 and count the number of such sides to the right of x0.

2. If that number is odd, the pixel (x0,y0) is inside P and if the number is even, it is outside.

The test is simple to implement, but the sheer number of tests makes the procedure inefficient unless the number of polygon sides is previously reduced by a method that simplifies the polygon on the outside of the scene boundaries.

4.4.8   Sampling ambiguity reduction options

Provided that the range ambiguity level of the radar is sufficiently small in the area of interest, **r**ange ambiguities have little, or no, influence on SAR-GMTI measurements. SAR-GMTI radars use the full, sampled along-track signal bandwidth to detect and measure moving targets. Since the along-track (azimuth) oversampling ratios are small (between 1.05 and 1.1) for space-based radars, the peak sampling-ambiguity levels for strip-mapping, space-based SAR-GMTI measurements will be large and will be detected as moving-target candidates by GMTI detectors.

Each ship target has a fore and an aft ambiguity with respect to the direction of travel of the radar. After range history estimation and adjusted SAR processing, the range and azimuth positions of target ambiguities are precisely known. **A**zimuth sampling ambiguities of strong targets appear at a predictable distance given by equation (15) and at a relative range distance given by

$$\Delta R = \sqrt{R_T^2 + d_{Amb}^2} - R_T \tag{50}$$

where R_T is the range to a target point and dAmb is the azimuth displacement of the ambiguity.

There are two cases of interest, sampling ambiguities from moving ships in the open ocean and sampling ambiguities from large cross-section shore targets.

For ships in the open sea, it is relatively easy to compare detections to pixel values at that azimuth distance, taking range curvature into account. Ghost ships (ambiguities) have a weaker response than the true targets and can be rejected. This method fails in the rare case that the ambiguity of one ship is super-imposed on the signal from another ship that is at the ambiguity location. For this case the ship or ambiguity decision can be based on the comparison of the ship target speed estimates with those expected for an ambiguity.

In littoral zones, sampling ambiguities from shore structures have similar properties to ship ambiguities but only the ambiguities that are superimposed on the water surface are of interest.

Littoral ambiguities can be characterized by their distance from prominent land scatterers and by their ATI phase, which depends deterministically on the system parameters and the imaging geometry.

One straight-forward way to mitigate this problem in SAR-GMTI applications relies on using the shoreline information. First, separate target lists are found for water and for land using land masking or water masking when extracting the background statistics for the two detectors. Then these two lists are joined so that ambiguity checking can be done based on the distance in the same way as ambiguity checking is done for the ships alone. Automated algorithms have been developed for sampling ambiguity suppression and have been proven to be effective in reducing the littoral ambiguities with MODEX, as will be shown in the presentation of the results from five Gibraltar passes in Section 4.6.

4.5 Micro-Doppler observations and ship-sea interactions in SAR-GMTI observations

Discussions to this point have focused on the problem of estimating and mitigating the effects of propulsion and sea-induced rigid-body motion of a ship target. The approaches discussed directly apply to all radar returns from the ship structure including radar side-lobes from strong radar reflectors that are part of the ship structure. There is another class of observed effects that result in azimuth-spreading (image smearing) of portions of the ship target that are found on the directly-illuminated side of the target.

This section explores several possible explanations for the observed phenomena. These include:

1. side-lobes from a glint (a reflection off a flat surface that is perpendicular to the radar line of sight) or from a strong reflection off a corner reflector in a ship structure,

2. signatures from a rotating marine radar antenna on the ship, and

3. double bounces off the water surface near the bow, stern, or sides (depending on the angle of illumination) of a ship.

4.5.1 Side-lobes of a bright target

Side-lobe structures from strong radar returns are symmetric with respect to the peak of the return. An examination of the signal structure for the observed asymmetric azimuth spread confirms or rejects the side-lobe hypothesis.

An example given in Figure 53 shows a typical, asymmetrical, azimuth spreading (smearing) effect -observed in the (SAR) imagery of a ship. Figure 53(a) is the DPCA range-compressed, azimuth uncompressed image of a ship; Figure 53(b) is the fully processed SAR image of the ship; and Figure 53 (c) is the same SAR ship image displayed in a 3D plot (image brightness shown as the height).

The location (in range) of the asymmetric azimuth spread in the focussed ship image, Figure 53(b), is identified by a downward (yellow) arrow in the azimuth uncompressed DPCA image in Figure 53(a) around the range samples 2856-2858. For this particular example, the signals that generated the azimuth "smearing" in the SAR image are very weak before the azimuth compression that they are not visually perceptible in Figure 53(a). There is no strong, radar reflection peak associated with the SAR image feature nor is there an identifiable focussed-signal peak in the 3D display of the azimuth processed image displayed in Figure 53(c).

The radar signal observations conclusively reject the hypothesis that the asymmetric azimuth spreading feature can be attributed to the side-lobes of a bright target or a glint.
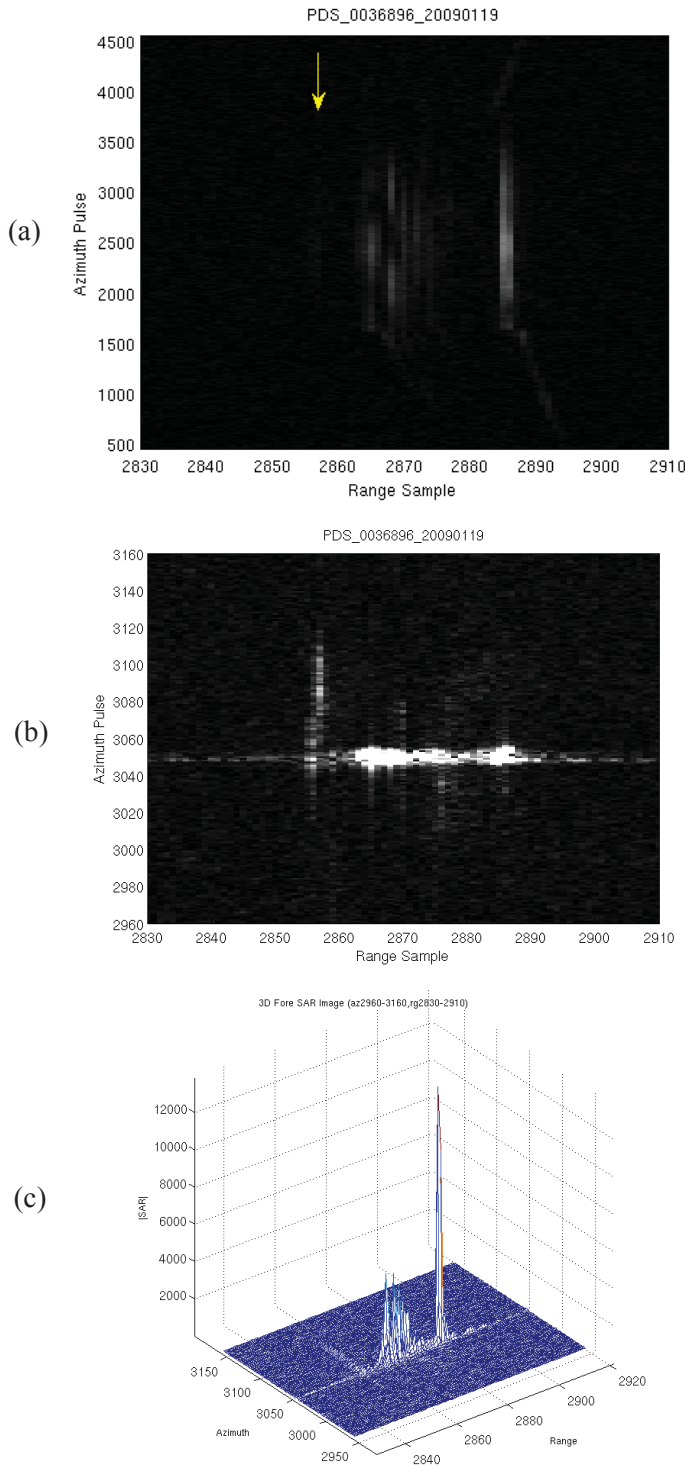
Figure 53: *An example of ship signatures from PDS_0036896 collected in the standard MODEX-1 mode: (a) DPCA range-compressed azimuth uncompressed image of a ship; (b) fully processed SAR image of the ship; and (c) 3D display of the same SAR image of the ship (image brightness shown as the height).*

4.5.2   Wigner-Ville time-frequency analysis

The asymmetric azimuth spreading phenomenon is further explored by analyzing the range-compressed, azimuth-uncompressed signals using the Wigner-Ville time frequency representation (WV-TFR) to examine the behavior of their Doppler signatures over the observation time. Figure 54 displays the WV-TFR results for the observed feature (for all azimuth samples at range sample 2857) shown in Figure 53. The negative chirp shown in Figure 54(a) corresponds to the bulk motion of a target observed by a linearly moving radar. The observed signals have a distinctive property that is not compatible with bulk ship motion effects, they are spread in both Doppler frequency and time. Analysis results show characteristics of multi-component chirp signals that require a secondary scattering center motion source for their generation. Figure 54(b) shows an enlargement of the time-frequency decomposition results in Figure 54(a) after the removal of the estimated ship and radar platform motion effects by a de-ramp operation.
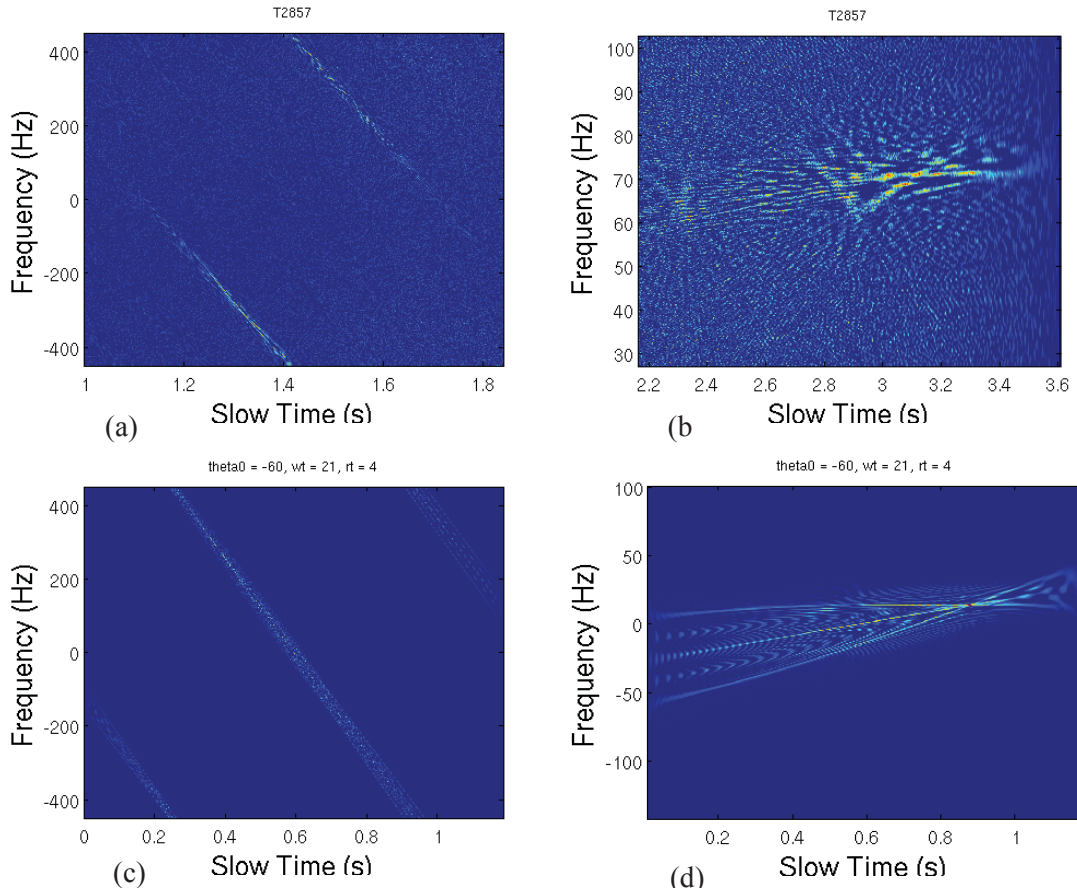
Figure 54: *Wigner-Ville Time-Frequency Representations of measured ship (smeared) echoes ((a) & (b)) and simulated ship antenna signals ((c) & (d)). The plots on the right are the de-ramped versions of the signals on the left.*

The observed multi-component Doppler signature suggests the presence of a secondary moving target whose motion is independent of the ship motion. Possibilities include rotating ship radar

antennas and double-bounce reflections from the ship's hull and the sea surface. Figures 54(c) and 54(d) display simulated results for a rotating antenna.

4.5.3 Echos from a rotating ship radar antenna

A plausible mechanism that could generate the observed multi-component chirp signals is the modulation of SAT-GMTI radar returns by the ship's rotating radar antenna as illustrated in Figure 55. A typical marine radar X-band navigation and S-band search radar antenna installation is shown in Figure 56.
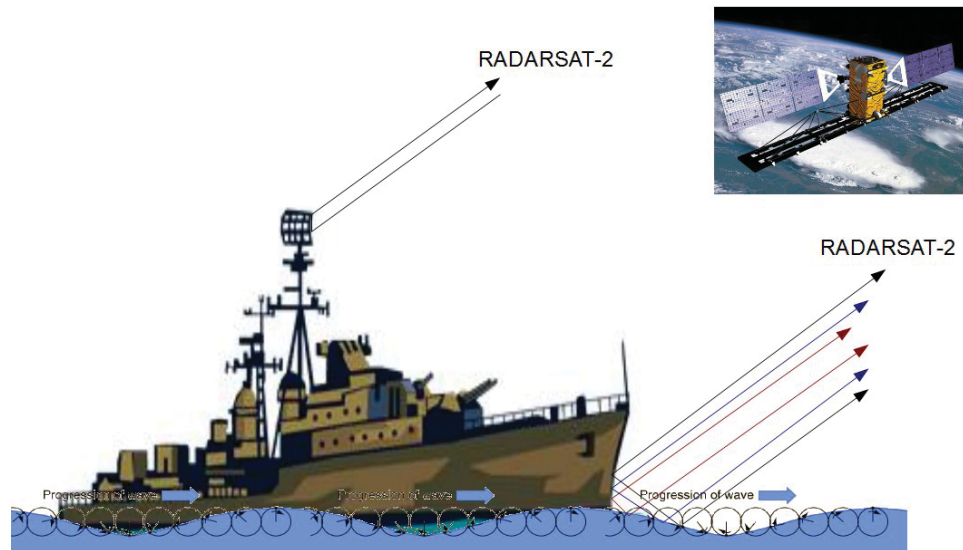
Figure 55: *A diagram showing radar return echoes being modulated by the ship's rotating antenna and by the circular motions of surface water particles near the ship.*

Figure 56: *A typical mounting configuration for ship radar antennas*

The antennas vary in length from 2.4 m (X-band) to 4 m (S-band) and rotate at rates between 15 and 24 RPM. The rectangular shape of the antennas could potentially generate radar return "flashes" when the long axis of the antenna is perpendicular to the SAR-GMTI radar line-of-sight. Due to the ship radar antenna rotation, the Doppler spectrum generated in the SAR-GMTI radar returns contains both positive and negative Doppler frequencies. To illustrate the micro-Doppler properties of a rotating ship antenna SAR-GMTI returns for a rotating antenna were modeled for RADARSAT-2 imaging geometry. The WV TFR plots of the simulated signals are shown in Figure 54(c) for a 4 foot (1.22 m) antenna rotating at 21 rpm. Figure 54(d) is the de-ramped version of Figure54(c). The simulated signals contain time-frequency features that are qualitatively similar to those observed from the asymmetric azimuth spreading effect shown in Figure 54(b) in that the signals show noticeably non-linear time-frequency characteristics.

The problems with the hypothesis that a rotating ship antenna is the source of the asymmetric radar feature in Figure 53 are the feature asymmetry and the fact that, when present, it is on the side of the ship that is illuminated by the SAR system as shown in Figure 57A. Due to their height above the ship buoyancy center, rotating ship antennas are subject to translational motions caused by roll and pitch dynamics. The translational motions result in radial speed contributions that yield azimuth shifts that are different from the bulk of the ship returns but are independent of the SAR illumination direction.

The illumination-dependence of the observed features means that the rotating antenna hypothesis must be rejected.
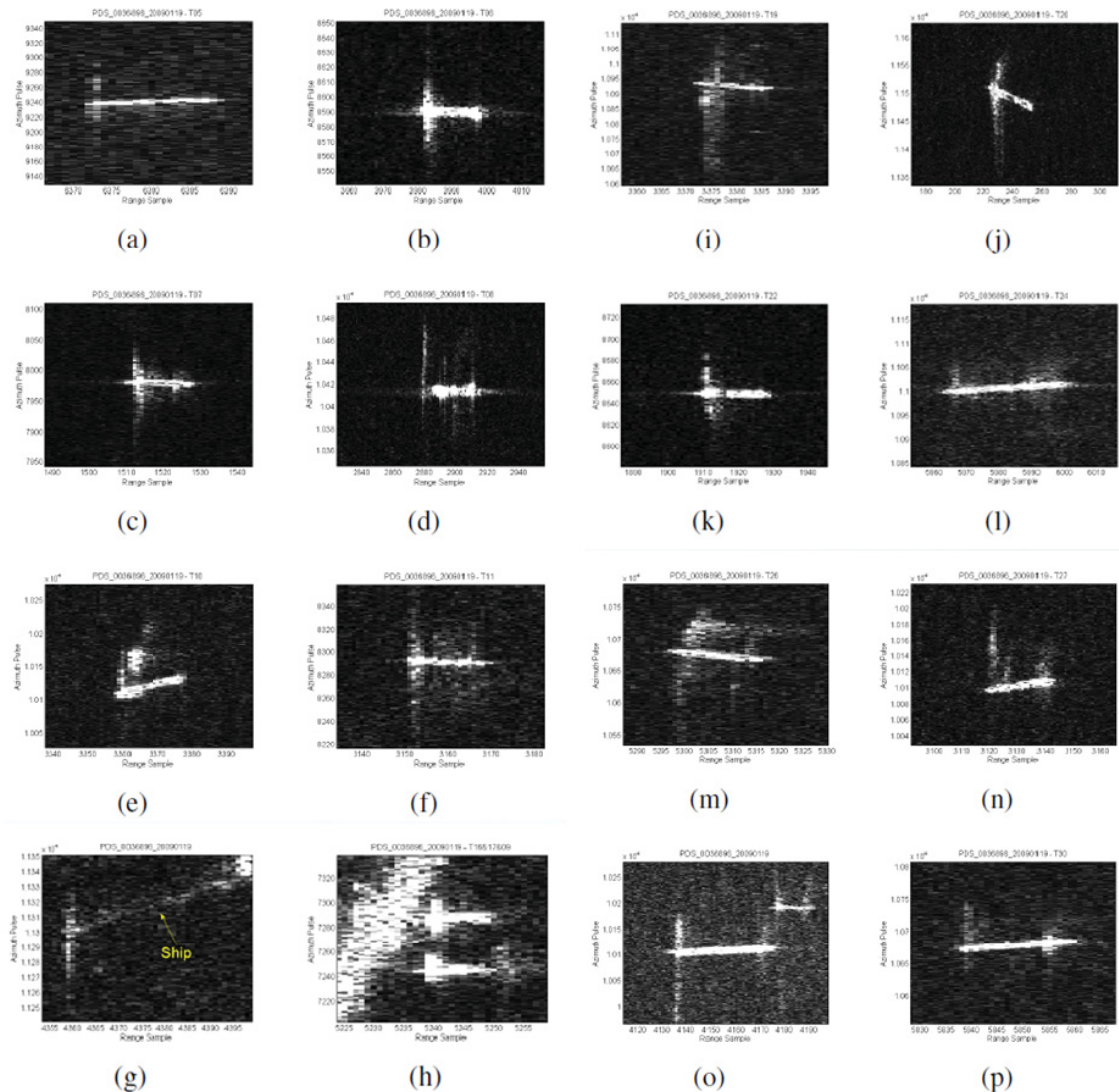
Figure 57(a): *Examples of ship SAR images collected by RADARSAT-2 in the MODEX-1 mode showing asymmetric azimuth distribution features in all cases on the side of the ship target that is closer to the radar (from dataset PDS_0036896).*
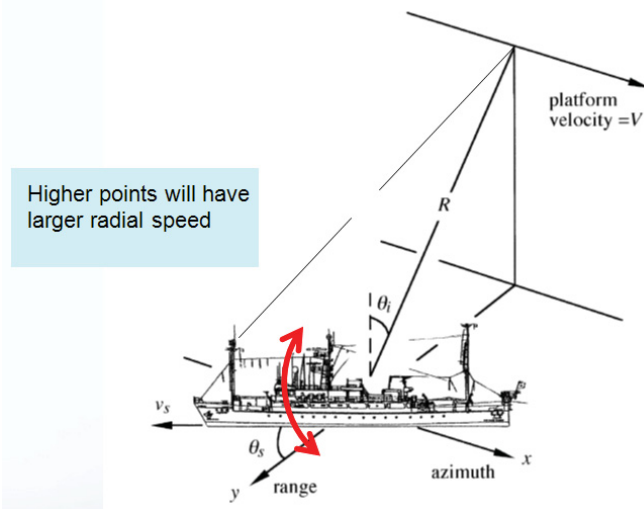
Figure 57(b): Higher portions of the ship will have larger speeds than the lower parts of the ship closer to the center of buoyancy.

4.5.4   Double-bounce reflections from the ship and a moving sea surface

The most plausible hypothesis is that the asymmetric azimuth spreading effect is created by double-bounce reflections from the ship's hull and small (capillary) waves that ride on gravity waves near the ship.

Multiple bounce radar scattering between small wave facets on the ocean surface and a ship has been considered in the model and the simulations described in [82]. That study did not predict the wide-spread azimuth smearing usually observed in SAR imagery since it did not include ship motion effects. The authors assumed correctly that ship's motion should be compensated for. However, the motion of small waves as radar mirrors is unrelated to ship's motion and cannot be compensated by any *a priori* model. This would explain why the reflections from the sea surface remain unfocused in SAR imagery. SAR observation geometry for ships travelling parallel to the SAR ground track favors the creation of multipath conditions anywhere along the side illuminated by the radar. Indeed, signatures of such ships usually appear defocused [5] in normal SAR imagery.

If we model a small area on the sea surface as a water particle, each water particle executes (and its capillary wave structure) can be shown to execute a circular motion, with little or no translational shift, as a gravity wave passes through. The shape of an ocean gravity wave is often depicted as a sine function, but the experimental wave shape is described as a "trochoid". A trochoid can be defined as the curve traced out by a point on a circle as it is rolled along a line as shown in Figure 58. Water particles are observed to execute a circular motion as a wave passes without significant net advance in their position (the advance is small compared to the overall circular motion). The motion of the water is forward as the peak of the wave passes, but backward as the trough of the wave passes, arriving again at nearly the same position when the next peak

arrives. The radius r of the circular motion of a surface water particle is, therefore, half the height of the wave, and its rotational speed ω is simply $2\pi=T$, where T is the period of the wave. The motion of a scatterer on ocean surface can be approximated by a circular motion with parameters r and ω.

In addition to this large circular motion of surface water particles, we also model the small capillary waves as small-amplitude sinusoidal capillary waves as shown at the bottom figure in Figure 59 and is given by

$$\frac{1}{2}H_{\text{ripple}}\sin(\omega_{\text{ripple}}t + \varphi_{\text{rand}}) \tag{51}$$

where H_{ripple} is the capillary wave amplitude, ω_{ripple} is the angular speed of the sinusoidal motion, and φ_{rand} is some random initial phase.
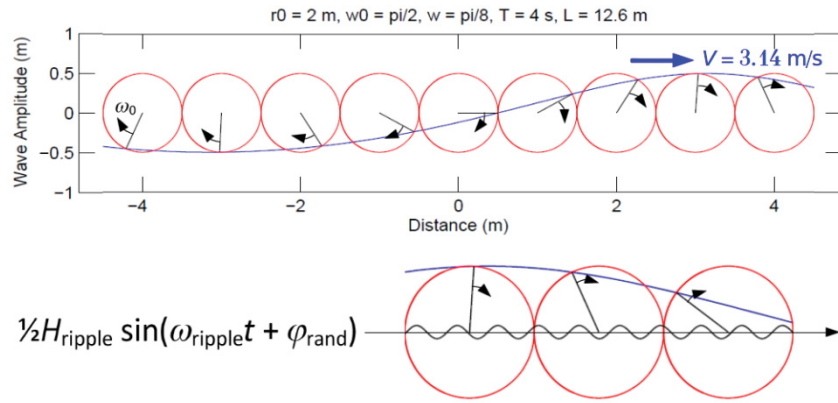
Figure 58: *A model of the motion of surface water particles with a large circular motion (top) and a small-amplitude vertical sinusoidal motion (bottom).*

The capillary wave structure is superimposed on the ocean gravity waves and determines the radar reflectivity of the ocean surface. In the Margarit model [82], they trace the motion of a water particle which provides the ocean motion component to the double-bounce reflection points for the radar signal interaction between the sea surface and the ship hull as illustrated in Figure 55.

The time-frequency properties of the ship-sea-surface double-bounce signatures were examined by modelling RADARSAT-2 observations of the double-bounce geometry for two cases and comparing them to the WV-TFR decompositions of the asymmetric azimuth spreading features. Figure 59 compares the findings for two ships in the Gibraltar data set.
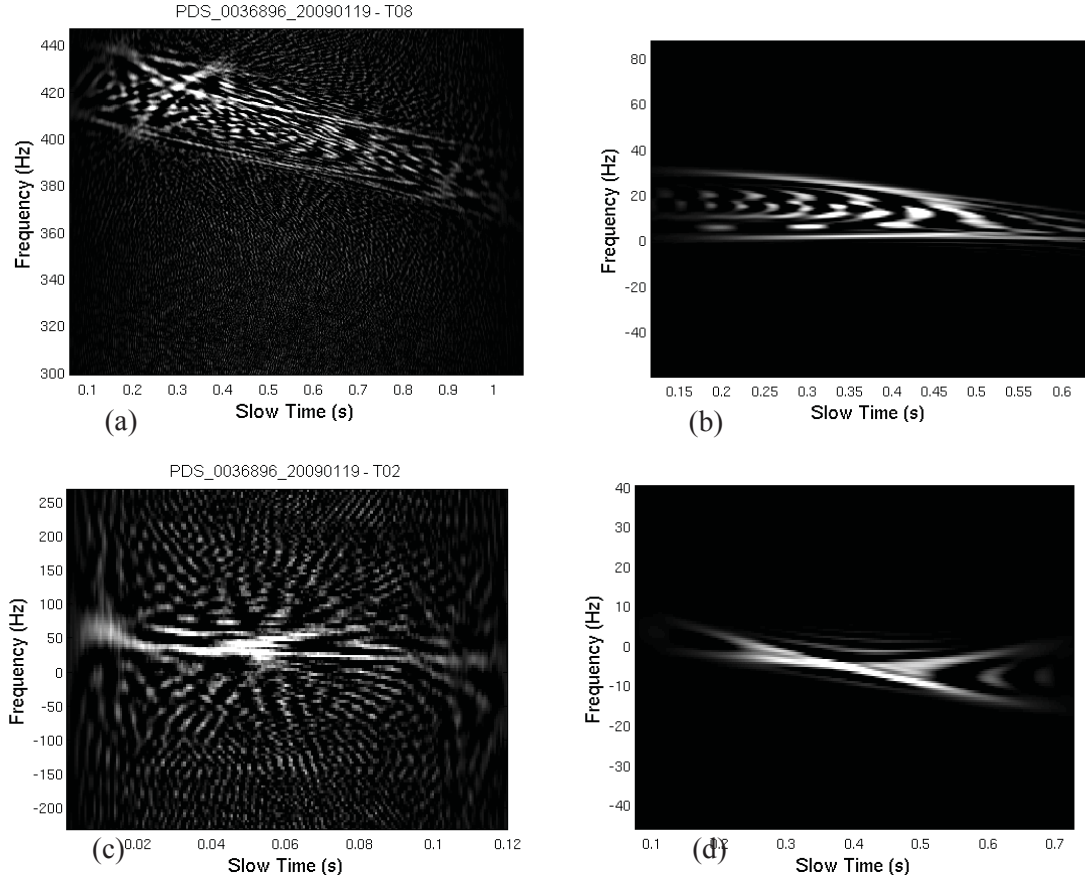
Figure 59: *Examples of Wigner-Ville TFR of measured ship smeared image signals (a) and (c) and the corresponding simulated double-bounce wave-motion modulated radar return signals (b) and (d).*

The double-bounce results have all of the observed properties of the asymmetric azimuth spreading features and qualitatively capture key features of the time-frequency decompositions. Detailed sea surface observations are not available for use in further exploring the time-frequency decomposition details.

4.6 Result validation using AIS data from the Strait of Gibraltar

Because of the heavy marine traffic flow in this area and the ready availability of routinely captured AIS data, the Strait of Gibraltar was selected as the primary validation area for GMTI measurements of large marine targets.

4.6.1 The Strait of Gibraltar data set

In this analysis 49 transiting ships are used from five scenes collected by RADARSAT-2 in the Strait of Gibraltar. A common set of SAR-GMTI processing algorithms was used for all scenes. Ground truth for these ships was extracted from shore-based AIS data. Another five ships with

AIS information were detected close to shore in the area of strong littoral ambiguities. They were moored and were not included in the full analysis.

In this section, each scene is presented and then the summary results are shown for the entire data set.

To minimize the raw data volume required for analysis, one signal data tile that includes all ships reported by the AIS intercepts was selected from each SAR-GMTI scene. Each selected tile contains some land (Spain and/or Morocco). The shoreline data within the tile are available from the GSHHS database and were used to define the coast line positions. The geographical location of the processed tiles and the GSHHS shoreline for the five selected tiles are presented as Mercator projections in Figures 60, 62, 64, 66 and 68. Ship locations at the imagingtime were time-interpolated from the AIS data and overlaid on the maps as small black boxes (square symbols). The AIS-reported ship headings are represented in the figures by lines emerging from these boxes where the line direction is the reported heading and the line length is proportional to the reported ship speed. High false-alarm rate (to minimize possible lost targets) SAR-GMTI detections were extracted from the radar target lists and overlaid in the image-plane as were repositioned ship locations derived from target confirmation and analysis based on the SAR-GMTI processing algorithms discussed previously. Relocated ship positions are shown by red dot markers and they are expected to fall into the boxes drawn from the AIS information. Markers of other colors are used for intermediate results. Each map is followed by an example of SAR imagery from that scene with overlaid color-coded targets as explained for each for each scene.

The first scene was acquired on 2009-01-19 using the HH polarized, 30 MHz bandwidth MODEX1 mode, at the largest incidence angle (52°) of the analysed scenes. The analysed tile is shown in Figure 61 and contains 19 reported ships that are crossing the strait or are transiting between the Atlantic ocean and the Mediterranean sea. Two fast catamaran ferries are crossing between Tarifa Spain and Tanger Morocco. Light blue markers show all pixel based detections, many of which are littoral ambiguities and ship ambiguities. These ambiguities are resolved automatically. Dark blue markers show the unambiguous target detections and they are relocated onto positions marked in red. Figure 61 shows the SAR image of the tile in Figure 62. Littoral ambiguities and displaced ships are visible in the imagery and the ship positions estimated from SAR-GMTI processing are overlaid on the image using dot markers. The markers are color coded according to the estimated radial speed of each ship. A small chip (represented by a rectangle containing the number 20 in the North West part in Figure 60 is also shown in Figure 61 as an enlarged detail from the full image.
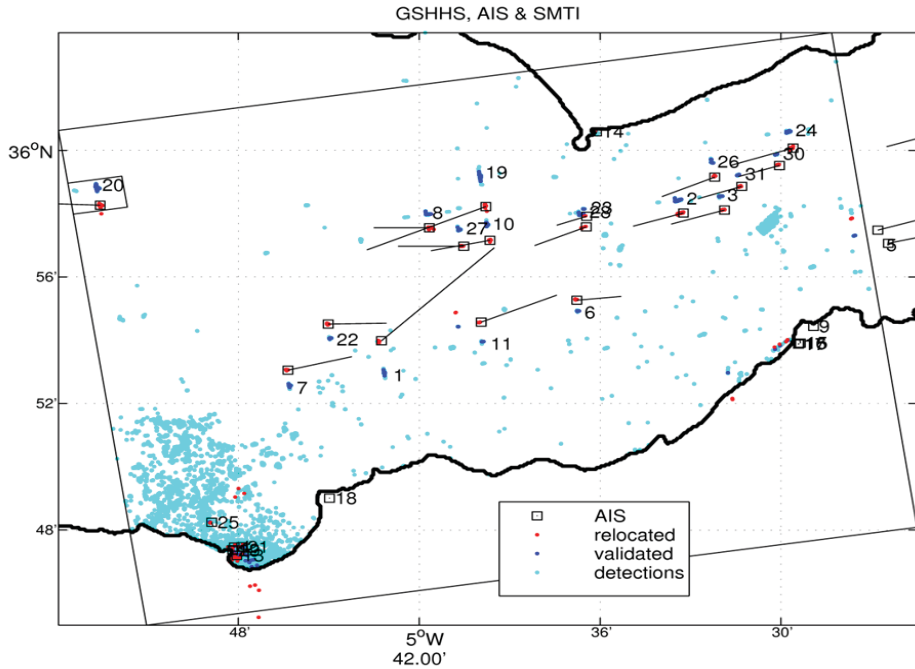
Figure 60: *The selected tile of the MODEX-1 scene from 2009-01-19 with marked known vessel positions (small squares) and velocities (lines extending from the squares), all detections (light blue), unambiguous detections (dark blue) and relocated vessel positions (red).*
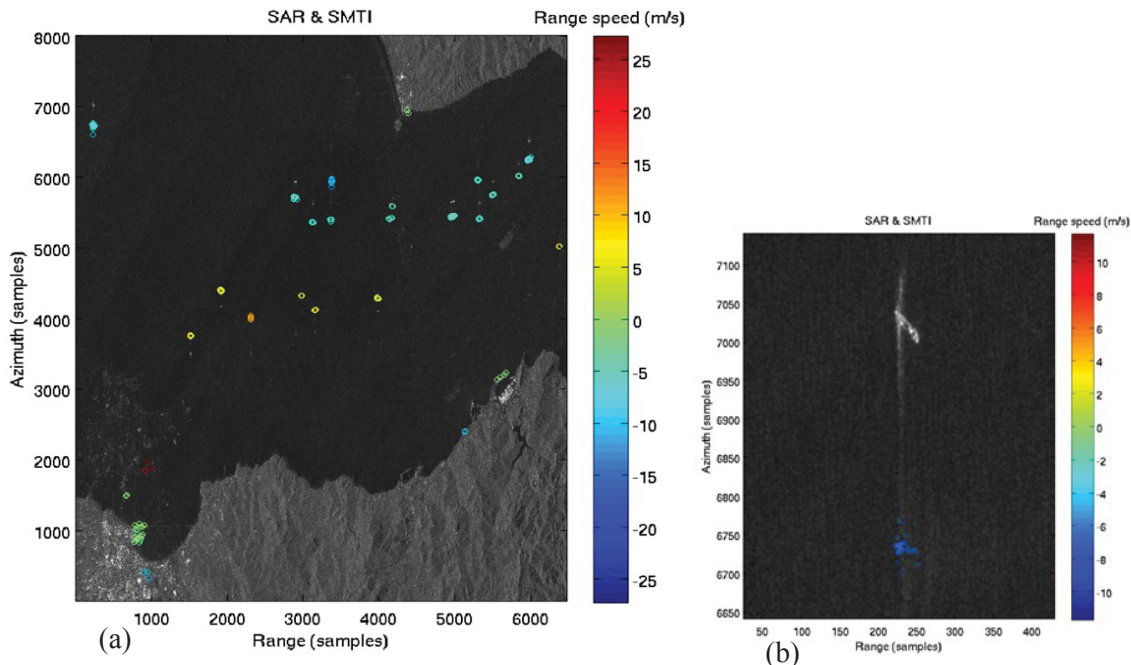
Figure 61: *(a) SAR image of the selected tile from 2009-01-19 with overlaid ship markers and (b) the zoomed SAR image chip with one imaged ship and the repositioned processed ship. The color of the repositioned image indicates the ship's radial speed.*

Figure 62 shows the analysed tile from the MODEX1 HH scene acquired on 2009-01-21. The tile includes the Atlantic ocean west of Africa. There are 10 processed ships in this tile and they have various velocity directions relative to the SAR trajectory. Ship ambiguities are detected (light blue markers) but are discarded by an automatic ambiguity identification algorithm based on equation (15) and the relative range of detected target pairs. True ship detections (dark blue markers) are correctly relocated (red markers) to the positions indicated by the AIS data (boxes). Two image chips from this scene are shown in Figure 63. The position of the chips is shown by rectangle containing numbers 5 and 2 and the rectangle containing the number 9 in Figure 62. Ocean features and ships are clearly visible in the imagery. The estimated ship positions are marked by dots, which are colored according to the estimated radial speed. The shape and the orientation of the relocated ship images differ significantly to the shape and orientation of these vessels in the reference SAR image.
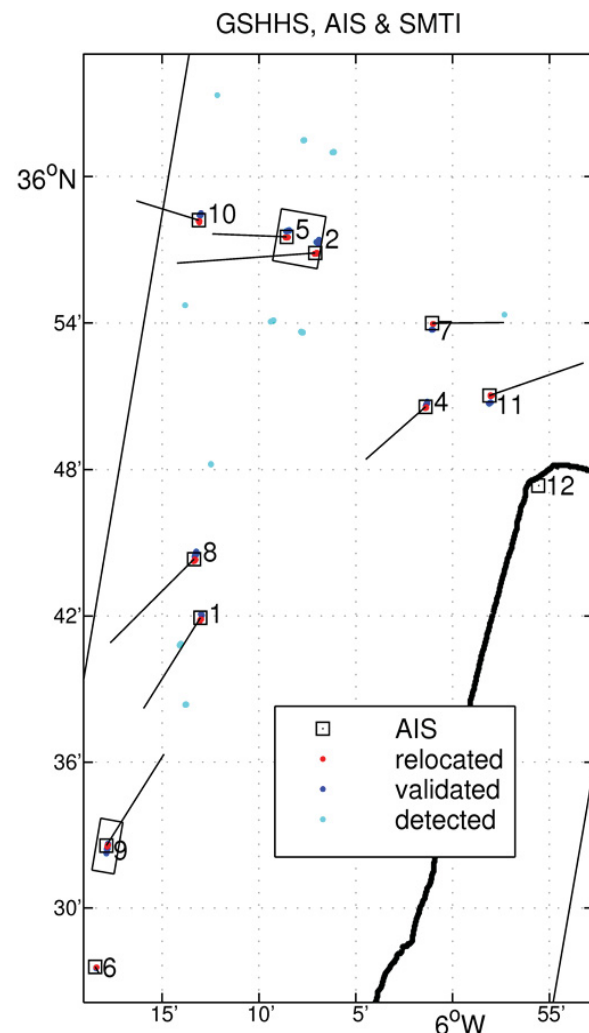
Figure 62: *The selected processing tile from the 2009-01-21 MODEX-1 with marked known vessel positions (small squares) and velocities (lines extending from the squares), all detections (light blue), unambiguous detections (dark blue) and relocated vessel positions.*
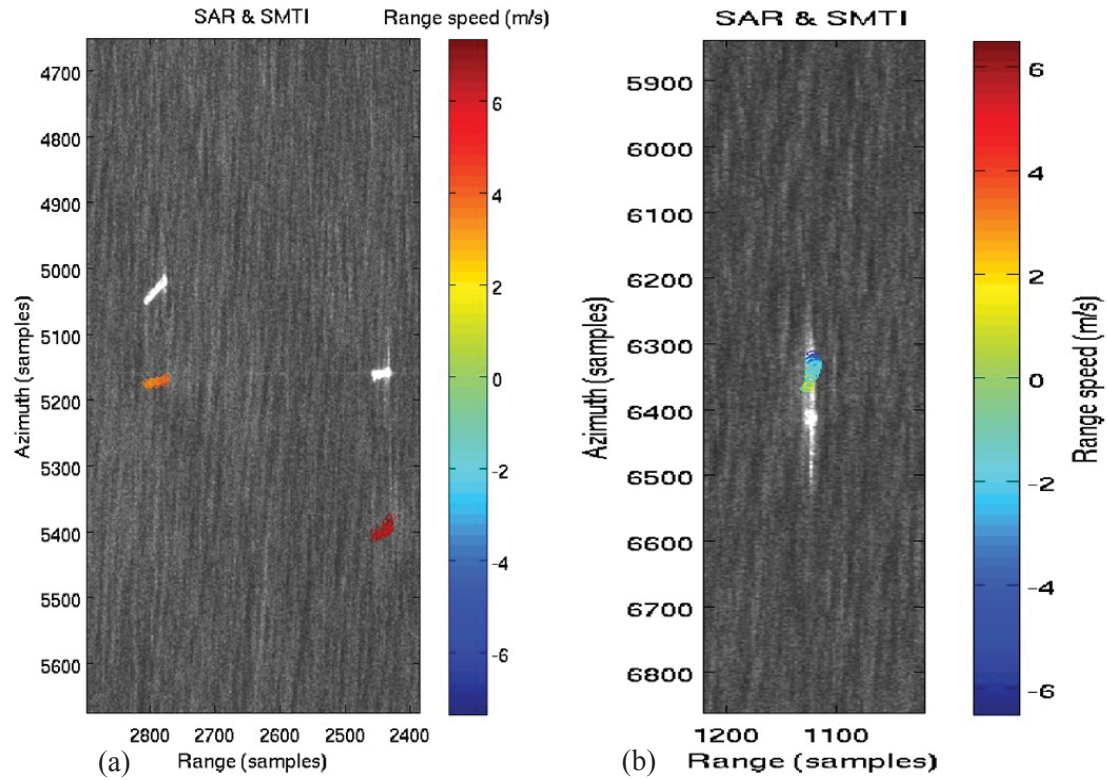
Figure 63: *(a) SAR image chip from 2009-01-21 with two imaged and marked ships from the north part of the analysed tile and (b) SAR image chip with a distorted ship image and overlaid ship markers from the southern part of the analysed tile.*

In Figure 63 (a) note the difference in orientation between the detected (white) and the repositioned (red) ship images.

Figure 64 presents the map of the MODEX1 VV tile from 2009-03-10, which repeats the data acquisition geometry of the 20-01-19 scene with a different polarization. Ten ships are captured in this scene. Detection and estimation results are overlaid on the map in the same way as for the previous scenes. Two image chips (indicated by the rectangles containing target number 2 and 7) are cropped from the SAR imagery and shown in Figure 65. The contrast in this VV scene is lower than in the corresponding HH scene due to the larger sea return at VV polarization for this incidence angle. One of the image chips shows a stationary ship (according to the AIS report). Even so, some small radial speeds are measured by SAR-GMTI.
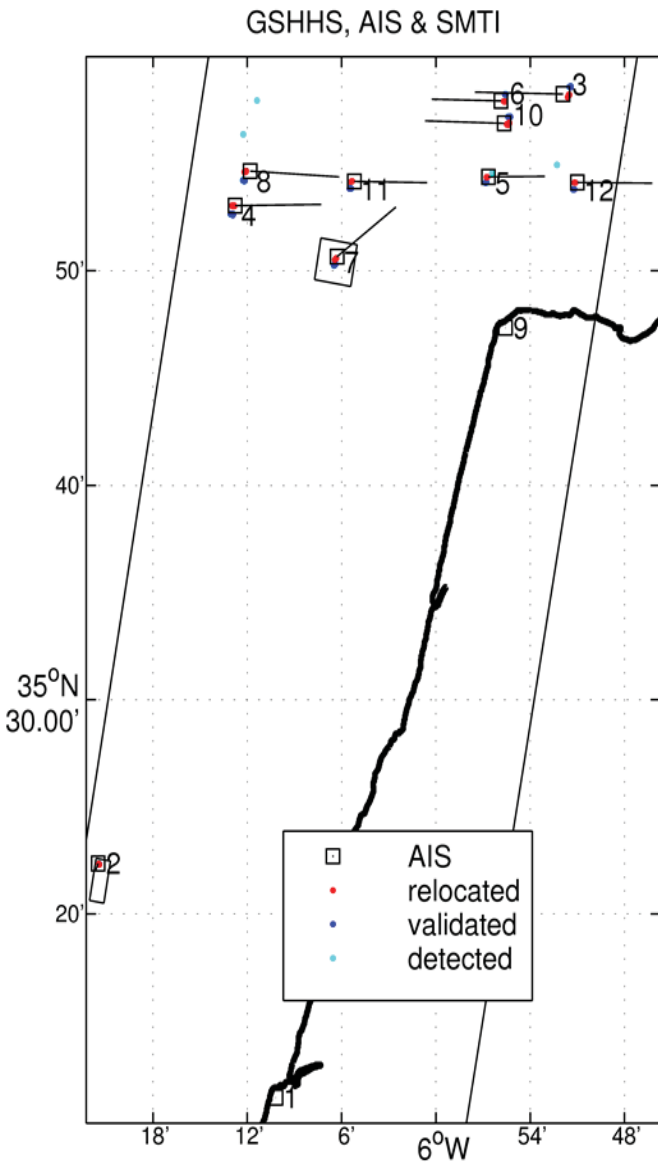
Figure 64: *The selected MODEX-1 tile from 2009-03-10 data acquisition with marked known vessel positions (small squares) and velocities (lines extending from the squares), all detections (light blue), unambiguous detections (dark blue) and relocated vessel positions.*
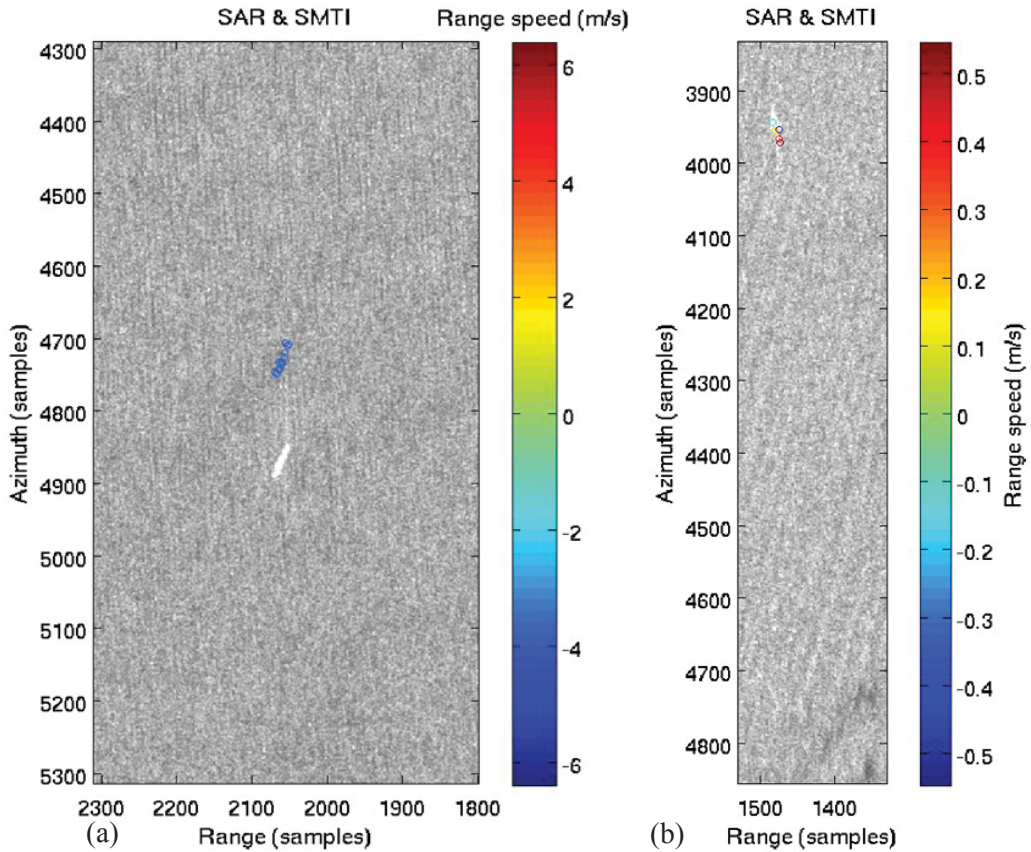
Figure 65: *(a) SAR image chip from 2009-03-10 with an imaged and marked ship from the northern part of the analysed tile and (b) SAR image chip with a distorted ship image and overlaid ship markers from the southern part of the analysed tile (right).*

Figure 66 presents the map of a selected tile from the MODEX2 HH scene acquired on 2009-10-05. The five moving ships were analysed. Two other ships were detected close to the African coast and correctly positioned, but were not used in further analysis. Some littoral ambiguities are present, but the processing algorithm rejected them. The SAR image corresponding to this tile is shown in Figure 67. Littoral ambiguities (from the city of Tangier) and ships are clearly seen. The estimated ship locations are shown by color coded markers according to the estimated radial speed.
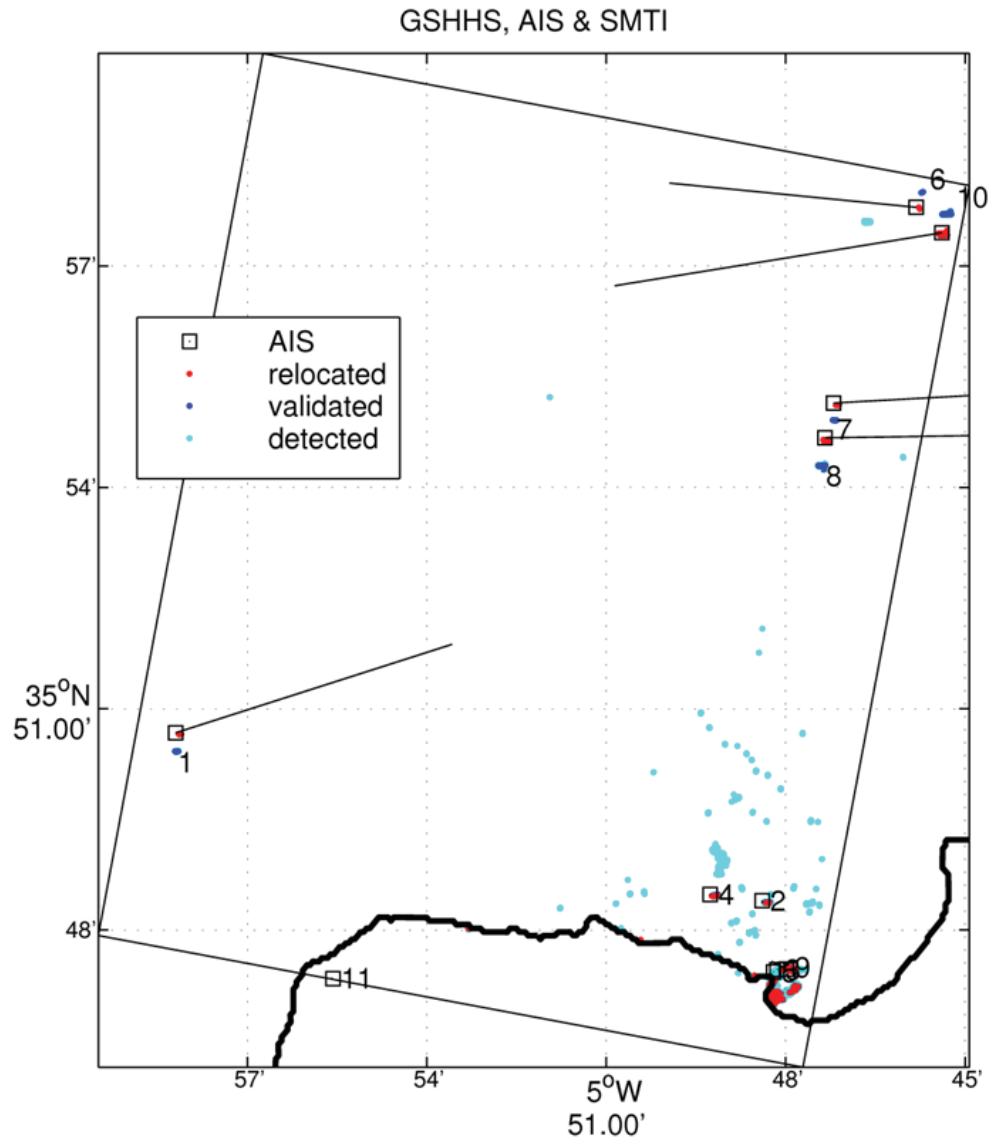
Figure 66: *The selected tile for the MODEX-2 data acquisition on 2009-10-05 with marked known vessel positions (small squares) and velocities (lines extending from the squares), all detections (light blue), unambiguous detections (dark blue) and relocated vessel positions.*
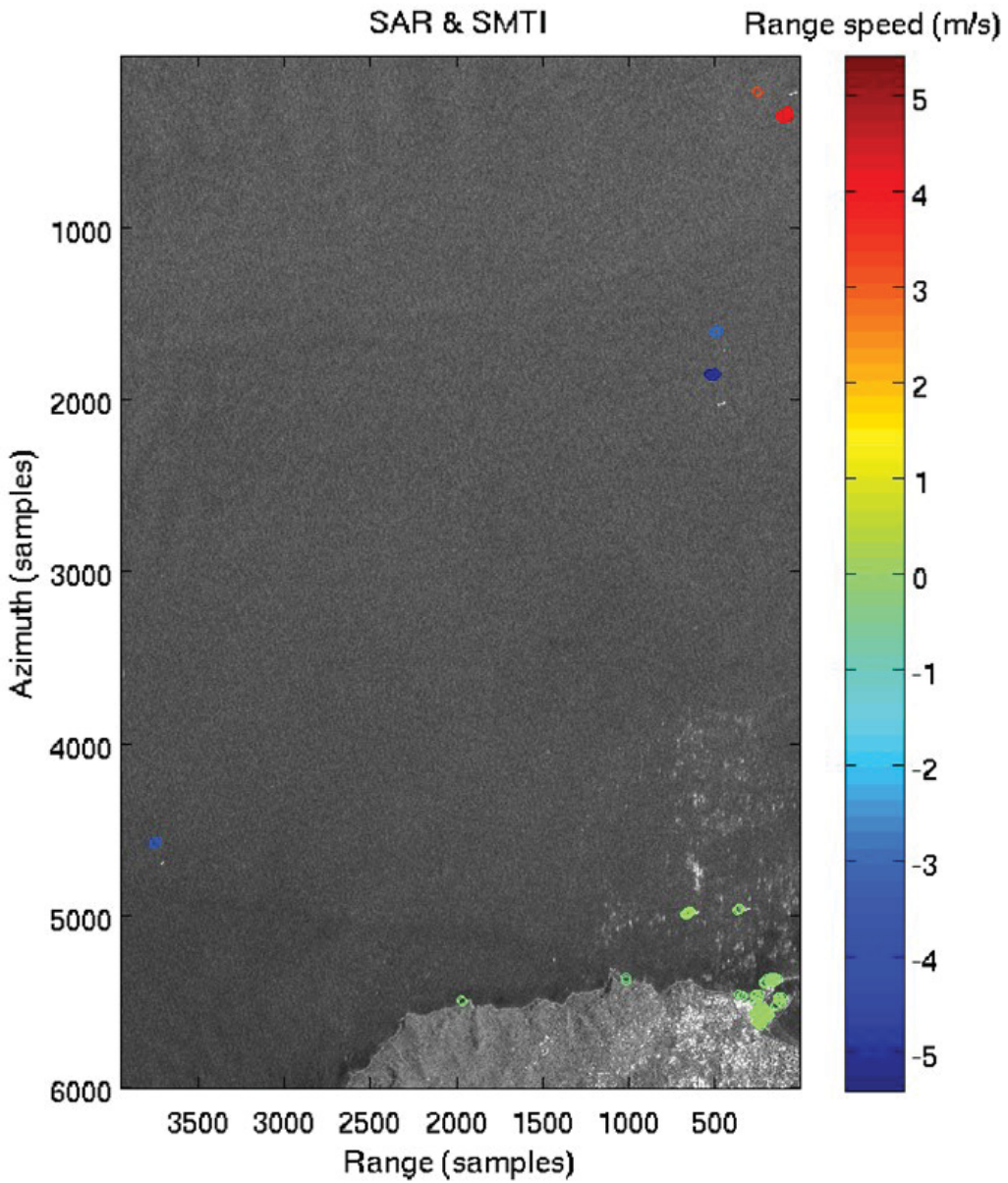
Figure 67: *SAR image of the selected tile from 2009-10-05 with overlaid ship markers.*

Figure 68 shows the tile from the last MODEX2 HH scene acquired on 2009-10-12. There are 5 moving ships captured in the tile. Four of them are travelling nearly perpendicularly to the SAR ground track, which is favourable for detection and estimation. The fifth ship is travelling parallel to the SAR ground track and it is in the zone of littoral ambiguities, which creates a challenging situation for detection and velocity estimation. Data for all five ships were analysed to generate moving target estimates. There are also three other ships at anchor in the area affected by city ambiguities. They were correctly detected and estimated, as indicated by the red markers in the

AIS boxes. However, they were not used in the detailed analyses. The SAR image corresponding to this tile is shown in Figure 69. The brightest features in the SAR image are the ships. City ambiguities and ship ambiguities are also clearly seen. The estimated ship locations are shown by color coded markers according to the estimated radial speed.
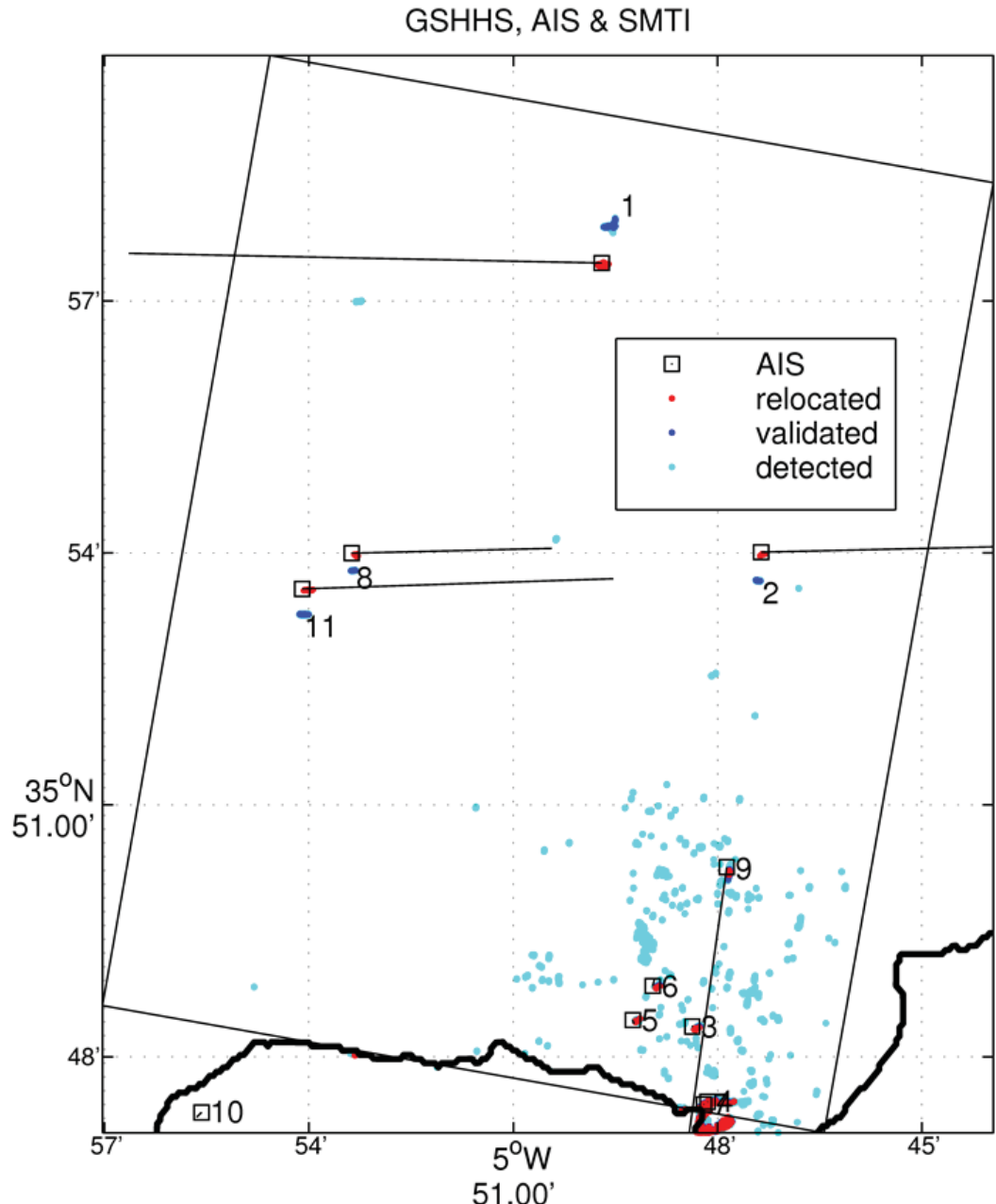
Figure 68: *The selected tile fro the MODEX-2 acquisition on 2009-10-12 with marked known vessel positions (small squares) and velocities (lines extending from the squares), all detections (light blue), unambiguous detections (dark blue) and relocated vessel positions.*

DRDC-RDDC-2014-R17
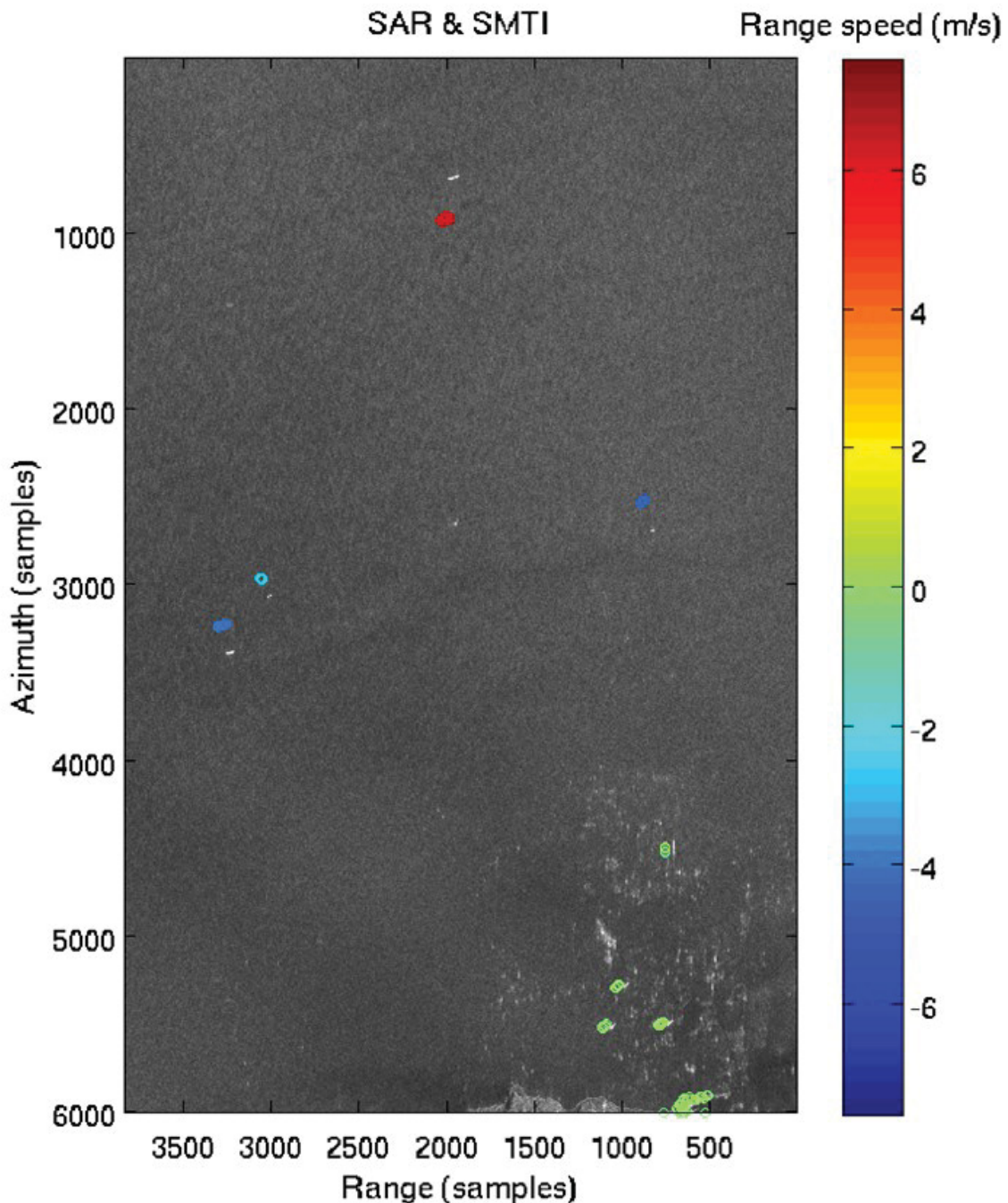
Figure 69: *SAR image of the selected tile from 2009-10-12 with overlaid ship markers.*

4.6.2 SMTI velocity estimate accuracy

Radial speed was estimated for each ship as a weighted mean of radial speeds estimated in the different scattering domains for each vessel. The weights used in averaging were the relative radar reflectivities for each clustered domain. The estimated radial speeds are compared to the

AIS values in the scatter plot presented in Figure 70 where data from different scenes are shown in different colors. The agreement is excellent and the GMTI ship speed estimates are within ± 0.26 m/s of the AIS reported speeds. The standard deviation of the location error is less than the average length of the ships in the data set. The largest errors in the estimated velocities come from 2009-01-21 HH polarized data set.
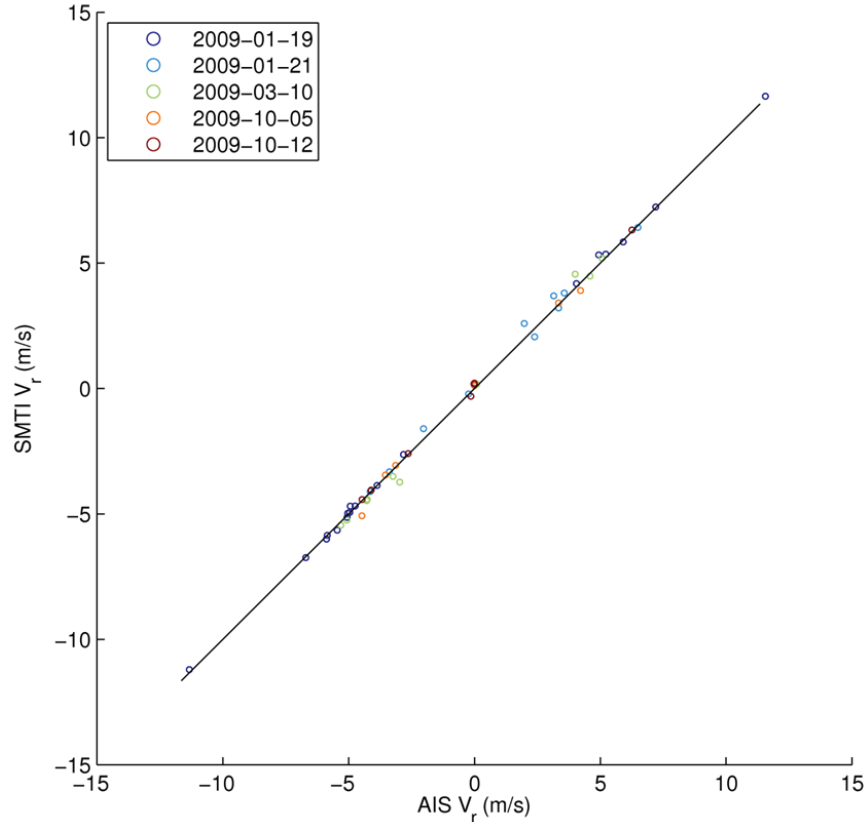
Figure 70: Scatterplot of estimated SMTI radial speeds against AIS speeds for 49 ships.

4.6.3   SMTI heading estimate accuracy

The headings of the analysed ships were estimated by fitting an ellipse to each cluster of ship samples and determining the geographic angle of the ellipse semi-major axis. This method was first applied to the cluster of detected pixels in the image domain. The comparison of these estimates and the AIS values is shown as a scatterplot in Figure 71 (a). Many estimates are in good agreement with the AIS data, but there are several outliers. The outliers all come from the January scenes (dark and light blue markers). Next, ships were repositioned using the domain method and then heading was estimated by fitting the ellipses to the repositioned clusters. The results are shown in the right part of Figure 71 (b). Repositioning always introduces a position variance due to the variance of errors in the speed estimates. However, it also removes the apparent heading bias due to ship's rotation at the moment of imaging. These are opposite trends. The mean error increased in the VV scene presumably due to the worse SCNR, but it decreased significantly in the two January HH scenes, which originally suffered from rotation effects and some azimuth smearing. Overall, the agreement between the heading estimates and the AIS

values was improved after GMTI processing and repositioning. Only two outliers remained in the set of 49 ships. They were captured in the scene from 2009-10-19. These two medium sized ships (length 86 m) ships were catamaran ferries and were the fastest vessels in the entire data set (radial speeds ~12 m/s). One of them is shown in Figure 72.
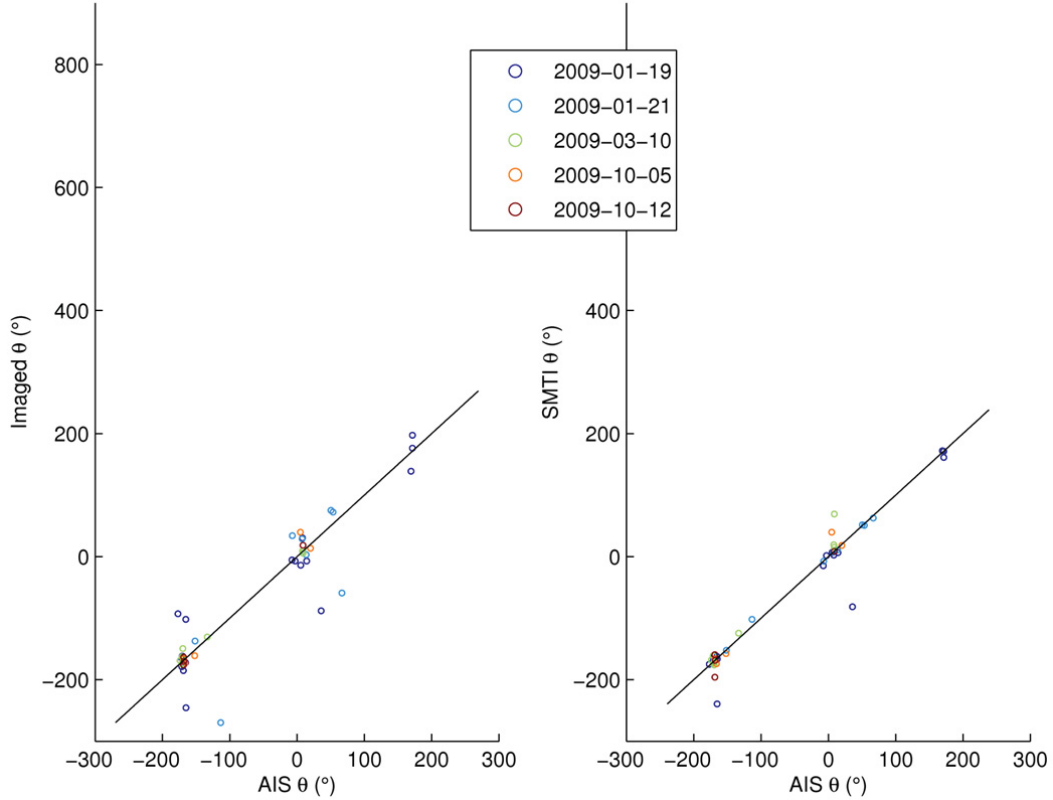
Figure 71: (a) Scatterplot of estimated detected image headings against AIS values for 49 ships from the SAR imagery and (b) from relocated SAR-GMTI estimates.

Figure 72: The high-speed catamaran ferries that had failed heading estimates.

The ship heading estimates from detected target clusters, shown in Figure 70 (a) for all data sets, have a standard deviation of 42.5°. Two of the five data sets, January 19, 2009 (standard deviation 44.8°) and January 21, 2009 (standard deviation 71°) contribute most of the point spread. The remaining three scenes had an aggregate standard deviation of 10°. The heading standard deviation of the aggregate repositioned ship data shown in Figure 71 (b) was 24°.

The significant outlier points in Figure 71 come from two ships of the type shown in Figure 72. An examination of the SAR focusing for these targets shows a serious mismatch between the radar signals and the anticipated range histories for target points belonging to these vessels. The combination of the ship radial speed for these targets with the velocity projections based on the heading estimates provide sufficient evidence to identify the results as anomalous. When these outlier points are removed from the data set, the standard deviation of the ship heading estimates becomes ±12.4° over the remaining 47 ship samples.

We will take a heading estimate accuracy of ± 12.4° to be typical for the target domain cluster-ellipse approach to ship heading estimation from SAR-GMTI measurements of large vessels.

4.6.4   Ship length estimate accuracy

The length of a ship is an important identification or classification parameter. There are different ways to measure the length of a ship in the SAR image domain, but it is well known that large estimation errors may occur [5]. Gross overestimates are common for azimuth travelling ships, which almost always create an azimuth smear in the image, while underestimates may happen if detected pixel clusters from the same ship appear as disconnected regions in the image [5].

One approach to estimating ship length from SAR-GMTI data is to find the best-fit ellipse to the cluster of detected or repositioned moving target sample points. The length of the major axis of the ellipse cannot be taken directly as a measurement of the vessel length because it only quantifies the spread of the detected pixels along that direction but it can be a useful indicator. In the image domain, the spatial distribution of the samples depends on the length and three dimensional structure of the ship, as well as the location of any side-lobes, double-bounce reflections, differential azimuth displacement due to the difference in radial speed from the bow to the stern, image smears due to poor focusing, and any other possible image artefacts. After relocation, the direction of the longer axis may change and the spread of the relocated cluster may decrease or increase. It will depend on the length and structure of the ship, as well as relocation errors due to the limited accuracy of the range speed measurements for the given SCNR.

The length of the major axis provides an indication of the ship length, but not a true length measurement. Figure 73 shows the comparison between the vessel lengths provided by the AIS data and the major axis length for the ellipses fitted to the detected sample clusters, Figure 73 (a), and relocated sample clusters Figure 73 (b) for each vessel [80]. The comparison is presented as scatter plots of ellipse major axis estimates as functions of the AIS-reported ship length where each plot marker represents on ship and the marker color identifies the source data set. The associated linear regression results are displayed as solid lines. For the detected data in Figure 73 (a) the regression slope is 0.8297, the ellipse major axis to ship length scale factor is 1.218 and the ship-length estimate standard deviation is 67 m. For the repositioned data in Figure 73 (b) the regression slope is 0.725, the ellipse major axis to ship length scale factor is 1.379 and the ship length standard deviation is 34.5 m.

Most data points cluster about the regression line but several data points are obvious outliers. One sample in Figure 73 (a) is significantly displaced from all others. The extreme outlier sample represents the azimuth-travelling ship shown in Figure 74 whose SAR image is shown in Figure 63 (b). After sample-point velocity estimation and spatial relocation using the sub-cluster domain approach Figure 73 (b), there were no extreme outliers. The processing and relocation process also suppressed the large length estimation errors for the January scenes. The ship length estimates from the March VV scene worsened after signal processing, presumably because the lower SCNR for this data set increases the error in ATI phase estimates.
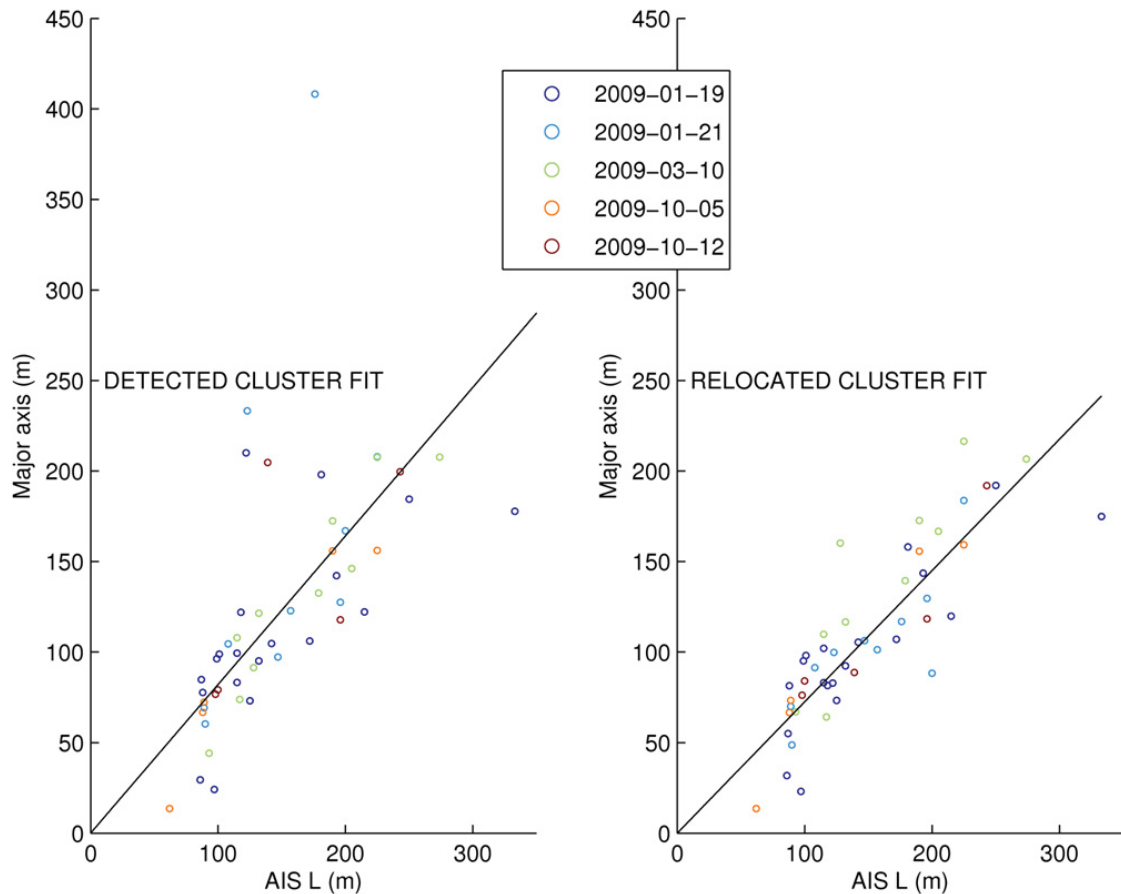
Figure 73: *Linear regression comparison of the AIS data and the ellipse method for the length estimation for 49 ships. The points in (a) represents estimates made from the moving target detection clusters and the points in (b) represent estimates made form processed, clustered and relocated samples.*

When all ship samples are considered, with the extreme outlier removed, 75 % of the data set (36 ships) have ellipse-based length estimates within 25% of their AIS-reported length, 92% of the data set (44 ships) have ellipse-based length estimates within 35% of their AIS-reported lengths and 4% of the data set (2 ships) have ellipse-based length-estimate errors as large as 70% of their AIS-reported lengths (95 m and 62 m). Of the two ships with the largest length errors, one is a general purpose cargo ship where only the stern of the vessel is contained in the SAR-GMTI

data set and the other is a 62 m yacht that is fully contained in the data set. Large ships have the smallest fractional error in ellipse-based ship length estimate errors.

Figure 74: *The ship that created a cluster of detections much longer than its real size. The ship was travelling parallel to the radar track when the estimate was made.*

To complete and examination of ship length estimates form the Gibraltar GMTI data sets three ship-length models were compared:

1. Ellipse approach for the detected clusters: $L_M = 0.8207 L_{AIS}$ where L_M is the major axis,

2. Ellipse approach for the relocated clusters: $L_M = 0.725 L_{AIS}$ L_M is the major axis, and

3. RCS approach [5] for co-polarized SAR imagery: $\sigma = 1.25\ L_{AIS}^{1.98}$ where σ is the ship RCS.

Ellipse-based ship-length estimation is discussed above, to test the RCS approach, the SAR-GMTI mode amplitude calibration coefficient was estimated for each scene using all channels in each scene to provide the best estimates and the RCS base length estimate for each ship was plotted against the AIS-reported length in Figure 75.
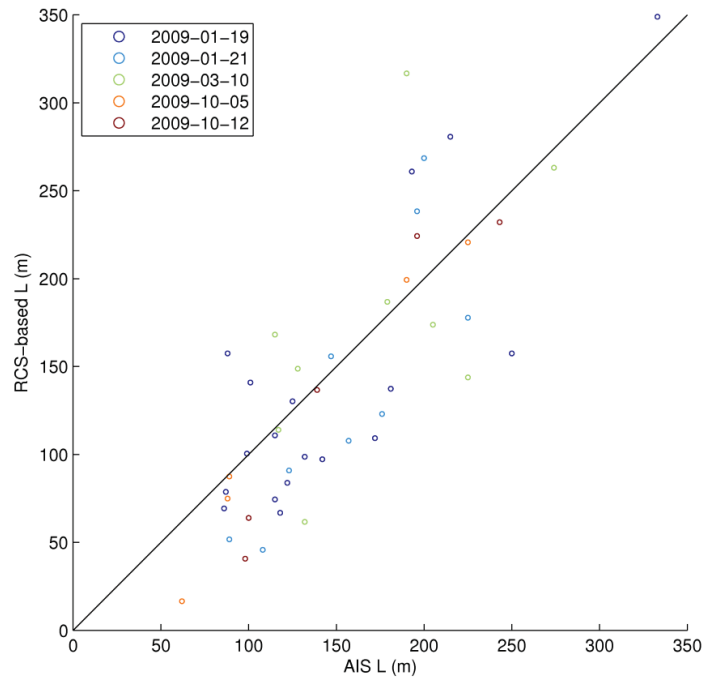
Figure 75: *Ship length from RCS estimates as a function of AIS ship length reports for the five Gibraltar SAR-GMTI scenes.*

The estimation errors for the ellipse method were compared to the estimation errors for the RCS method by scatter plots comparisons and by calculating the length-error correlation coefficients $C_{L=}\langle e_{EL}e_{RCS}\rangle/\sqrt{\langle e_{EL}^2\rangle\langle e_{RCS}^2\rangle}$ where e_{EL} and e_{RCS} are the estimation errors for the ellipse and the RCS methods, respectively. It was found that the correlation coefficient is -0.22 between the ellipse method for the detected clusters and the RCS method, while it was -0.11 between the ellipse method for the relocated clusters and the RCS method.

The ellipse method can be applied to any detected imagery and it may create overestimates compared to the RCS method, as seen in Figure 76 (a). The ellipse method can be applied to relocated clusters only if SAR GMTI measurements are available. The ellipse-based ship length estimates for detected ships are comparable in accuracy to the RCS method but have less bias towards ship-length underestimates as shown in Figure 76 (b).
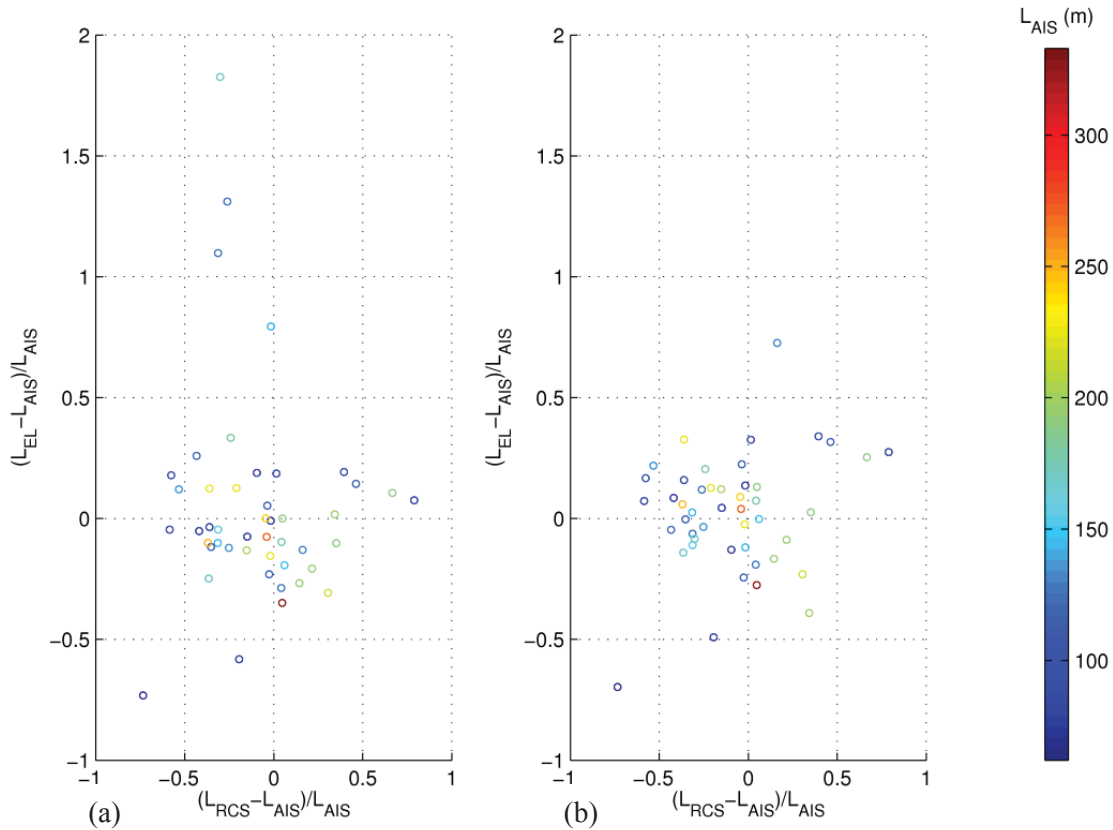
Figure 76: *(a) Comparison of detected ellipse-based ship-length estimation errors and RCS-based ship-length estimation errors, (b) Comparison of repositioned ellipse-based ship-length estimation errors and RCS-based ship-length estimation.*

In Figure 76, the point color is the AIS ship length as coded by the color bar.

Ship length estimates from SAR-GMTI radars are most accurate for domain-repositioned ship samples and, for large ships 90% of all estimates are within 35% of the true ship length. Estimate errors are expected to increase for smaller vessels due to the reduced number of radar sample points available for analysis. SAR-GMTI length estimate errors are greatest for ship headings that lie close to the radar track.

4.7   Strait of Georgia observations

RADARSAT-2 data collected in the Strait of Georgia in 2008 were supported both by the Canadian coast guard vessel Sir Wilfred Laurier acting as a collaborative target and by AIS measurements obtained from shore-based receivers. The AIS measurements show that the ship sizes range from lengths of 15 m to over 150 m. RADARSAT-2 was operated in a 30 MHz bandwidth, MODEX-1 mode with radar parameters shown in Table 6.

Table 6: RADARSAT-2 configurations for Georgia Strait.

Date UTC)	2008-11-04
Phase centers	2
Nominal adjacent channel baseline separation (m)	3.75
Transmit azimuth beam width (-3 dB)	0.21°
Receive azimuth beam width (-3 dB)	0.42°
Polarization	VV
Incidence angle (°)	42
Pulse bandwidth (MHz)	30
Pulse duration (μs)	41.6
PRF (Hz)	1818
Pass direction	Ascending
Pass time (Pacific Standard Time, November 3)	18:09:01

Figure 77 shows a Google Earth image of the Strait of Georgia with the RADARSAT-2 SAR-GMTI swath highlighted and AIS ship tracks superimposed on the RADARSAT-2 swath area.

The ship tracks are color coded according to length with red tracks corresponding to vessels over 50m, blue tracks to vessels between 25m and 50m, green tracks to vessels between 10m and 25m, orange tracks to vessels less than 10m and yellow tracks to vessels for which the AIS receiver did not get information about the ship length.

SAR image data show the sea conditions to be calm with no wave signatures visible and multiple surfactant slicks. Hourly meteorological reports from stations near the test area indicate that wind speeds in the central and northern part of the test area were 6 km/h (1.7 m/s) and wind speeds in the southern part of the test area varied from 2 km/h to 4 km/h at 18:00h Pacific standard time.
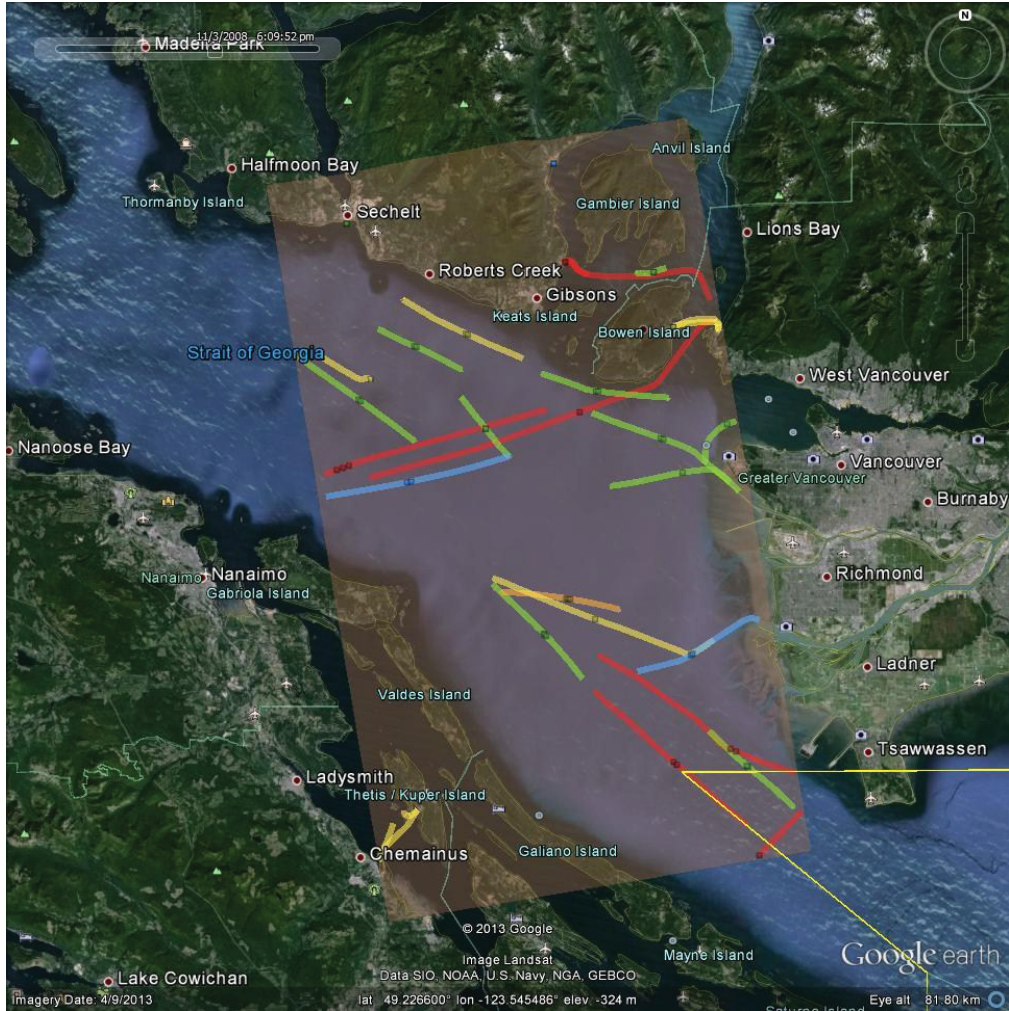
Figure 77: *Google earth representation of AIS ship tracks from Strait of Georgia 2008 RADARSAT-2 experiment.*

Figure 78 shows the estimated PDF of the land-masked data assuming several different distributions for a wind-roughened, calm sea surface. The horizontal axis in Figure 78 is the un-normalized test statistic value used in equation (21). None of the standard sea- surface statistical models is a good fit to the statistics of the observed sea returns for the calm conditions found in these data.

In Figure 78, model PDF distributions are plotted on a logarithmic scale to better show the low-probability distribution tails. The K-distribution model (χ^2) corresponds to the magenta line for un-texturized noise and as the cyan line for texturized noise. The normalized histogram crosses above the K-distribution and thus a false alarm threshold computed using the K-distribution will yield more false alarms than intended. It is not surprising that this effect is much more apparent when the data are modeled as homogeneous as shown by the black line. On the other hand, when the data are assumed to follow the F-distribution (χ^{-2}), illustrated the red and green lines, one sees that the computed threshold will yield fewer false alarms than intended. This of course, comes at the cost of poorer probability of detection.
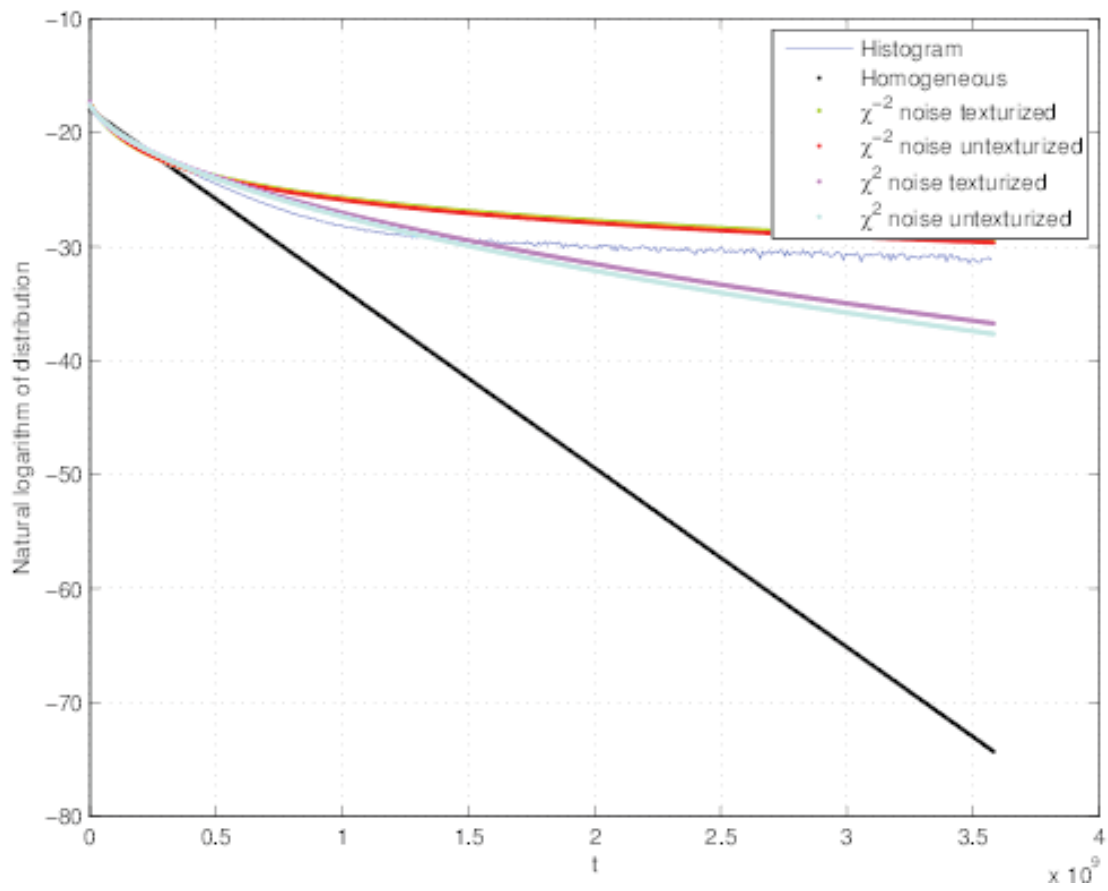
Figure 78: *Natural logarithm of the model PDF and histogram for land-masked sea surface clutter for the conditions found in the 2008 Strait of Georgia experiment.*

Figure 79 shows results for the land-masked data that have been processed with the $\boldsymbol{b} = \begin{bmatrix} 1 \\ 1 \end{bmatrix}$ vector, defined in Section 2.5.1 (equation (20)), and are detected using an adaptive [83] signal magnitude threshold. The detected targets in Figure 80 have been overlaid on un-masked SAR imagery.
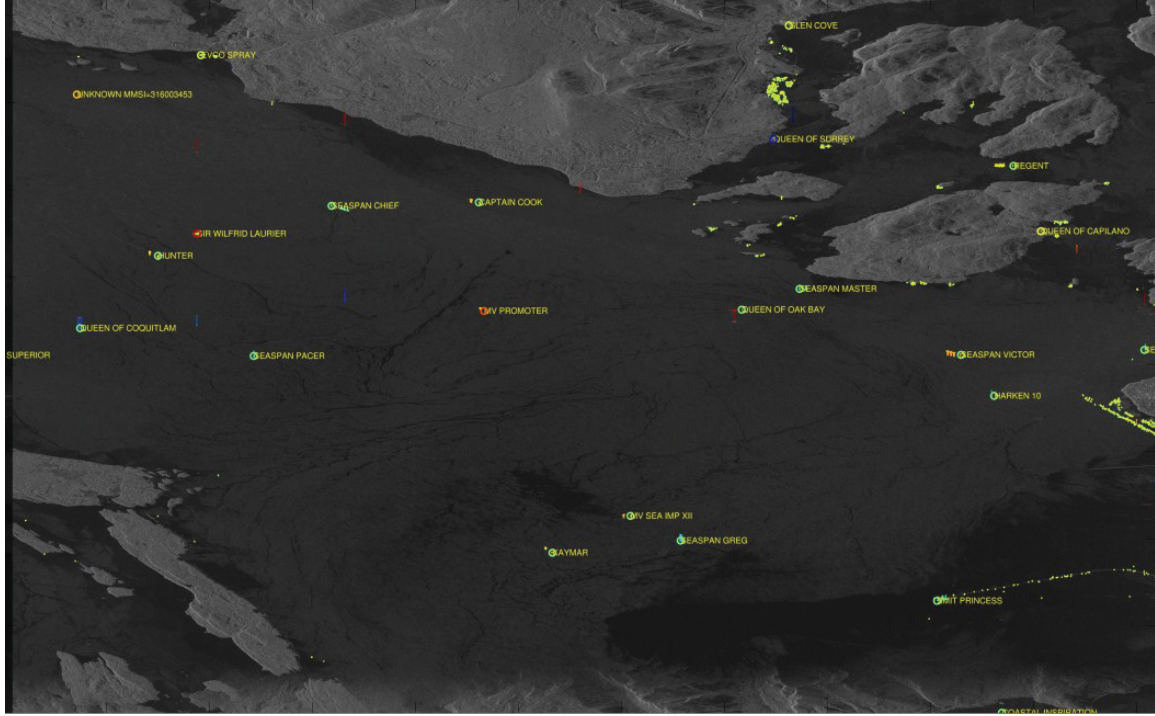
Figure 79: *Signal magnitude-detected ships after land suppression by a land mask. All AIS-reported ships over 25m in length are detected by the radar except for one tugboat. The barge string pulled by the tug, however, is detected.*

Note that stationary vessels in Gibson's harbor lie outside of the land mask and are detected.

Figure 80 illustrates the use of DPCA moving target detection ($\boldsymbol{b} = \begin{bmatrix} 1 \\ -1 \end{bmatrix}$) with adaptive thresholds [83] when no land mask is applied to the data set. Both the land and sea clutter are suppressed by this processing but moving targets on land are detected in the imagery. The detected and repositioned targets in Figure 81 have been inserted into the SAR imagery.

A fast moving target (with a ground-projected radial speed of 80 km/h), not recorded by AIS and not detected in the land-masked approach, is detected and circled. It is not possible to tell whether this target is a very fast moving small boat, not instrumented with AIS, or whether it is an aircraft. The repositioning of the suspected aircraft target indicates that the radial component of its motion is away from the radar (approximately eastward) and its ground-speed suggests that its flight track is less than 24° from the satellite track. The observations are not inconsistent with a small to medium sized aircraft departing from Vancouver international airport runway 30.
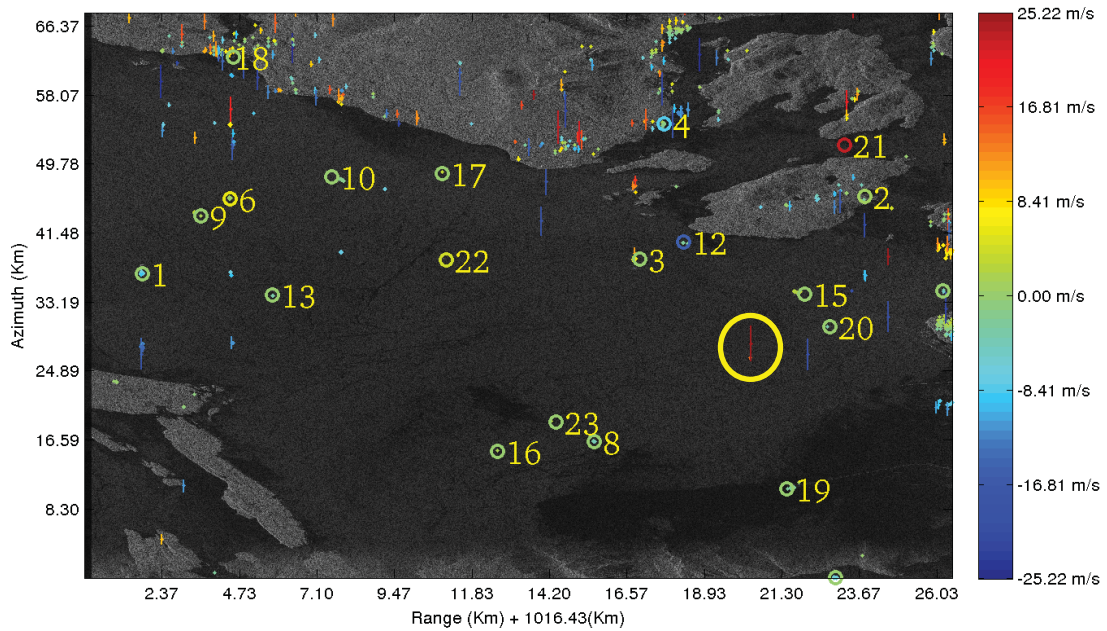
Figure 80: *Ship detection for clutter-cancelled ship detectioffn without a land-mask.*

The detections displayed in Figures 79 and 80 were SAR processed using a stationary-world assumption and are not optimized for estimated target motion. Although the radar polarization selected for the Strait of Georgia data set is best for sea surface observations, the low wind and sheltered waterway result in low sea returns and minimal sea motion. The ship numbers in Figure 80 match the entries in Table 7.

4.7.1   Signal processing for target extraction

The Strait of Georgia data set contains 23 small and medium sized ships that are moving at a wide range of speeds on a wind-ruffled calm sea surface. As has been previously noted, the background cancellation analysis associated with DPCA detectors also suppresses the signatures of slowly moving targets and particularly discriminates against those that have small radar cross sections. To provide measurement capability for small and slow targets, the EDPCA detection and estimation algorithm [66], which uses a parametric approach to detection (Section 4.4.2, equation (48)), was employed.

Table 7 displays the results of the EDPCA algorithm applied to two different versions of the data set. The first version retains the two channel character of the data set and the channels are balanced and registered to yield data sets for analysis. The antenna gain for these channels is two-way MODEX 1 antenna gain pattern. The second version sums the two channels as received to generate a single data channel whose antenna gain is that of the full RADARSAT-2 receive antenna. The two versions have the same number of data samples.

The EDPCA algorithm is computationally intensive in that it requires a sequence of scene processing iterations required for the maximization of a SINR (signal to interference plus noise ratio) parameter.

Table 7: Georgia Strait Ship results.

Ship	Length AIS reports	Width m	Radial Speed	Course degree	GMTI radial speed ship	Tow	RADARSAT-2 results Ampl. Detect.	SINR 1 dB	SINR 2 dB	ΔAz. m, ΔSR. m
Passenger Ferries										
1	139	29	-6.43	-105	-6.82		Yes	51.5	54.8	-1.4, 28.8
2	91	21	0.13	76	0.13		No (2)			
3	139	28	6.85	74	7.13		Yes	51.1	54.9	5.5, -44.8
4	139	29	-0.86	-135	-1.5		No (2)			
5	160	28	-5.13	-42	-5.4		Yes	56.7	57.5	38.8, 47.5
Coast Guard										
6	83	16	0.1	91	0.4		Yes	58.3	58.3	-3.1, -15.8
Fishing Vessel										
7	62	12	2.26	151	2.38		Yes	44.2	44.8	34.4, -0.6
Small cargo										
8	100	11	-3.63	-50	-3.79		Yes	43.3	44.5	17.7, -3.2
Tugs with and without tows										
9	23	8	1.81	147	1.57	1.47	Yes	25.7	30.6	-21.6, -3.1
10	25	8	-1.54	-48	-1.67	-1.67	No (2)	24.4	24.9	1.0, 2.8
11	21	8	-1.24	-30	-1.57	-1.57	Yes	32.2	33.3	63.5, -2.5
12	24	7	-2.27	-66	-2.88	None	Yes	31.0	33.0	-31.2, -3.5
13	30	9	-3.26	-94	-3.69	None	Yes	40.3	41.7	-20.2, 2.2
14	22	7	-3.22	-109	-3.29	None	Yes	33.5	34.5	29.8, 3.1
15	20	7	2.08	129	2.50	2.50	Yes	22.8	25.6	29.0, -1.2
16	21	6	1.31	155	1.67	1.67	Yes	31.7	33.0	13.7, -2.0
17	20	6	1.84	135	3.29	3.29	Yes	27.3	30.5	-21.7, -2.3
18	20	10	0	0	-0.15	-0.15	Yes	48.2	48.5	14.2, -11.5
19	27	8	-2.23	-121	-2.38	2.38	Yes	33.7	34.6	43.9, -1.4
20	18	7	-3.17	-87	-3.49	None	Yes	28.2	30.2	12.1, -18.0
21	15	4	0.54	78	0.56	0.56	Yes	35.3	35.8	31.6, -4.1
22	15	6	0.48	162	No	0.25	No	20.4	19.9	4.4, -5.2
23	7 (2)	11 (2)	1.89	118	2.07	2.07	Yes	28.0	29.2	2.5, -6.5

Table 7 legend and notes:

1. The AIS report data have been extracted from AIS reports that have been received at a shore station.
   a. The ship speed data has been converted to radial speed along the radar observation vector using the reported ship heading data and the local RADARSAT-2 observation geometry.
   b. The ship size data flagged by note (1) is an obvious AIS reporting error.
2. The RADARSAT-2 results have been obtained from an analysis of RADARSAT-2 signal data that were collected in the MODEX 1 configuration at 30 MHz bandwidth.
   a. The heading Ampl. Det. identifies the single-channel amplitude detection outcomes for each target. The note (2) indicates that the target was inside the land mask required for single channel ship detection.
   b. The heading SINR 1 is the single channel SINR estimate for each target.
   c. The heading SINR 2 is the two-channel SINR estimate for each target.
   d. The heading ΔAz is the difference between the AIS position of the target (mapped to the radar scene) and the repositioned radar azimuth position of the target centroid.
   e. The heading ΔSR is the reported AIS position of the target (mapped to the radar slant range plane) and the radar range position of the target centroid.

$$s_k = t_{sk} + c_k + n_k \tag{52}$$

where k indicates the kth sample of the scene, t_s is ship target data, C is sea clutter data and N is noise data at point k and the vector length is the number of channels (registered scenes) in the data set. For sea surface areas that contain no land or ship targets, the sea surface covariance matrix can be written as

$$\mathcal{R} = \sum_k (c_k + n_k)(c_k + n_k)^H \tag{53}$$

where H is the conjugate transpose operator. Define a steering vector

$$b = \begin{bmatrix} 1 \\ e^{j\theta(v_y)} \end{bmatrix} \tag{54}$$

where $\theta(v_y)$ is the ATI phase for a target moving with radial velocity v_y and a two aperture radar is assumed.

Process the scene for all trial v_y and find

$$SINR = max \mid_{v_y} \left(\left(\frac{|b^H \mathcal{R}^{-1} s|^2}{b^H \mathcal{R}^{-1} b} \right) > \eta \right) \tag{55}$$

where $\mathcal{R}^{-1}$ is the inverse of the clutter covariance matrix and η is a threshold derived from the distribution of the point statistics of *SINR* for areas where no ship targets are present. A polynomial curve fit to the SINR(v_y) results for each target was used to find the maxima.

Each target will generate a cluster of detections and since $\mathcal{R}$ and thus η will vary with v_y, the ship detection rule adapts to the processing model used. For two or more channels, the value of v_y that maximizes the SINR relationship will provide a reasonable radial motion measurement for the target. All sample points in the ship target cluster are assumed to move at the same radial velocity for this algorithm.

The scene processed for the value of v_y that generates the maximum SINR for each target repositions the target cluster to its correct slant-range plane position in azimuth. The (amplitude-weighted) centroid of each ship target cluster defines the radar position of the ship and is used to generate the data in the ΔAz, ΔSR column of Table 7.

Figure 81 shows a tug with a three barge tow (ship 10) from this data set. The repositioned ship and barges are shown in blue.
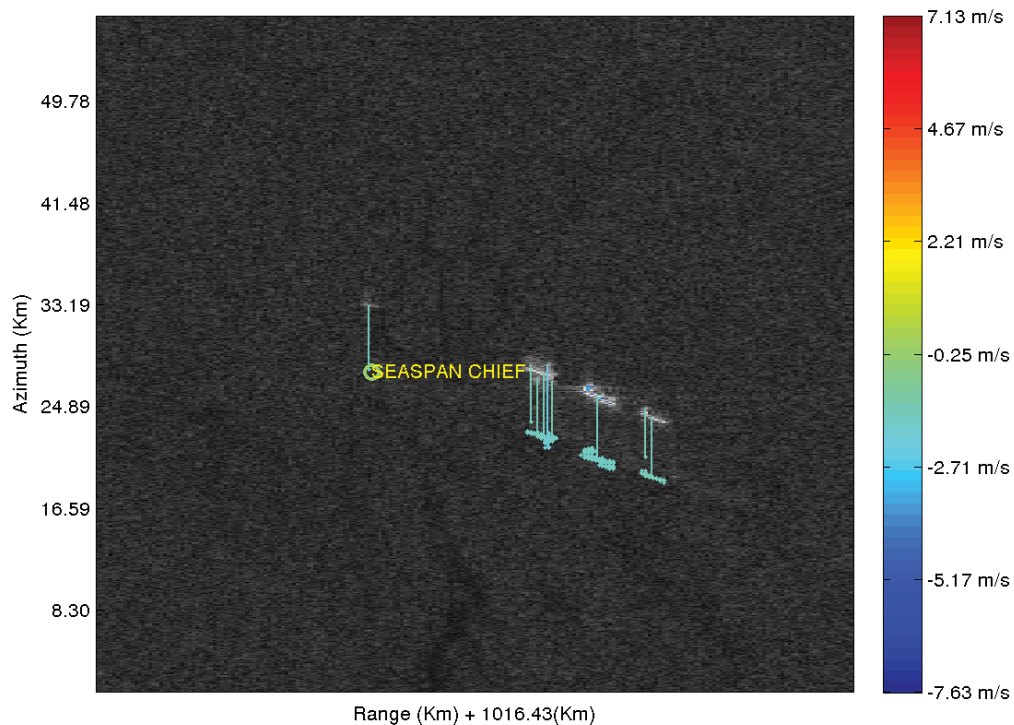
Figure 81: *Tugboat SeaSpan Chief with a three barge tow showing the detected (white) and repositioned (blue) target images.*

4.7.2   Results and discussion

Looking at the data selection choices that were made to compare one and two aperture target detection, we see that the single channel definition used in this study:

1. has an antenna gain that is less than or equal to than the two-channel case when the two channel measurements are combined according to equation(55), and

2. is incapable of discriminating between moving and stationary targets.

Structurally, the EDPCA algorithm is independent of the number of data channels and operates on the individual data samples. Increasing the number of channels increases the number of degrees of freedom and the number of target parameters that can be extracted from the analysis. We note that the covariance matrix used for background suppression is a quadratic function and contains intermodulation terms so that the test statistic used for detection and v_y estimation is properly SINR and not SCNR (signal to clutter plus noise ratio).

The use of single channel ship detection in littoral zones requires the application of a land mask to the data. If the land mask does not properly match the shoreline, either land returns will appear as potential ship targets or ships that are moving near shore will fall within the land mask. Table 7 contains three cases where the ship fell within the land mask and Figure 80 shows Gibson's harbor as a detected target. When two or more channels are available for target detection, the land mask is not required for detection but land moving targets and their sampling ambiguities will be included in the detection lists, as shown in Figure 81, and must be removed.

The relationship between the ship radial-velocity estimates from AIS reports and SAR-GMTI calculations is shown in Figure 81. The joint AIS and GMTI velocity estimation errors have a standard deviation of 0.33 m/s for the ships contained in this data set.
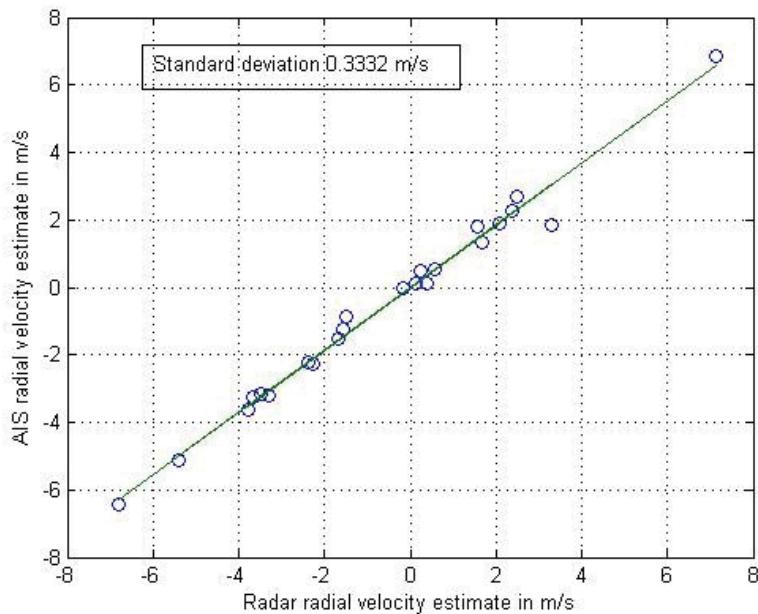
Figure 82: *Ship radial velocities estimated from AIS data and from GMTI data.*

An empirical relationship between ship radar cross section and ship length is discussed in Section 4.6.4 and is illustrated for the Gibraltar data set in Figure 75. The empirical data used to create the empirical model was based on a large sample of large ships. Figure 82 summarizes the observed relationship between ship length and SINR (which is proportional to the ship radar cross section) for the small to medium sized ships contained in the Strait of Georgia data set.

There is no clear relationship between ship length and the SINR for the tug boats in the Strait of Georgia scene. The SINR appears to be related to the vessel structure and deck configuration.
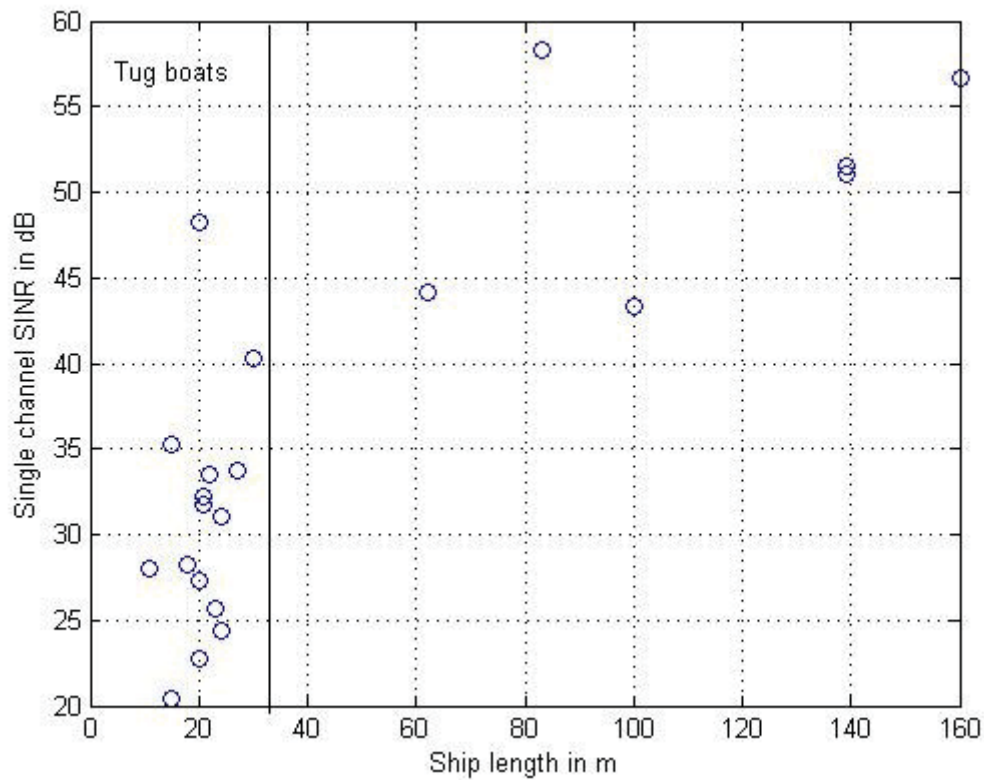
Figure 83: *The relationship between ship length and SINR for the Strait of Georgia data.*

The right hand column of Table 7 contains the difference between the AIS and SAR-GMTI azimuth position estimates and the difference between the AIS and SAR-GMTI range position estimates. These estimates capture contributions from several sources.

1. The AIS positions are interpolated between consecutive reports to estimate the ship position at the radar observation time. When the ship is maintaining a constant course, the interpolations should be quite accurate. For tug boats pulling a tow, the tug can shift its course to maintain the course of the tow. This will inject an error between the reported tug position and the mean course of the tug-tow combination.

2. The position reported by each ship is the position of its GPS antenna sampled at the required reporting interval.

3. SAR-GMTI ship positions are the position of the amplitude-weighted centroid of the velocity-repositioned detection cluster that represents the radar's view of the ship. For large vessels, the radar scattering centroid and the GPS antenna can be in different locations. This will introduce a systematic error in the position metric used. Other factors include:

a. SAR-GMTI speed estimation errors will contribute an azimuth displacement to the reported azimuth position error.

b. For large vessels, the height of the major scattering centers above the sea surface will contribute a range position error.

4. Errors in ship speed estimates will result in ship repositioning errors in the azimuth direction.

In the slant range plane, the standard deviation of ΔAz is 26.99 m and its mean value is 12.18 m and the standard deviation of ΔSR is 19.36 m and its mean value is 3.43 m. Projected to the sea surface plane, the standard deviation of the total position difference between the AIS reports and the SAR-GMTI position is 22.87 m and its RMS (root-mean square) value is 40.93 m. The mean value of the position difference is 13.21 m.

Ship 22 in Table 7 is the only vessel in the SAR-GMTI scene that was not detected using either of the one or two channel detection models. This case was a small, 15 m, tug (20 dB SINR) that was slowly pulling a log boom near the shore line. Ship 22 is the weakest target in the data set and the detection failure suggest that the detection cut off for the selected SINR threshold lies somewhere between 20 dB and 22.4 dB (the next weakest target). Although the ship was not detected, its tow was.

A comparison of the SINR1 and SINR2 columns in Table 7 shows that the presence of two channels in the analysis generally results in a SINR increase (target detection margin increase) that can exceed 3 dB in some cases. Then SINR margin for the two aperture case increases with the radial speed of the target.

5   Summary and conclusions

This report captures and summarizes GMTI studies of ship targets performed at DRDC between 2003 and 2013 using experimental data acquired by the RADARSAT-2 GMTI Demonstration project between 2003 and 2010. Data acquired in airborne and space-based SAR GMTI measurements were used to identify required theoretical studies and to validate algorithms that were generated from these studies. Where appropriate, results from land target studies were applied to marine target analysis and algorithm modifications for marine target applications were identified and tested. The experimental data sets used in the DRDC studies employed either dedicated GPS receivers (for cooperating targets) or AIS transmissions (for non-cooperating ship targets) to provide direct motion measurements for comparison with motions deduced from GMTI analysis. Where AIS reports did not correspond to the SAR-GMTI observation time, the AIS data were interpolated when possible to provide best estimates of ship motion. Otherwise a dead reckoning approach using ship location, speed, heading and the AIS report time was used to estimate the ship location at the GMTI observation time. Estimation errors for ship speed, position, heading and size contain components from both the radar data analysis and from the reference data when interpolated AIS reports were used to provide target reference information. The reference error statistics are unknown and measurement standard deviations are nominally assigned to the radar measurements.

5.1   Range history estimation

Particular attention was paid to the development of SAR-GMTI range-history models that are applicable to image focusing and the extraction of ship motion data from multi-aperture SAR-GMTI radar data that include sea-motion acceleration terms for both airborne and space-based observation geometries. When the coherent observation time of the radar equals or exceeds a significant wave-period fraction for waves that are long enough to influence ship motion, it was shown that sea motion terms could be estimated from distributed ship return samples and that the sea motion model estimates could successfully be used to focus ship images in moderately disturbed seas. This approach requires up to 10 seconds of coherent observation time and applies to airborne SAR GMTI systems that have large oversampling ratios. Since the observation time is the critical parameter for sea motion modeling, a similar approach could be successfully applied to long-dwell, space-based spotlight radars. Ocean surface conditions that generate pitch and heave motions can be compensated in SAR-GMTI data but roll motion effects are more difficult to deal with. Sea motion extraction uses time-Doppler frequency decompositions of signal sample groups distributed over the ship length and the sea component of the ship motion is modeled as the dominant sinusoidal wave components. Although all ships flex in response to the shape of the sea surface, the GMTI measurement process used in this work was not sufficiently precise to estimate ship flexure and rigid-body ship models were used.

The coherent observation times for currently available space-based SAR-GMTI radars are too short to allow useful sea-motion estimates for ships from a single radar but the TerraSAR-X / TanDEM constellation, operated in GMTI mode, might provide some useful data. This has not been tested.

The tested range history algorithms can accommodate sea motion effects on ship measurements provided that the sea motion component is known or can be estimated for the ship target under consideration.

It was noted that the ratio between the radar platform and target speeds is important for the estimation of target velocity components that are parallel to the radar flight direction (along-track target velocity) and that airborne sensors have a significant advantage for these measurements.

SAR-GMTI measurements of ship motion require that the sea-surface coherence time exceeds the registered GMTI aperture time interval. The Convair-580 SAR GMTI system had an aperture time interval of 2 ms and the RADARSAT-2 four-aperture ¾ toggled transmit mode has a maximum aperture time interval of 0.75 ms. The aperture interval for both radars is significantly less than the 20 ms to 170 ms sea surface decorrelation time. Tests using channel subtraction (DPCA) clutter cancellation have shown that sea surface decorrelation is not an issue for the SAR-GMTI observations discussed in this report.

5.2   Moving target detection

The majority of the SAR-GMTI moving ship detection algorithms used in the DRDC studies are non-parametric in form and detect moving ships as ensembles of radar resolution cells whose signals exceed a moving target detection threshold that is specific to the detector employed. All moving target detectors generate moving target candidates whose validity needs to be verified by subsequent analysis.

5.2.1   DPCA detectors

DPCA detectors are linear and can be applied either before or after SAR focusing operations. These detectors have the property that the detection threshold is derived from the probability density function (PDF) of the residual background clutter after channel subtraction and that the signals which exceed the threshold are the differences between moving target responses seen by both channels. The detected signals have magnitudes that depend on the signal magnitude multiplied by the absolute value of the sine of 2π times the radial displacement of the target point over the aperture interval normalized to the radar wavelength. Moving target signals are attenuated as a function of their speed. When seen in the ATI magnitude- velocity plane, the threshold maps into the absolute value of the sine function, centred at the ATI directional ambiguity speed. Target points exceeding the threshold have a statistical spread due to the target to clutter ratio at the (motion-displaced) target point location. Very strong target returns have very small clutter contributions. When the radial velocity component of a ship is small or is close to the sampling ambiguity speed, the DPCA detector can split the ship into two detection clusters that apparently move in opposite GMTI directions. Where more than two GMTI channels are available, the available DPCA detectors have multiple GMTI baselines. The extra degrees of freedom provided by multiple GMTI baselines can be used to optimize detection for a certain speed (slow vs fast targets) and/or to combine the DPCA technique with other operations within more complex algorithms.

5.2.2 Rare-event detector

Rare-event detectors are based on non-linear signal operations and must be applied to focused SAR-GMTI images. The rare-event detector uses an empirical estimate of the ATI amplitude-phase PDF to separate the stationary scene from the moving target candidates. Since the ATI amplitude-phase PDF does not have an easily used analytical representation, the detection boundary is estimated from sample point density. Noting that the ATI phase is a simple function of the radial and tangential velocity components of the target point (the radial component is dominant) and that the detection boundary follows the shape of the phase-amplitude PDF, the detected target candidates will be bounded by a function that depends on both the amplitude and the velocity of the target point. The low-speed target splitting effect observed with the DPCA detector will not be present but the point scatter will depend on the target to clutter ratio. The nonlinearity of the ATI process will introduce cross modulation between the clutter and target terms which maps sea motion into the detection process. When more than two GMTI channels are available, the rare-event detector can be usefully employed following clutter suppression by channel subtraction.

The rare-event detector is a two-channel algorithm whose sensitivity to slowly moving targets increases with GMTI aperture separation. For more than two apertures, averaging over two aperture channel pairs can somewhat reduce the influence of system noise and estimates that are based on the largest aperture separation can increase the detector sensitivity to slowly moving targets.

As with the DPCA case, the rare-event detector operates at a sample level and represents a large ship as an ensemble of target detections. Because of its explicit dependence on target velocity, it can also generate target-candidate speed estimates but cannot separate the radial and tangential speed components.

The rare-event detector is free from any PDF assumptions. This is its significant advantage over the other approaches especially for scene statistics where the PDFG is unknown.

5.3 Covariance-matrix detectors

When the target-free inter-channel covariance matrix is assumed known (or estimated accurately enough on the bulk of data), it can be used to suppress the clutter so that it is effectively levelled down to the noise floor. Although the covariance matrix itself represents a non-linear (second order) statistics on the data samples, once it is assumed known it can be used as a linear operator on the registered GMTI channels. The inverse of the covariance matrix decorrelates the sum of the mean ATI clutter and noise in the sample covariance data. Any moving targets that may be present in the clutter covariance data will be affected depending on their radial speed. After clutter suppression moving target candidates can be matched against a set of steering vectors tuned to particular trial speeds. The largest output is compared to the detection threshold and the winning steering vector provides the estimate of the radial speed. This concept has been successfully applied in the image domain to detect ship cluster pixels. A more advanced approach that works in the Doppler domain has been applied in Section 4.7. Where the sea surface clutter plus noise signal is sufficiently large, the EDPCA covariance-based detection and estimation approach based on the SINR test statistic, performs very well for slowly moving weak targets.

Radar returns from ocean surfaces under calm wind conditions and large incidence angles are frequently too small to allow a robust estimate of the clutter covariance matrix. For these conditions, covariance matrix inversion is not useful. From the CMOD 5 discussions in section 2.3 and Figure 11 the low wind speed condition corresponds to wind speeds smaller than 2 m/s and the large incidence angle condition applies to incidence angles greater than 40°. For higher wind speeds and small enough incidence angles, Figure 10 shows that robust clutter covariance matrix estimation is possible and matrix inversion provides a viable tool for background suppressions and, via Eigen vector definition allows the use of moving target detectors such as that discussed in Section 2.5.1.3.

Discussions in Annex A.1 show that the clutter covariance matrix elements are spatial (ensemble) averages of channel correlation values at each point in the clutter averaging area. Wind field variability over the sea surface imposes the condition that the sea returns in the area used to estimate the clutter are statistically identical to the sea returns containing the ship targets.

5.4   Land masks

In principle, land masking is unnecessary for multi-aperture GMTI data since land returns can be cancelled as stationary targets. In practice, knowledge of land boundaries has a role in the suppression of land ambiguities in littoral zones. Shoreline knowledge is particularly valuable for the suppression of sampling ambiguities from large cross-section land-based structures whose radar signatures prevent full cancellation using DPCA techniques. The NOAA GSHHS shoreline data base was tested for land mask formation along the shoreline approaching the Strait of Gibraltar and bordering the Strait of Georgia. The data base allows a land mask to be built with reasonable accuracy most of the time but the mask edges often need to be adjusted along the coastline boundary to correct for small edge position errors in the data base and to remove coastal structures (such as piers and break-waters) that are not contained in the mask.

The land mask approach has been successfully used for the identification and removal of land target ambiguities. In maritime scenes containing a littoral zone the land mask approach has been used for Doppler estimation and channel balancing over land areas to avoid the effects of ocean surface motion and uncertainty due to low clutter-to-noise ratio.

5.5   Sampling ambiguity suppression

Automated sampling ambiguity algorithms have been tested in open ocean and in littoral zone environments in the Strait of Gibraltar data set and in the Strait of Georgia data set. No lost ship targets have been detected from AIS reports and sampling ambiguity features have been successfully removed.

The automated algorithms have been validated to the extent possible with the available data.

5.6　Target parameter estimation

Target parameter estimation algorithms have been tested using AIS reports as the reference data base. Results presented are based on the analysis of 49 ships in the Strait of Gibraltar data set and 23 ships in the Strait of Georgia data set.

5.6.1　Domain clustering

Radar returns from each ship were clustered into contiguous sample domains containing 25 sample points and GMTI parameter estimates were averaged over each domain. The domain averaging approach was particularly valuable for estimating the geographic positions of GMTI processed sample points and decreased the repositioning uncertainty by more than a factor of two.

5.6.2　Ship velocity estimation

GMTI estimates of the bulk ship motion yielded ship speed uncertainties of ± 0.25 m/s when compared to AIS reported ship speeds for large vessels processed using a DPCA detection algorithm and ±0.33 m/s for medium sized and small vessels processed with the EDPCA algorithm. The DPCA MDV was not reached for large ships that have a large maximum RCS (>50 dBm^2) but showed target splitting for a vessel whose radial velocity was 2.0 m/s. The EDPCA algorithm successfully measured vessel speeds down to 0.15 m/s for a vessel with 48.5 dB SINR but failed to detect or measure a 20 dB SINR vessel moving at 0.25 m/s (although the tow speed could be estimated for this case due to the large RCS of the tow).

5.6.3　Ship repositioning

Strait of Gibraltar ship images that were repositioned after GMTI processing had position uncertainties of ± 34 m when compared to the expected ship positions at the GMTI observation times. These ships were processed using classical DPCA detection and domain-based ATI speed estimation algorithms. The Strait of Georgia ship images had an RMS position difference between the AIS and SAR-GMTI positions of 40.9 m and a mean difference of 13.2 m. The AIS derived ship positions at the SAR-GMTI measurement time were estimated from AIS ship position, speed and heading reports for both data sets.

5.6.4　Ship heading

Ship headings were estimated by the sign of the GMTI ship velocity estimates and by fitting an ellipse to the cluster of ship domain positions after GMTI processing. The headings were estimated from the inclination of the major axis of the ellipse and were accurate to within ± 12.4° standard deviation with respect to the AIS reports.

5.6.5　Ship length

Ship lengths were computed from the major axis lengths of the fitted ellipses multiplied by an empirically determined scale factor of 1.379. Using the AIS-reported ship lengths as reference values, the result standard deviation was ± 34.5 m. When normalized to AIS-reported ship length, 92% of the length estimates were within 35% of the reported ship length and 75% of the length estimates were within 25% of the reported ship length. The ship- length estimates from GMTI-

repositioned ship samples was a factor of two better than those obtained from the GMTI detected sample points.

The variance of ellipse-based length estimates for SAR-GMTI detections was shown to be equivalent to the variance of length estimates based on the ship RCS, that is often used with SAR data. The ellipse-based estimates had less length bias than the RCS-based estimates.

The small (<30 m) vessels in the Strait of Georgia data sets showed no relationship between the ship length and the SINR. In the small data set available (13 vessels) the ship lengths varied from 11 m to 30 m and the ship SINR varied from 19.9 dB to 48.5 dB.

5.7   Double-bounce feature

SAR images of ships in moderately calm oceans frequently display an asymmetric side-lobe-like feature on the illuminated side of the ship target. GMTI analysis has identified this to be a radar double bounce return from the ship structure and the sea surface. The double-bounce feature was not observed for the ships in the Strait of Georgia data set.

References/Bibliography

[1] Vachon.P, New RADARSAT capabilities improve maritime surveillance, http://geos2.nurc.nato.int/mreal)conf/reports/pdf (accessed February 19, 2013).

[2] LCdr A. Samoluk, DND Project Polar Epsilon, www.oceanSAR2006.com/presentations/67.pdf (accessed February 19, 2013).

[3] Cervera, M.A. and Ginesi, A., On the performance analysis of a satellite-based AIS system, Proc 10th international workshop on signal processing for space communications, Oct. 6-8, 2008.

[4] Eiden, G. and Martensen, T., Vessel density mapping, Technical Note 4.1, DG MARE Service Contract MARE/2008/06/S12.517298, 2010.

[5] Vachon, P.W., English(R.A.,and Wolfe, J., Ship signatures in synthetic aperture radar imagery, Proc IGARSS'07, Barcelona, 2007.

[6] Panagopoulos, G., Christoulas, G. and Anastassopoulos, V., Ship identification using signatures from cross-polarized images, Proc. 4th WISEAS International Conference on Remote Sensing, 2008.

[7] Marino, A., Walker, N. and Woodhouse, I., Ship detection using SAR polarimetry, the development of a new algorithm designed to exploit new satellite SAR capabilities for maritime surveillance, Proc SeaSAR'10, Frascati, 2010.

[8] Chiu, S. and Gierull, C., Multi-channel receiver concepts for RADARSAT-2 ground moving target indication, Proc. EUSAR, Desden, 2006.

[9] Chiu, S. and Dragosevic, M.V., Moving target indication via RADARSAT-2 multichannel synthetic aperture radar processing, EURASIP Journal on Advances in Signal Processing, V 2010.

[10] Waters, J.K., Mayer, R.H. and Kreibel, D.L., Shipping trends analysis, Department of Naval Architecture, U.S. Naval Academy, Milestone report 12 for U.S Army Corps of Engineers study: Impacts of navigation trends on Channel usage and design, September 2000.

[11] Guide for Safehull-dynamic loading approach for Vessels, American Bureau of Shipping, December 2006.

[12] Guidelines for ultra large container ships, Bureau Veritas, Marine Division, Guidance note NI 558 DT R00E, October 2010.

[13] Drummen, I., Challenging winds and waves: Strutural reality @ scale, MARIN presentation, httpc://afdelingen.kevineria.net/media.afdeligen/DOM100000166 (Accessed February27, 2013).

[14] Shoals, P.G. and Brunner, D.E. Ship Flexure measurement, Naval Ship Weapon System Engineering station, Port Huene Ca., report NSWSES-TR-284, 1973.

[15] Drummen, I., Wu, MK and Moan, T., Experimental and numerical studies of container ship responses in severe head seas, Marine Structures, 2008.

[16] Huang, J. and Peake, W.H., Electromagnetic scattering from a ship at sea, Ohio Stae University, ElectroScience Laboratory, Final report 710660-2, 1978.

[17] Gras, V. and Lamy, M., Study of the influence of the sea surface of the observability of a man-made target in SAR images, Proc. Oceans 2005, V 2, P. 1141-1146, 2005.

[18] Livingstone, C.E. and Dragosevic, M.V.,SAR-GMTI phasor sums and their impact on target velocity measurements, DRDC Ottawa TR 2011-177.

[19] Monaldo, F.M and Thompson, D.R., Applicability of conventional scatterometer model functions to high resolution wind retrievals: the effect of spatial averaging, Proc. OceanSAR2006, St Johns.

[20] Vachon, P. and Wolfe, J., C-band cross-polarization wind speed retrieval, IEEE Geoscience and Remote Sensing Letters V. 8, No. 3,P 456 to 459, 2011.

[21] Beal, R.C. Spaceborne synthetic aperture radar for Oceanography, Johns Hopkins University Press, 1981.

[22] Barale, v., Gower, J.F.R and Albertotanza, Oceanography from space revisited, Springer Science and Business Media, B.V., Dordrecht, Heidelberg, London, New York, 2010.

[23] Komen, G.J., Hasselman, S. and Hasselmann, K., On the existence of a fully developed wind-sea spectrum, J. Phusical Oceanography, V. 14, P. 1271-1285, 1984.

[24] Vachon, P.W. Synthetic aperture radar imaging of the ocean surface: Experiments with simulated and actual SAR imagery, University of British Columbia PhD thesis, 1987.

[25] Hersbach, H., CMOD5.N: A C-band geophysical model function for equivalent neutral wind, European Centre for Medium Range Weather Forecasts Technical Memorandum 554, 2008.

[26] Said, F. and Johnsen, H., Sea surface wind retrieval using both normalized radar cross section and polarization residual Doppler frequency from TerraSAR-X data, Proc. IGARSS'12, P2063-2066, 2012 .

[27] Hasselman, K., Barnett, T.P., Bourns, E., Carlson, H., Cartwright, D.E., Enke, K., Gunapp, H., Hasselman, D.E., Kruseman, P., Meerburg, A., Muller, P., Others, D.J., Tichter, K., Sell, W. and Walden, H., Measurements of wind-wave growth and swell decay during the Joint North Sea Wave Project (JONSWAP), Deutsches Hydorgraphisches Institut,, Hamberg, report A8, N0. 12, 1973.

[28] Janssen, P.A.E.M., Wave-induced stress and drag of air flow over sea waves, Journal of Physical Oceanography, V 19, P. 745-754, 1989.

[29] Hasselmann, K., Raney, R.K., Plant, W.J., Alpers, W. Shuchman, R.A., Lyzenga, D. R., Rufenach, C,L. and Tucker, M.J., Theory of SAR ocean wave imaging, J. Geophysical Research, V 90 C3, P. 4659-4686, 1985.

[30] Curlander, J.C. and McDonough, R.N., Synthetic Aperture Radar: Systems and signal processing, John Wiley & Sons, Inc., 1991.

[31] Franceschetti, G. and Lanari, R. Synthetic Aperture Radar Processing, CRC Press, 1999.

[32] Cumming, I.G. and Wong, F.H., Digital processing of synthetic aperture radar data: algorithms and implementation, Artech House Inc., Boston, London, 2005.

[33] Livingstone, C.E. and Thompson, A.A., The moving object detection experiment on RADARSAT-2, Canadian Journal of Remote Sensing, V30, No. 3, P355-368, 2004.

[34] Raney, R.K., Synthetic aperture imaging radar and moving targets, IEEE Trans. AES, VAES-7, No. 3, 1971.

[35] Sharma, J.J. and Collins, M.J., Simulation of SAR signals from moving vehicles: Focussing accelerating ground moving targets, Proc EUSAR 2004 Ulm May 25-27, 2004.

[36] Sharma, J.J., Gierull, C.H. and Collins, M.J., Compensating the effects of target acceleration in dual channel GMTI, IEE Proc. Radar, Sonar and Navigation, V. 153, P53-62, 2006.

[37] Chiu,S. and Dragosevic, M., Equations of motion of a ground moving target for a multi-channel spaceborne SAR, DRDC TM 2008-326, March 2009.

[38] Dragosevic, M., Henschel, M. and Livingstone, C., An adaptive technique for estimating ship motion in SAR data, Proc. EURAD,07, Munich, October 8-12, 2007.

[39] Meadows, P. and Wright, P., ASAR APP and APM image quality, Proc. Envisat validation Workshop, Frascotti, ESA SP 531, 2003.

[40] Livingstone, C. and Sikaneta, I., Focused moving targets / terrain imaged with moving target matched filters; A tutorial, DRDC TM-2004-160, 2004.

[41] Chiu, S., Clutter effects on ground moving target velocity estimation with SAR along-track interferometry, Proc. IGARSS'03, Toulouse, 2003.

[42] Chiu, S., Gierull, C.H. and Durak, A., Clutter effects on ground-moving target interferometric phase, Proc. IGARSS'04, Seoul, 2005.

[43] Gierull, C.H., Digital channel balancing of along-track interferometric SAR data, DRDC Ottawa TM-2003-024, 2003.

[44] Gierull, C.H., Sikaneta, I.C. and Livingstone, C.E., Two-aperture SAR channel calibration and GMTI for marine applications, Proc. 8th Annual International Conference for Marine and Coastal Environments, Halifax, 2005.

[45] Gierull, C., Unbiased coherence estimator for SAR interferometry with application to moving target detection, DREO TR-2001-045, 2001.

[46] Gierull, C., Moving target detection with along-track interferometry: a theoretical analysis, DREO TR-2002-084, 2002.

[47] Sikaneta, I., Gierull, C. and Chouinard, Y., Metrics for SAR-GMTI based on decomposition of the sample covariance matrix, Australian International Conference on Radar, 2003.

[48] Chiu, S., A constant false alarm rate (CFAR) detector for RADARSAT-2 along track interferometry, Canadian J. Remote Sensing, V 31, No. 1, P. 73-84, 2005.

[49] Sikaneta, I., Detection of ground moving targets with synthetic aperture radar, University of Ottawa, PhD. Thesis, 2005.

[50] Liu, C. and Gierull, C., Using ambiguities to aid in moving target detection in PolSAR images, Proc. EUSAR 2006, Dresdan 2006.

[51] Gierull, C.H. and Sikaneta, I., Raw data based two-aperture SAR ground moving target indication, Proc. IGARSS'03, Toulouse, 2003.

[52] Henschel, M., Dragosevic, M., and Livingstone, C., Characterization of vessel heave and horizontal velocities with airborne SAR, Proc. IEEE Radar Conference, Boston, April 17-20, 2007.

[53] Gierull, C. and Sikaneta, I., Ground moving target parameter estimation, Proc. EUSAR 2004, Ulm, 2004.

[54] Chiu, S. and Sikaneta, I., Applying fractional Fourier transform to two-channel SAR-GMTI, Proc. EUSAR 2004, Ulm 2004.

[55] Chiu, S., Two-channel SAR-GMTI via fractional Fourier transform, DRDC TN-2004-160, 2004.

[56] Jao, J. Amplitude distribution of composite terrain radar clutter and the K-Distribution Antennas and Propagation, IEEE Transactions on, 1984, 32, 1049-1062.

[57] Yueh, S. H.; Kong, J. A.; Jao, J. K.; Shin, R. T. & Novak, L. M. K--distribution and Polarimetric Terrain Radar Clutter Journal of Electromagnetics Waves and Applications, 1989, 3, 747-768.

[58] Ward, K. D.; Tough, R. J. A. & Watts, S. Sea Clutter: Scattering, the K Distribution and Radar Performance IET, 2006, 20.

[59] Chiu, S. and Livingstone, C., A comparison of displaced phase center antenna and along track interferometry techniques for RADARSAT-2 ground moving target indication, Canadian journal of Remote Sensing, V. 31, No. 1, P 37-51, 2005.

[60] Romeiser, R., Schwabisch, M., Schulz-Stellenfleth, J., Thompson, D.R., Seigmund, R., Niedermeier, A., Alpers, W. and Lehner, S., Study on concepts for radar interferometry from satellites for Ocean (and land) application: KoRIOLiS, http://www.ifn,uni-hamberg.de/~Romeiser/koriolis.htm, 2002, accessed March 11, 2013.

[61] Frasier, S.J. and Camps, A.J., Dual-beam interferometry for ocean surface current vector mapping, IEEE trans. Geoscience and Remote Sensing, V. 39, No. 2, P. 401-414, 2001.

[62] Sikaneta, I. and Gierull, C., Ground moving target detection for along-track interferometric SAR data, Proc. IEEE Aerospace Conference, 2004.

[63] Dragosevic, M., Burwash, W. and Chiu, S., Detection and estimation with RADARSAT-2 moving object detection experiment modes, IEEE Trans. On Geoscience and Remote Sensing, Vol. 50, No 9, pp. 3527-3543, 2012.

[64] Cerruti-Maori, D. and Sikaneta, I,, Optimum GMTI processing for space-based SAT/GMTI systems: Theoretical derivation, Proc. EUSAR, 2010, Aachen, 2010.

[65] Cerutti-Maori, D. and Sikaneta, I., Optimum GMTI processing for space-based SAT/GMTI systems: Simulation results, Proc. EUSAR, 2010, Aachen, 2010.

[66] Cerrutti-Maori, D., Sikaneta, I. and Gierull, C., RADARSAT MODEX 1 and MODEX 2,modes: Optimum signal processing and theoretical investigation of GMTI performance, DRDC Ottawa TR-2010-270, 2010.

[67] Livingstone, C.E. and Beaulne, P., Modelling RADARSAT-2 Doppler Centroids for Marine applications, DRDC Ottawa TM 2012-097, 2012.

[68] Dragosevic, M., Vachon, P., Estimation of ship radial speed by adaptive processing of RADARSAT-1 fine mode data, IEEE Geoscience and Remote Sensing Letters, Vol. 5, No. 4, pp. 678-682, 2008.

[69] Dragoevic, M., Henschel, M. and Livingstone, C., An approach to ship motion estimation with dual-receive antenna SAR, IEEE Radar Conference, Rome, Italy, 2008.

[70] Tunaley, J., The estimation of ship velocity from SAR imagery, Proc. IGARSS, pp. 191-193, 2003.

[71] Eldhuset, K., An automatic ship and ship wake detection system for spaceborne SAR images in coastal regions, IEEE Trans. On Geoscience and Remote Sensing, Vol. 34, No. 4, pp. 1010-1019, 1996.

[72] Dragosevic, M.V. and Chiu, S., Extending airborne SAR-ATI algorithms to the RADARSAT-2 Moving Object Detection Experiment (MODEX), Proc. IGARSS'08, Boston, 2008.

[73] Dragosevic, M.V. and Chiu, S., Space-based motion estimators: Evaluation with the first RADARSAT-2 MODEX data, IEEE Geoscience and Remote Sensing Letters, V. 6, No, 3, P438-442, 2009.

[74] Gierull, C.H. and Sikaneta, I., Ground moving target estimation for two-channel SAR, Proc. EUSAR''04, Ulm, 2004.

[75] Rieck,W., Time-frequency distribution of multi-channel SAR data for focussing moving targets, Proc. IEE Radar'97, P. 224-228, 1997.

[76] Dragosevic, M., Autofocusing of moving objects in SAR data based on adaptive notch filtering, IEEE Transactions on Aerospace and Electronic Systems, Vol. 44, no 1, pp.384-391, 2008.

[77] Livingstone, C.E., Gray, A.L., Hawkins, R.K., Vachon, P., Lukowski, T.I. and Lalonde, M., The CCRS airborne SAR systems: radar for remote sensing research, Canadian Journal of Remote Sensing, V21, No. 4, P 468-491, 1995.

[78] R. Schmidt, "Multiple emitter location and signal parameter estimation", IEEE trans. Antennas and Propagation, vol. 34, pp.276-280, 1986.

[79] Dragosevic, M. and Livingstone, C. ,"Demonstration of RADARSAT-2 Moving Object Detection Experiment (MODEX) capabilities for maritime surveillance", International Radar Symposium, Hamburg, Germany, 2009.

[80] Dragosevic, M., Chu, S. and Burwash, W., On ship signatures in multi-aperture SAR images, IET Radar Conference, Glasgow, 2012.

[81] Beaulne, P.D. and Livingstone, C.E., Evaluation of RADARSAT-2 Yaw steering for SMTI applications, Proc EuSAR 2010.

[82] G. Margarit, J.J. Mallorqui, J. Fortuny-Guasch, and C. Lopez-Martinez. Phenomenological vessel scattering study based on simulated inverse SAR imagery. IEEE Transactions on Geoscience and Remote Sensing, Vol. 47, no. 4, P 1212 –1223, April 2009.

[83] Sikaneta, I. C. & Gierull, C. H. Adaptive CFAR for Space-Based Multichannel SAR-GMTI, IEEE Transactions on Geoscience and Remote Sensing, 2012, P 1 -10.

[84] Perry. R.P., Dipietro, R.C. and Fante, R.L., SAR imaging of moving targets, IEEE Transactions on Aerospace and Electronic Systems, V 35, No, 1, P. 188-200, 1999.

[85] Doerry, A.W., Ship dynamics for maritime ISAR imaging, SANDIA report, SAND2008-1020, 2008.

Annex A   Properties of the sea surface GMTI covariance matrix

A.1   Covariance matrix estimation

Starting from the definition of a covariance matrix for an N channel GMTI system where the channels are balanced in amplitude and phase and are registered to each other we can define a complex signal vector for each data sample at position *(x,y)* as

$$S = \begin{bmatrix} s_1 \\ s_2 \\ \\ \\ s_N \end{bmatrix}_{(x,y)} \tag{A.1}$$

Where s_1, s_2,....s_N represent signals from the *N* channels. For an ocean surface area *A* that is sufficiently large that the statistics of $s_k^* s_m$, for channels *k* and *m* are stationary (* represents the complex conjugate), the function

$$\mathcal{R}_A = cov(S)_A = \langle [(s_k - < s_k >)^*(s_m - < s_m >)]_{N,N} \rangle_A \tag{A.2}$$

defines the elements of the *N x N* covariance matrix.. In equation A.2, $1 \leq k \leq N$, $1 \leq m \leq N$ and < > is the expectation operator defined over area *A*. Since the radar channels are balanced and registered, the channel mean signals <s$_k$> and <s$_m$> are zero and equation (A.2) defines the covariance matrix

$$cov(S) = [< s_k^* s_m >]_{NxN} \tag{A.3}$$

in which $< s_k^* s_m >$ is the power in channel k for k=m and is the mean ATI signal, $< s_k^* s_m > = a_{k,m} e^{j\varphi_{k,m}}$, for channels *k* and *m* when $k \neq m$ where $a_{k,m}$ is the mean ATI amplitude over *A* and $\varphi_{k,m}$ is the mean ocean ATI phase over area *A*. For land surfaces, $\varphi_{k,m}$ is nominally zero since coherent motion over large areas are seldom present. For the sea surface, where wind drifts and current motion can persist over large areas, $\varphi_{k,m}$ provides a measure of large-area coherent motion in the radial direction of the radar.

To extract the key points, consider a two aperture system where

$$cov\left(\begin{bmatrix} s_1 \\ s_2 \end{bmatrix}\right) = \begin{bmatrix} < s_1^* s_1 > & < s_1^* s_2 > \\ < s_2^* s_1 > & < s_2^* s_2 > \end{bmatrix}. \tag{A.4}$$

For a radar with matched antenna patterns and balanced channels we can write

$$\sigma^2 = < s_1^* s_1 > = < s_2^* s_2 > = \sqrt{< s_1^* s_1 > < s_2^* s_2 >} \tag{A.5}$$

where σ^2 is the mean channel power. In the real world, the radiation patterns of the GMTI array antenna apertures are slightly asymmetric in the flight direction because of boundary condition mismatches at the ends of the aperture arrays. The sequence free-space | array $\neq$ the sequence array | free-space. The discrepancies are usually small enough to ignore and we will do so.

Extracting the mean power term and noting that $\frac{<s_1^*s_2>}{\sqrt{<s_1^*s_1><s_2^*s_2>}} = \rho e^{j\varphi_{1,2}}$, equation A.4 becomes the standard form of the two channel covariance matrix

$$\mathcal{R}_2 = cov\left(\begin{bmatrix} s_1 \\ s_2 \end{bmatrix}\right) = \sigma^2 \begin{bmatrix} 1 & \rho e^{j\varphi_{1,2}} \\ \rho e^{-j\varphi_{1,2}} & 1 \end{bmatrix} \tag{A.6}$$

where ρ is the coherence of channel 2 with respect to channel 1 and $\varphi_{1,.2}$ is the two aperture mean ATI phase of area A. Note that the two off diagonal elements are complex conjugates of each other. The coherence ρ is primarily a function of the radar clutter to noise ratio and has been observed to exceed 0.94 for strong sea clutter seen in VV polarization.

The two channel inverse covariance matrix is given by

$$\mathcal{R}_2^{-1} = \frac{1}{\sigma^2(1-\rho^2)} \begin{bmatrix} 1 & -\rho e^{j\varphi_{1,2}} \\ -\rho e^{-j\varphi_{1,2}} & 1 \end{bmatrix}. \tag{A.7}$$

Proceeding to the four channel GMTI case and expressing the covariance matrix estimate in its primitive form we see

$$\mathcal{R}_4 = \begin{bmatrix} <s_1^*s_1> & <s_1^*s_2> & <s_1^*s_3> & <s_1^*s_4> \\ <s_2^*s_1> & <s_2^*s_2> & <s_2^*s_3> & <s_2^*s_4> \\ <s_3^*s_1> & <s_3^*s_2> & <s_3^*s_3> & <s_3^*s_4> \\ <s_4^*s_1> & <s_4^*s_2> & <s_4^*s_3> & <s_4^*s_4> \end{bmatrix}. \tag{A.8}$$

If the radar antenna is designed with four equal GMTI apertures spaced by phase center distance d in the flight direction, equation (A.8) has the following properties:

- The diagonal terms contain the mean power in each channel and are normally equal.

- The lower triangular matrix is the complex conjugate of the upper triangular matrix.

- The diagonal terms $<s_1^*s_2>, <s_2^*s_3> \ and \ <s_3^*s_4>$ represent the mean ATI response of A when the channel aperture separation is d.

- The diagonal terms $<s_1^*s_3> \ and \ <s_2^*s_4>$ represent the mean ATI response of A when the channel aperture separation is $2d$.

- The upper left term $<s_1^*s_4>$ represents the mean ATI response of A when the channel aperture separation is $3d$.

Since all terms represent a mean response to the random and dynamic sea surface the will be some statistical variability between one area and another, and when wind drift or ocean current effects are present, the phase terms may differ consistently one area to another.

Annex B   A DPCA operator for multi-channel signal vectors

B.1   Derivation

First, the projection matrix is defined as:

$$\mathbf{P}^{\perp} = \mathbf{I} - \frac{1}{N}\mathbf{u}\mathbf{u}^{\mathbf{H}} \tag{B.1}$$

Where $\mathbf{I}$ is the unity matrix and $\mathbf{u}$ is the vector of unit elements. As any projection matrix, $\mathbf{P}^{\perp}$ is idempotent and this property is shown below:

$$\mathbf{P}^{\perp}\mathbf{P}^{\perp} = \left(\mathbf{I} - \frac{1}{N}\mathbf{u}\mathbf{u}^{\mathbf{H}}\right)\left(\mathbf{I} - \frac{1}{N}\mathbf{u}\mathbf{u}^{\mathbf{H}}\right) = \mathbf{I} - \frac{1}{N}\mathbf{u}\mathbf{u}^{\mathbf{H}} - \frac{1}{N}\mathbf{u}\mathbf{u}^{\mathbf{H}} + \frac{1}{N^2}\mathbf{u}\mathbf{u}^{\mathbf{H}}\mathbf{u}\mathbf{u}^{\mathbf{H}} =.$$

$$\mathbf{I} - \frac{1}{N}\mathbf{u}\mathbf{u}^{\mathbf{H}} - \frac{1}{N}\mathbf{u}\mathbf{u}^{\mathbf{H}} + \frac{1}{N}\mathbf{u}\mathbf{u}^{\mathbf{H}} = \mathbf{I} - \frac{1}{N}\mathbf{u}\mathbf{u}^{\mathbf{H}} = \mathbf{P}^{\perp} \tag{B.2}$$

Another obvious property of the projection matrix is:

$$(\mathbf{P}^{\perp})^{H} = \mathbf{P}^{\perp} \tag{B.3}$$

Next, it can be shown that this projection matrix is an operator that removes the mean element value from a vector of samples:

$$\mathbf{P}^{\perp}\mathbf{S} = \mathbf{S} - \frac{1}{N}\mathbf{u}\mathbf{u}^{\mathbf{H}}\mathbf{S} = \mathbf{S} - \mathbf{u}\left(\frac{1}{N}\mathbf{u}^{\mathbf{H}}\mathbf{S}\right) = \begin{bmatrix} s_1 \\ \vdots \\ s_N \end{bmatrix} - \begin{bmatrix} 1 \\ 1 \\ 1 \end{bmatrix}\frac{1}{N}\Sigma_1^N s_p = \begin{bmatrix} s_1 - \bar{s} \\ \vdots \\ s_N - \bar{s} \end{bmatrix} \tag{B.4}$$

where the mean sample value is defined as:

$$\bar{s} = \frac{1}{N}\Sigma_1^N s_p \tag{B.5}$$

Using the above properties, the following quadratic form can be expanded as follows:

$$\mathbf{S}^{H}\mathbf{P}^{\perp}\mathbf{S} = \mathbf{S}^{H}\mathbf{P}^{\perp}\mathbf{P}^{\perp}\mathbf{S} = (\mathbf{P}^{\perp}\mathbf{S})^{H}\mathbf{P}^{\perp}\mathbf{S} = \begin{bmatrix} s_1 - \bar{s} \\ \vdots \\ s_N - \bar{s} \end{bmatrix}^{H}\begin{bmatrix} s_1 - \bar{s} \\ \vdots \\ s_N - \bar{s} \end{bmatrix} = \left|\Sigma_1^N(s_p - \bar{s})\right|^2 \tag{B.6}$$

This result can be interpreted as the Euclidean norm of the projected sample vector. It should be noted that the projected sample vector has $N - 1$ degrees of freedom although it has N elements (they are no longer independent).

For 2 channels, the result reads

$$\mathbf{S}^{H}\mathbf{P}^{\perp}\mathbf{S} = \left|\frac{1}{2}(s_1 - s_2)\right|^2 + \left|\frac{1}{2}(s_2 - s_1)\right|^2 \tag{B.7}$$

Which can be recognized as the regular DPCA criterion.

For four channels, the result becomes

$$\mathbf{S}^H \mathbf{P}^\perp \mathbf{S} = \left| \frac{1}{4}(3s_1 - s_2 - s_3 - s_4) \right|^2 + \left| \frac{1}{4}(3s_2 - s_1 - s_3 - s_4) \right|^2 +.$$

$$\left| \frac{1}{4}(3s_3 - s_1 - s_2 - s_4) \right|^2 + \left| \frac{1}{4}(3s_4 - s_1 - s_2 - s_3) \right|^2 \tag{B.8}$$

This criterion can be taken as one of many possible generalizations of the DPCA criterion:

$$T_{\mathrm{DPCA}} = \mathbf{S}(x,y)^H \mathbf{P}^\perp \mathbf{S}(x,y) = \sum |s_p(x,y) - \bar{s}(x,y)|^2 \tag{B.9}$$

B.2   Proof

The last identity can be proven in a more direct way.

First, the left hand side is expanded:

$$\mathbf{S}^H \mathbf{P}^\perp \mathbf{S} = \mathbf{S}^H \left(\mathbf{I} - \frac{1}{N} \mathbf{u}\mathbf{u}^H \right) \mathbf{S} = [s_1^* \quad \cdots \quad s_N^*] \begin{bmatrix} s_1 - \bar{s} \\ \vdots \\ s_N - \bar{s} \end{bmatrix} = \sum_{p=1}^{N} s_p^* (s_p - \bar{s}) =.$$

$$\sum_{p=1}^{N} s_p^* s_p - \frac{1}{N} \sum_{p=1}^{N} \sum_{q=1}^{N} s_p^* s_q \tag{B.10}$$

Next, the right hand side is expanded:

$$\sum_{p=1}^{N} \left((s_p - \bar{s})^* (s_p - \bar{s}) \right) = \sum_{p=1}^{N} \left(\left(s_p^* - \frac{1}{N}\sum_{q=1}^{N} s_q^* \right) \left(s_p - \frac{1}{N}\sum_{r=1}^{N} s_r \right) \right) =$$

$$\sum_{p=1}^{N} s_p^* s_p - \frac{1}{N} \sum_{p=1}^{N} \sum_{r=1}^{N} s_p^* s_r - \frac{1}{N} \sum_{p=1}^{N} \sum_{q=1}^{N} s_q^* s_p + \frac{1}{N^2} \sum_{p=1}^{N} \sum_{q=1}^{N} \sum_{r=1}^{N} s_q^* s_r =$$

$$\sum_{p=1}^{N} s_p^* s_p - \frac{1}{N} \sum_{p=1}^{N} \sum_{r=1}^{N} s_p^* s_r - \frac{1}{N} \sum_{p=1}^{N} \sum_{q=1}^{N} s_q^* s_p + \frac{1}{N} \sum_{p=1}^{N} \sum_{r=1}^{N} s_q^* s_r =.$$

$$\sum_{p=1}^{N} s_p^* s_p - \frac{1}{N} \sum_{p=1}^{N} \sum_{q=1}^{N} s_p^* s_q \tag{B.11}$$

Therefore, the two expressions for T_{DPCA} are equal.

List of symbols/abbreviations/acronyms/initialisms

3D	Three Dimensional
AIS	Automatic Information System
ATI	Along-Track Interferometry
CFAR	Constant False Alarm Rate
CNR	Clutter to Noise Ratio
DC	Doppler Centroid
DND	Department of National Defence
DPCA	Displaced Phase Center Antenna
DRDC	Defence Research and Development Canada
DSTKIM	Director Science and Technology Knowledge and Information Management
EC	Environment Canada
ECEF	Earth-Centered, Earth-Fixed
EDPCA	Extended Displaced Phase Center Antenna
EEZ	Exclusive Economic Zone
ESA	European Space Agency
FM	Frequency Modulation
GHz	Giga-Hertz
GMTI	Ground Moving Target Indication
GPS	Global Positioning System
GSHHS	Global Self-consistent, Hierarchical, High-resolution Shoreline
InSAR	Interferometric Syntheic Aperture Radar
INS	Inertial Navigation System
ISTAP	Integrated Space-Time Adaptive Processing
JONSWAP	Joint North Atlantic Sea Wave Project
MDV	Minimum Detectable Velocity
MODEX	Moving Object Detection Experiment
MSSR	Maritime Satellite Surveillance Radar
PDF	Probability Density Function
PRF	Pulse Repetition Frequency
PRF/V	Pulse repetition Frequency to Velocity ratio

RCM	RADARSAT Constellation Mission
RCS	Radar Cross Section
RMS	Root Mean Square
SAR	Synthetic Aperture Radar
ScanSAR	Burst-mode wide-swath SAR
SCNR	Signal to Clutter plus Noise Ratio
SINR	Signal to Interference plus Noise Ratio
SMTI	Surface Moving Target Indication
WV	Wigner-Ville
TFR	Time-Frequency Representation

	DOCUMENT CONTROL DATA		
	(Security markings for the title, abstract and indexing annotation must be entered when the document is Classified or Designated)		

1.	ORIGINATOR (The name and address of the organization preparing the document. Organizations for whom the document was prepared, e.g., Centre sponsoring a contractor's report, or tasking agency, are entered in Section 8.) Defence Research and Development Canada – Ottawa 3701 Carling Avenue Ottawa, Ontario K1A 0Z4	2a.	SECURITY MARKING (Overall security marking of the document including special supplemental markings if applicable.) UNCLASSIFIED
		2b.	CONTROLLED GOODS (NON-CONTROLLED GOODS) DMC A REVIEW: GCEC APRIL 2011

3.	TITLE (The complete document title as indicated on the title page. Its classification should be indicated by the appropriate abbreviation (S, C or U) in parentheses after the title.) Ship detection and measurement of ship motion by multi-aperture Synthetic Aperture Radar

4.	AUTHORS (last name, followed by initials – ranks, titles, etc., not to be used) Livingstone, Chuck; Dragosevic, Marina; Chu, Shen; Sikaneta, Ishuwa

5.	DATE OF PUBLICATION (Month and year of publication of document.) June 2014	6a.	NO. OF PAGES (Total containing information, including Annexes, Appendices, etc.) 172	6b.	NO. OF REFS (Total cited in document.) 85

7.	DESCRIPTIVE NOTES (The category of the document, e.g., technical report, technical note or memorandum. If appropriate, enter the type of report, e.g., interim, progress, summary, annual or final. Give the inclusive dates when a specific reporting period is covered.) Scientific Report

8.	SPONSORING ACTIVITY (The name of the department project office or laboratory sponsoring the research and development – include address.) Defence Research and Development Canada – Ottawa 3701 Carling Avenue Ottawa, Ontario K1A 0Z4

9a.	PROJECT OR GRANT NO. (If appropriate, the applicable research and development project or grant number under which the document was written. Please specify whether project or grant.)	9b.	CONTRACT NO. (If appropriate, the applicable number under which the document was written.)

10a.	ORIGINATOR'S DOCUMENT NUMBER (The official document number by which the document is identified by the originating activity. This number must be unique to this document.) DRDC-RDDC-2014-R17	10b.	OTHER DOCUMENT NO(s). (Any other numbers which may be assigned this document either by the originator or by the sponsor.)

11.	DOCUMENT AVAILABILITY (Any limitations on further dissemination of the document, other than those imposed by security classification.) Unlimited

12.	DOCUMENT ANNOUNCEMENT (Any limitation to the bibliographic announcement of this document. This will normally correspond to the Document Availability (11). However, where further distribution (beyond the audience specified in (11) is possible, a wider announcement audience may be selected.)) Unlimited

13. ABSTRACT (A brief and factual summary of the document. It may also appear elsewhere in the body of the document itself. It is highly desirable that the abstract of classified documents be unclassified. Each paragraph of the abstract shall begin with an indication of the security classification of the information in the paragraph (unless the document itself is unclassified) represented as (S), (C), (R), or (U). It is not necessary to include here abstracts in both official languages unless the text is bilingual.)

SAR (Synthetic Aperture Radar) GMTI (Ground Moving Target Indication) studies of ship signatures over a ten year period have developed an adaptive approach to the creation of ensembles of adaptive range-history models that characterize ship motion, ship length and ship heading from multi-aperture airborne and space-based radar measurements. The ships being detected and measured are assumed to be rigid bodies that move in response to propulsion and sea motion forces. Non-parametric moving target detection and motion estimation metrics are applied to radar returns from ship targets to represent each observed ship as an ensemble of spatially clustered moving targets whose motions, clustered into domains over the ship target area, estimated metrics are fed back to range-history models to improve the SAR focusing of the ship and to improve the motion estimation accuracy. DPCA (Displaced Phase Center Antenna) moving-target detection algorithms were used to generate lists of moving-target candidate points from two and four aperture SAR-GMTI scenes and the signal data corresponding to these points were analyzed to cancel sampling ambiguities from ships and littoral zone land targets prior to target motion estimation for each sample point. At the end of the estimation process target samples were clustered to extract the ensemble (bulk) properties of the ship target. When highly over-sampled GMTI data are acquired from airborne radars, coherent processing intervals that correspond to ocean wave periods that influence ship motion are obtained and ocean motion estimates can be extracted from the ship data using time-frequency analysis. The incorporation of the ocean motion estimates into the range history set that represents the ship allows fine SAR focussing of the ship image. An example is shown for a 167 m ship transiting off the coast of Newfoundland. The coherent processing interval for space-based SAR-GMTI data is too short for use in sea motion estimation, but the large platform velocity of space radars reduces the SAR sensitivity to sea motion and the sea motion effects on SAR focusing are not too severe for moderate sea states. SAR-GMTI results from 49 ships transiting the Strait of Gibraltar and from 23 ships in the Strait of Georgia used AIS (Automated Information System) reports to validate SAR-GMTI measurements made from RADARSAT-2 data. Results showed that the SAR-GMTI measurements can estimate ship speed to within $\pm$ 0.25 m/s, can estimate ship heading to within $\pm$ 12.4°, can estimate ship length to within 34.5 m ($\pm$ 35% of reported ship length) and can estimate ship position to within 37 m at one standard deviation.

Des études en matière de SAR-GMTI (radar à synthèse d'ouverture et indicateur de cible terrestre mobile) menées pendant dix ans sur les signatures de navires ont permis l'élaboration d'une méthode adaptative de création d'ensembles de modèles adaptatifs en fonction de l'historique de la distance, ensembles qui caractérisent le mouvement, la longueur et le cap d'un navire à partir de mesures relevées par radars spatiaux et aéroportés à ouverture multiple. Les navires détectés et mesurés sont considérés comme des corps rigides se déplaçant en fonction des forces de propulsion et du mouvement de la mer. Nous avons appliqué des mesures d'estimation du mouvement et de détection de cibles mobiles non paramétriques aux échos radar de navires afin de représenter chaque navire observé comme un ensemble de cibles mobiles spatialement regroupées dont les mesures estimées du mouvement, regroupées par domaines dans la zone des cibles, sont retransmises aux modèles en fonction de l'historique de la distance pour améliorer la focalisation du SAR sur le navire et l'exactitude de l'estimation du mouvement. Nous avons utilisé des algorithmes de détection de cibles mobiles par antenne à centre de phase déplacé (Displaced Phase Center Antenna – DPCA) pour générer des listes de points s candidats de cibles mobiles à partir de scènes SAR-GMTI à deux et à quatre ouvertures,

puis nous avons analysé les données de signaux correspondant à ces points afin d'éliminer toute ambiguïté d'échantillonnage de navires et de cibles terrestres le long du littoral, avant d'estimer le mouvement de la cible pour chaque point échantillon. Une fois l'estimation terminée, nous avons regroupé des échantillons de cibles pour extraire l'ensemble des propriétés du navire. Lorsque des données GMTI considérablement suréchantillonnées sont acquises par des radars aériens, on obtient les intervalles de traitement cohérent correspondant aux périodes des vagues océaniques qui influent sur le mouvement du navire, ce qui permet d'extraire des données de celui-ci les estimations du mouvement de l'océan au moyen d'une analyse temps-fréquence. L'intégration d'estimations du mouvement de l'océan à l'ensemble en fonction de l'historique de la distance représentant le navire permet une focalisation SAR fine de son image. Le rapport comporte l'exemple s'un navire de 167 m se déplaçant au large des côtes de Terre-Neuve. Bien que l'intervalle de traitement cohérent des données SAR-GMTI spatiales soit trop court pour être appliqué à une estimation du mouvement de la mer, la vitesse de plateforme élevée des radars spatiaux réduit la sensibilité SAR au mouvement de la mer, et celui-ci a peu d'incidence sur la focalisation SAR dans le cas d'états de mer modérés. Les résultats SAR-GMTI obtenus de 49 navires traversant le détroit de Gibraltar et de 23 autres dans le détroit de Georgia reposaient sur des rapports SIA (système d'information automatisé) destinés à valider les mesures SAR-GMTI calculées à partir de données RADARSAT-2. Les résultats ont montré que les mesures SAR-GMTI permettent d'estimer la vitesse d'un navire à ±0,25 m/s, le cap à ±12,4 °C, la longueur à 34,5 m près ou mieux (±35 % de la longueur signalée du navire) et la position à 37 m près ou mieux (à un écart-type).

14. KEYWORDS, DESCRIPTORS or IDENTIFIERS (Technically meaningful terms or short phrases that characterize a document and could be helpful in cataloguing the document. They should be selected so that no security classification is required. Identifiers, such as equipment model designation, trade name, military project code name, geographic location may also be included. If possible keywords should be selected from a published thesaurus, e.g., Thesaurus of Engineering and Scientific Terms (TEST) and that thesaurus identified. If it is not possible to select indexing terms which are Unclassified, the classification of each should be indicated as with the title.)

Ship motion, sea motion, GMTI, DPCA, ATI, EDPCA, range history, phase history, airborne SAR-GMTI, space-based SAR-GMTI, time-frequency decomposition, non-parametric detection, parametric detection, velocity estimation, ship length, ship heading